

APRIL 2022

AJNR

VOLUME 43 • PP 509–648

AJNR

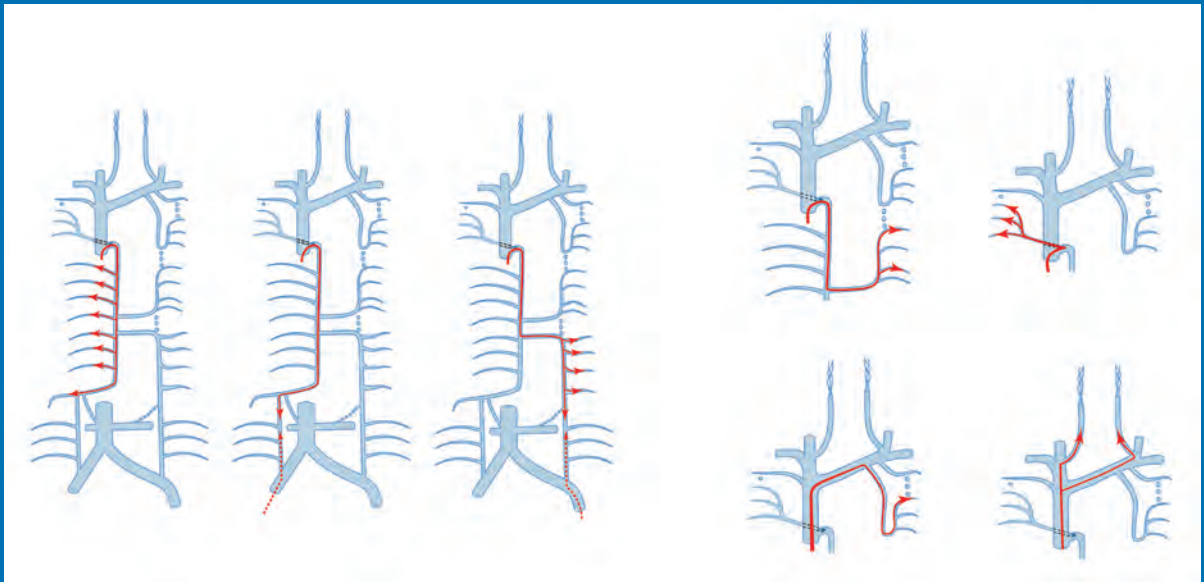
AMERICAN JOURNAL OF NEURORADIOLOGY

APRIL 2022
VOLUME 43
NUMBER 4
WWW.AJNR.ORG

THE JOURNAL OF DIAGNOSTIC AND
INTERVENTIONAL NEURORADIOLOGY

Anatomy of spinal venous drainage related to CSF-venous fistula treatment
Follow-up of intracranial aneurysms treated by flow diverters
Stent-assisted coiling of M2 segment MCA aneurysms
Photon-counting CT of the temporal bone

Official Journal ASNR • ASFNR • ASHNR • ASPNR • ASSR



WEB™ 17

Aneurysm Embolization System

LOWER PROFILE



NEW SIZES



MORE ACCESS OPTIONS



INDICATIONS FOR USE:

The WEB Aneurysm Embolization System is intended for the endovascular embolization of ruptured and unruptured intracranial aneurysms and other neurovascular abnormalities such as arteriovenous fistulae (AVF). The WEB Aneurysm Embolization System is also intended for vascular occlusion of blood vessels within the neurovascular system to permanently obstruct blood flow to an aneurysm or other vascular malformation.

POTENTIAL COMPLICATIONS:

Potential complications include but are not limited to the following: hematoma at the site of entry, aneurysm rupture, emboli, vessel perforation, parent artery occlusion, hemorrhage, ischemia, vasospasm, clot formation, device migration or misplacement, premature or difficult device detachment, non-detachment, incomplete aneurysm filling, revascularization, post-embolization syndrome, and neurological deficits including stroke and death. For complete indications, potential complications, warnings, precautions, and instructions, see instructions for use (IFU provided with the device).

VIA 21, 27, 33 - The VIA Microcatheter is intended for the introduction of interventional devices (such as the WEB device/stents/flow diverters) and infusion of diagnostic agents (such as contrast media) into the neuro, peripheral, and coronary vasculature.

VIA 17, 17 Preshaped - The VIA Microcatheter is intended for the introduction of interventional devices (such as the WEB device/stents/flow diverters) and infusion of diagnostic agents (such as contrast media) into the neuro, peripheral, and coronary vasculature.

The VIA Microcatheter is contraindicated for use with liquid embolic materials, such as n-butyl 2-cyanoacrylate or ethylene vinyl alcohol & DMSO (dimethyl sulfoxide).

The device should only be used by physicians who have undergone training in all aspects of the WEB Aneurysm Embolization System procedure as prescribed by the manufacturer.

RX Only: Federal law restricts this device to sale by or on the order of a physician.

For healthcare professional intended use only.



MicroVention Worldwide
Innovation Center

PH +1.714.247.8000

35 Enterprise
Aliso Viejo, CA 92656 USA
MicroVention UK Limited
MicroVention Europe, S.A.R.L.
MicroVention Deutschland GmbH
Website

PH +44 (0) 191 258 6777
PH +33 (1) 39 21 77 46
PH +49 211 210 798-0
microvention.com



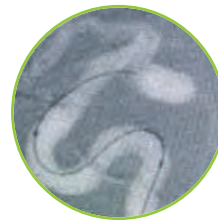
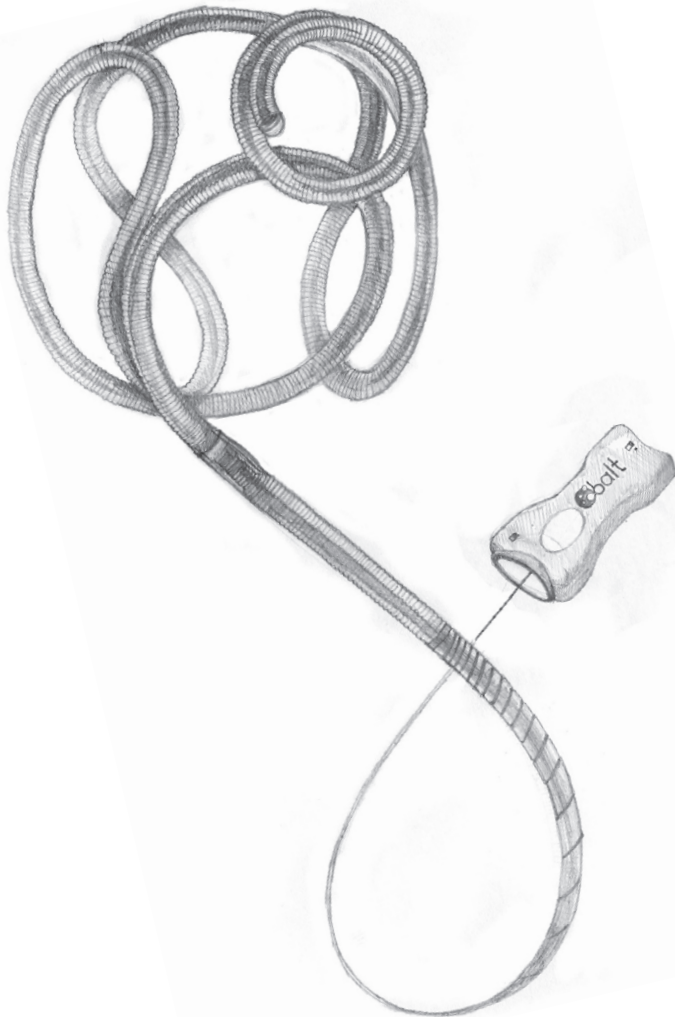
WEB™ and VIA™ are registered trademarks
of Sequent Medical, Inc. in the United States.

©2021 MicroVention, Inc. MM1184 WW 11/2021

OPTIMAX™

COIL

**VOLUME AND PERFORMANCE
FROM START TO FINISH**



OptiMAX Offers:

- Greater packing volume*
- Super Soft in 1mm to 3.5mm
- Complete portfolio in half sizes and unique lengths

Visit our products page at www.baltgroup.com to learn more.

For a list of indications, warnings, precautions, and contraindications, refer to IFU-057

*Compared to 10 system coil

Balt USA

29 Parker, Irvine, CA 92618
tel 949.788.1443 fax 949.788.1444

baltgroup.com

©2022 BALT USA MKTG-278 Rev. A

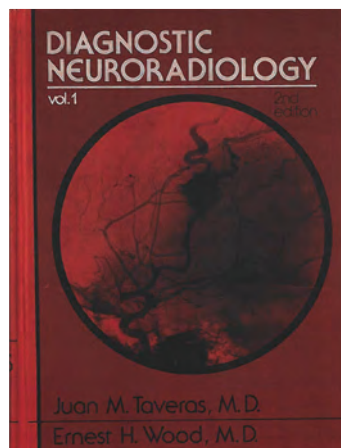
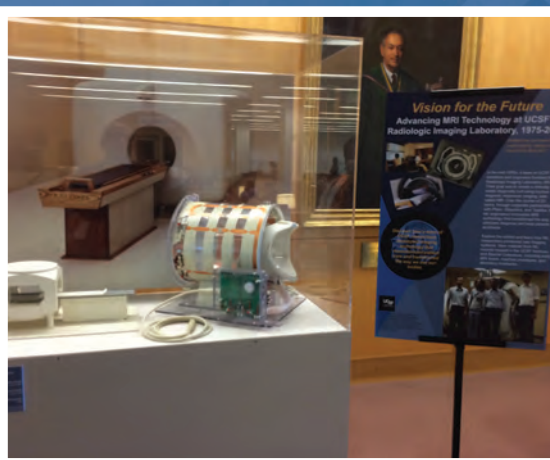


Celebrating 60 Years

1962-2022

The American Society of Neuroradiology was formed on April 18, 1962, in New York City. The following purposes of the organization were unanimously adopted by the fourteen founding members:

1. To develop and support standards for the training in the practice of Neuroradiology.
2. To foster independent research in Neuroradiology.
3. To promote a closer fellowship and exchange of ideas among Neuroradiologists.



Visit www.asnr.org for more photos, videos and historical facts and be sure to follow **#ASNR60th** on social media so you don't miss a single thing. We have lots planned for 2022!

AJNR *go green*

***AJNR* urges American Society of Neuroradiology members to reduce their environmental footprint by voluntarily suspending their print subscription.**

The savings in paper, printing, transportation, and postage directly fund new electronic enhancements and expanded content.

The digital edition of *AJNR* presents the print version in its entirety, along with extra features including:

- Publication Preview
- Case Collection
- Podcasts
- The *AJNR* News Digest
- The *AJNR* Blog

It also reaches subscribers much faster than print. An electronic table of contents will be sent directly to your mailbox to notify you as soon as it publishes.

Readers can search, reference, and bookmark current and archived content 24 hours a day on www.ajnr.org.

ASNR members who wish to opt out of print can do so by using the *AJNR* Go Green link on the *AJNR* Website (<http://www.ajnr.org/content/subscriber-help-and-services>). Just type your name in the email form to stop print and spare our ecosystem.

I am a trained neuroradiologist.

I am a teacher.

I am compassionate.

I am a researcher.

I am a leader.

I am part of a talented community.

I am curious.

I am a collaborative team player.

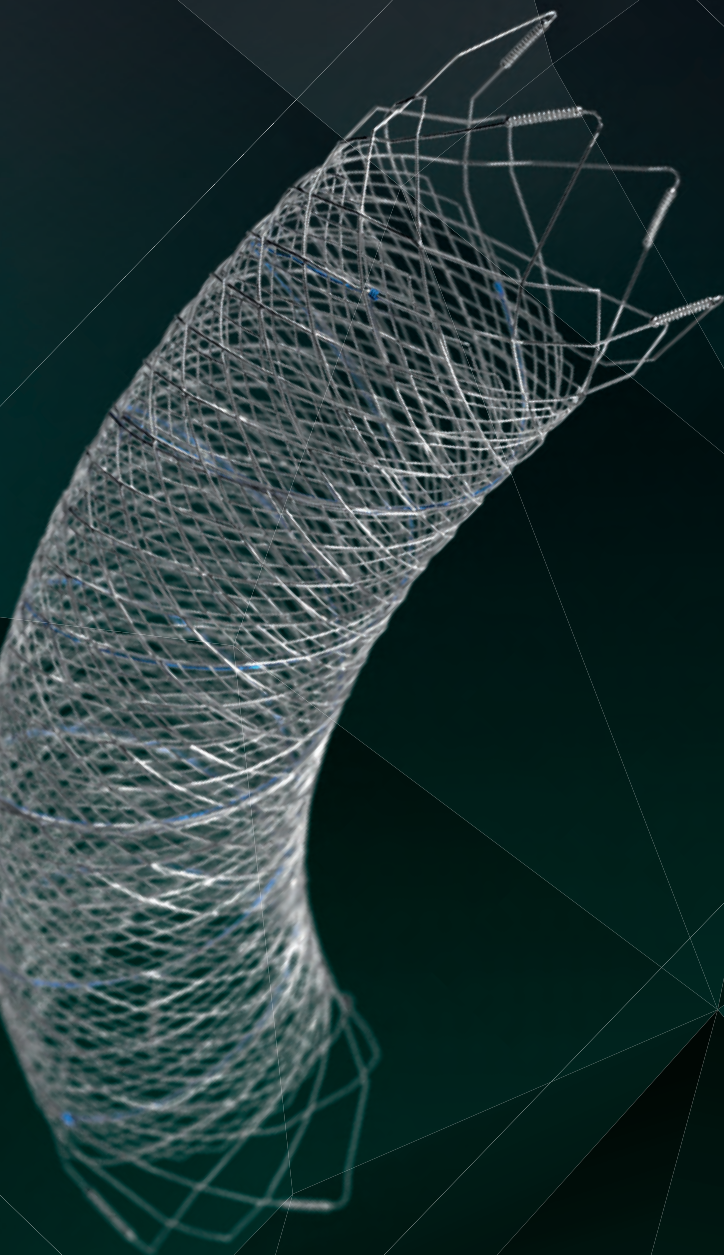
I am a volunteer.

I am ASNR.

Don't miss out on the tools, resources and relationships you've come to rely on. Log in and renew your ASNR membership today! www.asnr.org

ASNR
American Society of Neuroradiology

Introducing FRED™ X™



THE NEXT ADVANCEMENT IN FLOW DIVERSION TECHNOLOGY

The FRED™ X Flow Diverter features the same precise placement and immediate opening of the FRED™ Device, now with X Technology. X Technology is a covalently bonded, nanoscale surface treatment, designed to:

- » **Reduce material thrombogenicity¹**
- » **Maintain natural vessel healing response^{2,3,4}**
- » **Improve device deliverability and resheathing¹**

The only FDA PMA approved portfolio with a 0.021" delivery system for smaller device sizes, and no distal lead wire.



For more information, contact your local MicroVention sales representative or visit our website. www.microvention.com



* Data is derived from in vivo and ex vitro testing and may not be representative of clinical performance.

¹ Data on file

² Tanaka M et al. Design of biocompatible and biodegradable polymers based on intermediate water concept. *Polymer Journal*. 2015;47:114-121.

³ Tanaka M et al. Blood compatible aspects of poly(2-methoxyethylacrylate) (PMEA) – relationship between protein adsorption and platelet adhesion on PMEAs surface. *Biomaterials*. 2000;21:1471-1481.

⁴ Schiel L et al. X Coating™: A new biopassive polymer coating. *Canadian Perfusion Canadienne*. June 2001;11(2):9.

Indications for Use: The FRED X System is indicated for use in the internal carotid artery from the petrous segment to the terminus for the endovascular treatment of adult patients (22 years of age or older) with wide-necked (neck width 4 mm or dome-to-neck ratio < 2) saccular or fusiform intracranial aneurysms arising from a parent vessel with a diameter 2.0 mm and 5.0 mm.

Rx Only: Federal (United States) law restricts this device to sale by or on the order of a physician.

MICROVENTION, FRED and HEADWAY are registered trademarks of MicroVention, Inc. in the United States and other jurisdictions. Stylized X is a trademark of MicroVention, Inc. © 2022 MicroVention, Inc. MM1222 US 02/22

CALL FOR AJNR EDITOR-IN-CHIEF CANDIDATES

Over the last 41 years, the editorial team of the *American Journal of Neuroradiology (AJNR)* has played a pivotal role in shaping our specialty of neuroradiology. In June 2023, Jeffrey S. Ross, MD, will complete an 8-year term as the sixth Editor-in-Chief (EIC) of the *AJNR*. He was preceded by a number of distinguished editors including our first *AJNR* EIC, Juan M. Taveras, MD (1980-1989), followed by Michael S. Huckman, MD (1990-1997), Robert M. Quencer, MD (1997-2005), Robert I. Grossman, MD (2006-2007), and Mauricio Castillo, MD (2007-2015).

We especially wish to thank Dr. Jeffrey Ross for his extraordinary dedication and exceptional contributions to the *AJNR*. Under his strong leadership, the *AJNR* remains the premier clinical neuroimaging journal with high-quality, peer-reviewed articles that serve as a beacon for achieving excellence in patient care, research, and teaching. There are an impressive 6867 subscribers across the globe: 1389 are in print and 5472 are digital.

Dr. Ross has assembled a talented international editorial board during his tenure. The *AJNR* issues 12 journals each year (± 200 pages per issue)—all with peer-reviewed articles from highly respected researchers in the field. With 1700+ papers, the number of submissions to the journal was record-breaking in 2020. Over 80 COVID-19 papers have received expedited publication to date, and more than 1300 original submissions are projected for 2021. The *AJNR* website had an incredible 11.7 million visits in 2021. There is also a strong presence on social media and subscribers may now avail themselves of an enhanced website platform. There are 3 monthly podcasts including “*Issue Highlights*,” “*Fellows’ Journal Club*,” and “*Annotated Bibliography*,” which offers continuing medical education. In addition, during Dr. Ross’ tenure, the Impact Factor and h-index for the journal have steadily increased and contribute to the *AJNR*’s international recognition as the leading journal for all aspects of neuroimaging research, education, and best practice.

A search for a new Editor-in-Chief will begin in early 2022.

The new Editor-in-Chief will be announced in December 2022 and will transition into the position beginning in January 2023. The actual term will begin July 1, 2023. The EIC will provide leadership and strategic vision for the journal as well as report on all editorial matters to the ASNR Board of Directors (BOD). Other responsibilities include maintaining the journal’s standard of excellence building on its reputation nationally and internationally. The EIC will be responsible for conducting, directing, and/or supervising the solicitation, evaluation, revision, and selection of all scientific and other materials to be published in the *American Journal of Neuroradiology*. The incumbent will work efficiently with the journal’s online manuscript processing system to conduct initial screening of manuscripts; make timely decisions about reviewed and revised submissions; provide constructive comments for authors as appropriate; write editorials; and meet with *AJNR* staff.

In addition, the EIC shall decide upon and approve of the content and design of tables of contents, letters to the editor, book reviews, advertisements, and other pages published in the *AJNR* as well as oversight of social media related to the journal. The EIC will also work collaboratively with the journal’s editorial board to determine the organizational structure, titles, functions, appointments, and terms of all editorial positions including reviewers, editorial advisory boards, and senior editors. The EIC may appoint senior editors who must be senior members of the ASNR. The number of senior editors shall be budgeted and approved by the ASNR BOD. Senior editors will serve at the pleasure of the EIC who shall establish the terms of service, including supervising and evaluating performance, and will exercise the right to retain or replace any senior editor as the workflow or operational demands require. The appointments of senior editors will be for a term of 1 year initially and may be extended at the discretion of the EIC.

The EIC in performing duties will observe the general *Policies and Procedures* established by the ASNR BOD, and will operate within the budget approved by the Board of Directors. The EIC will be consulted about, and will participate in *AJNR* operations including advertising, publication channels, expense management, and new or renewed contracts. The EIC will report regularly to the ASNR BOD and will attend Board of Director Meetings and other meetings as requested by the Executive Director. Each year the Editor will develop a budget along with the Managing Editor for approval by the ASNR Financial Management Committee and Board of Directors. This will be done in a manner consistent with the fiscal policies established by the Society.

QUALIFICATIONS OF THE SUCCESSFUL CANDIDATE INCLUDE:

- MD degree; Senior Member of ASNR in North America, neuroradiology subspecialty certification
- Familiarity with *AJNR* and its mission
- Familiarity with ASNR and its mission

- Presently or recently engaged in a leadership role in neuroradiology with broad neuroradiology knowledge
- Excellent leadership and supervisory skills to motivate and inspire professional staff as well as interpersonal skills—impartiality, diplomacy, high ethical standards and integrity including a clear understanding of the ethical guidelines established for scholarly publishing
- Leadership needed to develop and articulate a vision and the ability to inspire people with that vision
- Demonstrated track record of academic excellence including extensive experience in both publishing in and reviewing for peer-reviewed journals
- Excellent communication and writing skills and experience in critically appraising scientific articles
- Creativity and passion about finding new ways to expand the journal content
- The ability to formulate a budget and assist leadership in oversight of journal business decisions such as selecting major vendors (e.g., printing, composition, redaction, copyediting, and other technical aspects affecting journal operations), as well as expense and revenue related decisions
- Ability to appoint a strong, diverse, and representative team of editors
- High level of organizational skills
- Editorial board or prior editorial experience preferred

The term is for 5 years renewable for an additional 3 years for a total of 8 years and subject to annual review by the ASNR Board of Directors. It is expected the EIC will devote 16-20 hours per week to these duties and a stipend will be provided.

A diverse, experienced, and knowledgeable search committee has been tasked with identifying leading candidates. The search committee consists of Tina Young Poussaint, MD, FACR, Chair, Mauricio Castillo, MD, FACR, Pina Sanelli, MD, MPH, FACR, Carolyn Meltzer, MD, FACR, Erin Simon Schwartz, MD, FACR, Joshua Nickerson, MD, Courtney Tomblinson, MD, and senior editors including Harry Cloft, MD, PhD, Christopher Filippi, MD, Thierry Huisman, MD, Peter D. Chang, MD, Lubdha Shah, MD, Gregory Zaharchuk MD, PhD, C. Douglas Phillips, MD, Yvonne Lui, MD, and Bryan Comstock. The search process will include recruiting and nominating candidates, interviewing candidates, and reviewing vision statements submitted by finalists. The appointment of the new *AJNR* Editor-in-Chief will be announced in December 2022.

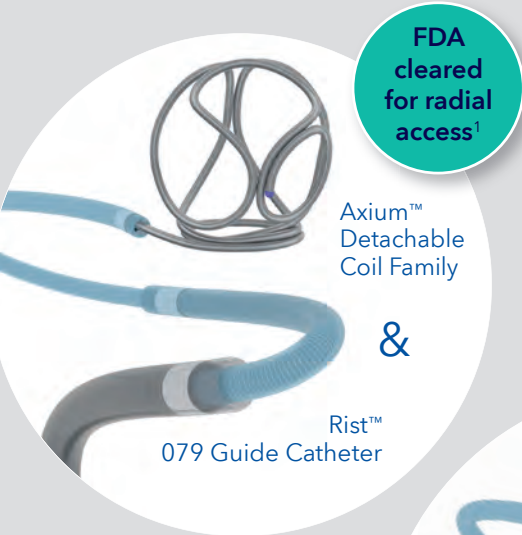
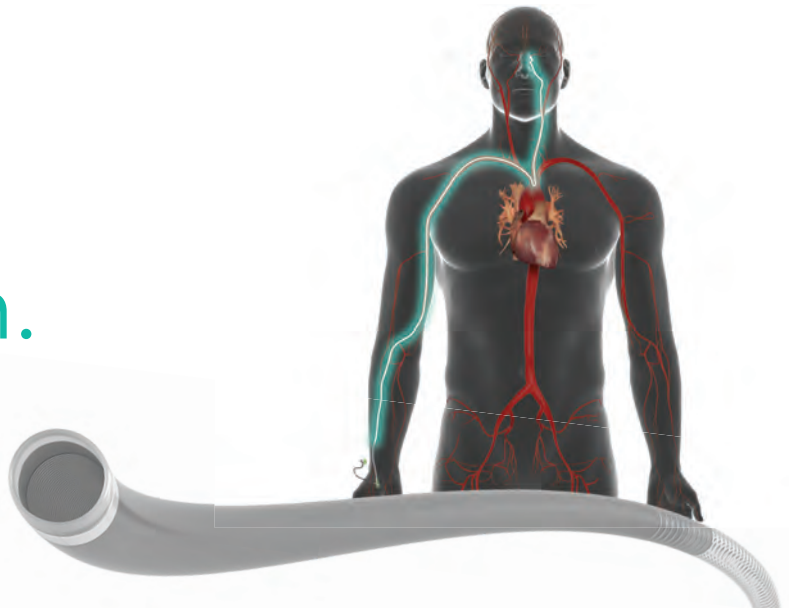
All interested physicians are invited to provide their curriculum vitae and a vision statement to Dr. Tina Young Poussaint, tina.poussaint@childrens.harvard.edu and Karen Halm, khalm@asn.org. To ensure a broad and diverse pool of candidates, the committee welcomes nominations from the ASNR membership. *The deadline for receipt of submissions is August 1, 2022.*

Tina Young Poussaint, MD, FACR
Chair, Editor-in-Chief Search Committee
President, American Society of Neuroradiology

Medtronic

The complete radial solution. Hands down.

Rist™ 079 Guide Catheter



Radial Ready

Radial focused training and support

1. K203432
2. P100018/S026

WARNING: The safety and effectiveness of this device for radial neurovasculature access indirect comparison to a transfemoral approach has not been demonstrated. The risks and benefits for radial access against a transfemoral approach should be carefully weighed and considered for each patient.

PRECAUTION: If using radial artery access, perform a screening examination of the radial artery per institutional practices to ensure that radial access is appropriate for the patient.

Potential complications include but not limited to: Neurological deficits including hand dysfunction, stroke, and death.

CAUTION: Federal (USA) law restricts this device to sale by or on the order of a physician. Indications, contraindications, warnings and instructions for use for Axiom™, Axiom™ Prime, and Axiom™ Prime (Frame) detachable coils can be found on the product labeling supplied with each device.

Indications, contraindications, warnings and instructions for use for the Rist™ 079 Radial Access Guide Catheter, Rist™ Radial Access Selective Catheter, and Pipeline™ Flex Embolization Device with Shield™ Technology can be found at www.medtronic.com/manuals.

UC202214834 EN © 2022 Medtronic. Medtronic, Medtronic logo, and Engineering the extraordinary are trademarks of Medtronic. All other brands are trademarks of a Medtronic company. 9775 Toledo Way, Irvine, CA 92618 USA | Tel 1-800-716-6700 | Fax 763-526-7888 | medtronic.com/NV



AJNR

AMERICAN JOURNAL OF NEURORADIOLOGY

APRIL 2022
VOLUME 43
NUMBER 4
WWW.AJNR.ORG

Publication Preview at www.ajnr.org features articles released in advance of print. Visit www.ajnrblog.org to comment on AJNR content and chat with colleagues and AJNR's News Digest at <http://ajnrdigest.org> to read the stories behind the latest research in neuroimaging.

509 **PERSPECTIVES** *M. Hauben*

REVIEW ARTICLES

- 510 **Endovascular Management of Intracranial Dural AVFs: Transvenous Approach** *K.D. Bhatia, et al.* **INTERVENTIONAL**
- 517 **Anatomy of Spinal Venous Drainage for the Neurointerventionalist: From Puncture Site to Intervertebral Foramen** *N. Borg, et al.* **INTERVENTIONAL**

GENERAL CONTENTS

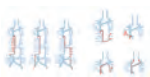
- 526 **Machine Learning in Differentiating Gliomas from Primary CNS Lymphomas: A Systematic Review, Reporting Quality, and Risk of Bias Assessment** *G.I. Cassinelli Petersen, et al.* **ADULT BRAIN FUNCTIONAL**
- 534 **SWI as an Alternative to Contrast-Enhanced Imaging to Detect Acute MS Lesions** *G. Caruana, et al.* **ADULT BRAIN FUNCTIONAL**
- 540 **Pulsatility Index in the Basal Ganglia Arteries Increases with Age in Elderly with and without Cerebral Small Vessel Disease** *V. Perosa, et al.* **ADULT BRAIN**
- 547 **Identification of Small, Regularly Shaped Cerebral Aneurysms Prone to Rupture** *S.F. Salimi Ashkezari, et al.* **INTERVENTIONAL**
- 554 **Follow-up of Intracranial Aneurysms Treated by Flow Diverters: Evaluation of Parent Artery Patency Using 3D-T1 Gradient Recalled-Echo Imaging with 2-Point Dixon in Combination with 3D-TOF-MRA with Compressed Sensing** *J. Burel, et al.* **INTERVENTIONAL**
- 560 **Safety, Efficacy, and Durability of Stent-Assisted Coiling Treatment of M2 (Insular) Segment MCA Aneurysms** *K. Aydin, et al.* **INTERVENTIONAL**
- 568 **A Meta-analysis of Combined Aspiration Catheter and Stent Retriever versus Stent Retriever Alone for Large-Vessel Occlusion Ischemic Stroke** *D.A. Scharztz, et al.* **INTERVENTIONAL**
- 575 **CT-Guided C2 Dorsal Root Ganglion Radiofrequency Ablation for the Treatment of Cervicogenic Headache: Case Series and Clinical Outcomes** *J.L. Chazen, et al.* **INTERVENTIONAL SPINE**
- 579 **A New Frontier in Temporal Bone Imaging: Photon-Counting Detector CT Demonstrates Superior Visualization of Critical Anatomic Structures at Reduced Radiation Dose** *J.C. Benson, et al.* **HEAD & NECK**

AJNR (Am J Neuroradiol ISSN 0195-6108) is a journal published monthly, owned and published by the American Society of Neuroradiology (ASNR), 820 Jorie Boulevard, Oak Brook, IL 60523. Annual dues for the ASNR include approximately 21% for a journal subscription. The journal is printed by Intellicor Communications, 330 Eden Road, Lancaster, PA 17601; Periodicals postage paid at Oak Brook, IL and additional mailing offices. Printed in the U.S.A. POSTMASTER: Please send address changes to American Journal of Neuroradiology, P.O. Box 3000, Denville, NJ 07834, U.S.A. Subscription rates: nonmember \$430 (\$505 foreign) print and online, \$320 online only; institutions \$495 (\$565 foreign) print and basic online, \$980 (\$1050 foreign) print and extended online, \$380 online only (basic), \$825 online only (extended); single copies are \$35 each (\$40 foreign). Indexed by PubMed/MEDLINE, BIOSIS Previews, Current Contents (Clinical Medicine and Life Sciences), EMBASE, Google Scholar, HighWire Press, Q-Sensei, RefSeek, Science Citation Index, SCI Expanded, ReadCube, and Semantic Scholar. Copyright © American Society of Neuroradiology.

-    **585** Prediction of Wound Failure in Patients with Head and Neck Cancer Treated with Free Flap Reconstruction: Utility of CT Perfusion and MR Perfusion in the Early Postoperative Period *Y. Ota, et al.* **HEAD & NECK**
-  **592** Revisiting CT Signs of Unilateral Vocal Fold Paralysis: A Single, Blinded Study *M.H. Bashir, et al.* **HEAD & NECK**
-  **597** Extraocular Muscle Enlargement in Growth Hormone–Secreting Pituitary Adenomas *B. Coutu, et al.* **HEAD & NECK**
-  **603** Radiomics Can Distinguish Pediatric Supratentorial Embryonal Tumors, High-Grade Gliomas, and Ependymomas *M. Zhang, et al.* **PEDIATRICS FUNCTIONAL**
-  **611** Different from the Beginning: WM Maturity of Female and Male Extremely Preterm Neonates—A Quantitative MRI Study *V.U. Schmidbauer, et al.* **PEDIATRICS FUNCTIONAL**
- 620** Third Trimester Structural and Diffusion Brain Imaging after Single Intrauterine Fetal Death in Monochorionic Twins: MRI-Based Cohort Study *M. Segev, et al.* **PEDIATRICS FUNCTIONAL**
-   **627** Diagnostic Value of Sylvian Fissure Hyperechogenicity in Fetal SAH *M. Zhang, et al.* **PEDIATRICS**
-  **633** Prenatal MR Imaging Phenotype of Fetuses with Tuberous Sclerosis: An Institutional Case Series and Literature Review *S.K. Goergen, et al.* **PEDIATRICS**
-  **639** Early Ultrasonic Monitoring of Brain Growth and Later Neurodevelopmental Outcome in Very Preterm Infants *V.A.A. Beunders, et al.* **PEDIATRICS**
-  **645** Same-Day Bilateral Decubitus CT Myelography for Detecting CSF-Venous Fistulas in Spontaneous Intracranial Hypotension *L. Carlton Jones, et al.* **SPINE**

BOOK REVIEWS *R.M. Quencer, Section Editor*

Please visit www.ajnrblog.org to read and comment on Book Reviews.



Roadmaps to each foramen, grouped by common venous drainage pathways in Borg et al, in this issue.



Indicates Editor's Choices selection



Indicates Fellows' Journal Club selection



Indicates open access to non-subscribers at www.ajnr.org



Indicates article with supplemental online data



Indicates article with supplemental online video



Evidence-Based Medicine Level 1



Evidence-Based Medicine Level 2

EDITOR-IN-CHIEF

Jeffrey S. Ross, MD

Professor of Radiology, Department of Radiology,
Mayo Clinic College of Medicine, Phoenix, AZ

SENIOR EDITORS

Harry J. Cloft, MD, PhD

Professor of Radiology and Neurosurgery,
Department of Radiology, Mayo Clinic College of
Medicine, Rochester, MN

Christopher G. Filippi, MD

Professor and Alice Ettinger-Jack R. Dreyfuss
Chair of Radiology,
Tufts University School of Medicine,
Radiologist-in-Chief
Tufts University Medical Center, Boston, MA

Thierry A.G.M. Huisman, MD

Radiologist-in-Chief, Texas Children's Hospital,
Houston, TX

Yvonne W. Lui, MD

Associate Professor of Radiology,
Chief of Neuroradiology,
New York University School of Medicine,
New York, NY

C.D. Phillips, MD, FACR

Professor of Radiology, Weill Cornell Medical
College, Director of Head and Neck Imaging,
New York-Presbyterian Hospital, New York, NY

Lubdha M. Shah, MD, MS

Professor of Radiology and Director of Spine
Imaging, University of Utah Department of
Radiology and Imaging Sciences, Salt Lake City, UT

STATISTICAL SENIOR EDITOR

Bryan A. Comstock, MS

Senior Biostatistician,
Department of Biostatistics,
University of Washington, Seattle, WA

ARTIFICIAL INTELLIGENCE DEPUTY EDITOR

Peter D. Chang, MD

Assistant Professor-in-Residence,
Departments of Radiological Sciences,
Computer Sciences, and Pathology,
Director, Center for Artificial Intelligence in
Diagnostic Medicine (CAIDM),
University of California, Irvine, Irvine, CA

EDITORIAL BOARD

Ashley H. Aiken, Atlanta, GA

Lea M. Alhilali, Phoenix, AZ

Mohammed A. Almekhlafi, Calgary, Alberta,
Canada

Joachim Berkefeld, Frankfurt, Germany

Aashim Bhatia, Pittsburgh, PA

Waleed Brinjikji, Rochester, MN

Judah Burns, New York, NY

Danielle Byrne, Dublin, Ireland

Federico Cagnazzo, Montpellier, France

J. Levi Chazen, New York, NY

James Y. Chen, San Diego, CA

Gloria C. Chiang, New York, NY

Daniel Chow, Irvine, CA

Kars C.J. Compagne, Rotterdam, The Netherlands

Arturo Consoli, Suresnes, France

Seena Dehkharghani, New York, NY

Nilesh K. Desai, Houston, TX

Yonghong Ding, Rochester, MN

Birgit Ertl-Wagner, Toronto, Ontario, Canada

Clifford J. Eskey, Hanover, NH

Massimo Filippi, Milan, Italy

Nils D. Forkert, Calgary, Alberta, Canada

Ana M. Franceschi, New York, NY

Frank Gaillard, Melbourne, Australia

Joseph J. Gemmete, Ann Arbor, Michigan

Wende N. Gibbs, Phoenix, AZ

Philipp Gölitz, Erlangen, Germany

Brent Griffith, Detroit, MI

Joseph M. Hoxworth, Phoenix, Arizona

Raymond Y. Huang, Boston, MA

Gábor Janiga, Magdeburg, Germany

Christof Karmonik, Houston, TX

Timothy J. Kaufmann, Rochester, MN

Hillary R. Kelly, Boston, MA

Toshibumi Kinoshita, Akita, Japan

Alexander W. Korutz, Chicago, IL

Stephen F. Kralik, Houston, TX

Alexander Lerner, Los Angeles, CA

Yinsheng Li, Madison, WI

Franklin A. Marden, Chicago, IL

Markus A. Möhlenbruch, Heidelberg, Germany

Kambiz Nael, Los Angeles, CA

Renato Hoffmann Nunes, Sao Paulo, Brazil

Sasan Partovi, Cleveland, OH

Johannes A.R. Pfaff, Salzburg, Austria

Laurent Pierot, Reims, France

Alireza Radmanesh, New York, NY

Prashant Raghavan, Baltimore, MD

Eytan Raz, New York, NY

Paul M. Ruggieri, Cleveland, OH

Sebastian Schafer, Madison, WI

Maksim Shapiro, New York, NY

Timothy Shepherd, New York, NY

James Shin, New York, NY

Mark S. Shiroishi, Los Angeles, CA

Bruno P. Soares, Burlington, VT

Jason F. Talbott, San Francisco, CA

Ruth Thiex, Everett, Washington

Vincent Thijs, Melbourne, Victoria, Australia

Anderanik Tomasian, Los Angeles, CA

Fabio Triulzi, Milan, Italy

Anja G. van der Kolk, Utrecht, the Netherlands

Arastoo Vossough, Philadelphia, PA

Elysa Widjaja, Toronto, Ontario, Canada

Leonard Yeo, Singapore

Woong Yoon, Gwangju, South Korea

David M. Yousem, Evergreen, CO

Carlos Zamora, Chapel Hill, NC

Chengcheng Zhu, Seattle, WA

EDITORIAL FELLOW

Vivek Yedavalli, Baltimore, MD

SPECIAL CONSULTANTS TO THE EDITOR

AJNR Blog Editor

Neil Lal, Denver, CO

Case of the Month Editor

Nicholas Stence, Aurora, CO

Case of the Week Editors

Matylda Machnowska, Toronto, Ontario, Canada

Anvita Pauranik, Calgary, Alberta, Canada

Vinil Shah, San Francisco, CA

Classic Case Editor

Sandy Cheng-Yu Chen, Taipei, Taiwan

Health Care and Socioeconomics Editor

Pina C. Sanelli, New York, NY

Physics Editor

Greg Zaharchuk, Stanford, CA

Podcast Editor

Courtney Tomblinson, Nashville, TN

Deputy Podcast Editor

Kevin Hiatt, Winston-Salem, NC

Twitter Editor

Jacob Ormsby, Albuquerque, New Mexico

Official Journal:

American Society of Neuroradiology

American Society of Functional Neuroradiology

American Society of Head and Neck Radiology

American Society of Pediatric Neuroradiology

American Society of Spine Radiology

Founding Editor

Juan M. Taveras

Editors Emeriti

Mauricio Castillo, Robert I. Grossman,

Michael S. Huckman, Robert M. Quencer

Managing Editor

Karen Halm

Assistant Managing Editor

Laura Wilhelm

Executive Director, ASNR

Mary Beth Hepp



Title: Weeping Higan Cherry Tree. The weeping Higan cherry tree (*Prunus Subhirtella*), seen here in early bloom, is head-turning and soothing. “Weeping” describes trees whose branches gracefully bend, droop, and cascade due to their softness. “Higan” is derived from the Japanese Buddhist equinox ceremony of Ohigan. Because the blossoms are so short-lived, they are symbolic of the ephemeral nature of life. While the blossoms are short-lived, the trees can display impressive longevity. Miharu Takizakura, a 1000 year-old weeping Higan cherry in Japan that was designated a national treasure in 1922, draws an estimated 300,000 visitors per year. Contributing to their longevity is a Lazarus-like process known as endocaulous rooting, in which a root growing inside a decaying trunk develops into a new trunk that may be revealed when the dead trunk drops off. Native to Japan, they were introduced into the United States and Europe in the late 19th century, where cherry blossom festivals have taken root. Kobayashi Issa, regarded as one of “great four” Haiku masters of Japan, wrote: “What a strange thing! to be alive beneath cherry blossoms” and “In the cherry blossom’s shade there’s no such thing as a stranger.”

Manfred Hauben, MD, MPH, Pfizer Inc and NYU Langone Health, New York City

Endovascular Management of Intracranial Dural AVFs: Transvenous Approach

 K.D. Bhatia,  H. Lee,  H. Kortman,  J. Klostranec,  W. Guest,  T. Wälchli,  I. Radovanovic,  T. Krings, and  V.M. Pereira



ABSTRACT

SUMMARY: In this third review article on the endovascular management of intracranial dural AVFs, we discuss transvenous embolization approaches. Transvenous embolization is increasingly popular and now the first-line approach for ventral dural AVFs involving the cavernous sinus and hypoglossal canal. In addition, transvenous embolization is increasingly used in lateral epidural dural AVFs in high-risk locations such as the petrous and ethmoid regions. The advantage of transvenous embolization in these locations is the ability to retrogradely embolize the draining vein and fistula while reducing the risk of ischemic cranial neuropathy or brain parenchymal infarction commonly feared from a transarterial approach. By means of coils \pm ethylene-vinyl alcohol copolymer, transvenous embolization can achieve angiographic cure rates of 80%–90% in ventral locations. Potential complications include transient cranial neuropathy, neurologic deterioration due to venous outflow obstruction, and perforation while navigating pial veins. Transvenous embolization should be considered when dural AVFs arise in proximity to the vasa nervosum or extracranial-intracranial anastomoses.

ABBREVIATIONS: CCF = carotid cavernous fistula; dAVF = dural AVF; ECA = external carotid artery; EC-IC = external carotid to internal carotid; EVOH = ethylene-vinyl alcohol copolymer; IPS = inferior petrosal sinus; JR-NET3 = Japanese Registry of Neuro Endovascular Therapy; RPC = reverse pressure cooker; TAE = transarterial embolization; TVE = transvenous embolization

In this third review article on the endovascular management of intracranial dural AVFs (dAVFs), we discuss transvenous approaches. Transvenous embolization (TVE) is an increasingly popular approach for the treatment of intracranial dAVFs and the preferred approach for ventral skull base locations due to the risk of cranial neuropathy from arterial approaches.^{1,2} Treatment goals, favorable anatomic locations, technical approaches, alternative access strategies, outcomes, and complications are discussed in this review.

Treatment Goals

As with all treatment approaches to intracranial dAVFs, the clinical goal of TVE is to reduce the risk of future hemorrhage or non-hemorrhagic neurologic deficits (see the first article in this series on Principles). Therefore, disconnection of dangerous cortical venous reflux is more important than angiographic cure of the dAVF. In selected low-risk benign dAVFs (Borden I/Cognard I), the clinical goal is, instead, to ameliorate disabling symptoms such as intractable pulsatile tinnitus.

TVE can be considered analogous to microsurgical disconnection for dAVFs in that the angiographic goal is to follow the proximal venous course and occlude the proximal aspect of the draining vein or sinus, ie, the “foot” of the vein.³ By means of a retrograde approach to the fistulous point, TVE with ethylene-vinyl alcohol copolymer (EVOH) and/or coils can occlude the foot of the draining vein and the fistulous point in situations in which transarterial embolization (TAE) is technically difficult or dangerous.⁴ Also analogous to microsurgery,^{3,5} disconnection of cortical venous reflux can downgrade the dAVF from an aggressive to a benign lesion.

Indications


TVE is indicated for dAVFs in which TAE approaches are associated with a moderate risk of the following:

1. Ischemic cranial neuropathy due to adjacent vasa nervosum

Received February 5, 2021; accepted after revision July 9.

From the Division of Neuroradiology (K.D.B., H.L., H.K., J.K., W.G., T.K., V.M.P.) and Division of Neurosurgery (T.W., I.R., T.K., V.M.P.), Toronto Western Hospital, Toronto, Ontario, Canada; Division of Medical Imaging (K.D.B.), Sydney Children's Hospital Network, Westmead, New South Wales, Australia; Division of Paediatrics (K.D.B.), Faculty of Medicine, University of Sydney, Camperdown, New South Wales, Australia; Division of Paediatrics (K.D.B.), Faculty of Medicine, University of New South Wales, Kensington, New South Wales, Australia; Division of Medical Imaging (K.D.B.), Faculty of Medicine, Macquarie University, Macquarie Park, New South Wales, Australia; Department of Neurosurgery (H.L.), Stanford University School of Medicine, Stanford, California; Division of Neuroradiology (H.K.), Elisabeth-TweeSteden Ziekenhuis Hospital, Tilburg, the Netherlands; Division of Interventional Neuroradiology (J.K.), McGill University Health Centre, Montreal, Quebec, Canada; and Division of Interventional Neuroradiology (W.G., V.M.P.), St. Michael's Hospital, Toronto, Ontario, Canada.

Please address correspondence to Kartik Dev Bhatia, MD, Department of Medical Imaging, Sydney Children's Hospital Network, Corner Hawkesbury Rd and Hainsworth St, Westmead, NSW, 2145, Australia; e-mail: Kartik.bhatia@health.nsw.gov.au

 Indicates open access to non-subscribers at www.ajnr.org

<http://dx.doi.org/10.3174/ajnr.A7300>

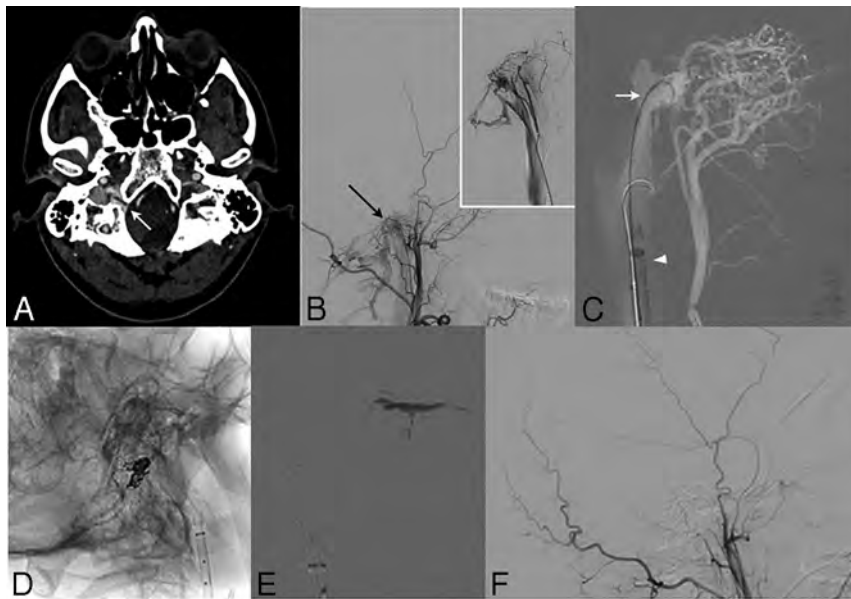


FIG 1. Transvenous embolization of a right hypoglossal canal (anterior condylar) dAVF using a reverse pressure cooker technique in a 47-year-old man for management of refractory pulsatile tinnitus. *A*, CT angiogram (axial) demonstrates increased vascularity surrounding the right hypoglossal canal (*white arrow*) with arterialization of the right anterior condylar vein, suggestive of a dAVF. *B*, Right lateral ECA cerebral angiography confirms the diagnosis, with primary arterial supply via neuromeningeal trunk branches (*black arrow*) of the right ascending pharyngeal artery (inset, selective right ascending pharyngeal artery injection). *C*, Lateral fluoroscopy roadmap of transvenous treatment shows a 6F Destination sheath (Terumo) positioned in the right internal jugular vein (*white arrowhead*), through which a SONIC 1.5F microcatheter (Balt) with a 4.5-cm detachable tip was positioned at the fistulous point (*white arrow*). *D*, A 1.5F Marathon microcatheter (Covidien) was placed in the anterior condylar confluence to deploy 7 detachable coils, with the coil mass demonstrated in the working projection. *E*, The Marathon microcatheter was removed, and the SONIC microcatheter was primed with dimethyl-sulfoxide before forming an Onyx (Covidien) cast at the fistulous point. *F*, Right ECA lateral projection angiography demonstrates complete occlusion of the fistula.

2. Parenchymal infarction from external carotid to internal carotid (EC-IC) anastomoses
3. Inability to reach a distal embolization position due to tortuosity or small-vessel caliber.

These anatomic and angioarchitectural factors are particularly associated with dAVFs adjacent to the ventral skull base² (eg, cavernous, condylar, or clival). However, increasing use of TVE techniques for lateral and dorsal dAVFs is a notable trend.^{4,6-8}

Anatomic Locations

In this series of articles, in addition to using the Borden and Cognard classification systems, we also reference the classification system of Geibprasert et al¹ when stratifying dAVFs by anatomic locations. This classification system, based on the anatomic-embryologic venous drainage pattern of the fistula and divided into ventral, lateral, and dorsal epidural groups,¹ is detailed in the first article in this series (Principles).

TVE is particularly useful in ventral skull base locations due to these dAVFs involving external carotid artery (ECA) branches to the blood supply of cranial nerves that traverse the ventral skull base foramina.¹ These ventral locations also have extensive adjacent EC-IC or external carotid-vertebral artery anastomoses.²

Ventral locations for which TVE is now the most common approach include the cavernous sinus and ventral aspect of the foramen magnum (eg, hypoglossal canal).⁹⁻¹³ An example of a TVE for a hypoglossal canal dAVF is demonstrated in Fig 1.

Carotid-cavernous fistulas (CCFs) can be divided into direct (Barrow classification type A) and indirect (Barrow B-D) types.¹⁴ Direct CCFs involve a single-hole high-flow communication between the cavernous ICA and the cavernous sinus, occurring after trauma or dissection.⁹ Indirect CCFs are multi-hole dAVFs that drain into the cavernous sinus and are, therefore, analogous to other dAVFs being considered in this series of articles.^{9,14,15} Direct CCFs represent a different type of disease than other dAVFs, and their management lies beyond the scope of this article but has been well-described.^{15,16} The endovascular treatment of indirect CCFs (Barrow B-D), historically undertaken using TAE, has evolved with TVE now the established first-line approach.^{9,13,15} A sample case of TVE for bilateral indirect CCFs is demonstrated in Fig 2.

Petrous dAVFs, though lateral epidural in location, also pose a potential risk of facial nerve palsy during TAE because they receive at least partial arterial supply from vessels that form the facial nerve arterial arcade.⁴ Petrous dAVFs can be treated via TAE, TVE, or microsurgical disconnection, with the proximity of the fistulous point to the facial arcade being the primary consideration.⁴ TVE and microsurgical disconnection for petrous dAVFs both aim to occlude the draining superior petrosal vein of Dandy.³⁻⁵ A sample case of TVE for a petrous dAVF with proximity to the facial arcade is demonstrated in Fig 3.

Ethmoidal dAVFs, embryologically also classified as lateral epidural shunts,¹ pose a risk of retinal artery occlusion during TAE due to their supply via the ethmoidal branches of the ophthalmic artery.¹⁷ Additionally, the tortuosity and small caliber of the ethmoidal arteries can hinder distal microcatheter access.^{6,8} Ethmoid dAVFs are surgically accessible by an anterior cranial fossa approach, and this approach is typically the primary treatment.^{3,17,18} However, TVE is increasingly used as an alternative to craniotomy, with recent evidence that TVE has a significantly improved cure rate compared with TAE with low complication rates.^{6,8}

Other lateral epidural shunts that can be approached with TVE include falcotentorial dAVFs, which are often supplied by small-caliber arterial feeders from the ICA (meningohypophyseal trunk branches) and posterior circulation (posterior meningeal artery, artery of Davidoff and Schechter), which make TAE approaches more

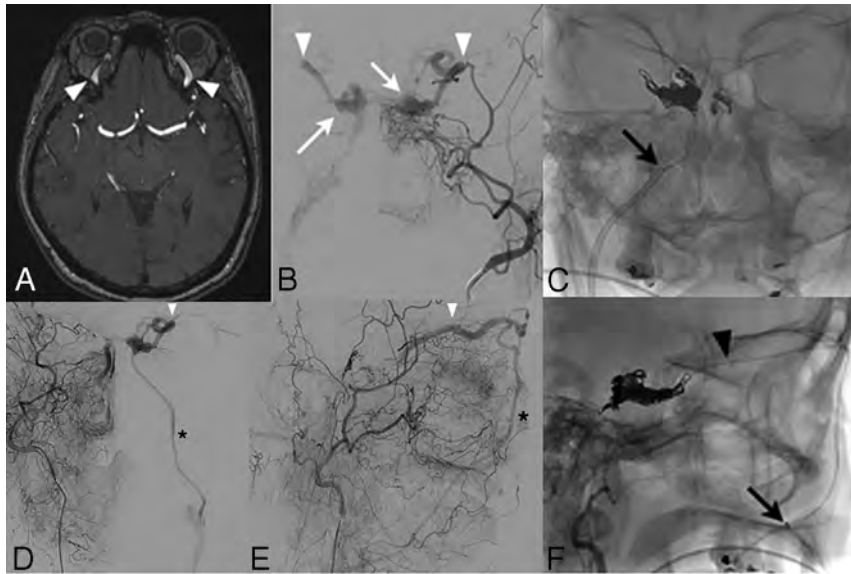


FIG 2. Bilateral indirect CCFs treated with transvenous embolization via right inferior petrosal sinus and left facial vein approaches. *A*, A 64-year-old woman presented with right-sided ptosis and loss of vision, investigated with a TOF-MRA that demonstrates arterialization of the bilateral superior ophthalmic veins (*white arrowheads*). *B*, Frontal-projection left ECA angiography demonstrates an indirect CCF with supply from dural branches of the bilateral ECAs and ICAs, with the right cavernous sinus opacifying earlier than the left (*white arrows*) and reflux into the bilateral superior ophthalmic veins (*white arrowheads*). *C*, Transvenous treatment fluoroscopy in a frontal projection shows positioning of a 6F Envoy catheter (Cordis) (*black arrow*) into the proximal right inferior petrosal sinus, with an Excelsior SL-10 microcatheter (Stryker) advanced into the right cavernous sinus. Subsequent coil embolization of the proximal right superior ophthalmic vein, right cavernous sinus, and medial left cavernous sinus through the intercavernous sinus was followed by injection of 33% glue (Glubran *n*-BCA; GEM Italy) in Lipiodol (Guerbet) into the right-sided coil mass. There was resolution of the patient's symptoms; however, a few weeks later she developed left-sided chemosis. Frontal (*D*) and lateral (*E*) projection right ECA angiography demonstrates progression in the left cavernous sinus arteriovenous shunting, with prominence of the left superior ophthalmic (*white arrowhead*) and facial (*asterisk*) veins. No outflow is identified into the left inferior petrosal sinus, which is likely thrombosed. *F*, Lateral-projection fluoroscopy shows how a 6F Navien intermediate catheter (Covidien) was advanced via the left internal jugular vein into the left facial vein (*black arrow*) mounted on a Prowler Plus microcatheter (Codman Neurovascular). The Prowler Plus was then navigated through the left facial, angular, and superior ophthalmic veins into the left cavernous sinus (*black arrowhead*) and used to embolize with coils.

difficult.^{5,7} However, because these dAVFs predominantly drain into the vein of Galen, detailed angiographic assessment is required to ensure that the deep cerebral structures are not still dependent on the vein of Galen for venous outflow.

A traditional TVE approach for transverse sinus dAVFs (dorsal epidural location) is sinus sacrifice via transvenous coil occlusion.¹⁹⁻²¹ However, this approach in isolation has suboptimal outcomes: In a large study of 150 patients with transverse-sigmoid dAVFs, 64% required additional TAE procedures following TVE coil occlusion.²⁰ In addition, this approach may not be feasible in patients with a contralateral hypoplastic sinus. Deconstructive approaches to transverse-sigmoid dAVFs are progressively being replaced by reconstructive TAE approaches with venous sinus balloon protection (see the second article in this series on TAE).^{21,22} As our knowledge of the angioarchitecture of transverse-sigmoid dAVFs has evolved, there is increasing awareness of a parasinus or common arterial collector in the wall of many of these dAVFs that can be selectively targeted via TVE.²³

Another dorsal epidural location that can be considered for TVE includes the superior sagittal sinus, which can receive extensive bilateral arterial feeders converging on a long segment of the sinus, rendering TAE more difficult. If the healthy brain is not dependent on that segment of the sinus, as is typical due to the high-flow nature of the dAVF, transvenous sacrifice of the sinus segment can be curative.¹⁹

Technical Approaches. Technical approaches for TVE include the following:

1. Coil occlusion
2. EVOH (\pm coil) occlusion
3. Reverse pressure cooker (RPC) technique
4. Reverse dual-lumen balloon microcatheter.

As a general principle of TVE, arterial access is also required to obtain intraprocedural angiography and road-map guidance. This is because venography alone will not visualize the fistulous points and will be unable to determine whether the embolization has been successful in obliterating the dAVF.

Coil Occlusion

TVE using coil occlusion of the draining sinus has been used since the 1990s and is still a common approach for indirect CCFs and transverse-sigmoid sinus dAVFs.^{10,15,19,20} The technique involves transvenous placement of a guide catheter in the ipsilateral jugular

vein (usually via femoral access, though upper limb access is also feasible²⁴); microcatheter advancement into the draining sinus usually via the inferior petrosal sinus (IPS) when treating cavernous dAVFs;^{9,15} and construction of an occlusive coil mass with the aim of inducing complete thrombosis of the sinus (Fig 2).¹⁹ Due to the extensive number of coils required and associated financial costs, the use of pushable or fibered coils is described.²⁵

Successful obliteration rate for indirect CCFs using TVE with coils alone was reported as 87% in a large multicenter series of 267 patients, identifying a lower complication rate using coils alone compared with other embolic agents.²⁶ In a series of anterior condylar dAVFs, TVE with coils resulted in a cure in 9 of 14 cases.²⁷

EVOH Occlusion

EVOH is increasingly popular because it can be used to progressively occlude the proximal aspect of the draining vein and fistulous points in a controlled fashion, resulting in higher rates of

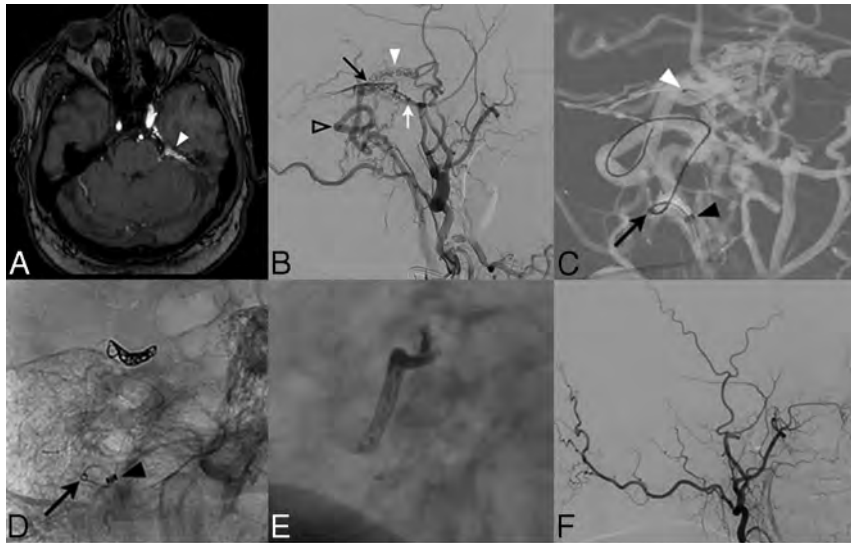


FIG 3. Transvenous embolization of a left petrous ridge dAVF using a modified reverse pressure cooker technique. A 49-year-old man presented with a 3-month history of headache and left-sided pulsatile tinnitus. A, TOF-MRA demonstrates prominence of vessels along the left petrous ridge with arterialization of the left superior petrosal vein of Dandy (*white arrowhead*). B, Lateral-projection left ECA angiography confirms the presence of a left petrous dAVF centered on the superior petrosal vein of Dandy (*black arrow*), with direct cortical venous drainage (*open arrowhead*) supplied by left middle meningeal artery petrous branches (*white arrow*) and a left accessory meningeal artery (*white arrowhead*). C, Transvenous treatment was performed to avoid embolization of the neighboring facial arcade. A left ECA roadmap in a lateral projection demonstrates a 6F Destination sheath placed in the left internal jugular vein (*black arrowhead*), with a Fargo-Mini intermediate catheter (Balt Extrusion) (*black arrow*) used to support advancement of a Marathon microcatheter to the fistulous site (*white arrowhead*). Lateral-projection fluoroscopy was performed after 3 coils were deployed (D) and then after Onyx-18 was used to embolize the distal arterial feeders, fistula site, and proximal draining vein, creating a coil-Onyx mass (E). This was a modification of the reverse pressure cooker technique using a single flow-directed microcatheter (Marathon) without a detachable tip to perform both the coiling and the EVOH injection. This modification was required due to the extensive tortuosity of the transvenous course that impeded attempts to place 2 microcatheters and required the use of a low-profile intermediate catheter (Fargo-Mini) (*black arrow*). The Marathon microcatheter could not be removed and was left in situ and cut at the level of the right femoral subcutaneous soft tissue. This procedure is typically well-tolerated in the venous system, and the patient was placed on a 6-month course of anticoagulation. F, Follow-up lateral-projection left ECA angiography at 6 months demonstrates complete occlusion of the fistula.

cure.²⁸⁻³² The successful use of EVOH alone during TVE has been described for indirect CCFs and is associated with shorter procedural and fluoroscopy times.³³ Because the microcatheter can be advanced into the constrained space of the cavernous sinus and the goal of treatment in this situation is occlusion of the sinus, indirect CCFs are an ideal indication for EVOH. However, the ability of EVOH to retrogradely penetrate arterial feeders can increase the risk of temporary or even permanent cranial neuropathy. Higher complication rates have been described when using EVOH alone for the treatment of indirect CCFs.²⁶

Transverse-sigmoid dAVFs are classically not well-suited for TVE using EVOH alone due to the large diameter of the sinus and the large venous outflow back to the pulmonary circulation, factors that will necessarily predispose to EVOH deposition in the lungs.³⁴ An exception to this statement would be transverse-sigmoid dAVFs with an isolated segment,³⁵ where there is thrombotic occlusion proximal and distal to the sinus drainage point resulting in

significant cortical venous reflux, classified as Borden type III.³⁶ However, even in this situation transvenous access to the isolated segment can be difficult due to the distal thrombosis.³⁷

Hypoglossal/condylar dAVFs at the ventral aspect of the foramen magnum can also be treated using EVOH alone.³⁸ However, because the anterior condylar vein drains directly into the internal jugular vein and then the pulmonary circulation, the formation of a coil mass before embolization with EVOH has the advantages of reducing the flow rate and creating a “scaffold” on which EVOH can accumulate and then extend in a retrograde fashion into the fistulous point rather than down the internal jugular vein, allowing more control of the agent (Fig 1). Alternatively, placement of a sinus-protection balloon in the sigmoid sinus/internal jugular vein while embolizing the anterior condylar vein using EVOH is described.³⁹

RPC Technique

The RPC technique is a transvenous modification of the original transarterial pressure cooker technique described by Chapot et al,⁴⁰ in 2014. In the original technique (described in detail in the second article in this series), flow control is achieved by placing 2 microcatheters side by side in the vessel of interest, with placement of an occlusive coil/glue mass adjacent to the detachable tip of a second microcatheter.⁴⁰

EVOH is then administered via the detachable-tip microcatheter with the advantages of maintained antegrade flow and limited reflux. In the RPC technique, the coil/glue mass and detachable-tip microcatheter are placed in the draining vein, allowing flow reversal in the vein, with retrograde transmission of EVOH to reach the fistulous point.⁴¹

When undertaking the transvenous RPC technique, the detachable-tip microcatheter is advanced via venous access as close as possible to the foot of the draining vein, to minimize the amount of embolic agent required. This procedure may require navigation across tortuous draining pial veins, during which a gentle technique and use of a tight J-curve on the microwire are useful to reduce the risk of venous rupture. Two sample cases using transvenous RPC technique are demonstrated in Figs 1 and 3.

Dual-Lumen Balloon Retrograde Embolization Technique

As with TAE, TVE could also be undertaken using a dual-lumen balloon microcatheter with the balloon inflated in the draining vein. In our experience, the seal created by the balloon in

distensible veins is suboptimal to achieve sustained retrograde flow of EVOH.

Postoperative Management

Overnight admission to an intensive care or high-dependency unit is required for all our patients following embolization for a dAVF. In addition, if a large segment of the draining vein has been occluded during the TVE procedure or there is sluggish flow in adjacent veins on the final control angiogram, we typically anticoagulate the patient with heparin for 24 hours to avoid excess venous thrombosis. Because venous thrombosis can result in adjacent edema and inflammatory changes that can cause significant headache, we frequently place patients on a weaning course of dexamethasone for 1–2 weeks in these cases.

Alternative-Access Techniques. Alternative-access techniques play an important role in TVE, particularly for the treatment of cavernous⁴² and transverse-sigmoid dAVFs.⁴³ Indirect CCFs have at least 8 potential venous exit pathways from the cavernous sinus.^{44,45} Thrombosis of ≥ 1 of these channels can result in venous outflow limitation, leading to increased pressure and cortical venous reflux.⁴⁶ The most accessible venous pathway to reach the cavernous sinus is via the IPS (Fig 2 A–C), but this can be limited by the presence of IPS thrombosis.

Recanalization of the IPS

In the presence of a nonvisualized IPS on angiography, considerations include a hypoplastic IPS or thrombosis of a normal/enlarged IPS. Assessment of CT using thin-section bone window reconstructions allows visualization of the inferior petrosal sulcus, a bony groove formed at the junction of the basiocciput and petrous temporal bone. In the presence of a congenital hypoplastic IPS, the inferior petrosal sulcus may be asymmetrically small. If the IPS is thrombosed, recanalization can be undertaken⁴² by cannulating the ostium of the IPS at the anteromedial surface of the jugular bulb with an angled-tip guide catheter through which an angled tip 0.035 hydrophilic Glidewire (Terumo Inc., Japan) is gently rotated across the thrombosis to create a channel. A microcatheter can then be advanced across the channel to reach the cavernous sinus.⁴² The Glidewire can be removed under negative roadmap conditions to demonstrate the pathway under fluoroscopy.³⁵ These same techniques are also useful for gaining access across an occluded transverse sinus to reach an isolated segment.³⁵

Transfacial Venous Access

In the setting of IPS thrombosis, the inferior and superior ophthalmic veins are an alternative access approach.⁴² These can be reached by cannulating the facial vein from the internal jugular vein and then navigating across the angular vein to reach the ophthalmic veins.^{47,48} A sample case of venous access to an indirect CCF via the facial vein is demonstrated in Fig 2 D–F.

Transorbital Access

Direct cutdown over the eyelid for access to the superior ophthalmic vein and cavernous sinus was first described by Uflacker et al⁴⁹ for management of traumatic direct CCFs. The technique was later adapted for treatment of indirect CCFs.^{33,50} Because the superior ophthalmic vein can be tortuous and easily displaced

within the orbital fat, it can be difficult to achieve stable access. Thus, direct transorbital access to the cavernous sinus is useful, using a micropuncture needle via an infra- or supraocular approach to reach the inferior or superior orbital fissures and thus cannulate the cavernous sinus at its anterior margin.⁵⁰ A 4F dilator and microcatheter can then be used to deploy coils and/or EVOH.⁵¹

Open Surgical Access

Open surgical access to the transverse sinus via a burr-hole or craniotomy is well-described to allow placement of occlusive coils superior to a thrombosed sinus segment.^{43,52} Similarly, a subtemporal or even endoscopic surgical approach can allow access to the cavernous sinus.⁵³

Outcomes. The Japanese Registry of NeuroEndovascular Therapy (JR-NET3) published the largest known dataset for TVE of cranial dAVFs.¹⁰ TVE alone was undertaken in 910 cases with the use of coils in 97% of cases (liquid embolics in only 2%).¹⁰ Favorable clinical outcomes (30-day mRS score of 0–2) were achieved in 92% of cases.¹⁰

Cavernous dAVFs treated with TVE alone demonstrated complete angiographic occlusion rates of 87% in a large series of 199 patients²⁶ and 81% in another series of 141 patients.⁵⁴ Transvenous coil packing for transverse-sigmoid dAVFs in a large series by Kuwayama,⁵⁵ in 2016 ($n = 389$), resulted in angiographic cure in 53.2%. A systematic review of TVE for hypoglossal/condylar dAVFs identified an angiographic occlusion rate of 93%.¹²

These results suggest that TVE using coils \pm EVOH results in angiographic cure in 80%–90% of cases at ventral anatomic locations for which TVE is indicated. The much larger JR-NET3 dataset had a lower angiographic cure rate (68%), but liquid embolic agents were used in only 2% of cases owing to restricted access to EVOH in Japan.¹⁰

Complications. The JR-NET3 database identified complications in 7.8% of cases of TVE ($n = 71$) with mortality of 0.7% and morbidity of 2.8%.¹⁰ Complication rates were higher for dAVFs at the craniocervical junction (15.8%) than for those at the transverse-sigmoid (7.3%) or cavernous (8.7%) sinus.¹⁰ The most common complications (in descending order) were nonhemorrhagic neurologic deterioration resulting from venous occlusion, vessel perforation, hemorrhage from venous occlusion, and arterial thromboembolic events.¹⁰ Transient cranial nerve palsy following TVE of cavernous dAVFs was not discussed by the JR-NET3 authors but has been reported as occurring in 11% of TVE cases.⁵⁶ Conservative monitoring and oral corticosteroids are generally effective for such cases.^{2,54,56}

Complications Related to Venous Occlusion

Hemorrhagic and nonhemorrhagic neurologic complications can occur from TVE procedures due to nontarget venous occlusion or venous rerouting, resulting in congestion and infarction.^{10,56–58} Occlusion of venous outflow pathways, even when intended, can result in rerouting of venous flow from the normal brain parenchyma. In most instances, accessory venous pathways will compensate, but occasionally such pathways are lacking due to anatomic variation or thrombotic disease.^{56–59} Venous congestion

and infarction with neurologic deterioration following TVE have been described when treating cavernous^{56,59} and transverse sinus⁵⁷ dAVFs, most often impacting the cerebellum.

Similarly, patients undergoing microvascular decompression for trigeminal neuralgia can have cerebellar venous infarction if the superior petrosal vein of Dandy is sacrificed intraoperatively and there are limited alternative outflow pathways.⁶⁰ While these cases are rare, the common theme appears to be that normal brain (particularly cerebellar) parenchymal venous outflow pathways should be assessed on pre-embolization angiography.

EVOH embolization with resultant thrombotic occlusion of the cavernous sinus during embolization of cavernous AVFs, though being part of the treatment goal, typically results in swelling and inflammatory change. These can cause transient or even permanent neuropathy of cranial nerves III–VI.^{26,59,61} A weaning course of corticosteroids for 4–6 weeks is typically helpful in these situations.^{26,59} Nontarget retrograde filling of arterial feeders is also a concern if excess EVOH is used, which could result in transmission of EVOH into the ICA, causing parenchymal infarction.^{59,61}

The advantages of a transvenous route when treating dural AVFs include lower risks of cranial neuropathy or transmission of the embolic agent across EC-IC anastomoses compared with TAE. These advantages are partially offset by the increased risks of venous congestion or rupture of a pial vein when navigating tortuous draining veins to reach the fistulous point. Thus, the choice of TVE versus TAE should be made on the basis of the individual angioarchitecture of each dAVF. When a transvenous approach to the fistulous point is easily accessible and the length of the draining vein likely to be occluded during embolization is short, TVE is probably safer than TAE options.

CONCLUSIONS

TVE is now the first-line treatment for ventral dAVFs and is increasingly used for some lateral dAVFs due to the lower risks of cranial nerve palsy or embolization across EC-IC anastomoses. Angiographic cure rates of 80%–90% can be achieved with TVE in these locations. Potential complications include transient cranial neuropathy, neurologic deterioration from venous occlusion, and vessel perforation.

Disclosures: Timo Krings: UNRELATED: Consultancy: Stryker, Penumbra, Medtronic, Cerenovus Royalties: Thieme Stock/Stock Options: Marblehead. Vitor Mendes Pereira: RELATED: Consulting Fee or Honorarium: Medtronic, Comments: research fellow support.

REFERENCES

1. Geibprasert S, Pereira V, Krings T, et al. **Dural arteriovenous shunts: a new classification of craniocervical epidural venous anatomical bases and clinical correlations.** *Stroke* 2008;39:2783–94 CrossRef Medline
2. Geibprasert S, Pongpech S, Armstrong D, et al. **Dangerous extracranial-intracranial anastomoses and supply to the cranial nerves: vessels the neurointerventionalist needs to know.** *AJNR Am J Neuroradiol* 2009;30:1459–68 CrossRef Medline
3. Radovanovic I, Wallace M. **Cranial dural arteriovenous fistula disconnection.** In: Jandial R, McCormick P, Black P, eds. *Core Techniques in Operative Neurosurgery.* Elsevier; 2019
4. Bhatia KD, Kortman H, Lee H, et al. **Facial nerve arterial arcade supply in dural arteriovenous fistulas: anatomy and treatment strategies.** *AJNR Am J Neuroradiol* 2020;41:687–92 CrossRef Medline
5. Lawton MT, Sanchez-Mejia RO, Pham D, et al. **Tentorial dural arteriovenous fistulae: operative strategies and microsurgical results for six types.** *Neurosurgery* 2008;62:110–24; discussion 124–25 CrossRef Medline
6. Dabus G, Kan P, Diaz C, et al. **Endovascular treatment of anterior cranial fossa dural arteriovenous fistula: a multicenter series.** *Neuroradiology* 2020;63:259–66 CrossRef Medline
7. Bhatia KD, Kortman H, Walchli T, et al. **Artery of Davidoff and Schechter supply in dural arteriovenous fistulas.** *AJNR Am J Neuroradiol* 2020;41:300–04 CrossRef Medline
8. Roa JA, Dabus G, Dandapat S, et al. **Ethmoidal dural arteriovenous fistulas: endovascular transvenous embolization technique.** *J Neurointerv Surg* 2020;12:610 CrossRef Medline
9. Henderson AD, Miller NR. **Carotid-cavernous fistula: current concepts in aetiology, investigation, and management.** *Eye (Lond)* 2018;32:164–72 CrossRef Medline
10. Hiramatsu M, Sugiu K, Hishikawa T, et al. **Results of 1940 embolizations for dural arteriovenous fistulas: Japanese Registry of Neuroendovascular Therapy (JR-NET3).** *J Neurosurg* 2019 Jun 28 [Epub ahead of print] CrossRef Medline
11. Hellstern V, Aguilar-Pérez M, Schob S, et al. **Endovascular treatment of dural arteriovenous fistulas of the anterior or posterior condylar vein: a cadaveric and clinical study and literature review.** *Clin Neuroradiol* 2019;29:341–49 CrossRef Medline
12. Spittau B, Millán DS, El-Sherifi S, et al. **Dural arteriovenous fistulas of the hypoglossal canal: systematic review on imaging anatomy, clinical findings, and endovascular management.** *J Neurosurg* 2015;122:883–903 CrossRef Medline
13. Ducruet AF, Albuquerque FC, Crowley RW, et al. **The evolution of endovascular treatment of carotid cavernous fistulas: a single-center experience.** *World Neurosurg* 2013;80:538–48 CrossRef Medline
14. Barrow DL, Spector RH, Braun IF, et al. **Classification and treatment of spontaneous carotid-cavernous sinus fistulas.** *J Neurosurg* 1985;62:248–56 CrossRef Medline
15. Miller NR. **Diagnosis and management of dural carotid-cavernous sinus fistulas.** *Neurosurg Focus* 2007;23:E13 CrossRef Medline
16. Chi CT, Nguyen D, Duc VT, et al. **Direct traumatic carotid cavernous fistula: angiographic classification and treatment strategies—study of 172 cases.** *Interv Neuroradiol* 2014;20:461–75 CrossRef Medline
17. Agid R, Terbrugge K, Rodesch G, et al. **Management strategies for anterior cranial fossa (ethmoidal) dural arteriovenous fistulas with an emphasis on endovascular treatment.** *J Neurosurg* 2009;110:79–84 CrossRef Medline
18. Mayfrank L, Reul J, Huffmann B, et al. **Microsurgical interhemispheric approach to dural arteriovenous fistulas of the floor of the anterior cranial fossa.** *Minim Invasive Neurosurg* 1996;39:74–77 CrossRef Medline
19. Roy D, Raymond J. **The role of transvenous embolization in the treatment of intracranial dural arteriovenous fistulas.** *Neurosurgery* 1997;40:1133–41; discussion 1141–44 CrossRef Medline
20. Kirsch M, Liebig T, Kuhne D, et al. **Endovascular management of dural arteriovenous fistulas of the transverse and sigmoid sinus in 150 patients.** *Neuroradiology* 2009;51:477–83 CrossRef Medline
21. Xu K, Yang X, Li C, et al. **Current status of endovascular treatment for dural arteriovenous fistula of the transverse-sigmoid sinus: a literature review.** *Int J Med Sci* 2018;15:1600–10 CrossRef Medline
22. Vollherbst DF, Ulfert C, Neuberger U, et al. **Endovascular treatment of dural arteriovenous fistulas using transarterial liquid embolization in combination with transvenous balloon-assisted protection of the venous sinus.** *AJNR Am J Neuroradiol* 2018;39:1296–1302 CrossRef Medline
23. Shapiro M, Raz E, Litao M, et al. **Toward a better understanding of dural arteriovenous fistula angioarchitecture: superselective transvenous embolization of a sigmoid common arterial collector.** *AJNR Am J Neuroradiol* 2018;39:1682–88 CrossRef Medline
24. Ramos AD, Sundararajan S, Santillan A, et al. **Single arm access venous sinus stenting (SAVeS) technique: technical note.** *Interv Neuroradiol* 2020;26:501–05 CrossRef Medline

25. Yamaguchi S, Horie N, Hayashi K, et al. **Point-by-point parent artery/sinus obliteration using detachable, pushable, 0.035-inch coils.** *Acta Neurochir (Wien)* 2016;158:2089–94 CrossRef Medline
26. Alexander MD, Halbach VV, Hallam DK, et al. **Long-term outcomes of endovascular treatment of indirect carotid cavernous fistulae: superior efficacy, safety, and durability of transvenous coiling over other techniques.** *Neurosurgery* 2019;85:E94–100 CrossRef Medline
27. Hsu YH, Lee CW, Liu HM, et al. **Endovascular treatment and computed imaging follow-up of 14 anterior condylar dural arteriovenous fistulas.** *Interv Neuroradiol* 2014;20:368–77 CrossRef Medline
28. Moeninghoff C, Pohl E, Deuschl C, et al. **Outcomes after Onyx embolization as primary treatment for cranial dural arteriovenous fistula in the past decade.** *Acad Radiol* 2020;27:e123–31 CrossRef Medline
29. Ayad M, Eskioglu E, Mericle RA. **Onyx: a unique neuroembolic agent.** *Expert Rev Med Devices* 2006;3:705–15 CrossRef Medline
30. Rabinov JD, Yoo AJ, Ogilvy CS, et al. **ONYX versus n-BCA for embolization of cranial dural arteriovenous fistulas.** *J Neurointerv Surg* 2013;5:306–10 CrossRef Medline
31. Rangel-Castilla L, Barber SM, Klucznik R, et al. **Mid and long term outcomes of dural arteriovenous fistula endovascular management with Onyx: experience of a single tertiary center.** *J Neurointerv Surg* 2014;6:607–13 CrossRef Medline
32. Gross BA, Albuquerque FC, Moon K, et al. **Evolution of treatment and a detailed analysis of occlusion, recurrence, and clinical outcomes in an endovascular library of 260 dural arteriovenous fistulas.** *J Neurosurg* 2017;126:1884–93 CrossRef Medline
33. Bhatia KD, Wang L, Parkinson RJ, et al. **Successful treatment of six cases of indirect carotid-cavernous fistula with ethylene vinyl alcohol copolymer (Onyx) transvenous embolization.** *J Neuroophthalmol* 2009;29:3–8 CrossRef Medline
34. Jiang Y, Li Y, Wu Z. **Onyx distal embolization in transarterial embolization of dural arteriovenous fistula with subtotally isolated transverse-sigmoid sinus: a case report.** *Interv Neuroradiol* 2009;15:223–28 CrossRef Medline
35. Brunozzi D, Alaraj A. **Operative nuances of blind catheterization of occluded sinuses using negative road map technique: 2-dimensional operative video.** *Oper Neurosurg (Hagerstown)* 2020;19:E599 CrossRef Medline
36. Borden JA, Wu JK, Shucart WA. **A proposed classification for spinal and cranial dural arteriovenous fistulous malformations and implications for treatment.** *J Neurosurg* 1995;82:166–79 CrossRef Medline
37. Lucas C. D P, Mounayer C, Spelle L, et al. **Endoarterial management of dural arteriovenous malformations with isolated sinus using Onyx-18: technical case report.** *Neurosurgery* 2007;61:E293–94; discussion E294 CrossRef Medline
38. Takemoto K, Tateshima S, Rastogi S, et al. **Onyx embolization of anterior condylar confluence dural arteriovenous fistula.** *J Neurointerv Surg* 2014;6:e13 CrossRef Medline
39. Ye M, Zhang P. **Transvenous balloon-assisted Onyx embolization of dural arteriovenous fistulas of hypoglossal canal.** *Neuroradiology* 2018;69:971–78 CrossRef Medline
40. Chapot R, Stracke P, Velasco A, et al. **The pressure cooker technique for the treatment of brain AVMs.** *J Neuroradiol* 2014;41:87–91 CrossRef Medline
41. Koyanagi M, Mosimann PJ, Nordmeyer H, et al. **The transvenous retrograde pressure cooker technique for the curative embolization of high-grade brain arteriovenous malformations.** *J Neurointerv Surg* 2021;13:637–41 CrossRef Medline
42. Castro-Afonso LH, Trivelato FP, Rezende MT, et al. **The routes for embolization of dural carotid cavernous fistulas when the endovascular approach is indicated as a first-line strategy.** *Interv Neuroradiol* 2019;25:66–70 CrossRef Medline
43. Caplan JM, Kaminsky I, Gailloud P, et al. **A single burr hole approach for direct transverse sinus cannulation for the treatment of a dural arteriovenous fistula.** *J Neurointerv Surg* 2015;7:e5 CrossRef Medline
44. Suh DC, Lee JH, Kim SJ, et al. **New concept in cavernous sinus dural arteriovenous fistula: correlation with presenting symptom and venous drainage patterns.** *Stroke* 2005;36:1134–39 CrossRef Medline
45. Aralasmak A, Karaali K, Cevikol C, et al. **Venous drainage patterns in carotid cavernous fistulas.** *ISRN Radiol* 2014;2014:760267 CrossRef Medline
46. Robert T, Sylvestre P, Blanc R, et al. **Thrombosis of venous outflows of the cavernous sinus: possible aetiology of the cortical venous reflux in case of indirect carotid-cavernous fistulas.** *Acta Neurochir (Wien)* 2017;159:835–43 CrossRef Medline
47. Luo CB, Chang FC, Teng MM, et al. **Anatomic variation of facial vein in carotid-cavernous fistula and trans-facial vein embolization.** *World Neurosurg* 2015;84:90–96 CrossRef Medline
48. Biondi A, Milea D, Cognard C, et al. **Cavernous sinus dural fistulae treated by transvenous approach through the facial vein: report of seven cases and review of the literature.** *AJNR Am J Neuroradiol* 2003;24:1240–46 Medline
49. Uflacker R, Lima S, Ribas GC, et al. **Carotid-cavernous fistulas: embolization through the superior ophthalmic vein approach.** *Radiology* 1986;159:175–79 CrossRef Medline
50. Phan K, Xu J, Leung V, et al. **Orbital approaches for treatment of carotid cavernous fistulas: a systematic review.** *World Neurosurg* 2016;96:243–51 CrossRef Medline
51. Wenderoth J. **Novel approaches to access and treatment of cavernous sinus dural arteriovenous fistula (CS-DAVF): case series and review of the literature.** *J Neurointerv Surg* 2017;9:290–96 CrossRef Medline
52. Youssef PP, Schuette AJ, Cawley CM, et al. **Advances in surgical approaches to dural fistulas.** *Neurosurgery* 2014;74 (Suppl 1):S32–41 CrossRef Medline
53. Sur S, Menaker SA, Alvarez C, et al. **Multimodal management of carotid-cavernous fistulas.** *World Neurosurg* 2020;133:e796–803 CrossRef Medline
54. Kirsch M, Henkes H, Liebig T, et al. **Endovascular management of dural carotid-cavernous sinus fistulas in 141 patients.** *Neuroradiology* 2006;48:486–90 CrossRef Medline
55. Kuwayama N. **Epidemiologic survey of dural arteriovenous fistulas in Japan: clinical frequency and present status of treatment.** *Acta Neurochir Suppl* 2016;123:185–88 CrossRef Medline
56. Kim DJ, Kim DI, Suh SH, et al. **Results of transvenous embolization of cavernous dural arteriovenous fistula: a single-center experience with emphasis on complications and management.** *AJNR Am J Neuroradiol* 2006;27:2078–82 Medline
57. Lv X, Jiang C, Liang S, et al. **The variant with the absence of the superior petrosal venous and sinus: a potential pitfall of transvenous balloon-assisted embolisation of Borden type II transverse-sigmoid dural arteriovenous fistula.** *Interv Neuroradiol* 2019;25:474–77 CrossRef Medline
58. Halbach VV, Higashida RT, Hieshima GB, et al. **Transvenous embolization of dural fistulas involving the transverse and sigmoid sinuses.** *AJNR Am J Neuroradiol* 1989;10:385–92 Medline
59. Kuwayama N, Endo S, Kubo M, et al. **Pitfalls in endovascular treatment of dural arteriovenous fistulas involving the cavernous sinus.** *Interv Neuroradiol* 1997;3(Suppl 2):88–92 CrossRef Medline
60. Liebelt BD, Barber SM, Desai VR, et al. **Superior petrosal vein sacrifice during microvascular decompression: perioperative complication rates and comparison with venous preservation.** *World Neurosurg* 2017;104:788–94 CrossRef Medline
61. Elhammady MS, Wolfe SQ, Farhat H, et al. **Onyx embolization of carotid-cavernous fistulae.** *J Neurosurg* 2010;112:589–94 CrossRef Medline

Anatomy of Spinal Venous Drainage for the Neurointerventionalist: From Puncture Site to Intervertebral Foramen

 N. Borg,  J. Cutsforth-Gregory,  S. Oushy,  T. Huynh,  L.E. Savastano,  H.J. Cloft,  G. Lanzino, and  W. Brinjikji



ABSTRACT

SUMMARY: CSF-venous fistula is a relatively novel entity that is increasingly being recognized as a cause for spontaneous intracranial hypotension. Recently, our group published the first series of transvenous embolization of CSF-venous fistulas in this journal. Having now performed the procedure in 60 patients, we have garnered increasing familiarity with the anatomy and how to navigate our way through the venous system to any intervertebral foramen in the cervical, thoracic, and lumbar spine. The first part of this review summarizes the organization of spinal venous drainage as described in classic anatomy and interventional radiology texts, the same works that we studied when attempting our first cases. In the second part, we draw mostly on our own experience to provide a practical roadmap from the puncture site to the foramen. On the basis of these 2 parts, we hope this article will serve to collate the relevant anatomic knowledge and give confidence to colleagues who wish to embark on transvenous spinal procedures.

ABBREVIATIONS: IVC = inferior vena cava; SVC = superior vena cava

Spinal venous anatomy is a lesser-known subject among neurointerventionalists, while we are generally well-adept at navigating the arteries of the central nervous system. Both blood supply and drainage of the spine should be core topics of the training of every neurointerventionalist, especially given the growing interest in transvenous routes for the treatment of CNS diseases.

In 2014, CSF-venous fistulas (Fig 1) were first described as a cause of spontaneous intracranial hypotension.¹ More recently, a novel technique for the treatment of CSF-venous fistulas has been described that depends on navigation of the paraspinous and epidural venous system.² Since then, we have noted a steep rise in the number of patients referred for embolization at our center and have seen the procedure performed at multiple additional centers in North America and Europe.

With the emergence of these new procedures comes a need to revive a part of our knowledge that, in recent years, has been neglected for lack of clinical need. A thorough review of spinal and paraspinous venous anatomy is, therefore, both timely and relevant.

Here we seek to draw on previously published anatomic studies within the fields of anatomy and neurointervention, combined with the lessons we have learned in the process of performing our first 60 transvenous embolizations of CSF-venous fistulas. Rather than taking a purely anatomic approach, the aim was to provide the neurointerventionalist with a practical roadmap from a common femoral vein to any intervertebral foramen in the cervical, thoracic, or lumbar spine.

Historical Anecdote


We are not the first generation of neurointerventionalists to require transvenous access to the spine. Decades ago, venography of the epidural venous plexus was frequently used to diagnose mass lesions such as intervertebral disc prolapses and tumors.³ The advancement of cross-sectional imaging rendered invasive diagnostic spinal venographic techniques obsolete. Nevertheless, the anatomic lessons learned in the past by the masters of that art still hold true today and provide an invaluable foundation for our current knowledge.

When embarking on our first transvenous embolization of a CSF-venous fistula in 2020, we needed to plot an anatomic route of access. Having found a distinct lack of recent publications on the topic, we leaned quite heavily on the seminal texts of Théron and Moret⁴ as well as articles from Théron and Djindjian,⁵ published in the 1970s. These texts must have been labors of love produced by physicians with a deep understanding of classic, embryologic, and radiologic anatomy. They cannot be recommended highly enough for the interested reader.

Received August 18, 2021; accepted after revision October 20.

From the Departments of Neurologic Surgery (N.B., S.O., L.E.S., G.L.), Neurology (J.C.-G.), and Radiology (H.J.C., W.B.), Mayo Clinic, Rochester, Minnesota; and Department of Neurologic Surgery (T.H.), Mayo Clinic, Jacksonville, Florida.

Please address correspondence to Nicholas Borg, MD, Department of Neurologic Surgery, Mayo Clinic, 200 First St SW, Rochester, MN 55905; e-mail: borg.nicholas@mayo.edu; @BorgNicholas

 Indicates open access to non-subscribers at www.ajnr.org

<http://dx.doi.org/10.3174/ajnr.A7409>

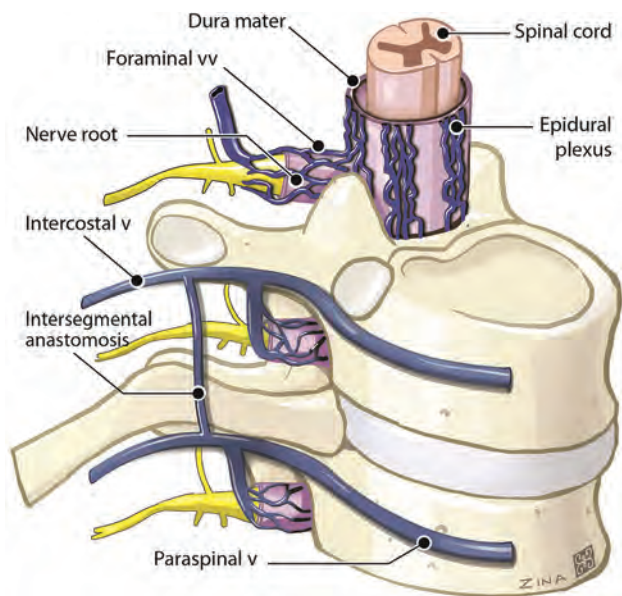


FIG 1. The site of the CSF leak in the patients with CSF-venous fistula is the nerve root foramen. The nerve root is covered with a dural sleeve, which, in turn, is surrounded by a plexus of veins that forms the foraminal vein. This joins the segmental vein above to form the paraspinal vein. There may be anastomotic veins running perpendicular to the segmental veins that provide a direct connection between adjacent levels. v indicates vein; vv, veins.

Spinal Venous Compartments

The veins draining the spinal cord and vertebral column can be conceptually divided into 3 compartments: intradural (intrinsic and extrinsic), extradural, and paraspinal (Fig 2). The intrinsic system refers to veins within the spinal cord itself, and the extrinsic system comprises the pial venous networks, the longitudinally-oriented venous system, and the intradural radiculomedullary veins. This intradural compartment has been described in high-quality articles elsewhere⁶⁻⁸ and for now remains beyond the reach of our microcatheters.

The scope of this review extends to the extradural and paraspinal compartments, specifically the efferent pathways that connect the spine to the great veins that ultimately drain into the heart. The first part summarizes the organization of the venous system, while the second part focuses on the practicalities and nuances of navigating these routes.

Understanding the Extradural and Paraspinal Compartments

In 1940, Batson⁹ described a plexus of valveless veins that runs the entire length of the spine and serves as an important route for hematogenous spread of pelvic metastases to the spine. This plexus also serves a number of important physiologic roles. It can drain venous blood from the brain in cases of internal jugular vein occlusion or compression and can provide an alternate route of venous return in the setting of inferior vena cava (IVC) obstruction or when intrathoracic or intra-abdominal pressure is increased. While Batson's plexus serves as a single unit functionally, it encompasses both the epidural and paravertebral venous plexuses described below. The nomenclature of the subdivisions

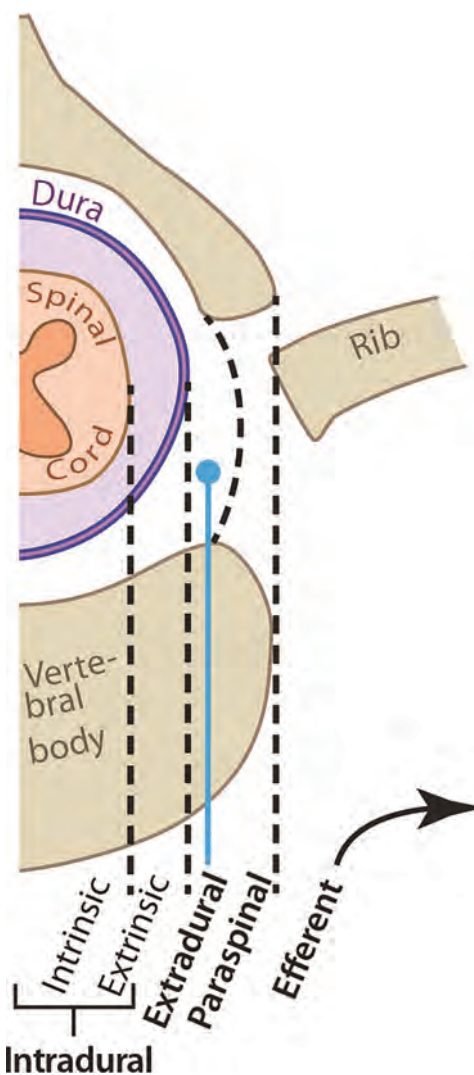


FIG 2. The venous drainage of the spine can be separated into 3 compartments, from medial to lateral. The intradural compartment is further subdivided into intrinsic and extrinsic components. The extradural compartment refers to the epidural venous plexus, also referred to as the internal vertebral plexus. The paraspinal compartment is also called the external vertebral plexus. Efferent pathways are arranged in a segmental fashion, carrying venous blood toward the great veins and on to the right atrium.

of Batson's plexus and the onward efferent pathways merits some clarification in the interest of standardization.

Extradural Compartment. The extradural compartment described in the previous section refers to the internal vertebral venous plexus, also known as the epidural plexus. It sits within the spinal canal, embedded in the epidural fat that surrounds the main thecal sac, and drains the spinal cord and the vertebral bodies. Although the internal venous plexus effectively surrounds the dura circumferentially, Gray's *Anatomy of the Human Body* describes 4 longitudinal channels where the plexus is more prominent, 2 anteriorly and 2 posteriorly.¹⁰ Radiologically, superimposition of the anterior and posterior plexuses on a frontal view results in the appearance of 2 "lateral epidural plexuses" running longitudinally on either side of the spinal canal (Fig 3).

Venous rings at the midlevel of each vertebral body allow communication between the 2 anterior and 2 posterior internal plexuses. On a frontal view, these appear as transverse channels connecting the left and right lateral plexuses. These rings also drain the basivertebral veins from the posterior aspect of the vertebral bodies into the epidural plexus. These osteal tributaries are morphologically distinct on fluoroscopy. Awareness of their existence and relationship to the epidural plexus can help distinguish them from epidural veins when

they appear during injection of a liquid embolic agent. As mentioned previously, the epidural plexus is both rich and valveless. Both of these features have made it surprisingly straightforward for navigating microcatheters through the epidural space, in our experience.

Paraspinal Compartment. The paravertebral compartment is also referred to as the external vertebral, paravertebral, or paraspinal venous plexus (Fig 4). It is richest in the cervical region and is

also divided into 2 anterior and 2 posterior columns that freely communicate with each other. The anterior external plexuses lie adjacent to the vertebral bodies and also drain the aforementioned basivertebral and foraminal veins.¹⁰ The posterior external plexuses run outside the lamina and drain the deep paraspinal muscles via tributaries such as the lateral and posterior muscular veins. They also communicate with the posterior internal plexuses and, in the cervical region, anastomose with the vertebral, occipital, and deep cervical veins.

Foraminal Veins. The internal and external vertebral plexuses are functionally and anatomically connected through each intervertebral foramen via the foraminal veins (Fig 5), which form a plexus surrounding each nerve root. In some texts, these are also referred to by the term “intervertebral vein.” In our experience, both microcatheters and embolic agents injected here behave more like a plexus.

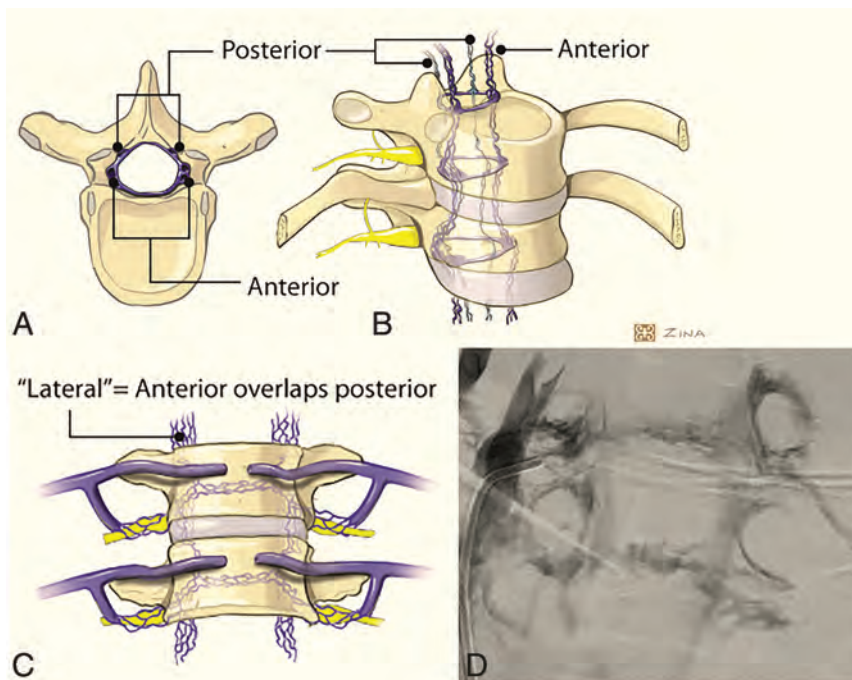


FIG 3. A–C, The epidural plexus is richest in 2 anterolateral and 2 posterolateral columns. The 4 columns are joined by circumferential rings surrounding the thecal sac at the midlevel of each vertebral body. When viewed from anterior to posterior, the 4 columns, rings, and foraminal veins form a characteristic hexagonal shape. D, The composite view of the anterior and posterior columns on a frontal view is referred to as the lateral epidural plexus.

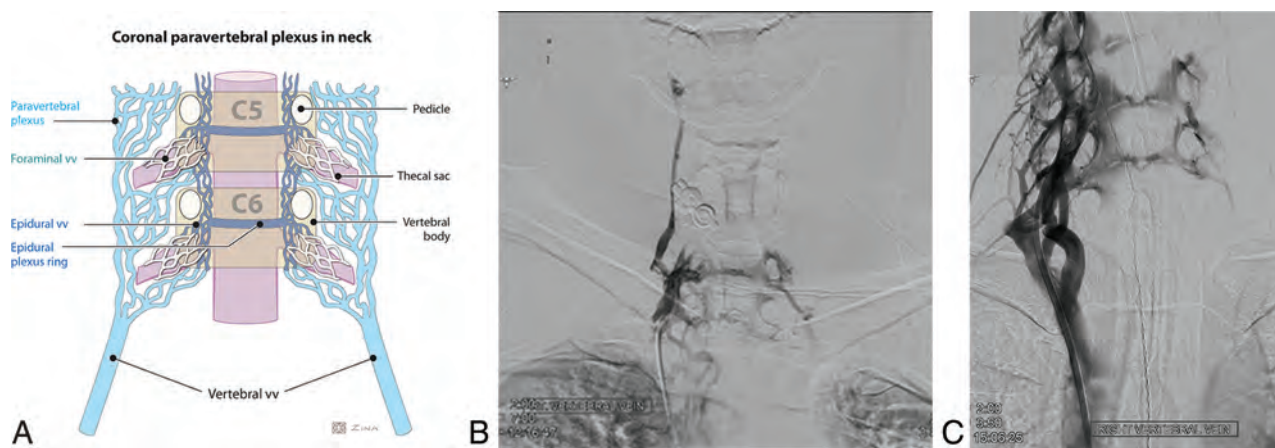


FIG 4. A, Coronal view in the cervical region showing that the rich plexus adjacent to the vertebral bodies is anatomically continuous and functionally analogous to the epidural plexus. Inferiorly, the paravertebral plexus condenses into the vertebral veins. B and C, Vertebral venograms rapidly opacify the paravertebral plexus, foraminal veins, and epidural plexus. Filling defects just adjacent to the vertebral bodies represent the pedicles. The more lateral filling defects represent the vertebral artery running through transverse foramina. Between adjacent pedicles is the foraminal vein. Lateral to the pedicle is the paravertebral plexus; medial to it is the epidural plexus, with its characteristic hexagonal shape. v indicates vein; vv, veins.

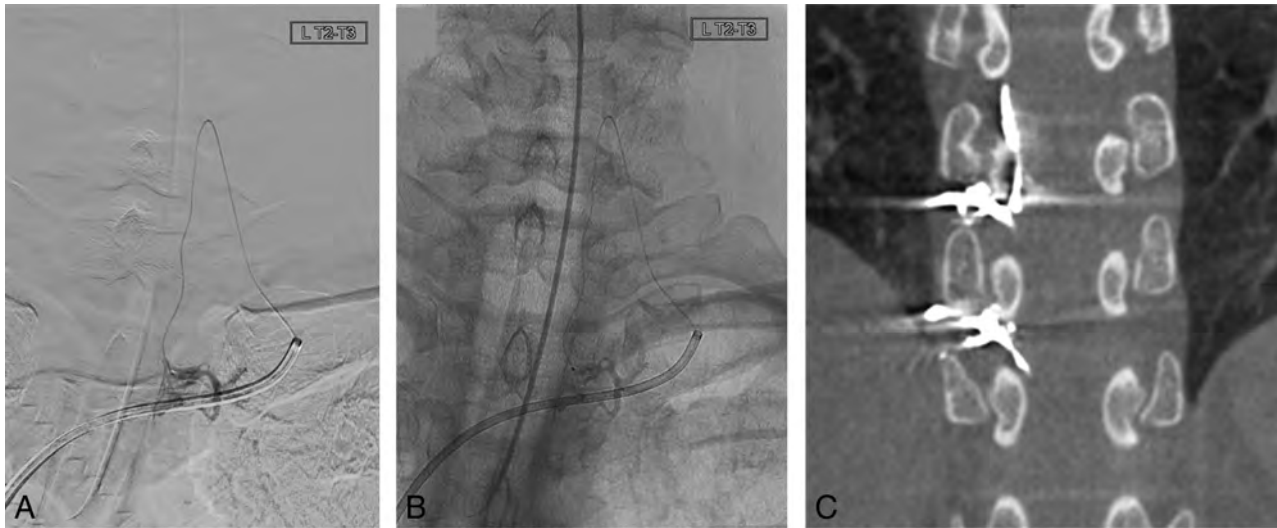


FIG 5. Examples of the appearance of the lateral epidural space at different levels. Subtracted (A) and unsubtracted (B) microcatheter venography performed at the left T2 lateral epidural plexus fills the foraminal veins. In this case, the guide catheter is in the left brachiocephalic vein. The microcatheter enters the left C6 foramen via the vertebral vein, before forming a hairpin turn and traveling caudally across 3 levels through the lateral epidural plexus. C, Postembolization conebeam CT in a different patient shows the embolic agent within the right T8 and T9 foraminal veins and the adjacent lateral epidural plexus.

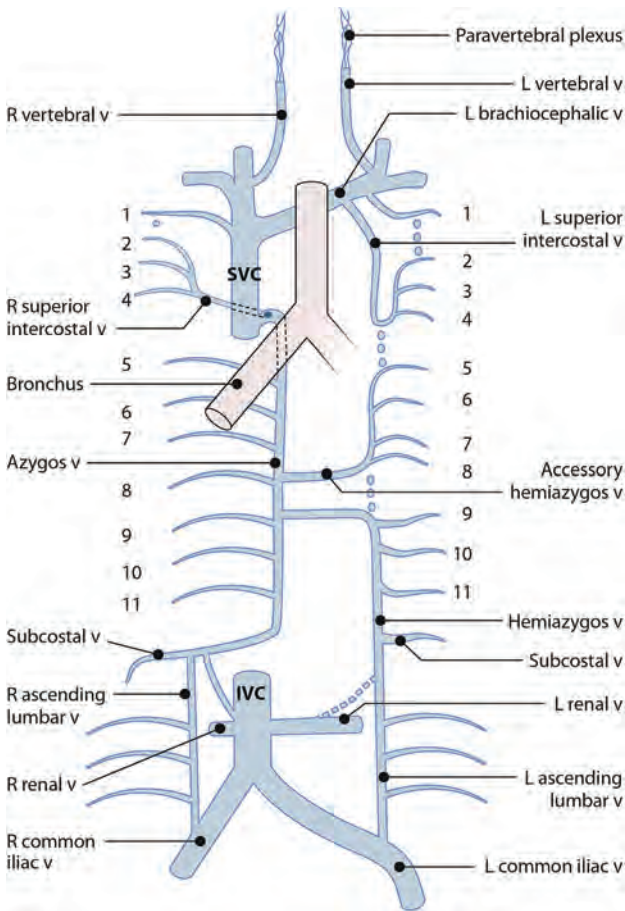


FIG 6. Overview of the azygos system and its main tributaries. The right mainstem bronchus is included as a landmark for the arch of the azygos vein. R indicates right; L, left; v, vein.

Most important, in the thoracolumbar spine, these veins drain directly into the adjacent segmental vein (such as an intercostal vein) at each level. Their role is, therefore, crucial in navigating a microcatheter or liquid embolic agent as close as possible to the nerve root sleeve, the site of pathology in patients with CSF-venous fistulas (Fig 1).

Efferent Pathways. The term “segmental vein” is a general term encompassing the posterior intercostal, subcostal, and lumbar veins. “Paraspinal vein” refers to the part of the segmental vein that runs adjacent to the vertebral body. It effectively begins medial to where the foraminal vein joins the intercostal or lumbar vein and ends by draining into a larger vein such as the azygos vein (Fig 1).

Although textbooks usually describe this segmental arrangement, in practice, we have found the arrangement to be slightly more complex, with intersegmental veins anastomosing adjacent segments. This subtle point is worth remembering when injecting liquid embolic agents, lest the operator be caught out by the unexpected appearance of an unfamiliar structure. We have had several cases in which Onyx (Medtronic) injected at 1 level (eg, T10) traveled a level above or below via this pathway. Occasionally, we have traversed this vein with a microcatheter when a more direct route to the foramen was challenging. The onward drainage of each segmental vein varies in different parts of the spine. The next section covers the gross organization of efferent pathways from segmental veins at various levels toward the superior vena cava (SVC).

Gross Organization of Spinal Venous Drainage

Venous blood from the posterior aspect of the axial skeleton of the trunk, including the spine, drains chiefly via the azygos system, which comprises the azygos vein itself and the hemiazygos and accessory hemiazygos veins (Fig 6). Spinal venous drainage is



FIG 7. Subtracted (A) and unsubtracted (B) views of azygos venography. To the right of the vertebral bodies, the guide catheter is seen to ascend from the IVC to the SVC, before coursing backward into the azygos vein. The trachea and carina are seen in relation to the arch of the azygos vein. Numerous venous stumps (black arrows) along the azygos vein represent reflux into paraspinous veins at each level. In this image, an embolic agent cast is seen filling the right superior intercostal vein (white arrow), which drains into the superior aspect of the arch of the azygos. There is also some opacification of 2 bronchial veins (asterisks).

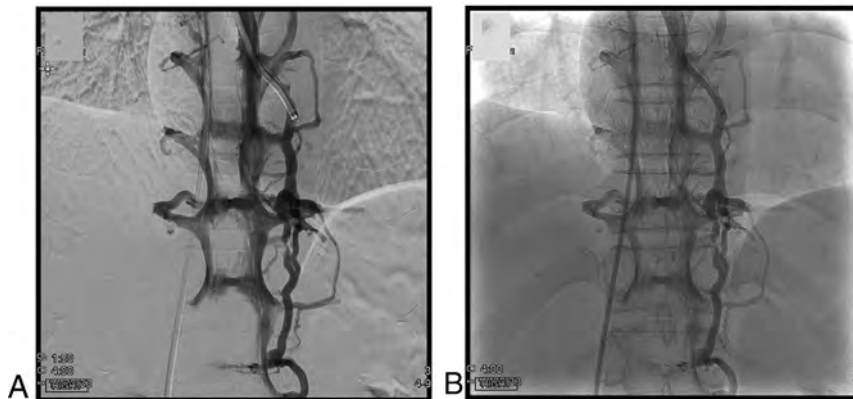


FIG 8. Subtracted (A) and unsubtracted (B) images showing a 6F guide catheter crossing the midline from the azygos to the hemiazygos vein at the level of T9. Also apparent is the hexagonal shape of the epidural plexus, with a central filling defect at the level of the intervertebral disc. The subtracted image below shows the corresponding bony landmarks.

segmental, more uniformly so in the trunk than in the neck. In the thoracolumbar spine, segmental veins drain directly or indirectly into the azygos system, which, in turn, drains into the SVC.

In the cervical spine, a rich paravertebral venous plexus drains into the paired vertebral veins, themselves tributaries of the innominate veins, and, in turn, the SVC. The anatomy of cervical spinal venous drainage is, therefore, addressed separately from the thoracolumbar spine.

Azygos System. The azygos system comprises the azygos vein on the right and the hemiazygos (lower thoracic) and accessory hemiazygos (upper thoracic) veins on the left. It connects the SVC and IVC and serves as an alternative route for venous return to the heart when either the SVC or IVC is compromised.

The azygos vein is a right-sided longitudinal paravertebral structure in the thorax.¹¹ It is formed by the union of the right

ascending lumbar vein with the right subcostal vein at the level of T12. From there, it ascends in the posterior mediastinum before coursing anteriorly to form an arch above the right main bronchus and draining into the posterior aspect of the SVC (Fig 7). Conventionally, there is a single channel, though primitive duplicate channels can persist. Although classically described as a right-sided structure, we have observed several cases in which the azygos vein ran in the midline or even slightly to the left.

Apart from draining the right side of the posterior trunk, the azygos vein also carries the burden of draining blood from its left-sided counterparts into the SVC. On the left, the hemiazygos vein drains the ascending lumbar vein, left subcostal, and 9th-to-11th intercostal veins, usually coursing around the anterior aspect of the T9 vertebral body to drain into the azygos vein (Fig 8). The accessory hemiazygos vein usually drains the fifth-to-eighth intercostal veins on the left, before also crossing the midline at the level of T8 to drain into the azygos vein. The hemiazygos and accessory hemiazygos veins may also be directly connected to each other.

Variability exists with regard to the level at which the hemiazygos and accessory hemiazygos veins join the azygos vein. The interventionalist must, therefore, keep an open mind, use venography to obtain a roadmap, and review prior cross-sectional venous imaging.

Azygos Tributaries Above. On the right, the second-to-fourth intercostal veins drain into the superior intercostal vein, which, in turn, drains into the arch of the azygos vein close to its junction with the SVC just above the right main bronchus. The left superior intercostal vein usually drains the second-to-fourth intercostal veins into the left innominate vein but may also communicate with the accessory hemiazygos vein (Fig 6). The supreme (or highest) intercostal veins on each side may drain into the innominate, superior intercostal, or vertebral veins.

Azygos Tributaries Below. In the lumbar spine, the segmental veins converge to form the ascending lumbar veins on either side of the midline (Fig 6). While the right ascending lumbar vein almost always ends in the origin of the azygos vein, the left ascending lumbar vein can either cross the midline to drain directly into the azygos vein or remain to the left of the midline to join the left subcostal vein in forming the hemiazygos vein.



FIG 9. Venography performed with a catheter in the superior aspect of the left internal jugular vein (larger and more lateral, *black arrow*) shows contrast draining via the condylar vein (*asterisk*) into the vertebral vein (medial and smaller, *white arrow*), which inferiorly drains into the junction of the internal jugular vein with the left brachiocephalic vein. Along its course, multiple tributaries drain into the vertebral vein from the paravertebral plexus and foraminal veins. A catheter and wire are angled medially and superiorly from the junction of the brachiocephalic vein with the internal jugular vein to select the vertebral vein from below.

Vertebral Veins. Unlike in the thorax and abdomen, the skeletal arteries and veins in the neck are not arranged in a strictly metameric fashion. A rich venous network surrounds the cervical spine and communicates with the internal jugular vein and the venous plexuses surrounding the foramen magnum and skull base. The vertebral veins are paired longitudinal paravertebral structures that drain the cervical intervertebral foramina and paravertebral plexuses. In the lower neck, each vertebral vein usually exists as a uniform single channel, but higher up, its configuration consists of a rich, confluent, and valveless paravertebral plexus (Figs 4 and 9). This plexus begins at the level of C1, surrounds the vertebral artery within the transverse foramina of C2–C6, and funnels inferiorly into a large, single channel at the level of C6. Medially, the paravertebral plexus is continuous with the epidural plexus within the spinal canal via the foraminal veins.

Road to the Foramen

The spinal nerve root sleeve is a recognized site of CSF absorption into venous blood under normal physiologic conditions. In patients with a CSF-venous fistula, this mechanism appears to be exaggerated at ≥ 1 level for reasons that are as yet unclear.

Since publishing the first transvenous embolizations, we have embolized 78 fistulas in 60 patients. Our experience has shown that in the thoracic spine, right-sided fistulas are more common than left-sided ones, which is fortuitous because they are more easily accessible than their left-sided counterparts. In the cervical spine, they do not seem to be biased for one side over the other. Fortunately, again, access is reasonably straightforward on both sides.

Access to the SVC. We have approached most of our cases via a common femoral vein puncture. The antecubital vein can be used to access the azygos system, lending itself well to upper thoracic lesions. Overall, our preference remains for groin access, which is better suited to the layout of our neurointervention suites, the length of our usual catheters, and the general familiarity of our team with this setup.

All the efferent pathways draining the spine converge on the SVC before draining into the right atrium. The first part of each procedure is, therefore, virtually always the same, navigating from the groin sheath to the SVC by directing the wire and catheters through the abdomen, through the right atrium, and out again in a straight trajectory directed cranially.

The following sections group the neural foramina by their common venous drainage (or endovascular access) pathways. Numbers in parentheses represent the number of fistulas embolized in our first 60 patients.

Right T5–12 (41 Fistulas, 52.6%). The most common site for CSF-venous fistulas is the right T5–12, and fortunately, we have generally found access to the draining vein to be relatively straightforward.

Recalling that the azygos vein courses over the right main bronchus to drain into the posterior aspect of the SVC, when the guide catheter reaches the level of the right main bronchus in the lower part of the SVC, one would direct an angled intermediate catheter posteriorly and advance a curved wire. The wire is seen to curve over itself and head inferiorly, posteriorly, and to the left toward the midline. Once enough wire has been advanced to ensure stability, the intermediate catheter and guide catheter follow into the azygos vein.

A common obstacle when accessing the azygos vein is the presence of a valve at its junction with the SVC.¹² In most cases, this can be crossed just by advancing the wire, but at other times, it requires a few tries and inhalational maneuvers in awake patients. Once the guide is inside the azygos vein, venography is

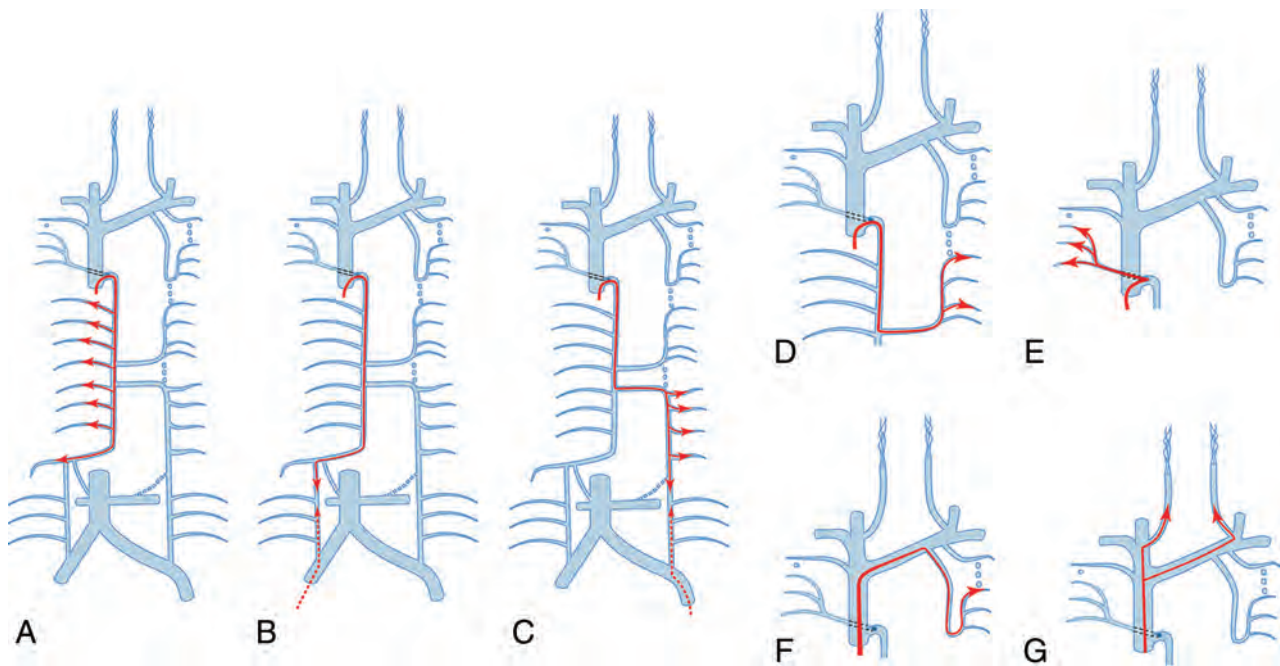


FIG 10. Roadmaps to each foramen, grouped by common venous drainage pathways. A, Right T5–12. B, Right lumbar. C, Left T9–12 and lumbar. D, Left T5–8. E, Right T1–4. F, Left T1–4. G, Cervical.

performed, providing a roadmap for further navigation. Usually, a stump is seen at the level of each segmental tributary. A microwire and microcatheter are then navigated into the stump of interest and pushed out laterally (Fig 10A).

In cases in which a stump is not seen at the desired level, directing a curved microwire to the right of the azygos vein at the level of the target intervertebral foramen usually results in the wire finding the segmental vein. The microcatheter is then tracked into the segmental vein before advancing the wire further. As the segmental vein courses from the anterior to the lateral aspect of the vertebral body, the trajectory of the wire turns to run anterior-to-posterior. At this point, advancing the wire forward a few centimeters at the hub results in the tip appearing to move either very slowly or not at all on a frontal view. Pushing further is usually enough to see the wire start to course laterally again as the vein wraps around from the vertebral body to the rib. If one is in doubt, an oblique projection can provide better visualization of the wire tip and its behavior.

Once the microcatheter tip is close to the intervertebral foramen, microcatheter venography is performed to show the intercostal vein and foraminal venous plexus. This is then used as a roadmap for injection of the liquid embolic agent.

As we have gained experience and confidence with the procedure, we have tried to direct the microcatheter tip further into the foramen, usually by directing a sharply shaped microwire inferiorly from the segmental vein adjacent to the foramen. Although by no means essential, when this step succeeds it allows the foraminal plexus to be embolized by using a smaller volume of embolic agent in a more controlled fashion and minimizing the risk of reflux into the azygos vein.

The ideal cast aims to obliterate any possible route for CSF egress by filling the foraminal plexus circumferentially around the nerve root with modest extension into the lateral epidural plexus, intercostal vein, and paraspinous vein. Extension into the

basivertebral veins is harmless and should not preclude further injection. Extension into intersegmental anastomoses also does not appear to carry any clear risk and may even provide further confidence that the pathway for CSF leak has been adequately obliterated. Despite seeming initially unnerving, injecting into the epidural plexus on a regular basis has so far not resulted in the development of any neurologic deficits from the procedure, though we accept that only time (and more procedures) will give us a fuller idea of the safety profile of the procedure.

T5 itself deserves a note of caution. The fifth intercostal vein drains into the azygos vein close to its junction with the SVC, meaning that there is only a short segment of the azygos vein for the guide catheter to sit in, which makes it harder to obtain a stable position. In addition, the guide catheter is expected to make a sharp turn as it transits from the SVC to the azygos vein; soon after this, a microcatheter is expected to make another sharp turn to the right (combining to make a 270° turn clockwise on an anterior-posterior projection, from heading cranially to heading right lateral) into the fifth intercostal vein. This turn is less of an issue at T6, where the additional length of the catheter within the azygos vein provides better stability. From T7 on, this essentially becomes a nonissue.

Right Lumbar (1 Fistula, 1.3%). The right ascending lumbar vein is caudally contiguous with the azygos vein (Fig 10B). The route of access to the azygos vein is described in the section above. Once azygos venography is acquired, the microcatheter and wire are directed caudally, staying out of the segmental veins and the hemiazygos vein, to the level of the target vein. Note that the lumbar segmental veins can join the ascending lumbar vein at an oblique angle. Any uncertainty over the direction required to reach the target can be resolved by performing venography from the lowermost part of the azygos vein at the level of T12. Once inside the

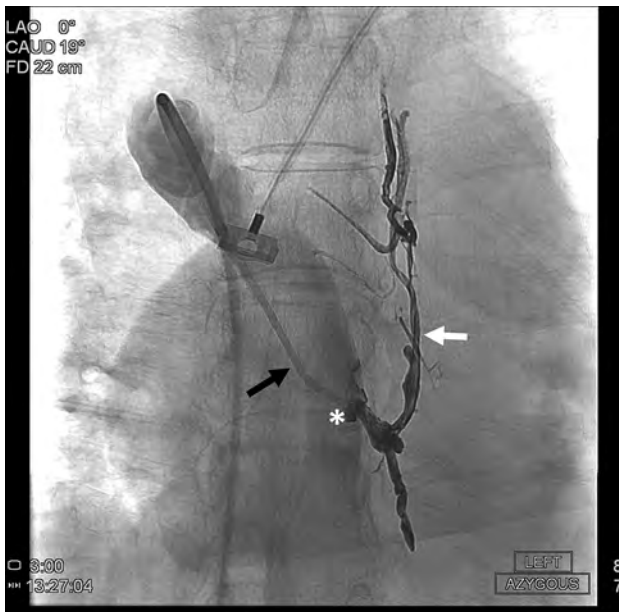


FIG 11. Postembolization image showing the liquid embolic agent in the accessory hemiazygos vein (*white arrow*) in a patient with multiple left-upper-thoracic CSF-venous fistulas. The catheter is seen to ascend in the SVC, course around the arch down the azygos vein (*black arrow*), and then cross the midline (*asterisk*) to enter the accessory hemiazygos vein.

lumbar segmental vein, onward navigation toward the foramen follows the route described in the previous section.

The right ascending lumbar vein arises from the right common iliac vein below. Sometimes we are able to take a microcatheter directly from the common iliac vein up the ascending lumbar vein, but often this vein has multiple interruptions, which make superior navigation all but impossible beyond a couple of levels.

Left T9–12 and Left Lumbar (11 Fistulas, 14.1%). Left T9–12 all drain into the hemiazygos vein (Fig 10C). The route begins by placing a guide catheter in the azygos vein at the level of T8 or T9 and performing venography. This process usually provides good visualization of the hemiazygos vein crossing the midline and draining into the azygos vein. A microcatheter is taken across the midline and navigated down the hemiazygos vein to the desired level, before performing microcatheter venography and proceeding from there. Alternatively, a microcatheter can sometimes be taken directly from the left common iliac vein into the ascending lumbar vein.

Left T5–8 (6 Fistulas, 7.7%). Getting to the accessory hemiazygos vein starts off again by placing a guide catheter in the azygos vein, this time just above where the accessory hemiazygos vein crosses the midline (usually around the level of T8) to drain into the azygos vein. Venography is acquired within the azygos vein, and a microcatheter is used to cross over to the left and then ascend within the accessory hemiazygos vein to the desired level, from which microcatheter venography is performed (Fig 10D).

Right T1–4 (8 Fistulas 10.3%). Fistulas between T2 and T4 on the right drain into the right superior intercostal vein, which itself drains into the superior aspect of the arch of the azygos. From the

SVC, the guide catheter is placed just within the azygos vein, which unfortunately limits its stability. The microcatheter and wire are then directed cranially and posteriorly into the superior intercostal vein (Fig 10E). The embolic agent cast in Fig 7 illustrates where the superior intercostal vein connects to the arch of the azygos.

Access to the right supreme intercostal vein for the treatment of right T1 fistulas is variable, as described above. Usually, it can be found from the superior intercostal vein. Occasionally, it requires navigating through the vertebral vein. If the supreme intercostal vein cannot be found, a microcatheter can be navigated into the T2 foramen, through the lateral epidural plexus, and cranially toward the T1 foramen.

Left T1–4 (5 Fistulas, 6.4%). The left superior intercostal vein can be accessed from either above or below. Access from below requires navigation through the accessory hemiazygos vein (see the section on the left T5–8) and directing a microcatheter further cranially (Fig 11). Access from above requires navigation from the SVC to the left innominate vein to cross the midline to the left. At approximately the lateral border of the vertebral body, the superior intercostal vein can be found on the posterior and inferior aspects of the innominate vein (Fig 10F). Cannulating its origin may require a sharply-angled or even reverse-facing intermediate catheter such as a 5F Mikaelsson catheter (Merit Medical).

Accessing the neural foramen in this region can, at times, be extremely difficult. Lately, we have resorted to accessing the lateral epidural plexus of the cervical spine on the left and navigating downward until we reach the target foramen (Fig 5).

Access to the left supreme intercostal vein is about as variable as it is on the right. It may drain into the innominate, superior intercostal, or vertebral veins and may require some trial and error to get there. Preintervention CT venography can help to plan routes to both the right and left supreme intercostal veins.

Cervical (6 Fistulas, 7.7%). Foraminal veins in the neck, together with their rich adjacent paravertebral and epidural plexuses, converge on the vertebral veins at approximately the level of C6 to drain into the innominate veins bilaterally. From the respective innominate vein, a wire is directed posteriorly, superiorly, and medially (Fig 10G). Entering the vertebral vein can be challenging due to the presence of a valve at its junction with the innominate vein and may require a few attempts or even inspiratory maneuvers in self-ventilating patients. Once the vertebral vein is found, venography is performed and serves as a roadmap for onward navigation.

The typical appearance of vertebral venography is complex (Figs 4 and 9). This complexity can serve as an ally to the interventionalist by providing a choice of pathways. In our experience, we have been able to direct microcatheters through the paravertebral plexus (outside the vertebral column) to the desired level before the microcatheter then courses medially toward the foraminal vein. At other times, we have been able to access the foramen above or below our target, enter the lateral epidural plexus, and ascend or descend from there.

It has also been possible to perform embolization from the vertebral vein itself, allowing the embolic agent to travel

through its complex system of tributaries and eventually opacify the target foramen. Thus far, we have not encountered any adverse events from embolizing the whole of the vertebral vein, presumably on account of its anastomoses and functional interchangeability with its contralateral counterpart and the venous plexuses around the skull base. The chances of success, however, do diminish if the embolic agent does not travel all the way to the foramen.

CONCLUSIONS

Spinal venous navigation is infrequently performed in most neurointerventional units, including ours until recently. This article provides a comprehensive summary of the organization of venous drainage throughout various regions of the spine, together with practical guidance on navigating microcatheters to each foramen. It is entirely possible that with further experience, we will encounter additional routes to the spine, but we hope that the experience we have garnered so far will serve to provide confidence to any colleagues who may wish to embark on transvenous access to the spine.

Disclosure forms provided by the authors are available with the full text and PDF of this article at www.ajnr.org.

REFERENCES

1. Schievink WI, Moser FG, Maya MM. **CSF-venous fistula in spontaneous intracranial hypotension.** *Neurology* 2014;83:472–73 CrossRef Medline
2. Brinjikji W, Savastano LE, Atkinson JL, et al. **A novel endovascular therapy for CSF hypotension secondary to CSF-venous fistulae.** *AJNR Am J Neuroradiol* 2021;42:882–87 CrossRef Medline
3. Lasjaunias P, Berenstein A, Ter Brugge KG. *Surgical Neuroangiography*. 2nd ed. Springer; 2001;1:159–64
4. Théron J, Moret J. *Spinal Phlebography*. Springer-Verlag; 1978:43–57
5. Théron J, Djindjian R. **Cervicovertebral phlebography using catheterization.** *Radiology* 1973;108:325–31 CrossRef Medline
6. Thron AK. *Vascular Anatomy of the Spinal Cord*. Springer; 2nd ed. 2016:85–136
7. Griessenauer CJ, Raborn J, Foreman P, et al. **Venous drainage of the spine and spinal cord: a comprehensive review of its history, embryology, anatomy, physiology, and pathology.** *Clin Anat* 2015;28:75–87 CrossRef Medline
8. Santillan A, Nacarino V, Greenberg E, et al. **Vascular anatomy of the spinal cord.** *J Neurointerv Surg* 2012;4:67–74 CrossRef Medline
9. Batson OV. **The function of the vertebral veins and their role in the spread of metastases.** *Ann Surg* 1940;112:138–49 CrossRef Medline
10. Gray H. *Anatomy of the Human Body*. Elsevier; 20th ed. 1918:668–69
11. Heitzman ER. *The Mediastinum: Radiologic Correlations with Anatomy and Pathology*. 2nd ed. Springer-Verlag; 1988:215–29
12. Yeh BM, Coakley FV, Sanchez HC, et al. **Azygos arch valves: prevalence and appearance at contrast-enhanced CT.** *Radiology* 2004;230:111–15 CrossRef Medline

Machine Learning in Differentiating Gliomas from Primary CNS Lymphomas: A Systematic Review, Reporting Quality, and Risk of Bias Assessment

G.I. Cassinelli Petersen, J. Shatalov, T. Verma, W.R. Brim, H. Subramanian, A. Brackett, R.C. Bahar, S. Merkaj, T. Zeevi, L.H. Staib, J. Cui, A. Omuro, R.A. Bronen, A. Malhotra, and M.S. Aboian



ABSTRACT

BACKGROUND: Differentiating gliomas and primary CNS lymphoma represents a diagnostic challenge with important therapeutic ramifications. Biopsy is the preferred method of diagnosis, while MR imaging in conjunction with machine learning has shown promising results in differentiating these tumors.

PURPOSE: Our aim was to evaluate the quality of reporting and risk of bias, assess data bases with which the machine learning classification algorithms were developed, the algorithms themselves, and their performance.

DATA SOURCES: Ovid EMBASE, Ovid MEDLINE, Cochrane Central Register of Controlled Trials, and the Web of Science Core Collection were searched according to the Preferred Reporting Items for Systematic Reviews and Meta-Analyses guidelines.

STUDY SELECTION: From 11,727 studies, 23 peer-reviewed studies used machine learning to differentiate primary CNS lymphoma from gliomas in 2276 patients.

DATA ANALYSIS: Characteristics of data sets and machine learning algorithms were extracted. A meta-analysis on a subset of studies was performed. Reporting quality and risk of bias were assessed using the Transparent Reporting of a multivariable prediction model for Individual Prognosis Or Diagnosis (TRIPOD) and Prediction Model Study Risk Of Bias Assessment Tool.

DATA SYNTHESIS: The highest area under the receiver operating characteristic curve (0.961) and accuracy (91.2%) in external validation were achieved by logistic regression and support vector machines models using conventional radiomic features. Meta-analysis of machine learning classifiers using these features yielded a mean area under the receiver operating characteristic curve of 0.944 (95% CI, 0.898–0.99). The median TRIPOD score was 51.7%. The risk of bias was high for 16 studies.

LIMITATIONS: Exclusion of abstracts decreased the sensitivity in evaluating all published studies. Meta-analysis had high heterogeneity.

CONCLUSIONS: Machine learning–based methods of differentiating primary CNS lymphoma from gliomas have shown great potential, but most studies lack large, balanced data sets and external validation. Assessment of the studies identified multiple deficiencies in reporting quality and risk of bias. These factors reduce the generalizability and reproducibility of the findings.

ABBREVIATIONS: AI = artificial intelligence; AUC = area under the receiver operating characteristic curve; CNN = convolutional neural network; ML = machine learning; PCNSL = primary CNS lymphoma; PRISMA = Preferred Reporting Items for Systematic Reviews and Meta-Analyses; PROBAST = Prediction model study Risk Of Bias Assessment Tool; TRIPOD = Transparent Reporting of a multivariable prediction model for Individual Prognosis Or Diagnosis

Gliomas are the most common primary malignancy of the CNS.¹ An important differential diagnosis for gliomas is

primary CNS lymphoma (PCNSL), a more uncommon but highly malignant neoplasia.² Correct differentiation of these tumor entities is an important challenge for clinicians because

Received July 26, 2021; accepted after revision January 31, 2022.

From the Department of Radiology and Biomedical Imaging (G.I.C.P., T.V., H.S., R.C.B., S.M., T.Z., L.H.S., J.C., R.A.B., A.M., M.S.A.), Cushing/Whitney Medical Library (A.B.), and Department of Neurology (A.O.), Yale School of Medicine, New Haven, Connecticut; Universitätsmedizin Göttingen (G.I.C.P.), Göttingen, Germany; University of Richmond (J.S.), Richmond, Virginia; New York University (T.V.), New York, New York; and Whiting School of Engineering (W.R.B.), Johns Hopkins University, Baltimore, Maryland.

This work was supported by a American Society of Neuroradiology Fellow Award 2018 (M.S.A.). This publication was made possible by KL2 TR001862 from the National Center for Advancing Translational Science, components of the National Institutes of Health and National Institutes of Health Roadmap for Medical Research.

Its contents are solely the responsibility of the authors and do not necessarily represent the official view of National Institutes of Health.

Please address correspondence to Mariam Aboian, MD, PhD, Department of Radiology, Yale School of Medicine, 333 Cedar St, New Haven, 06510 CT; e-mail: mariam.aboian@yale.edu; @GabrielCassine1

Indicates open access to non-subscribers at www.ajnr.org

Indicates article with online supplemental data.

<http://dx.doi.org/10.3174/ajnr.A7473>

therapy differs vastly: High-grade gliomas are treated with surgery and adjuvant radiochemotherapy,³ while standard PCNSL treatment consists of high-dose methotrexate chemotherapy.^{4,5} Surgery, in the latter group, is mostly reserved for either biopsy and decompressive surgery in cases of increased intracranial pressure.⁶ Currently, the standard diagnostic approach for suspected PCNSL consists of stereotactic biopsy and histopathologic analysis.⁷ Nonetheless, this diagnostic method has morbidity and mortality rates of up to 6% and 3%, respectively.^{8,9} Furthermore, while maximum surgical resection is the standard-of-care initial treatment for gliomas, its effectiveness in treating PCNSL has yet to be convincingly demonstrated.^{4,10} Therefore, surgical biopsy poses important risks and yields no benefit besides histopathologic diagnosis. In this context, a noninvasive diagnostic procedure would be beneficial. An important candidate for this is artificial intelligence (AI)-assisted radiologic diagnosis.

PCNSL typically appears as a homogeneously contrast-enhancing parenchymal mass without necrosis,¹¹ while glioblastoma as an intra-axial tumor with irregular infiltrative margins and a central heterogeneously enhancing core, reflecting necrosis and hemorrhage.^{12,13} While these qualitative features provide valuable clues for differentiation in typical cases, there are atypical presentations: PCNSL with ring-enhancing lesions and central necrosis can be observed in up to 13% of non-AIDS- and up to 75% of AIDS-related cases.¹¹

An important tool that has recently emerged to improve the radiologic diagnosis is machine learning (ML). ML pipelines learn quantitative image features that are not visible to the human eye and correlate them to a clinical outcome.¹⁴ In the past decades, considerable effort has been put into developing ML-based classification algorithms for differentiating gliomas and PCNSLs. This work has led to much data that should be identified, systematically evaluated, and synthesized. So far, 1 systematic review on this topic has been presented by Nguyen et al,¹⁵ in 2018, but it was performed only on a single bibliographic data base. Prior studies have shown that single data base searches are insensitive and limit the scope of systematic reviews.¹⁶ Therefore, we performed a more comprehensive search using 4 established data bases and wider-reaching keywords.

In this systematic review, we synthesized and evaluated the quality of reporting, risk of bias, data bases, algorithms, and their performance achieved thus far. We hope to provide an accurate picture of the current state of development, identifying shortcomings and providing recommendations to increase model performance, reproducibility, and generalizability to enable implementation into routine clinical practice.

MATERIALS AND METHODS

Search Strategy and Information Sources

This systematic review was performed in accordance with the Preferred Reporting Items for Systematic Reviews and Meta-Analyses (PRISMA) guidelines.¹⁷ The study was registered with the International Prospective Register of Systematic Reviews (PROSPERO, CRD42020209938). A data base search of Ovid EMBASE, Ovid MEDLINE, and the Cochrane Central Register of Controlled Trials (CENTRAL), and the Web of Science Core Collection was performed by a clinical librarian from anytime

until February 2021. The search strategy included the following keywords and controlled vocabulary combining the terms for the following: “AI,” “machine learning,” “deep learning,” “radiomics,” “MR imaging,” “glioma” as well as related terms (Online Supplemental Data). The search strategy was independently reviewed by a second institutional librarian. All publications were screened on Covidence (Veritas Health Innovation) software by a neuroradiology attending physician, a radiology resident, an AI graduate student, and a senior medical student.

Selection Process and Eligibility Criteria

To select relevant studies, the 4 reviewers undertook the following steps independently: Initially, after duplicate removal, all study abstracts were screened to exclude studies not pertaining to neuro-oncology or not using ML methods. Next, full-text review was performed to exclude publications that met the following criteria: 1) were only abstracts; 2) were not original articles; 3) did not involve artificial intelligence or ML; 4) did not involve gliomas; 5) were not done on humans; 6) were not performed with either MR imaging, PET, or MR spectroscopy; and 7) were not in English. Lastly, only studies evaluating differentiation of gliomas versus PCNSL were included for data extraction. In an initial search, studies that used only logistic regression were excluded. These studies were, however, later included by filtering the excluded studies in Covidence by the terms “lymphoma” and “pcnsl.” Here, studies that used logistic regression and differentiated gliomas from PCNSL were selected after abstract screening and full-text review. When disagreement between reviewers occurred, the neuroradiology attending physician made the final decision.

Data-Collection Process and Data Items

Data was extracted independently by 2 reviewers using a custom-built data-extraction form (Online Supplemental Data). Disagreement was resolved by reaching a consensus through discussion. Data was collected on 1) the report (title, authors, year); 2) the patient characteristics (number of patients included, source of data, glioma/PCNSL case ratio, immune status of the patients with lymphoma, percentage of patients in training and testing, and use of an independent test cohort); 3) the tumor type studied and the definition of ground-truth (type of glioma, criterion standard for diagnosis); 4) the ML method used (classic ML or deep learning, algorithms studied, type and number of features used); 5) the imaging procedures performed (type of imaging studies used, magnetic field strength of MR imaging machine, MR imaging sequence studied); and 6) performance metrics as described in detail below.

Reporting Quality and Risk of Bias Assessment

Reporting quality and risk of bias assessment was performed independently by 2 reviewers using the Transparent Reporting of a multivariable prediction model for Individual Prognosis Or Diagnosis (TRIPOD) checklist¹⁸ and the Prediction model study Risk Of Bias Assessment Tool (PROBAST), respectively.¹⁹ TRIPOD is composed of 77 individual questions that address 30 different scorable domains, 29 of which are applicable to our study after excluding item 11 as listed in the Online Supplemental Data. The final TRIPOD score was calculated as described in the

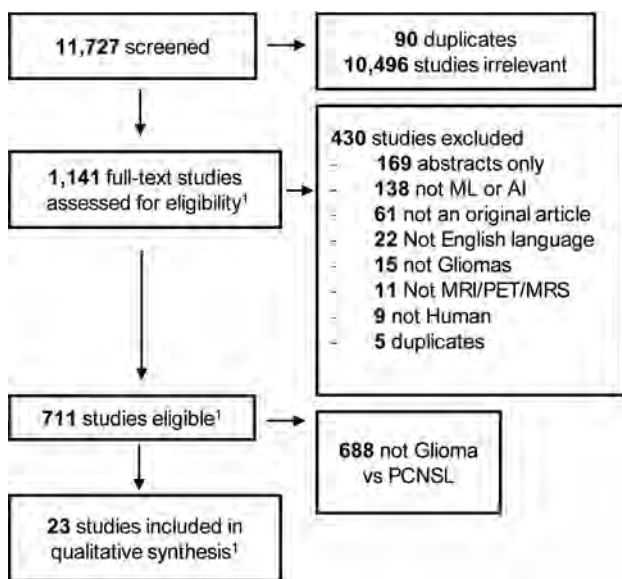


FIG 1. PRISMA flow diagram. This chart delineates the selection process that yielded the 23 studies included in this systematic review.¹ The initial search yielded 1135 studies for full-text review, and 704 were eligible, and 16 were included. A second literature search yielded 6 additional studies.

TRIPOD Adherence Assessment Form. For each study, the percentage of successfully reported TRIPOD items applicable to the individual study was reported. Additionally, for every item in the assessment, we report an adherence index, which we calculated as the average achieved across all studies. PROBAST is a checklist composed of 4 domains and 20 signaling questions, useful for assessing the risk of bias in multivariate diagnostic prediction models.¹⁹ The Cohen's κ was used to calculate the interrater reliability of the assessment between the 2 independent reviewers, and interpreted as delineated by Altman.²⁰

Data Analysis and Synthesis

To assess the performance of the classifiers from each study, we extracted primarily the reported area under the receiver operating characteristic curve (AUC) and its corresponding 95% confidence interval if available. Other threshold-based performance metrics that were extracted were accuracy, sensitivity, and specificity. Different studies test the interaction of classifiers with different feature-selection methods, resulting in many permutations of the same classifier. Only the results of the best performing version of each studied classifier were reported because we deemed this information most relevant. We grouped the performance metrics according to whether they were calculated during training, internal or external validation. To plot graphs, we used the performance on validation. If a study reported both internal and external validation, only external validation was plotted. Some studies compared ML models with the performance of different neuroradiologists. In these cases, we reported only the results of the highest performing radiologist, unless stated otherwise.

We performed a meta-analysis on the AUC values of a subset of studies that used conventional radiomic features and conventional ML algorithms for model development. Studies were only included if they reported an AUC with a 95% CI in a validation set and if

they used conventional radiomic features for model development. Studies that used a deep learning-based classifier were also excluded in the meta-analysis. These exclusion criteria were chosen to decrease the methodic diversity and increase the comparability of the studies included in the meta-analysis. If both internal and external validation were reported, we used the performance on external validation. The meta-analysis used a random-effects model, as described by Zhou et al,²¹ and was performed on MedCalc (MedCalc Software). The calculated heterogeneity among studies is reported using Higgins I^2 , which describes the percentage of total variation attributable to heterogeneity rather than chance alone.²²

RESULTS

Study Selection

The study-selection process is presented in Fig 1. The literature search yielded 11,727 studies. After duplicate removal, 10,496 studies were excluded, 1141 studies underwent full-text review, and finally 23 articles were included in our systematic review as per our criteria.²³⁻⁴⁵ Of note, the selection process was performed in two steps since 6 studies that were finally included, were initially excluded solely because only a Logistic Regression model was developed. Data was extracted from these studies for qualitative synthesis. An outline of the data sets and the developed ML pipelines of the individual studies can be found in the Online Supplemental Data.

Data Sets for Model Development

The data sets had a mean size of 99 patients per study (range: 17–259 patients) (Fig 2A), with a mean ratio of 1.9 glioma cases for every PCNSL case (range: 7.9–0.4 cases), with only 2 studies having a 1:1 ratio (Fig 2B); 56.5% ($n = 13$) of the studies used data from single-center hospital data bases, and 17.4% ($n = 4$) used private multicenter hospital data bases. The source of patients could not be determined in 26.1% ($n = 6$) of articles (Fig 2C). No study used public brain tumor data sets such as Brain Tumor Segmentation (BraTS) or The Cancer Imaging Archive (TCIA).

More than half of the studies did not use external validation, instead relying on k-fold cross-validation or randomly sampling subjects into 2 cohorts, training and validation. Five studies did not report any type of validation (Fig 2D). Among the 6 studies that externally validated their algorithm, 4 sampled the external data set from a different institution (geographic validation),^{28,30,33,43} and 2, on a different timepoint (temporal validation)^{31,37} than the training set.

Tumor Entities

All studies used PCNSL and gliomas in their data sets. Among the gliomas, all studies included glioblastomas: 2 included World Health Organization grade III gliomas,^{23,41} and 1, lower-grade gliomas.⁴¹ 5 also included meningiomas³⁴ and/or metastatic lesions.^{33,34,36,45} 3 studies specified that they incorporated atypical glioblastomas, defined as glioblastomas without central necrosis,^{29,35,39} while 3 explicitly included atypical PCNSLs.^{28,30,39} We also investigated whether the immune status of patients with lymphoma was reported. 5 studies included only immunocompetent patients,^{28,29,31,38,44} whereas 2 included both immunocompetent and immunosuppressed patients.^{23,45} The remaining studies did

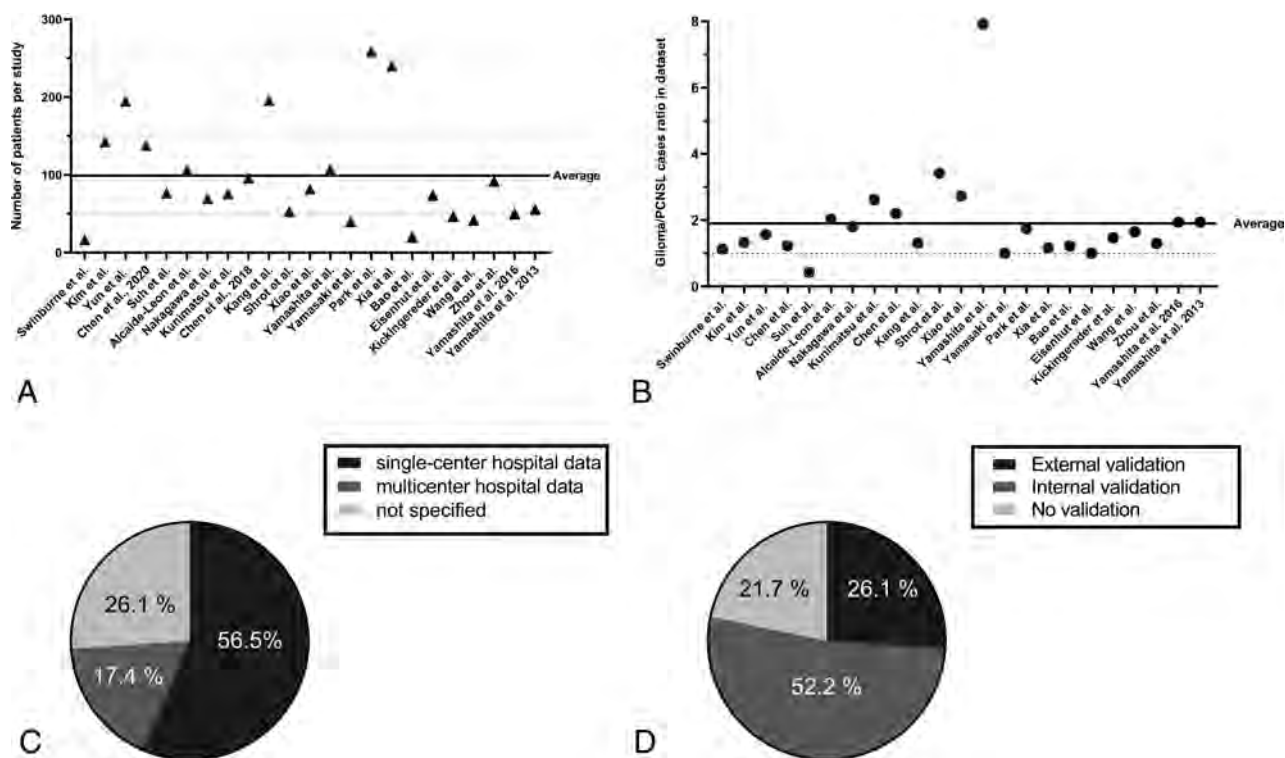


FIG 2. A, Scatterplot displaying the number of patients included in the data sets. B, Scatterplot of the glioma/PCNSL case ratio in the data sets. A ratio of >1 means more gliomas, a ratio of <1 means more PCNSL, and a ratio = 1 means equal number. C, Source of patients in the data sets. D, Type of validation performed in the studies.

not specify immunologic status. Importantly, all except 2 studies solely used images of tumors whose final diagnosis had been histopathologically confirmed. The other 2 combined histopathologic and clinicoradiologic criteria for diagnosis.^{40,42}

Image Features and Classification Algorithms

Nineteen studies used classic ML: 2 solely deep learning methods;^{33,41} and 2 a combination of both.^{36,43} Ten studies used combinations of shape and conventional radiomic features (first order, texture matrices, and wavelet-transformed images). Among these, the mean number of features used for model development was 29 (range, 3–80). A combination of diffusion and perfusion features was used in 8 studies,^{24,27,29,34,36,40,42,45} while 1 also included SWI-derived features.²⁹ Other types of image features were used such as scale-invariant feature transform features,^{26,46} luminance histogram range,³⁹ temporal patterns of time-signal intensity curves from DSC perfusion imaging extracted with the help of an autoencoder neural network,³³ and [¹⁸F] PET-derived metrics.^{40,42,44} After feature selection, the number of features ranged from 1 to 496.^{26,36}

For classification, 10 different classic ML and 3 different deep learning algorithm types were used. The most common classic ML methods were support vector machines and logistic regression (each $n = 11$), a multilayer perceptron network ($n = 3$), and a convolutional neural network (CNN) ($n = 2$) for deep learning. Other algorithms were random forests ($n = 4$), decision tree ($n = 3$), Naïve Bayes ($n = 2$), linear discriminant analysis ($n = 2$), generalized linear model ($n = 2$), XGBoost ($n = 1$), AdaBoost ($n = 1$), and k-nearest neighbor ($n = 1$).

Imaging

All studies except for 1 were performed on MR images. MR imaging sequences used were contrast-enhanced T1 (100% of studies performing MR imaging, $n = 22$), noncontrast T1 (50%, $n = 11$), T2 (59.1%, $n = 13$), FLAIR (50%, $n = 11$), DWI (68.2%, $n = 15$), intravoxel incoherent motion (4.6%, $n = 1$), and perfusion images (45.5%, $n = 10$). Three studies implemented [¹⁸F] FDG PET/CT imaging.

Model Performance and Meta-analysis

The reported metrics varied among different studies. AUC, accuracy, sensitivity, and specificity were reported in 91.3%, 65.2%, 73.9%, and 69.6% of the studies, respectively. The highest validation AUC of every study and respective 95% CI, if reported, are shown in the Online Supplemental Data. For a summary of the performance of every classifier by study, please refer to the Online Supplemental Data.

The classifiers that reached the highest AUC and accuracy in external validation were logistic regression³⁰ (AUC = 0.961) and a support vector machine³⁰ and logistic regression model³⁷ (both accuracy = 91.2%), respectively. All were trained on conventional radiomic features extracted from routine and DWI sequences. An XGBoost classifier³² and a support vector machine classifier trained on scale-invariant feature transform features²⁶ were the only models that reached an AUC of >0.98 in internal validation but were not explored further in external validation.

Some studies compared the classification performance of ML models with that of radiologists tasked with comparing the same set of images,^{23,28,32,35,43} and 2 studies examined the effect of

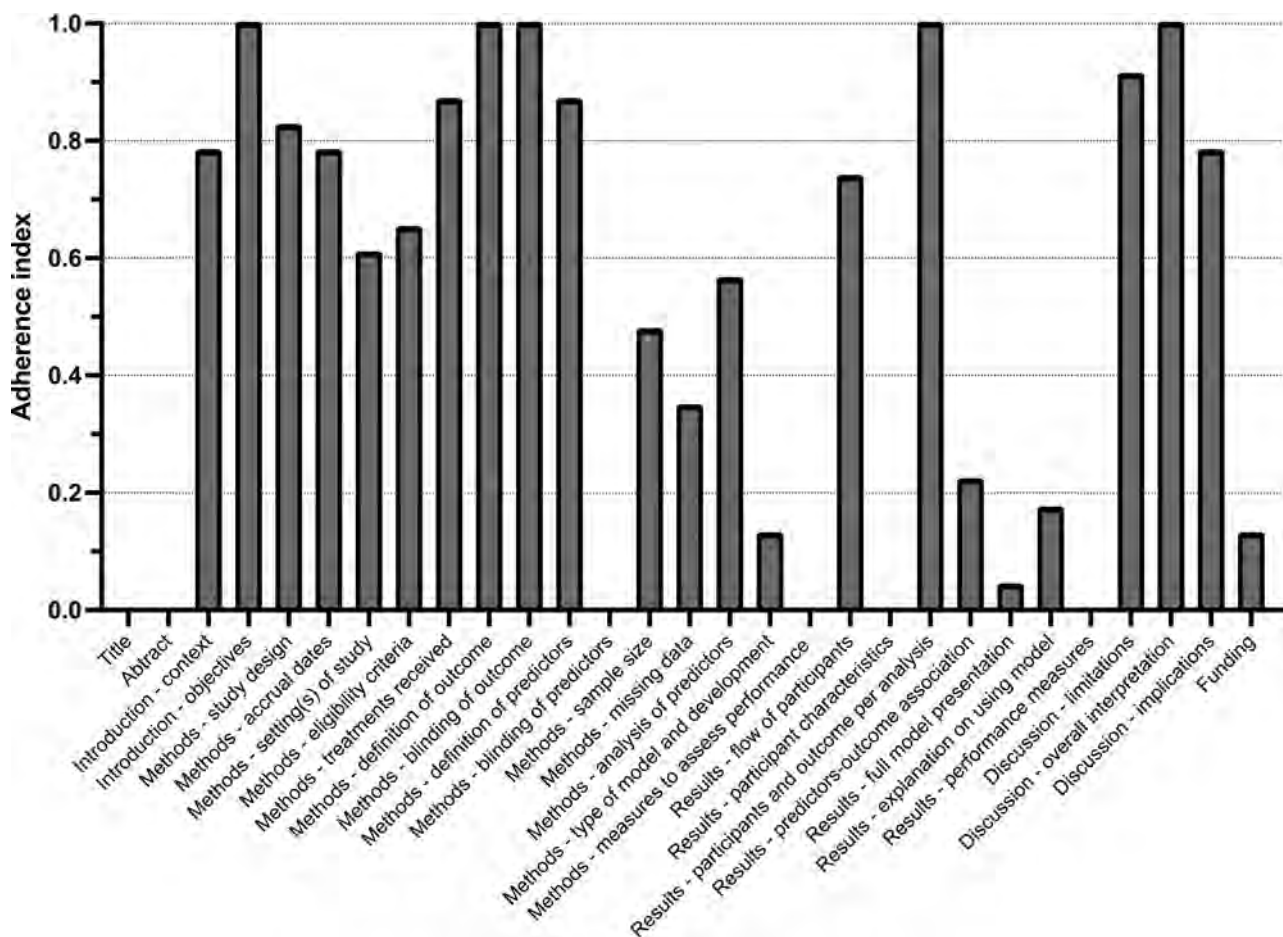


FIG 3. TRIPOD adherence index. The adherence index for a particular item was calculated as the average points achieved across all studies.

integrating the results of an ML algorithm in the radiologists' decision process (Online Supplemental Data).^{37,41} Two publications found the ML algorithm superior,^{32,35} while one found it significantly noninferior.²³ Both Yamashita et al⁴¹ and Xia et al³⁷ found that incorporating ML models into the classification of novice radiologists significantly improved the AUC to levels comparable with their more experienced counterparts. Among experienced neuro-radiologists, the effect was smaller-but-significant in 1 study.

Because conventional radiomics was the most used type of feature, we decided to conduct a random-effects AUC meta-analysis on a subset of studies that used these features in classic ML classifiers. We identified 6 studies that reported AUCs with confidence intervals in a validation test.^{23,28,31,33,35,43} We excluded one because the radiomic features it used were not conventional³³ and one because its best classifier was a deep learning model.⁴³ In total, 4 studies were included in the meta-analysis.^{23,28,31,35} The pooled AUC was calculated as 0.944 (95% CI, 0.918–0.980; $I^2 = 74.3\%$). A forest plot of the meta-analysis can be seen in the Online Supplemental Data.

Adherence to Reporting Standards and Risk of Bias Assessment

We performed a reporting quality assessment according to the TRIPOD checklist. Thirteen studies had an adherence index of <50%. Overall, the median TRIPOD score among all studies was

51.7% (interquartile range, 41.4%–62.1%). The individual adherence index for every item is shown in Fig 3 and the Online Supplemental Data. We performed a risk of bias assessment using the PROBAST tool. The overall risk of bias was deemed high in 69.6% ($n = 16$) of studies and unclear in the rest. The risk of bias per PROBAST domain is further specified in the Online Supplemental Data. The interrater reliability between the 2 independent reviewers was very good in both the reporting quality ($\kappa = 0.965$; 95% CI, 0.945–0.985) and risk of bias assessment ($\kappa = 0.851$; 95% CI, 0.809–0.892).

DISCUSSION

Our systematic review identified and analyzed 23 articles that published ML-based classification algorithms for noninvasive differentiation of gliomas and PCNSL.^{23–45}

Analysis of study data sets revealed them to be predominantly small and unbalanced because glioma cases were overrepresented compared with PCNSL. This finding likely reflects the difficulty in sampling lymphoma cases due to their low prevalence. Moreover, a minority of studies validated their algorithm externally.^{28,30,31,33,37,43} These factors decreased the generalizability of the findings and increased the risk of overlooking overfitted classifiers. Thus, we encourage multicenter collaborations to create larger, more balanced data sets. Additionally, cross-center

collaborations would facilitate the construction of geographically distinct external validation data sets on which to test these models.

We were also interested in the specific tumor entities that researchers used for model development. Strikingly, only a few articles specified the inclusion of atypical glioblastomas and lymphomas.^{28-30,35,39} Considering that it is the atypical variants of the tumors that appear most similar, only including typical-appearing tumors might make classification easier without reflecting the everyday challenges faced by diagnosticians. Similarly, only 7 studies reported the immune status of the included patients with lymphoma.^{23,28,29,31,38,44,45} Overall, we recommend inclusion of atypical cases in future data sets and clear reporting of their fraction and patients' immune status.

Classic ML classifiers trained on conventional radiomic features of routine sequences and DWI reached AUCs of >0.95 and the highest accuracies in external validation.^{30,37} These findings, along with the high mean AUC in the meta-analysis, suggest that radiomic features extracted from conventional sequences are powerful in differentiating gliomas from PCNSL. This finding should make clinical implementation faster, considering that open-source packages for conventional radiomic feature extraction, like PyRadiomics,⁴⁷ are readily available. XGBoost, a decision tree-based algorithm popular among data scientists, performed very well in internal validation but was not tested on external validation.³² Considering that random forest models (also decision-tree based) performed well in external validation, it would be reasonable to also expect good performance with XGBoost and hence encourage further research using this algorithm. These results are in line with other systematic reviews on ML in neuro-oncology. Our research group has also performed systematic reviews on the role of ML in predicting glioma grade and differentiating gliomas from brain metastases.^{48,49} Both studies found, similar to our findings, a high mean accuracy despite small data sets. Overall, these findings are encouraging because they show that even though PCNSL is a rarer disease than other brain neoplasms, the development of ML applications for its diagnosis is on a par with that for other tumor entities.

Deep learning classifiers were explored by only 4 different studies.^{33,36,41,43} Yun et al⁴³ developed a CNN-based model that showed good performance in internal validation (AUC = 0.879), but performance decreased drastically when externally validated (AUC = 0.486). CNNs, if not regularized properly, are prone to overfitting and benefit from large multisite data sets.⁵⁰ Using multiple sites facilitates larger data sets and incorporates valuable heterogeneity for training. Park et al³³ also developed a CNN-based model which achieved a higher AUC (0.89) in external validation. Overall, further evaluation of applications of CNN in the classification of gliomas from lymphomas in larger data sets is needed.

In recent years, the utility of ML algorithms as computer-aided diagnosis systems in oncologic practice has been repeatedly postulated.^{51,52} By showing that ML can achieve a performance similar to that of radiologists (and sometimes even surpass them), the studies included in this systematic review support this notion.^{37,41} Furthermore, Xia et al³⁷ and Yamashita et al⁴¹ highlight the special utility of ML algorithms in helping radiologists in training achieve diagnostic performance comparable with that of their more experienced colleagues.

We performed a reporting quality assessment using the TRIPOD checklist.¹⁸ TRIPOD addresses topics similar to those on the Checklist for Artificial Intelligence in Medical Imaging but is structured in 77 clearly defined questions and is, to our knowledge, the most comprehensive checklist for reporting quality assessment.⁵³ Adherence to reporting standards was generally low. Important shortcomings were found in reporting the full model to enable individual predictions, methods for measuring performance, the performance measures themselves, and incomplete disclosure of funding. Moreover, no study provided the programming code that was used to create the model, severely hindering reproducibility. Furthermore, no study reported calibration measurements, and only <50% reported confidence intervals of performance metrics, limiting the reader's ability to assess the achieved performance. These results are in line with a previously published systematic review that showed similar TRIPOD adherence indices in studies regarding radiomics in oncologic studies.⁵⁴ TRIPOD assessments were also performed in the above-mentioned systematic reviews from our group. Both studies found very similar TRIPOD adherence indices (44% and 48%) as well as similar deficiencies in the individual items.^{55,56} Our results suggest that deficiencies in transparent reporting are a broader issue in the field of neuro-oncologic imaging.

We also performed a risk of bias assessment using the PROBAST tool.¹⁹ PROBAST uses 20 signaling questions organized in 4 domains to assess the risk of bias related to the selection of participants, definition and measurement of predictors, definition and determination of outcomes, and quality of analysis methods in studies developing predictive diagnostic models.¹⁹ While all studies included in this systematic review had a low risk of bias in the domains concerned with defining and measuring predictors and outcomes, a high proportion of high or unclear risk of bias was determined for most studies in participant selection and analysis. Regarding PROBAST Domain 1, the main concern rose from a selection of patients that did not represent the intended target population: Three studies excluded immunosuppressed patients,^{31,38,44} and 1, hemorrhagic tumors,²⁴ likely skewing the participant population in the direction of typical patients and making discrimination easier for classifiers. The main concerns raised in Domain 4 were the low patient-to-feature ratio and the exclusion of participants with missing data in several studies. These factors have the potential of introducing bias because the former can lead to overfitting and thus to overestimation of performance metrics, while the latter is risky in small data sets because it can skew the patient population and render it not representative.¹⁹ The risk of bias of several studies remained, nonetheless, unclear because of the several reporting deficiencies discussed above.

This systematic review had several limitations. First, by excluding studies that were presented only as abstracts, we reduced the sensitivity of our systematic review. We, nonetheless, accepted this loss of information because the inherent brevity of abstracts impedes a comprehensive appraisal of the study design, methods, and results.^{57,58} Moreover, the developed pipelines and data sets are different and hence not always comparable. Using public brain tumor data sets, such as BraTS, could make comparisons between classifiers easier, though images in these data sets

are highly curated and might not reflect variable quality of images encountered in clinical practice. The meta-analysis was performed on a small subset of studies because most publications did not report sufficient data for statistical synthesis. Interestingly, the studies included in the meta-analysis showed high heterogeneity, reflecting the diversity of the ML model pipelines used. This level of heterogeneity is lower but comparable to one calculated in another published meta-analysis on ML in neuroradiological diagnosis.⁵⁹ The TRIPOD and PROBAST checklists are applicable to ML-based prediction models but were developed with conventional multivariate regression-based models in mind.^{18,19,60} Due to the use of slightly different terminology and the lack of ML-based examples in both PROBAST's and TRIPOD's Elaboration and Examples document, the reporting quality assessment was burdensome at times. The TRIPOD and PROBAST creators have, however, acknowledged these shortcomings in a communication released in 2019 and announced the development of TRIPOD-AI and of PROBAST-AI.⁶⁰ We welcome and encourage this development to help improve transparent reporting and risk of bias assessment of ML-based prediction models.

CONCLUSIONS

ML models for the differentiation of gliomas from PCNSL have great potential and have demonstrated high-level performance, sometimes even comparable with that of senior subspecialty-trained radiologists. ML models have also been shown to be powerful computer-aided diagnosis tools that can improve diagnostic performance, especially among junior radiologists. However, to be able to implement these into clinical practice, it is still necessary to perform further model development in larger, more balanced, and heterogeneous data sets that include other disease entities as well as test the robustness of models in external data sets. This more extensive development should increase the generalizability and reliability of the developed model. In addition, transparent reporting of model development should always be a priority, and we recommend adherence to the TRIPOD statement in future publications. This reporting will increase reproducibility, potentially enabling incorporation of these techniques into routine clinical practice.

ACKNOWLEDGMENTS

We would like to acknowledge Thomas Mead, Mary Hughes, and Vermetha Polite from the Harvey Cushing/John Hay Whitney Medical Library for their support in doing this research.

Disclosure forms provided by the authors are available with the full text and PDF of this article at www.ajnr.org.

REFERENCES

- Ostrom QT, Gittleman H, Liao P, et al. **CBTRUS Statistical Report: primary brain and other central nervous system tumors diagnosed in the United States in 2010-2014.** *Neuro Oncol* 2017;19:v1-88 CrossRef Medline
- Villano JL, Koshy M, Shaikh H, et al. **Age, gender, and racial differences in incidence and survival in primary CNS lymphoma.** *Br J Cancer* 2011;105:1414-18 CrossRef Medline
- Tan AC, Ashley DM, Lopez GY, et al. **Management of glioblastoma: state of the art and future directions.** *CA Cancer J Clin* 2020;70:299-312 CrossRef Medline
- Hoang-Xuan K, Bessell E, Bromberg J, et al; European Association for Neuro-Oncology Task Force on Primary CNS Lymphoma. **Diagnosis and treatment of primary CNS lymphoma in immunocompetent patients: guidelines from the European Association for Neuro-Oncology.** *Lancet Oncol* 2015;16:e322-32 CrossRef Medline
- Batchelor TT. **Primary central nervous system lymphoma: a curable disease.** *Hematol Oncol* 2019;37(Suppl 1):15-18 CrossRef Medline
- Elder JB, Chen TC. **Surgical interventions for primary central nervous system lymphoma.** *Neurosurg Focus* 2006;21:E13 CrossRef Medline
- Yang H, Xun Y, Yang A, et al. **Advances and challenges in the treatment of primary central nervous system lymphoma.** *J Cell Physiol* 2020;235:9143-65 CrossRef Medline
- Malikova H, Liscak R, Latnerova I, et al. **Complications of MRI-guided stereotactic biopsy of brain lymphoma.** *Neuro Endocrinol Lett* 2014;35:613-18 Medline
- Malone H, Yang J, Hershman DL, et al. **Complications following stereotactic needle biopsy of intracranial tumors.** *World Neurosurg* 2015;84:1084-89 CrossRef Medline
- Weller M, Martus P, Roth P, et al; German PCNSL Study Group. **Surgery for primary CNS lymphoma? Challenging a paradigm.** *Neuro Oncol* 2012;14:1481-84 CrossRef Medline
- Haldorsen IS, Espeland A, Larsson EM. **Central nervous system lymphoma: characteristic findings on traditional and advanced imaging.** *AJNR Am J Neuroradiol* 2011;32:984-92 CrossRef Medline
- Yuguang L, Meng L, Shugan Z, et al. **Intracranial tumoural haemorrhage: a report of 58 cases.** *J Clin Neurosci* 2002;9:637-39 CrossRef Medline
- Villanueva-Meyer JE, Mabray MC, Cha S. **Current clinical brain tumor imaging.** *Neurosurgery* 2017;81:397-415 CrossRef Medline
- Wang S, Summers RM. **Machine learning and radiology.** *Med Image Anal* 2012;16:933-51 CrossRef Medline
- Nguyen AV, Blears EE, Ross E, et al. **Machine learning applications for the differentiation of primary central nervous system lymphoma from glioblastoma on imaging: a systematic review and meta-analysis.** *Neurosurg Focus* 2018;45:E5 CrossRef Medline
- Whiting P, Westwood M, Burke M, et al. **Systematic reviews of test accuracy should search a range of databases to identify primary studies.** *J Clin Epidemiol* 2008;61:357-64 Medline
- Page MJ, McKenzie JE, Bossuyt PM, et al. **The PRISMA 2020 statement: an updated guideline for reporting systematic reviews.** *BMJ* 2021;372:n71 CrossRef Medline
- Collins GS, Reitsma JB, Altman DG, et al. **Transparent reporting of a multivariable prediction model for individual prognosis or diagnosis (TRIPOD): the TRIPOD statement.** *BMJ* 2015;350:g7594 CrossRef Medline
- Moons KG, Wolff RF, Riley RD, et al. **PROBAST: a tool to assess risk of bias and applicability of prediction model studies: explanation and elaboration.** *Ann Intern Med* 2019;170:W1-33 CrossRef Medline
- Altman DG. *Practical Statistics for Medical Research.* Chapman and Hall; 1991
- Zhou XH, Obuchowski NA, McClish DK. *Statistical Methods in Diagnostic Medicine.* Wiley; 2011
- Higgins JP, Thompson SG, Deeks JJ, et al. **Measuring inconsistency in meta-analyses.** *BMJ* 2003;327:557-60 CrossRef Medline
- Alcaide-Leon P, Dufort P, Geraldo AF, et al. **Differentiation of enhancing glioma and primary central nervous system lymphoma by texture-based machine learning.** *AJNR Am J Neuroradiol* 2017;38:1145-50 CrossRef Medline
- Bao S, Watanabe Y, Takahashi H, et al. **Differentiating between glioblastoma and primary CNS lymphoma using combined whole-tumor histogram analysis of the normalized cerebral blood volume and the apparent diffusion coefficient.** *Magn Reson Med Sci* 2019;18:53-61 CrossRef Medline

25. Chen C, Zheng A, Ou X, et al. **Comparison of radiomics-based machine-learning classifiers in diagnosis of glioblastoma from primary central nervous system lymphoma.** *Front Oncol* 2020;10:1151 CrossRef Medline
26. Chen Y, Li Z, Wu G, et al. **Primary central nervous system lymphoma and glioblastoma differentiation based on conventional magnetic resonance imaging by high-throughput SIFT features.** *Int J Neurosci* 2018;128:608–18 CrossRef Medline
27. Eisenhut F, Schmidt MA, Putz F, et al. **Classification of primary cerebral lymphoma and glioblastoma featuring dynamic susceptibility contrast and apparent diffusion coefficient.** *Brain Sci* 2020;10:886 CrossRef Medline
28. Kang D, Park JE, Kim YH, et al. **Diffusion radiomics as a diagnostic model for atypical manifestation of primary central nervous system lymphoma: development and multicenter external validation.** *Neuro Oncol* 2018;20:1251–61 CrossRef Medline
29. Kickingereder P, Wiestler B, Sahm F, et al. **Primary central nervous system lymphoma and atypical glioblastoma: multiparametric differentiation by using diffusion-, perfusion-, and susceptibility-weighted MR imaging.** *Radiology* 2014;272:843–50 CrossRef Medline
30. Kim Y, Cho HH, Kim ST, et al. **Radiomics features to distinguish glioblastoma from primary central nervous system lymphoma on multi-parametric MRI.** *Neuroradiology* 2018;60:1297–1305 CrossRef Medline
31. Kunimatsu A, Kunimatsu N, Yasaka K, et al. **Machine learning-based texture analysis of contrast-enhanced MR imaging to differentiate between glioblastoma and primary central nervous system lymphoma.** *Magn Reson Med Sci* 2019;18:44–52 CrossRef Medline
32. Nakagawa M, Nakaura T, Namimoto T, et al. **Machine learning based on multi-parametric magnetic resonance imaging to differentiate glioblastoma multiforme from primary cerebral nervous system lymphoma.** *Eur J Radiol* 2018;108:147–54 CrossRef Medline
33. Park JE, Kim HS, Lee J, et al. **Deep-learned time-signal intensity pattern analysis using an autoencoder captures magnetic resonance perfusion heterogeneity for brain tumor differentiation.** *Sci Rep* 2020;10:21485 CrossRef Medline
34. Shrot S, Salhov M, Dvorski N, et al. **Application of MR morphologic, diffusion tensor, and perfusion imaging in the classification of brain tumors using machine learning scheme.** *Neuroradiology* 2019;61:757–65 CrossRef Medline
35. Suh HB, Choi YS, Bae S, et al. **Primary central nervous system lymphoma and atypical glioblastoma: differentiation using radiomics approach.** *Eur Radiol* 2018;28:3832–39 CrossRef Medline
36. Swinburne NC, Schefflein J, Sakai Y, et al. **Machine learning for semi-automated classification of glioblastoma, brain metastasis and central nervous system lymphoma using magnetic resonance advanced imaging.** *Ann Transl Med* 2019;7:232 CrossRef Medline
37. Xia W, Hu B, Li H, et al. **Multiparametric-MRI-based radiomics model for differentiating primary central nervous system lymphoma from glioblastoma: development and cross-vendor validation.** *J Magn Reson Imaging* 2021;53:242–50 CrossRef Medline
38. Xiao DD, Yan PF, Wang YX, et al. **Glioblastoma and primary central nervous system lymphoma: preoperative differentiation by using MRI-based 3D texture analysis.** *Clin Neurol Neurosurg* 2018;173:84–90 CrossRef Medline
39. Yamasaki T, Chen T, Hirai T, et al. **Classification of cerebral lymphomas and glioblastomas featuring luminance distribution analysis.** *Comput Math Methods Med* 2013;2013:619658 CrossRef Medline
40. Yamashita K, Hiwatashi A, Togao O, et al. **Diagnostic utility of intravoxel incoherent motion MR imaging in differentiating primary central nervous system lymphoma from glioblastoma multiforme.** *J Magn Reson Imaging* 2016;44:1256–61 CrossRef Medline
41. Yamashita K, Yoshiura T, Arimura H, et al. **Performance evaluation of radiologists with artificial neural network for differential diagnosis of intra-axial cerebral tumors on MR images.** *AJNR Am J Neuroradiol* 2008;29:1153–58 CrossRef Medline
42. Yamashita K, Yoshiura T, Hiwatashi A, et al. **Differentiating primary CNS lymphoma from glioblastoma multiforme: assessment using arterial spin labeling, diffusion-weighted imaging, and (1)(8)F-fluorodeoxyglucose positron emission tomography.** *Neuroradiology* 2013;55:135–43 CrossRef Medline
43. Yun J, Park JE, Lee H, et al. **Radiomic features and multilayer perceptron network classifier: a robust MRI classification strategy for distinguishing glioblastoma from primary central nervous system lymphoma.** *Sci Rep* 2019;9:5746 CrossRef Medline
44. Zhou W, Wen J, Hua F, et al. **(18)F-FDG PET/CT in immunocompetent patients with primary central nervous system lymphoma: differentiation from glioblastoma and correlation with DWI.** *Eur J Radiol* 2018;104:26–32 CrossRef
45. Wang S, Kim S, Chawla S, et al. **Differentiation between glioblastomas, solitary brain metastases, and primary cerebral lymphomas using diffusion tensor and dynamic susceptibility contrast-enhanced MR imaging.** *AJNR Am J Neuroradiol* 2011;32:507–14 CrossRef Medline
46. Lowe DG. **Distinctive image features from scale-invariant keypoints.** *Int J Comput Vis* 2004;60:91–110 CrossRef
47. van Griethuysen JJM, Fedorov A, Parmar C, et al. **Computational radiomics system to decode the radiographic phenotype.** *Cancer Res* 2017;77:e104–07 CrossRef Medline
48. Bahar R, Merkaj S, Brim WR, et al. **NIMG-23: machine learning methods in glioma grade prediction: a systematic review.** *Neuro-Oncology* 2021;23:vi133 CrossRef
49. Brim WR, Jekel L, Petersen GC, et al. **OTHR-12. The development of machine learning algorithms for the differentiation of glioma and brain metastases: a systematic review.** *Neuro-Oncology Advances* 2021;3:iii17 CrossRef
50. Lee JG, Jun S, Cho YW, et al. **Deep learning in medical imaging: general overview.** *Korean J Radiology* 2017;18:570–84 CrossRef Medline
51. Takahashi R, Kajikawa Y. **Computer-aided diagnosis: a survey with bibliometric analysis.** *Int J Med Inform* 2017;101:58–67 CrossRef Medline
52. Booth TC, Williams M, Luis A, et al. **Machine learning and glioma imaging biomarkers.** *Clin Radiol* 2020;75:20–32 CrossRef Medline
53. Mongan J, Moy L, Kahn CE Jr. **Checklist for Artificial Intelligence in Medical Imaging (CLAIM): a guide for authors and reviewers.** *Radiol Artif Intell* 2020;2:e200029 CrossRef Medline
54. Park JE, Kim D, Kim HS, et al. **Quality of science and reporting of radiomics in oncologic studies: room for improvement according to radiomics quality score and TRIPOD statement.** *Eur Radiol* 2020;30:523–36 CrossRef Medline
55. Jekel L, Brim WR, Petersen GC, et al. **OTHR-15. Assessment of TRIPOD adherence in articles developing machine learning models for differentiation of glioma from brain metastasis.** *Neuro-oncology Advances* 2021;3:17–18 CrossRef
56. Merkaj S, Bahar R, Brim W, et al. **NIMG-35: machine learning glioma grade prediction literature: a TRIPOD analysis of reporting quality.** *Neuro-Oncology* 2021;23:vi136 CrossRef
57. Scherer RW, Saldanha IJ. **How should systematic reviewers handle conference abstracts? A view from the trenches.** *Syst Rev* 2019;8:264 CrossRef Medline
58. Scherer RW, Sieving PC, Ervin AM, et al. **Can we depend on investigators to identify and register randomized controlled trials?** *PLoS One* 2012;7:e44183 CrossRef Medline
59. Bhandari AP, Liang R, Koppen J, et al. **Noninvasive determination of IDH and 1p19q status of lower-grade gliomas using MRI radiomics: a systematic review.** *AJNR Am J Neuroradiol* 2021;42:94–101 CrossRef Medline
60. Collins GS, Moons KG. **Reporting of artificial intelligence prediction models.** *Lancet* 2019;393:1577–79 CrossRef Medline

SWI as an Alternative to Contrast-Enhanced Imaging to Detect Acute MS Lesions

G. Caruana, C. Auger, L.M. Pessini, W. Calderon, A. de Barros, A. Salerno, J. Sastre-Garriga, X. Montalban, and À. Rovira

ABSTRACT

BACKGROUND AND PURPOSE: Acute inflammatory activity of MS lesions is traditionally assessed through contrast-enhanced T1-weighted MR images. The aim of our study was to determine whether a qualitative evaluation of non-contrast-enhanced SWI of new T2-hyperintense lesions might help distinguish acute and chronic lesions and whether it could be considered a possible alternative to gadolinium-based contrast agents for this purpose.

MATERIALS AND METHODS: Serial MR imaging studies from 55 patients with MS were reviewed to identify 169 new T2-hyperintense lesions. Two blinded neuroradiologists determined their signal pattern on SWI, considering 5 categories (hypointense rings, marked hypointensity, mild hypointensity, iso-/hyperintensity, indeterminate). Two different blinded neuroradiologists evaluated the presence or absence of enhancement in postcontrast T1-weighted images of the lesions. The Fisher exact test was used to determine whether each category of signal intensity on SWI was associated with gadolinium enhancement.

RESULTS: The presence of hypointense rings or marked hypointensity showed a strong association with the absence of gadolinium enhancement ($P < .001$), with a sensitivity of 93.0% and a specificity of 82.9%. The presence of mild hypointensity or isohyperintensity showed a strong association with the presence of gadolinium enhancement ($P < .001$), with a sensitivity of 68.3% and a specificity of 99.2%.

CONCLUSIONS: A qualitative analysis of the signal pattern on SWI of new T2-hyperintense MS lesions allows determining the likelihood that the lesions will enhance after administration of a gadolinium contrast agent, with high specificity albeit with a moderate sensitivity. While it cannot substitute for the use of contrast agent, it can be useful in some clinical settings in which the contrast agent cannot be administered.

MS is a progressive inflammatory, demyelinating, and neurodegenerative autoimmune disease of the CNS. Its inflammatory process is thought to be caused and propagated by an autoimmune cascade, which involves T-cells and mechanisms of molecular mimicry, leading to the development of focal perivascular infiltrates of mononuclear inflammatory cells, microglia activation, demyelination, and axonal degeneration. Gadolinium-enhancement on MR imaging can reveal the presence of blood-brain barrier disruption due to acute inflammation, and it is considered an acute sign of focal inflammatory activity. There is evidence that the magnetic susceptibility of MS lesions tends to increase considerably as they evolve from an enhancing to

nonenhancing stage after gadolinium administration, a finding proved using quantitative MR imaging methods.¹⁻⁸ This feature has been mainly related to iron accumulation inside macrophages and activated microglia at the outer margins of MS lesions.^{1,2,9} Due to the paramagnetic characteristics of iron, SWI is an MR imaging technique that permits in vivo measurement of iron levels in tissues. The aim of our study was to determine whether a visual, qualitative evaluation of SWI of new T2-hyperintense MS lesions could be useful to differentiate acute and chronic lesions and whether it could be considered a possible alternative to gadolinium-based contrast agents for this purpose.

MATERIALS AND METHODS

We retrospectively reviewed the medical records and MR images from a group of patients with MS to detect those who had developed new T2-hyperintense lesions on a follow-up MR imaging.

The study was approved by the hospital research and ethics committee and informed consent was obtained from each participant for the use of their anonymized MR imaging studies for research purposes.

Received September 17, 2021; accepted after revision February 4, 2022.

From the Neuroradiology Section (G.C., C.A., L.M.P., W.C., A.d.B., A.S., À.R.), Department of Radiology, and Servei de Neurologia-Neuroimmunologia (J.S.-G., X.M.), Centre d'Esclerosi Múltiple de Catalunya, Institut de Recerca Vall d'Hebron, Hospital Universitari Vall d'Hebron, Universitat Autònoma de Barcelona, Barcelona, Spain.

Please address correspondence to Àlex Rovira, MD, Passeig de la Vall d'Hebron, 119, 08035 Barcelona, Spain; e-mail: alex.rovira.idi@gencat.cat
<http://dx.doi.org/10.3174/ajnr.A7474>

Patients

A search was performed in a prospectively collected data base of 1312 patients with MS at our center. All the patients had been diagnosed with MS on the basis of the 2010 revision of the McDonald criteria¹⁰ and were regularly followed up at our institution (Vall d'Hebron University Hospital, Barcelona, Spain). Medical records and MR imaging studies acquired between January 2011 and December 2018 were retrospectively reviewed to identify patients who had developed new T2-hyperintense lesions. Inclusion criteria were the following: 1) 18–65 years of age; 2) relapsing course of MS; 3) MR imaging studies performed on a 3T MR imaging scanner using a standardized imaging protocol; 4) available MR imaging follow-up scans performed with the same scanner and protocol between 3 and 18 months from the baseline MR imaging; and 5) the presence of new T2-hyperintense brain lesions with a diameter of ≥ 3 mm on the follow-up MR imaging. Exclusion criteria were the following: 1) lack of a standardized MR imaging protocol or examinations performed on a 1.5T scanner; 2) absence of new T2-hyperintense WM lesions; 3) clinical conditions that could lead to WM lesions (such as atherosclerosis, diabetic microangiopathy, migraine or traumatic brain injury); and 4) pregnancy and steroid therapy within the 30 days before the follow-up MR imaging.

After meeting the above criteria, a total of 55 patients (37 women, 18 men) were included in our study, with a mean age at the follow-up MR imaging of 34.3 years (range, 20.0–48.4 years), a mean disease duration of 2.3 years (range, 0.8–26.7 years), and a mean Expanded Disability Status Scale score of 1.3 (range, 0–3.5). The mean interval between the baseline and the follow-up MR imaging was 9.3 months (range, 4.8–15.6 months).

MR Imaging Protocol

All MR imaging examinations were performed on a 3T system (Magnetom Trio, A Tim System; Siemens), with a 16-channel radiofrequency head coil using the same imaging protocol. T2- and proton density-weighted images were obtained using a 2D dual-echo fast spin-echo sequence in the axial plane (TR = 2500 ms; TE = 16/91 ms; flip angle = 120°; echo-train length = 6; section thickness = 3 mm). To obtain SWI data, we acquired a fully flow-compensated 3D spoiled gradient recalled-echo sequence using the following parameters: TR = 32 ms; TE = 24.6 ms; flip angle = 15°. Magnitude and filtered-phase information was automatically processed and combined to obtain SWI, which had an in-plane resolution of 0.65×0.65 mm and a section thickness of 3.0 mm. Finally, a 2D T1-weighted gradient-echo sequence (TR = 297 ms; TE = 2.46 ms; flip angle = 66°; section thickness = 3 mm) was obtained after contrast administration, using a gadolinium-based hydrophilic and neutral macrocyclic contrast agent (gadobutrol, 0.1 mmol/kg, Gadovist; Bayer HealthCare Pharmaceuticals) with a 5- to 10-minute delay.

Image Analysis

Initial imaging analysis was performed on the dual-echo spin-echo sequence, blinded to the postcontrast images, to identify all new MS lesions by comparing baseline and follow-up MR imaging scans. All new T2-hyperintense lesions were visually identified by a neuroradiologist (L.M.P.), with 4 years'

experience. The lesions were manually marked on axial T2-weighted images and tagged with an identification number. Two sets of DICOM images were anonymized and stored in a dedicated local hard drive: the first one containing SWI data and the second one containing postcontrast T1-weighted data. Also, T2-weighted data were included in each set for a location reference of each lesion.

The SWI data set was reviewed independently and in a blinded manner by 2 neuroradiologists (G.C. and W.C., with 2 years' experience) for a qualitative analysis of the signal intensity on SWI within each lesion. We considered 5 categories: 1) hypointense rings, 2) marked hypointensity, 3) mild hypointensity, 4) iso-/hyperintensity, and 5) indeterminate. The choice of these categories was based both on our experience and on a revision of the literature.^{11–15} Lesions with hypointense rings were defined as those with a complete or partial circumferential peripheral hypointensity (Fig 1A, -B). Marked hypointensity included any lesions with well-defined intralésional hypointensity, irregular- or dot-shaped (Fig 1C, -D). Lesions with a mild hypointensity were those with a slight low signal intensity affecting the whole lesion or its central part (Fig 1E). Iso-/hyperintense lesions were defined as those with an MR imaging signal equal to or higher than the surrounding WM (Fig 1F).

Lesions could be classified both in “hypointense ring” and “marked hypointensity” categories, because these features could coexist in the same lesions, while the other 3 categories were mutually exclusive.

During lesion classification, special caution was adopted not to confuse the presence of a central vein sign (central thin dots or lines) with one of the categories considered. When the assessment varied between the 2 readers, consensus was reached with the help of a senior neuroradiologist (A.R., with > 30 years' experience). Lesions that did not meet any of the previous criteria were classified as “indeterminate.”

Two different neuroradiologists (A.B. and A.S., with >5 years' experience) analyzed the postcontrast T1-weighted data set in consensus, to determine the presence of contrast enhancement in each new lesion. New T2-hyperintense lesions were considered acute or chronic according to the presence or absence of enhancement on T1-weighted postcontrast MR images.

Statistical Analysis

The results were exported into SPSS Statistics for Windows, Version 23.0 (IBM) for statistical analysis.

The Fisher exact test was used to determine whether each category of SWI signal intensity was associated with gadolinium enhancement. $P < .05$ was considered indicative of a significant association. Sensitivity, specificity, and positive and negative predictive values were calculated for each category. The aforementioned parameters were also calculated dividing SWI signal intensity categories in 2 groups: those associated with the absence of gadolinium enhancement (hypointense rings and marked hypointensity) and those associated with the presence of gadolinium enhancement (mild hypointensity and iso-/hyperintensity). The Cohen κ statistic was used to measure the interobserver agreement for the qualitative SWI signal analysis.

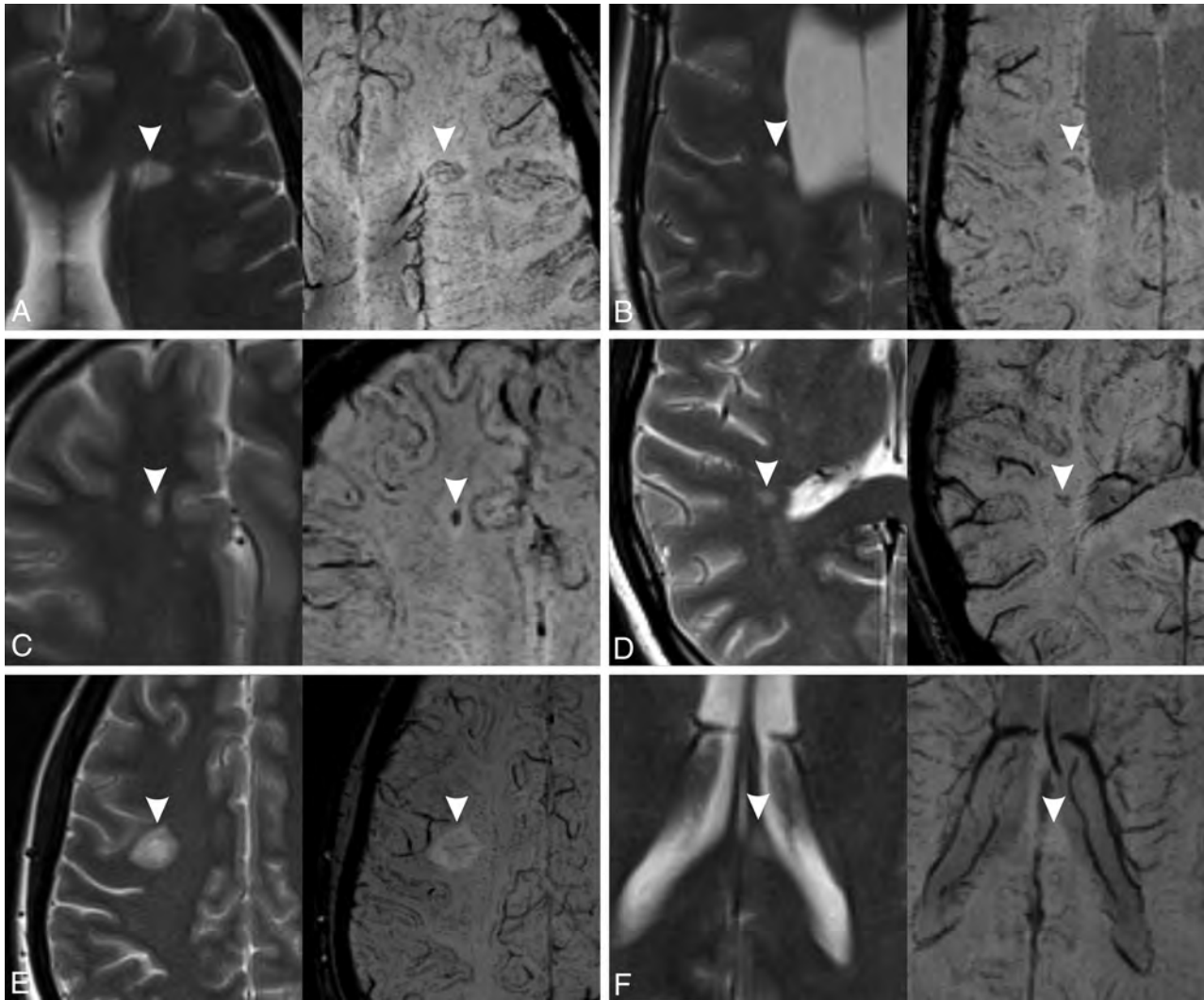


FIG 1. Signal categories on SWI (right) with the corresponding T2-weighted images (left). The lesions are marked with *arrowheads*. A, Hypointense ring (complete). B, Hypointense ring (partial). C, Marked hypointensity (*dot-shaped*). D, Marked hypointensity (*irregularly shaped*). E, Mild hypointensity. F, Iso-/hyperintensity. In A, B, and E, the central vein sign is also visible.

Table 1: Distribution of SWI signal characteristics in new MS lesions

SWI Signal	No. (%)	Gd+	Gd–
Hypointense rings	52 (30.8%)	4 (7.7%)	48 (92.3%)
Marked hypointensity	88 (52.1%)	3 (3.4%)	85 (96.6%)
Mild hypointensity	11 (6.5%)	10 (90.9%)	1 (9.1%)
Iso/hyperintensity	18 (10.7%)	18 (100.0%)	0 (0.0%)
Indeterminate	14 (8.3%)	6 (42.9%)	8 (57.1%)

Note:—Gd+ indicates gadolinium-enhancing lesions; Gd–, gadolinium-nonenhancing lesions.

RESULTS

In our cohort of 55 patients, a total of 169 new T2-hyperintense lesions with diameters of ≥ 3 mm were detected after comparing the baseline and follow-up examinations. All these lesions had the typical demyelinating lesion characteristics, round or ovoid with high signal on T2-weighted images.

Forty-one (24.3%) of these new lesions showed enhancement (acute lesion group), and 128 (75.7%) showed no enhancement (chronic lesion group) on postgadolinium T1-weighted images.

Regarding SWI signal categories, 88 lesions showed marked hypointensity, 52 lesions showed hypointense rings, 11 lesions showed mild hypointensity, 18 lesions showed iso-/hyperintensity, and 14 lesions were classified as indeterminate, as detailed in Table 1.

Table 2 shows the sensitivity, specificity, and positive and negative predictive values of each SWI signal category according to the presence or the absence of gadolinium enhancement, as well as Fisher exact test *P* values. The table also shows the statistical analysis regarding the group of SWI categories associated with the absence of gadolinium enhancement (hypointense rings and marked hypointensity) and with the presence of gadolinium enhancement (mild hypointensity and iso-/hyperintensity).

The presence of hypointense rings or marked hypointensity is strongly associated with the absence of gadolinium enhancement ($P < .001$, Fig 2A, -B), showing a sensitivity of 93.0% and a specificity of 82.9%. The presence of mild hypointensity or iso-/hyperintensity is strongly associated with the presence of gadolinium enhancement ($P < .001$, Fig 2C, -D), showing a sensitivity of

Table 2: Association of each SWI signal category with the presence or absence of gadolinium enhancement^a

SWI Signal	Sensitivity	Specificity	PPV	NPV	P
Association with Gd-					
Hypointense rings	37.5% (29.6%–46.1%)	90.2% (77.5%–96.1%)	92.3% (81.8%–97.0%)	31.6% (23.9%–40.5%)	<.001
Marked hypointensity	66.4% (57.9%–74.0%)	92.7% (80.6%–97.5%)	96.6% (90.5%–98.8%)	46.9% (36.4%–57.7%)	<.001
Hypointense rings or marked hypointensity	93.0% (87.2%–96.3%)	82.9% (68.7%–91.5%)	94.4% (89.0%–97.3%)	79.1% (64.8%–88.6%)	<.001
Association with Gd+					
Mild hypointensity	24.4% (13.8%–39.3%)	99.2% (95.7%–99.9%)	90.9% (62.3%–98.4%)	80.4% (73.5–85.8%)	<.001
Iso-/hyperintensity	43.9% (29.9%–59.0%)	100.0% (97.1%–100.0%)	100.0% (82.4%–100.0%)	84.8% (78.2%–89.6%)	<.001
Mild hypointensity or iso-/hyperintensity	68.3% (53.0%–80.4%)	99.2% (95.7%–99.9%)	96.6% (82.8%–99.4%)	90.7% (84.8%–94.5%)	<.001

Note:—PPV indicates positive predictive values; NPV, negative predictive values.

^aNumbers in parentheses represent 95% confidence intervals. P values are Fisher exact test P values.

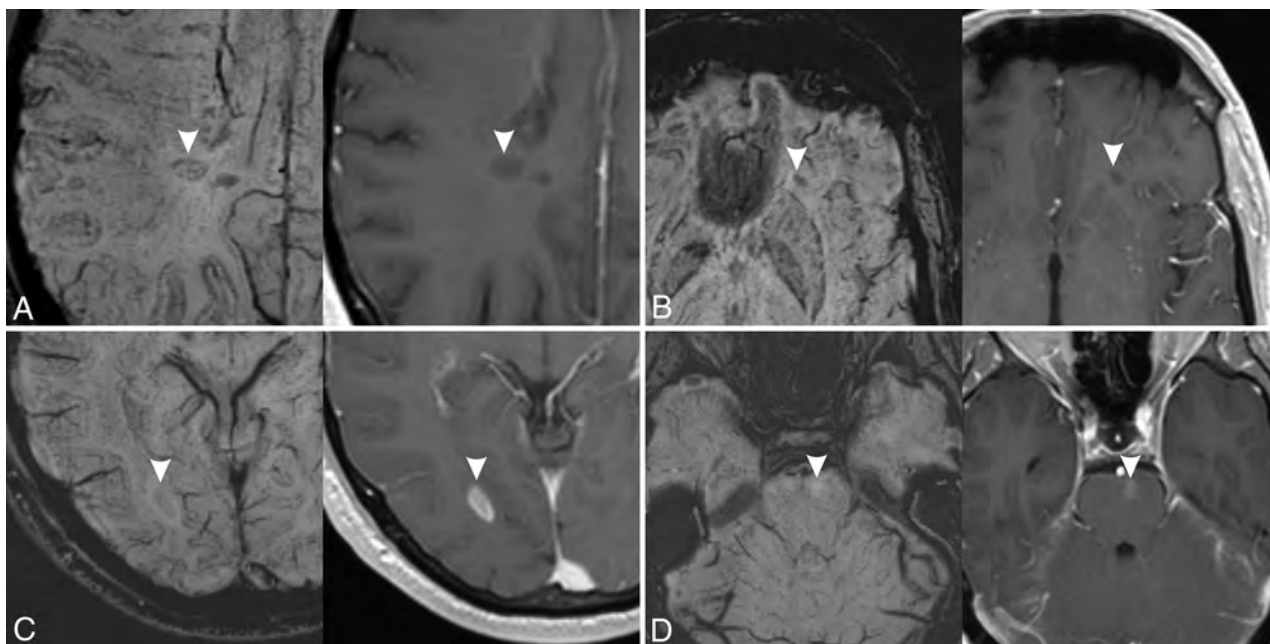


FIG 2. Examples of MS lesions (arrowheads) with different signal patterns on SWI (left) and corresponding contrast-enhanced T1-weighted images (right). A, Hypointense ring. B, Marked hypointensity (dot-shaped). C, Mild hypointensity. D, Iso-/hyperintensity. Lesions in A and B do not show enhancement on postcontrast images, while lesions on C and D show enhancement on postcontrast images.

68.3% and a specificity of 99.2%. The indeterminate category did not show any statistically significant association with gadolinium enhancement ($P = .11$).

The interobserver agreement was substantial, with Cohen κ values ranging from 0.68 to 0.77 for each single category ($P < .001$). Considering only 2 groups of categories, those associated with gadolinium enhancement and those not associated with it, the agreement was slightly better (Cohen $\kappa = 0.78$).

DISCUSSION

Our study showed the existence of an association between the presence of specific signal patterns in SWI and the presence/absence of enhancement on T1-weighted postcontrast images in new T2-hyperintense MS lesions. In particular, the finding of

mild hypointensity or iso-/hyperintensity was associated with the presence of gadolinium enhancement, while the observation of hypointense rings and/or marked hypointensity at any site of lesions was associated with the absence of gadolinium enhancement.

SWI hypointensities in MS lesions are considered mainly due to iron deposition within inflammatory cells and in a minor grade to demyelination.^{1,2,9} Acute MS lesions initially show enhancement on postcontrast images because of the increased permeability of the blood-brain barrier that lasts for an average period of 3 weeks.¹⁶ In this phase, the initial myelin degradation and uptake by macrophages do not lead to significant demyelination or iron accumulation, making lesions isointense or slightly hypointense on SWI.³ A hyperintense signal in some of the acute lesions could be due to a T2-shinethrough effect.

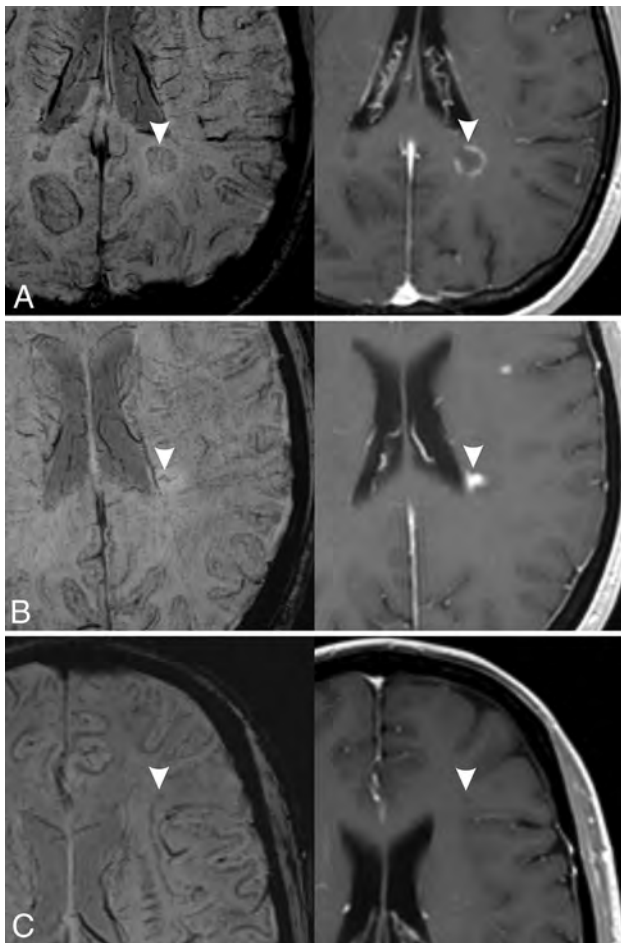


FIG 3. Exceptions to the associations found in our study. Three different MS lesions (arrowheads) are shown (left, SWI; right, contrast-enhanced T1-weighted image). A, Hypointense ring pattern on SWI with enhancement in postcontrast image. B, Marked hypointensity pattern on SWI (irregular dots) with enhancement in postcontrast image. C, Mild hypointensity pattern on SWI without enhancement in postcontrast T1-weighted image.

It has been observed using quantitative methods that the susceptibility of MS lesions increases from values similar to those of normal-appearing WM in the acute, enhanced stage to significantly higher values than those of normal-appearing WM in the early-to-intermediate, nonenhanced stage (0.5–3 years) and then back to values similar to those of normal-appearing WM in the chronic non-enhanced stage (3–6 years).^{1–7} A different increase of patterns of susceptibility can be visualized on SWI, mainly in the form of a core hypointensity or of a peripheral ringlike hypointensity. The pathophysiologic correlate of these imaging findings is not fully understood. It has been hypothesized that the hypointense core is either the consequence of a loss of diamagnetic myelin because of severe demyelination or that it is secondary to paramagnetic iron deposits.^{11,15,17} Regarding peripheral hypointensity, several studies have demonstrated the existence of a subset of chronic demyelinating lesions, slowly expanding lesions, smoldering lesions, or chronic active lesions, present mainly in patients with longstanding MS.^{12,17,18} These lesions often show a hypointense ring on SWI, related to the accumulation of iron-enriched microglia, which could have a role in maintaining an ongoing inflammation, even in the

absence of gadolinium enhancement because the blood-brain barrier has been repaired at this stage.^{11,12,14,17,19–22} This finding could explain the presence of hypointense rings in several new nonenhancing MS lesions in our study (30.8%).

Thirteen enhancing lesions did not have SWI pattern associated to acute lesions. Six of these lesions were classified as “indeterminate”; mainly their small size made performing a reliable visual evaluation difficult. Four lesions showed a hypointense ring (Fig 3A); this finding is not totally unexpected, considering that previous studies have demonstrated the presence of a paramagnetic rim on enhancing lesions.^{5,15,21,23,24} In particular, using a 7T system, Absinta et al²¹ described the presence of thin paramagnetic rings in some acute, enhancing lesions and the presence of thicker rings in chronic lesions. They postulated that the rings in acute lesions are not due to iron accumulation but rather to myelin debris-enriched macrophages. It is possible that in our study, using a lower magnetic field, some of these paramagnetic rings were identified in acute lesions and that they could not be distinguished from the thicker rings of chronic lesions in a visual evaluation. Zhang et al⁵ found a paramagnetic rim in a high percentage of enhancing lesions (50%), in contrast to a smaller percentage in our study (9.8%), but they used quantitative susceptibility mapping, a more sensitive technique that is usually not included in routine MR imaging protocols. However, Blindenbacher et al¹⁵ found a percentage of SWI hypointense rings in enhancing lesions, in line with our study findings (15%). Finally, 3 enhancing lesions showed a marked central hypointensity (Fig 3B). A possible explanation is that the central hypointensity was due to a prominent central vein, which, in some cases, is difficult to recognize and be differentiated from other types of hypointensity. Blindenbacher et al also found that 30% of enhancing lesions had a hypointense core on SWI images. This finding is in line with our results if we consider the frequency of both marked and mild hypointensity in enhancing lesions (7.3% + 24.4% = 31.7%).

Most nonenhancing new lesions (93%), with an age that could range from 4.8 to 15.6 months, showed hypointense rings and/or the presence of a marked hypointensity on SWI. This finding is in agreement with the results of previous studies^{1–5} that observed a susceptibility increase in lesions with early-intermediate age (6–36 months). Eight nonenhancing lesions (6.3%) were not classifiable (indeterminate) on SWI, and 1 was classified as having a mild hypointensity (Fig 3C), a finding that could be due to the difficulty of precisely differentiating marked and mild hypointensity in a visual evaluation.

As previously mentioned, a mild hypointensity and/or an iso-/hyperintensity on SWI was significantly associated with the presence of gadolinium enhancement. Unfortunately, the relatively low sensitivity of this sign (68.3%) does not allow proposing the use of a qualitative evaluation of SWI as a substitute for gadolinium enhancement to assess the stage of a new MS lesion. Nevertheless, the very high specificity (99.2%) of the sign allows some clinical applications, such as in patients refusing to receive gadolinium-based contrast agents or when its administration is contraindicated (eg, severe renal insufficiency, pregnant women). In these patients, a new T2-hyperintense lesion that shows the aforementioned sign could be reliably considered acute without the need to proceed to contrast agent administration.

Our study has some limitations. First, we included only new T2-hyperintense lesions in our analysis; therefore, we did not evaluate SWI signal changes in pre-existing lesions, even if some of them were still showing gadolinium enhancement. We chose this approach because the visual evaluation of the SWI characteristics of all existing lesions would be very time-consuming and not applicable in a clinical setting. Second, all patients were imaged using a 3T scanner; therefore, the results may be not generalizable to 1.5T scanners, which are still frequently used for monitoring patients with MS. Third, our population was relatively small due to our strict selection criteria, including only patients with MR imaging studies performed on a 3T scanner using a standardized protocol. Moreover, almost all patients were undergoing a disease-modifying treatment; therefore, it was relatively uncommon to find new, T2-hyperintense lesions of ≥ 3 mm on follow-up studies and even more difficult to find enhancing lesions. Finally, we did not perform a quantitative evaluation, which is considered more objective than a visual evaluation because the aim of our study was to test a practical method applicable in daily practice. Nevertheless, the interobserver agreement was fairly good, and we believe it was sufficient to allow a nonquantitative assessment to be used.

CONCLUSIONS

On the basis of the results of our study, we suggest that the qualitative analysis of the SWI signal of new T2-hyperintense MS lesions in a follow-up MR imaging scan allows determining the likelihood that the lesions will enhance after gadolinium-based contrast agent administration. In particular, lesions with an iso- or hyperintense signal on SWI, as well as lesions with a mild hypointense signal, are more likely to enhance after gadolinium administration. While these features are not sensitive enough to replace the use of gadolinium-based contrast agents, their high specificity can be useful to recognize the acute state of new T2-hyperintense lesions in patients who refuse gadolinium-based contrast agents or when its administration is contraindicated. On the other hand, lesions showing hypointense rings or a marked hypointensity on SWI are more likely to have no enhancement, with a good sensitivity and a fair specificity.

Disclosure forms provided by the authors are available with the full text and PDF of this article at www.ajnr.org.

REFERENCES

- Chen W, Gauthier SA, Gupta A, et al. **Quantitative susceptibility mapping of multiple sclerosis lesions at various ages.** *Radiology* 2014;271:183–92 CrossRef Medline
- Zhang Y, Gauthier SA, Gupta A, et al. **Longitudinal change in magnetic susceptibility of new enhanced multiple sclerosis (MS) lesions measured on serial quantitative susceptibility mapping (QSM).** *J Magn Reson Imaging* 2016;44:426–32 CrossRef Medline
- Zhang Y, Gauthier SA, Gupta A, et al. **Quantitative susceptibility mapping and R2* measured changes during white matter lesion development in multiple sclerosis: myelin breakdown, myelin debris degradation and removal, and iron accumulation.** *AJNR Am J Neuroradiol* 2016;37:1629–35 CrossRef Medline
- Vinayagamani S, Sabarish S, Nair SS, et al. **Quantitative susceptibility-weighted imaging in predicting disease activity in multiple sclerosis.** *Neuroradiology* 2021;63:1061–69 CrossRef Medline
- Zhang XS, Nguyen TD, Ruá SM, et al. **Quantitative susceptibility mapping of time-dependent susceptibility changes in multiple sclerosis lesions.** *AJNR Am J Neuroradiol* 2019;40:987–93 CrossRef Medline
- Chawla S, Kister I, Wuerfel J, et al. **Iron and non-iron-related characteristics of multiple sclerosis and neuromyelitis optica lesions at 7T MRI.** *AJNR Am J Neuroradiol* 2016;37:1223–30 CrossRef Medline
- Chawla S, Kister I, Sinnecker T, et al. **Longitudinal study of multiple sclerosis lesions using ultra-high field (7T) multiparametric MR imaging.** *PLoS One* 2018;13:e0202918 CrossRef Medline
- Caruana G, Pessini LM, Cannella R, et al. **Texture analysis in susceptibility-weighted imaging may be useful to differentiate acute from chronic multiple sclerosis lesions.** *Eur Radiol* 2020;30:6348356 CrossRef Medline
- Deh K, Ponath GD, Molvi Z, et al. **Magnetic susceptibility increases as diamagnetic molecules breakdown: myelin digestion during multiple sclerosis lesion formation contributes to increase on QSM.** *J Magn Reson Imaging* 2018;48:1281–87 CrossRef Medline
- Polman CH, Reingold SC, Banwell B, et al. **Diagnostic criteria for multiple sclerosis: 2010 revisions to the McDonald criteria.** *Ann Neurol* 2011;69:292–302 CrossRef Medline
- Bian W, Harter K, Hammond-Rosenbluth KE, et al. **A serial in vivo 7T magnetic resonance phase imaging study of white matter lesions in multiple sclerosis.** *Mult Scler* 2013;19:69–75 CrossRef Medline
- Mehta V, Pei W, Yang G, et al. **Iron is a sensitive biomarker for inflammation in multiple sclerosis lesions.** *PLoS One* 2013;8:e57573 CrossRef Medline
- Bozin I, Ge Y, Kuchling J, et al. **Magnetic resonance phase alterations in multiple sclerosis patients with short and long disease duration.** *PLoS One* 2015;10:e0128386 CrossRef Medline
- Eisele P, Fischer K, Szabo K, et al. **Characterization of contrast-enhancing and non-contrast-enhancing multiple sclerosis lesions using susceptibility-weighted imaging.** *Front Neurol* 2019;10:1–7 CrossRef Medline
- Blindenbacher N, Brunner E, Asseyer S, et al. **Evaluation of the ‘ring sign’ and the ‘core sign’ as a magnetic resonance imaging marker of disease activity and progression in clinically isolated syndrome and early multiple sclerosis.** *Mult Scler J Exp Transl Clin* 2020;6:2055217320915480 CrossRef Medline
- Cotton F, Weiner HL, Jolesz FA, et al. **MRI contrast uptake in new lesions in relapsing-remitting MS followed at weekly intervals.** *Neurology* 2003;60:640–46 CrossRef Medline
- Hametner S, Wimmer I, Haider L, et al. **Iron and neurodegeneration in the multiple sclerosis brain.** *Ann Neurol* 2013;74:848–61 CrossRef Medline
- Frischer JM, Weigand SD, Guo Y, et al. **Clinical and pathological insights into the dynamic nature of the white matter multiple sclerosis plaque.** *Ann Neurol* 2015;78:710–21 CrossRef Medline
- Dal-Bianco A, Grabner G, Kronnerwetter C, et al. **Slow expansion of multiple sclerosis iron rim lesions: pathology and 7 T magnetic resonance imaging.** *Acta Neuropathol* 2017;133:25–42 CrossRef Medline
- Bagnato F, Hametner S, Yao B, et al. **Tracking iron in multiple sclerosis: a combined imaging and histopathological study at 7 Tesla.** *Brain* 2011;134:3602–15 CrossRef Medline
- Absinta M, Sati P, Gaitán MI, et al. **Seven-Tesla phase imaging of acute multiple sclerosis lesions: a new window into the inflammatory process.** *Ann Neurol* 2013;74:669–78 CrossRef Medline
- Kaunzner UW, Kang Y, Zhang S, et al. **Quantitative susceptibility mapping identifies inflammation in a subset of chronic multiple sclerosis lesions.** *Brain* 2019;142:133–45 CrossRef Medline
- Suzuki M, Kudo K, Sasaki M, et al. **Detection of active plaques in multiple sclerosis using susceptibility-weighted imaging: comparison with gadolinium-enhanced MR imaging.** *Magn Reson Med Sci* 2011;10:185–92 CrossRef Medline
- Jang J, Nam Y, Choi Y, et al. **Paramagnetic rims in multiple sclerosis and neuromyelitis optica spectrum disorder: a quantitative susceptibility mapping study with 3-T MRI.** *J Clin Neurol* 2020;16:562–72 CrossRef Medline

Pulsatility Index in the Basal Ganglia Arteries Increases with Age in Elderly with and without Cerebral Small Vessel Disease

V. Perosa, T. Arts, A. Assmann, H. Mattern, O. Speck, J. Oltmer, H.-J. Heinze, E. Düzel, S. Schreiber, and J.J.M. Zwanenburg

ABSTRACT

BACKGROUND AND PURPOSE: Cerebral small vessel disease contributes to stroke and cognitive impairment and interacts with Alzheimer disease pathology. Because of the small dimensions of the affected vessels, in vivo characterization of blood flow properties is challenging but important to unravel the underlying mechanisms of the disease.

MATERIALS AND METHODS: A 2D phase-contrast sequence at 7T MR imaging was used to assess blood flow velocity and the pulsatility index of the perforating basal ganglia arteries. We included patients with cerebral amyloid angiopathy ($n = 8$; identified through the modified Boston criteria), hypertensive arteriopathy ($n = 12$; identified through the presence of strictly deep or mixed cerebral microbleeds), and age- and sex-matched controls ($n = 28$; no cerebral microbleeds).

RESULTS: Older age was related to a greater pulsatility index, irrespective of cerebral small vessel disease. In hypertensive arteriopathy, there was an association between lower blood flow velocity of the basal ganglia and the presence of peri-basal ganglia WM hyperintensities.

CONCLUSIONS: Our results suggest that age might be the driving factor for altered cerebral small vessel hemodynamics. Furthermore, this study puts cerebral small vessel disease downstream pathologies in the basal ganglia region in relation to blood flow characteristics of the basal ganglia microvasculature.

ABBREVIATIONS: BG = basal ganglia; CAA = cerebral amyloid angiopathy; cSS = cortical superficial siderosis; CSVD = cerebral small vessel disease; EPVS = enlarged perivascular spaces; HA = hypertensive arteriopathy; ICH = intracerebral hemorrhage; MBs = microbleeds; PC = phase-contrast; PI = pulsatility index; Vmean = mean blood flow velocity; WMH = WM hyperintensities

Awareness of sporadic cerebral small vessel disease (CSVD) is growing due to its involvement in hemorrhagic¹ and ischemic stroke,² cognitive impairment,^{3,4} as well as the overlap between vascular and Alzheimer disease pathology.^{5,6} CSVD affects brain vessels of <1 mm and can be detected in vivo mainly

by various downstream pathology neuroimaging markers, ie, microbleeds (MBs), cortical superficial siderosis (cSS), WM hyperintensities (WMH), lacunes, enlarged perivascular spaces (EPVS), and microinfarcts.⁷ MR imaging markers of CSVD⁸⁻¹⁰ and pathologic evidence of remodeling of the small-vessel wall can be found in older adults without any CSVD-related symptoms and also in the absence of vascular risk factors.¹¹

The 2 common subtypes of sporadic CSVD are cerebral amyloid angiopathy (CAA) and hypertensive arteriopathy (HA). CAA and HA have different distributions: CAA affects mainly the cortical and leptomeningeal vessels, while HA affects the deep perforating ones.¹²⁻¹⁴

The pathologic manifestations of CSVD (eg, loss of smooth-muscle cells and amyloid- β accumulation in CAA, lipohyalinosis, fibrinoid necrosis) result in remodeling and stiffening of the vessel walls.^{2,15} Animal studies suggest that this, subsequently, contributes to decreased microvascular blood flow velocity and alterations of pulsatility of the microvasculature.¹⁶⁻¹⁸ Alterations of blood flow and pulsatility of small cerebral vessels are of pivotal pathophysiologic importance and could be related to blood-

Received October 1, 2021; accepted after revision January 5, 2022.

From the Department of Neurology (V.P., A.A., J.O., H.-J.H., S.S.), Institute of Physics (H.M.), and Institute of Cognitive Neurology and Dementia Research (E.D.), Otto-von-Guericke University, Magdeburg, Germany; German Center for Neurodegenerative Diseases (V.P., O.S., H.-J.H., E.D., S.S.), Magdeburg, Germany; J. Philip Kistler Stroke Research Center (V.P.), Massachusetts General Hospital, Harvard Medical School, Boston, Massachusetts; Department of Radiology (T.A., J.J.M.Z.), University Medical Center Utrecht, Utrecht, the Netherlands; Leibniz-Institute for Neurobiology (O.S., H.-J.H.), Magdeburg, Germany; Center for Behavioral Brain Sciences (O.S., H.-J.H., E.D.), Magdeburg, Germany; and Institute of Cognitive Neuroscience (E.D.), University College London, London, UK.

S. Schreiber and J.J.M. Zwanenburg contributed equally to this work.

This work was supported by Neural Resources of Cognition, CRC 1436.

Please address correspondence to Valentina Perosa, MD, John Philip Kistler Stroke Research Center, Massachusetts General Hospital and Harvard Medical School, 175 Cambridge St, Boston, MA 02114; e-mail: vperosa@mgh.harvard.edu; @ValentinaPerosa

Indicates article with online supplemental data.

<http://dx.doi.org/10.3174/ajnr.A7450>

Table 1: Demographics of subjects and vascular risk factors^a

	CAA (n = 8)	HA (n = 12)	Controls (n = 28)	Group Difference
Age (mean) (yr)	69.6 (SD, 7.3)	71.4 (SD, 9.8)	71.6 (SD, 8.0)	P = .94
Female (%)	50.0	75.0	53.6	P = .79
Arterial hypertension (%)	100.0	83.3	50.0	CAA > controls P = .016 ^b
Diabetes mellitus (%)	12.5	33.3	10.7	P = .92
Hyperlipidemia (%)	50.0	75.0	39.3	P = .65
BMI (mean) (SD) (kg/m ²)	26.8 (SD, 2.4)	26.9 (SD, 3.9)	24.9 (SD, 2.3)	P = .08

Note:—BMI indicates body mass index

^a The table reports the characteristics of the study participants showing mean (SD) and percentage (%), differentiating between participants with CAA and HA and controls. Differences between groups were assessed using the Kruskal-Wallis and Mann-Whitney U tests as post hoc tests.

^b Significant differences between groups.

brain barrier dysfunction,¹⁹ clearance,²⁰ and, thus, self-reinforcing mechanisms of CSVD advancement. While increased pulsatility in large cerebral arteries has been assessed in human studies, the use of 2D phase-contrast (PC) MR imaging at 7T^{21–23} now allows recording blood flow velocity in the small penetrating vessels of the centrum semiovale and the basal ganglia (BG).

From these velocity traces, pulsatility can be quantified by calculating the pulsatility index (PI), considering maximum, minimum, and mean observed blood flow velocity in the small vessels.

An association between increased pulsatility in the large cerebral arteries and the burden of CSVD neuroimaging markers, namely WMH and EPVS, has recently been identified.^{24–26} A previous study that used 2D PC MR imaging at 7T reported that patients with HA with symptomatic hemorrhagic or ischemic stroke presented with increased PI in the small BG vessels.²⁷ However, apart from this single-site study, few data on the relationship between microvascular cerebral blood flow, pulsatility, age, and MR imaging CSVD downstream pathologies exist; these data could aid in a better understanding of the relationship between microvascular hemodynamics and tissue damage. It is important to assess the same measures in a different cohort with similar characteristics and from another study site. Most important, measuring blood flow in the small vessels could allow inferring conclusions about how blood flow velocity and PI relate to mechanisms such as blood-brain barrier leakage and clearance dysfunction. In addition, these measures have the potential to become early detection tools to target presymptomatic disease stages.

In this study, we used 2D PC MR imaging at 7T, measuring blood flow velocity and the pulsatility of the BG perforating arteries in a cohort that included patients with asymptomatic CSVD covering the spectrum of CAA and HA. Including CSVD imaging markers (MBs, WMH, lacunes, and EPVS) helped us to investigate the relationship between microvascular blood flow characteristics and CSVD downstream pathologies.

MATERIALS AND METHODS

Participants

In the present study, we included 48 older adults (mean age, 71 [SD, 8.3] years; 40% women) recruited between December 2016 and July 2018.

Twenty of the participants were selected from a longitudinal 3T MR imaging study on the pathophysiology of CSVD, conducted by the University Clinic of Magdeburg and the German Center for Neurodegenerative Disease. The inclusion criterion for the 3T study was the presence of hemorrhagic CSVD markers, ie, MBs or cSS on MR imaging iron-sensitive sequences (gradient recalled-echo T2*-weighted or susceptibility-weighted imaging) on a prior clinical MR imaging performed for a diagnostic work-up (eg, due to headache, epileptic seizures, gait disturbances, cognitive impairment, and TIA).

MBs (classified through their localization as strictly lobar, deep [BG, thalamus], or mixed²⁸), cSS, and asymptomatic intracerebral hemorrhage (ICH) (hypointense lesions of >1 cm, deep or lobar) were confirmed on 3T iron-sensitive sequences. 3T MR imaging was further rated for the existence and severity of CSVD downstream pathologies in the region of the BG, including WMH following the peripheral outline of the BG (peri-BG WMH, existent/not existent, which were identified on a FLAIR sequence); deep lacunes (number; defined in T1-weighted sequence as fluid-filled, 3- to 15-mm large cavities in the BG²⁹); and BG EPVS (severity: 0 = no EPVS; 1 = 1–10 EPVS; 2 = 11–20 EPVS; 3 = 21–40 EPVS; 4 = >40 EPVS; counted on a T2-weighted sequence).³⁰ A specialist neurologist (S.S., with 10 years' experience) performed the rating.

CAA was diagnosed by applying the modified Boston criteria, which define probable CAA by the presence of at least 2 lobar hemorrhages (ICH and/or MBs) or 1 lobar hemorrhage and at least focal cSS, which had an alternative cause, in patients 55 years of age or older.³¹ For a diagnosis of possible CAA, the presence of 1 lobar hemorrhage is sufficient.³¹ Patients with HA were identified through the presence of strictly deep MBs and/or ICHs or mixed deep and lobar MBs and/or ICHs.³²

The remaining 28 participants were community-dwelling controls recruited from an existing pool of cognitively healthy volunteers at the German Center for Neurodegenerative Disease in Magdeburg without hemorrhagic CSVD markers on 3T MR imaging. Multiple WMH subcortical spots and grade I EPVS in the BG or centrum semiovale were allowed in all controls, because they represent a common finding in aging (Table 1).

Participants with large-artery stenosis of the circle of Willis, genetic neurologic disease, and a history of psychiatric disease, alcohol or drug abuse, and cerebrovascular malformations were excluded from the study. No patient had a cardiac ejection fraction of <45%, whereas these data were not available for controls. Contraindications for scanning at 7T, according to the recommendations of the German Ultrahigh-Field Imaging Network, were considered and represented a further exclusion criterion from our study. Each participant was subject to a neurologic examination to detect undiagnosed neurologic conditions and further underwent an extensive neuropsychological test battery (Online Supplemental Data) to exclude severe dementia and

depression, which can be a cause of pseudodementia. Cardiovascular risk factors were additionally recorded for all participants (Table 2). Arterial hypertension was identified when blood pressure exceeded 130/80 mm Hg. Diabetes mellitus was diagnosed as a fasting plasma glucose level of >7.0 mmol/L or >11.1 mmol/L 2 hours after a glucose tolerance test. Hyperlipidemia was defined as abnormal blood levels of low-density lipoprotein cholesterol (>2.6 mmol/L) and/or triglycerides (>1.7 mmol/L).

All participants provided written informed consent according to the Declaration of Helsinki and were compensated for travel costs. The study was approved by the University Clinic of Magdeburg Ethics Committee (93/17; 28/16).

7T MR Imaging

Scanning of all participants was performed on a whole-body 7T scanner (Siemens; “classic” 7T), equipped with a quadrature transmit and 32-channel receive head coil (Nova Medical). First, a T1-weighted sequence with 3D-MPRAGE (voxel size = 1 mm³ isotropic) was acquired for anatomic reference, to plan the acquisition of the 2D PC sequence and to individualize the BG as an ROI during imaging analysis. The parameters were the following: TE = 2.89 ms, TR = 2250 ms, flip angle = 5°, TI = 1050 ms, receiver bandwidth = 130 Hz/pixel, echo spacing = 8.3 ms, 3D matrix dimensions = 256 × 256 × 176. A generalized autocalibrating partially parallel acquisition was performed with an acceleration factor of 2 and 32 reference lines.

We implemented the previously described^{21,22} 2D PC sequence on our scanner, using the multisite protocol as defined in the

European Ultrahigh-Field Imaging Network for Neurodegenerative Diseases.³³ The sequence was acquired in a single section at the level of the BG and was planned manually on sagittal images of the T1-weighted sequence so that it crossed the anterior commissure and was tangential to the genu and splenium of the corpus callosum (Fig 1A). Thus, we ensured that the single section was approximately perpendicular to the perforating arteries. The reproducibility of this method has been tested in previous studies.²¹ Sequence parameters were the following: voxel size = 0.3 × 0.3 × 2 mm,³ TE = 16.6 ms, TR = 27.6 ms, 2 segments (phase-encoding steps per cardiac cycle), flip angle = 45°, receiver bandwidth = 59 Hz/pixel. Encoding velocity was 20 cm/s in the direction perpendicular to the section. The sequence was retrospectively gated with an acquired temporal resolution of 110.5 ms, and blood flow velocity was reconstructed at 14 time points of the cardiac cycle (ie, approximately 71 ms for a heart rate of 60 beats per minute). The scan time for the 2D PC sequence was approximately 3 minutes at a heart rate of 60 beats per minute.

Image Processing

Quality control was performed by visual inspection of the scans by T.A., especially with regard to motion artifacts (ghosting, blurring). If motion caused extensive ghosting and blurring that would hamper the analysis, the subject was excluded. To process and analyze flow-encoded PC images, we used a Matlab (2015b; MathWorks) tool, developed at the University Medical Center of Utrecht.²² This tool performs several steps as described in more detail elsewhere.^{22,34} Briefly, perforating arteries were identified as voxels on the velocity map with nonzero mean velocity, using the following steps:³⁴ First, a phase correction was applied on the background to make the mean velocity of tissue 0 cm/s by median-filtering the time-averaged velocity map and subtracting it from the velocity map of each cardiac time point. Then, velocity SNR maps were calculated from magnitude SNR estimates that were based on the SD of the magnitude over the cardiac cycle. Furthermore, given the velocity SNR, the 2-sided 95% velocity CIs were estimated for the mean blood flow velocity (*V*_{mean}) to enable consistent selection of vessels with significant flow (ie, nonzero *V*_{mean} with a statistical significance of .05). All voxels inside the BG mask without 0 cm/s within their CI of *V*_{mean} and hyperintense signal in the magnitude image were considered significant.

Every group of neighboring significant voxels was defined as belonging to the same perforating artery. The voxel with the highest mean velocity of such a group was taken as representative of the perforating artery and used for further analysis.

Detection of perforating vessels was confined to the BG on both sides by manually segmenting the area delimited by the ventricles, the interhemispheric fissure, and laterally by the insula (Fig 1B). Multiple detections of a single vessel and tangentially intersected vessels were manually excluded from the analysis by a neurologist

Table 2: Neuroimaging markers of CSVD^a

Neuroimaging Marker of CSVD	CAA (n = 8)	HA (n = 12)
Strictly lobar MBs	7	0
Strictly deep MBs	0	2
Mixed (deep/lobar) MBs	0	10
Presence of cSS	3	0
ICH lobar	3	0
ICH deep	0	1
Lacunae deep	2	8
EPVS (BG)	4	7
Peri-BG WMH	2	4

^aReported is the number of subjects in which the relative marker of CSVD was observed.

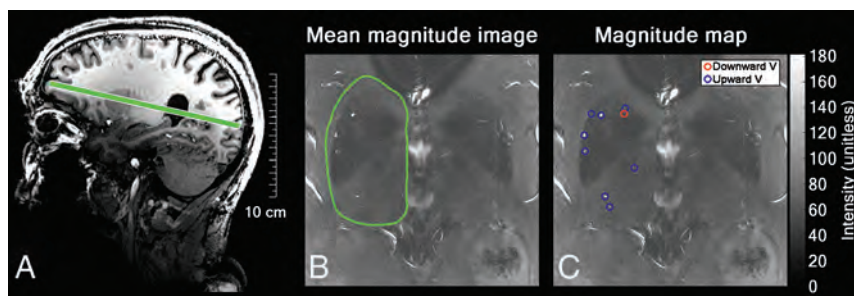


FIG 1. Image processing. Section position of the 2D phase-contrast acquisition through the BG was planned on the T1-weighted sequence (A). Mean magnitude image and determination of the ROI in which vessel detection was performed (B). Circles mark detected perforating vessels in the ROI, distinguishing between upward (blue) and downward (red) blood flow directions. Only vessels with an upward flow direction were considered (C), to ascertain inclusion of arteries only (no veins). *V* indicates velocity.

(V.P., with 4 years of experience), and only vessels with an upward blood flow direction (positive velocity) were considered, to avoid inclusion of veins. In each subject, the generated output of the imaging analysis listed all detected perforators (ie, number of vessels), together with the velocity curves. The location of the detected vessels was visualized on the magnitude image (Fig 1C). Image processing was performed by V.P.

Statistics

Differences in risk factors between groups were calculated using the 1-way ANOVA or Kruskal-Wallis test when appropriate.

The blood flow velocity of each perforator at each of the 14 time points of the cardiac cycle was registered and averaged over all selected vessels, obtaining a mean velocity curve over the cardiac cycle for each subject. Averaging this mean velocity curve over the time points measured resulted in a V_{mean} in the subject's perforators of both hemispheres.

Besides the mean velocity curve, we also computed the mean normalized velocity curve by averaging over the normalized velocity curves of all selected vessels. This normalization was performed to give each vessel an equal weight before determining the PI from the mean normalized velocity curve according to the following equation:

$$PI = \left| \frac{V_{max} - V_{min}}{V_{mean}} \right|.$$

In this equation, V_{max} is the maximum velocity; V_{min} , the minimum velocity, and V_{mean} , the mean velocity of the mean normalized velocity curve ($V_{mean} = 1$ for normalized velocity curves but is still shown for clarity). The use of the averaged normalized curve to perform the PI calculation instead of calculating it in each single vessel was based on previous work that showed that with this method, the overestimation of PI due to noise was greatly reduced.

We further aimed to investigate the relationship between CSVD downstream pathologies in the region of the BG and the blood flow velocity and pulsatility of the BG perforating arteries. Quantile regression analysis was, therefore, performed, setting the mean velocity, PI, and number of detected vessels, respectively, as dependent variables and age, sex, group (CAA, HA, controls), number of deep MBs, the presence of peri-BG WMH, number of deep lacunes, and the severity grade of BG EPVS as independent variables. Quantile regression was applied to the whole cohort as a method of regression analysis robust against outliers and was able to understand the distribution of a continuous variable across different quantiles. We applied this method to calculate the 25th, 50th, and 75th quantiles. To determine to which participants' group the effects were pertinent, we calculated the Spearman correlations for significant factors in each group separately. P values were adjusted for multiple comparisons using the Bonferroni method, accounting for the number of predictors ($n = 7$) in the quantile regression models and the number of subgroups ($n = 3$) for the Spearman correlations. Results were considered significant at $P < .05$. For all analyses described so far, the software R, Version 3.6.0 (www.R-project.org), was used.

To investigate possible differences in blood flow velocity of the perforating vessels between groups, we created a combined mean

velocity curve of all subjects within a group. To this end, the method previously described by Geurts et al²⁷ to synchronize all individuals was used and applied to the large vessels in the BG section. The large-vessel curves were obtained by selecting pixels in the image with the highest intensities, and the group mean velocity curve of the large vessels in the BG section was used for time lag synchronization. This mean large-vessel curve was iteratively updated with the synchronized personal velocity traces of the large vessels until no time lag changes occurred. These time lags were then used to synchronize each subject's mean small-vessel velocity trace. After averaging, we obtained a group mean small-vessel velocity trace. Flow-velocity curves between subgroups with CSVD (CAA versus HA) and healthy controls were visually compared.

RESULTS

One subject from the control group was excluded due to motion artifacts that did not allow a proper analysis of the PC sequence. All remaining data were included in the analysis.

Eight of the 20 participants with CSVD (40%) were classified as patients with possible (1/8) or probable (7/8) CAA (mean age, 69.6 [SD, 7.3] years; 50% women).³¹ The remaining 12 participants with CSVD had HA (mean age, 71.4 [SD, 9.8] years; 75% women).³²

Patients with both CAA and HA had a higher cardiovascular risk (higher prevalence of arterial hypertension, diabetes mellitus, hyperlipidemia, greater body mass index) compared with controls, with significant group differences between those with CAA and controls for arterial hypertension (Table 1). There were no group differences with respect to age and sex (Table 1). CSVD neuroimaging markers in the BG region are reported in Table 2, for each group separately. The presence of cSS and strictly lobar MBs/ICHs is a defining marker of CAA and was, accordingly, found only in this group (Table 2). There were 4 participants with asymptomatic ICH in lobar or deep regions, respectively (3 belonging to the CAA group and 1 to the HA group) (Table 2). The lesions were located outside the section measured by the 2D PC sequence.

Blood Flow Velocity

There were no group differences for V_{mean} . V_{mean} curves of the study groups are shown in Fig 2. The curves indicate that HA is related to a less steep increase in the BG blood flow velocity across the cardiac cycle.

In the quantile regression analysis, peri-BG WMH showed a significant negative relationship to V_{mean} at the 50th percentile across the whole group (-0.65 [SD, 0.25] cm/s; $P = .021$), suggesting that the presence of WMH in the proximity of the perforating BG arteries is related to a slower blood flow (Online Supplemental Data). This relationship was driven by the HA group (Spearman $\rho = -0.79$; $P = .006$), while no association was found in the remaining groups. In our sample, blood flow velocity in the small arteries of the BG did not show any association with age, sex, and the remaining CSVD neuroimaging markers.

PI

There were no group differences for the PI. Age had a significant positive relation to the PI in the quantile regression analysis at

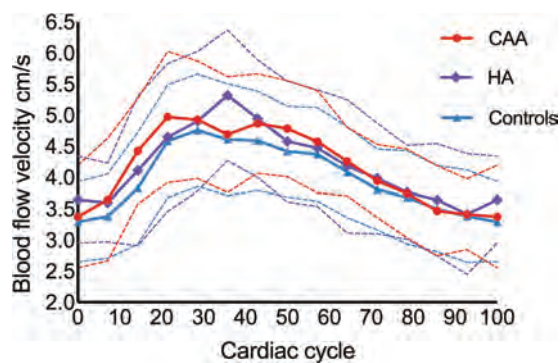


FIG 2. Blood flow velocity curves. Mean blood flow velocity curves (solid lines) over the cardiac cycle (from 0% to 100%, starting at end-diastole) are shown for participants with CAA (red) and HA (purple), compared with healthy controls (blue). The dashed lines represent 1 SD. Blood flow velocity at each of the 14 available cardiac timeframes was averaged over the group. The blood flow velocity curve of patients with HA shows a slightly different pattern than in the other groups.

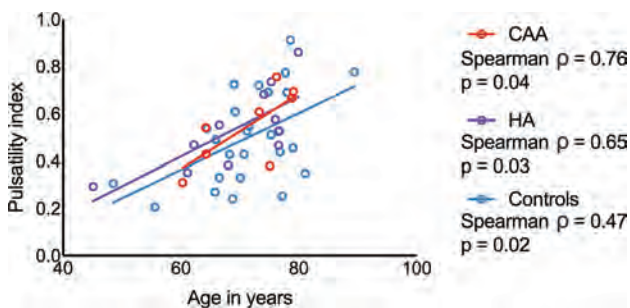


FIG 3. Association between the PI and age. The PI was positively correlated with age in each subgroup, independent of the presence or subtype of CSVD. The Spearman correlation was used.

the 25th and 75th percentiles across the whole group (25th percentile: 0.01 [SD, 0.004]; $P = .002$; 75th percentile: 0.01 [SD, 0.005]; $P = .019$) (Online Supplemental Data). A medium-to-large effect size association between age and PI was, thereby, found in each group (CAA: Spearman $\rho = 0.76$; $P = .04$; HA: Spearman $\rho = 0.65$; $P = .03$; controls: Spearman $\rho = 0.47$; $P = .02$) (Fig 3). In other words, the PI increased with age, irrespective of belonging to a subgroup. There was no relationship between the PI and sex or CSVD-related lesions.

Number of Detected Vessels

There were no group differences for the number of detected vessels. A decreased number of detected vessels could have occurred due to lower blood velocity, net cerebral blood flow, or a narrower lumen of the vessel. Furthermore, there was no relationship between vessel number, age, sex, or CSVD downstream pathologies (Online Supplemental Data).

DISCUSSION

The main purpose of this 7T MR imaging study was to measure blood flow velocity and the PI in the small perforating BG arteries in both healthy elderly controls and patients with CSVD (CAA

and HA). We found that older age related to a higher PI in the small perforating BG arteries independent of CSVD existence or subtype, while flow velocity was not age-dependent. Furthermore, there was an association between lower blood flow velocity in the deep perforators and peri-BG WMH in the HA subgroup.

The relationship between age and a greater PI is consistent with previous data, revealing a higher PI in healthy elderly compared with young subjects in both large cerebral vessels such as the MCA³⁵ and the lenticulostriate arteries.²³ Although our study population was limited to elderly participants, a positive association between age and pulsatility existed. These results can be explained by the lower compliance of the cerebral vasculature in older age, which is likely to occur through stiffening of the arterial wall.³⁶ Moreover, an age-related stiffening of the whole vessel tree, especially of the aorta, can lead to a diminished wave reflection and thus transmission of excessive pulsatility to the microvasculature.²⁴ No difference in PI was observed between the groups, suggesting that age might be the driving factor influencing this measure, irrespective of CSVD. On the contrary, a previous study, which used the same method and compared a cohort of patients with CSVD with symptomatic stroke (deep ICH or lacunar infarcts) with healthy elderly controls²⁷ found that the PI in the BG was higher in the subjects with stroke. Possible explanations for this discrepancy are, on the one side, different degrees of disease severity (patients in the present study were supposedly less affected because only 1 presented with deep-but-asymptomatic ICH). Additionally, the current implementation of the 2D PC MR imaging sequence appears to be less sensitive on the Siemens platform than on the Philips Healthcare platform as reported before,³³ underscoring the challenge of harmonizing sequences.

Another factor that might have contributed is a different approach in the data processing. During the course of our study, J.J.M.Z (author on both the present article and the previous study²⁷) learned that the PI in the previous study was, accidentally, first calculated per vessel and subsequently averaged to get a single PI per subject, whereas it was intended to be calculated from the average normalized velocity curve from all vessels. Calculating per vessel makes the PI more susceptible to noise and yields numerically larger PIs. Nonetheless, the PI calculated from the average velocity curves from the previous study did still show a significant difference in the PI between patients with lacunar infarcts and controls (data not shown). Our results definitely confirm the importance of reproducing previous studies.

Our study uncovered a relationship between lower blood flow velocity in the perforating arteries of the BG and the presence of peri-BG WMH. That association was obvious even after correcting for other CSVD markers in the BG region (deep MBs, deep lacunes, BG EPVS), age, and sex, supporting its robustness. The relation was pertinent to the HA group, consistent with the pattern of cerebral lesions caused by hypertensive disease and the vulnerability of the BG vessels associated with this condition.³⁷ In these patients, CSVD-related lesions are, in fact, mainly found in the deep cerebral regions,¹² but the mechanistic process leading to them remains a matter of debate. This finding goes along with those in previous studies in which lower blood flow velocity measured in larger vessels (eg, the MCA) was associated with

WMH severity.³⁸ A decrease in cerebral blood flow surrounding WMH³⁹ and at the whole-brain level (including normal-appearing WM)⁴⁰ was associated with larger WMH volume in cognitively healthy elderly controls. Further studies found that higher arterial stiffness in the central arteries (eg, the aorta), measured by pulse wave velocity, was an independent predictor of high overall WMH burden.²⁴⁻²⁶ Furthermore, elderly subjects with WMH showed higher MCA pulsatility,⁴¹ an association that was stronger than the one with central artery pulsatility. However, none of the so-far reported studies directly measured blood flow in the perforating small BG arteries. The exact sequence of changes in blood flow measures of small arteries and the development of WMH are still debated, and dedicated longitudinal studies are needed to unravel them.⁴²

Contrary to what might be expected given these premises, blood flow characteristics (mean velocity and PI) in the perforating arteries of patients with HA from our cohort were not significantly different from those of patients with CAA and controls. While the stage of the disease might have played a role in determining this result, it could also suggest that blood flow velocity and PI do not sufficiently explain CSVD-related microvascular hemodynamics. For example, conflicting evidence exists about the role played by arterial pulsatility in clearance mechanisms.^{43,44} Other factors such as cerebrovascular reactivity⁴² might be more relevant. The profile of the blood flow velocity curves was different in patients with HA compared with the other groups and showed a less steep increase than in the remaining subgroups. The meaning of the shift in the flow velocity curve should not be overestimated but is coherent with the predominant vulnerability of the BG vessels in patients with HA (compared with CAA).

There was no effect with respect to the number of detected vessels in the BG. Even though the spatial resolution of the 2D PC sequence is sufficient to detect a perforating artery of average diameter (0.47 mm) and below,²¹ some arteries likely remained unobserved.

One obvious limitation of our study is the small number of subjects and the relatively high number of tests performed on the data, so the results need to be considered as exploratory. This aspect needs to be set in the context of the difficulty of performing 7T MR imaging, with all its contraindications, of patients clinically affected by cerebrovascular disease. However, the use of 7T MR imaging was here necessary to provide sufficiently high resolution, high SNR, and short acquisition times. Moreover, the use of a robust statistical method such as quantile regression analysis, which can suitably be applied to small samples and when the conditions for linear regression analysis are not met, minimizes this issue.⁴⁵ Nonetheless, broader studies are needed to make more conclusive observations. This recommendation applies also to the relationship between age and PI, which should be investigated within the frame of a life span study and in a set of longitudinal measures. A further limitation concerns the lack of pulsatility measurements in larger arteries, such as the M1 segment of the MCA, which would allow establishing whether the results reported in this study are dependent only on the downstream circulation system. However, a previous study suggested the existence of damping beyond the major cerebral arteries, which

could compensate for left ventricular function and arterial input.⁴⁶

In the present study, we investigated the characteristics of blood flow in the perforating arteries of the BG. However, using 2D PC MR imaging to the cortical or perforating WM arteries could help to shed more light on the hemodynamic consequences of CAA as well, which mainly interests these vessels.

CONCLUSIONS

Our study combined, for the first time, the analysis of CSVD markers with measures of blood flow obtained through ultra-high-resolution 7T MR imaging. Decreased blood flow velocity in the perforating BG arteries was associated with the presence of peri-BG WMH in HA. Furthermore, age proved to be the driving factor for an increase in the PI in our cohort, irrespective of CSVD. Even if further and broader studies are needed to pinpoint the applicability of measures of blood flow as a functional marker, our results already point toward the potential of 2D PC MR imaging to aid in the understanding of vascular aging and CSVD.

ACKNOWLEDGMENTS

We are very grateful to all participants who volunteered to take part in the study. We thank Anna Ludwig and Denver Huff for help in subject recruitment and data collection. We also wish to thank Renate Blobel-Lüer, Claus Tempelmann, and Daniel Stucht for their dedicated efforts in scanning, standardization, and quality assurance.

Disclosure forms provided by the authors are available with the full text and PDF of this article at www.ajnr.org.

REFERENCES

1. Charidimou A, Pantoni L, Love S. **The concept of sporadic cerebral small vessel disease: a road map on key definitions and current concepts.** *Int J Stroke* 2016;11:6-18 CrossRef Medline
2. Pantoni L. **Cerebral small vessel disease: from pathogenesis and clinical characteristics to therapeutic challenges.** *Lancet Neurol* 2010;9:689-701 CrossRef Medline
3. Xiong L, Davidsdottir S, Reijmer YD, et al. **Cognitive profile and its association with neuroimaging markers of non-demented cerebral amyloid angiopathy patients in a stroke unit.** *J Alzheimers Dis* 2016;52:171-78 CrossRef Medline
4. Pantoni L, Poggesi A, Inzitari D. **Cognitive decline and dementia related to cerebrovascular diseases: some evidence and concepts.** *Cerebrovasc Dis* 2009;27:191-96 CrossRef Medline
5. Greenberg SM, Bacskai BJ, Hernandez-Guillamon M, et al. **Cerebral amyloid angiopathy and Alzheimer disease: one peptide, two pathways.** *Nat Rev Neurol* 2020;16:30-42 CrossRef Medline
6. Sweeney MD, Montagne A, Sagare AP, et al. **Vascular dysfunction: the disregarded partner of Alzheimer's disease.** *Alzheimers Dement* 2019;15:158-67 CrossRef Medline
7. Wardlaw JM; STandards for ReportIng Vascular changes on nEuroimaging (STRIVE v1). **Neuroimaging standards for research into small vessel disease and its contribution to ageing and neurodegeneration.** *Lancet Neurol* 2013;12:822-38 CrossRef Medline
8. Wardlaw JM. **Prevalence of cerebral white matter lesions in elderly people: a population based magnetic resonance imaging study: the Rotterdam Scan Study.** *J Neurol Neurosurg Psychiatry* 2001;70:2-3 CrossRef Medline

9. Caunca MR, De Leon-Benedetti A, Latour L, et al. **Neuroimaging of cerebral small vessel disease and age-related cognitive changes.** *Front Aging Neurosci* 2019;11:145 CrossRef Medline
10. Gladman JT, Corriveau RA, Debette S, et al. **Vascular contributions to cognitive impairment and dementia: research consortia that focus on etiology and treatable targets to lessen the burden of dementia worldwide.** *Alzheimers Dement (N Y)* 2019;5:789–96 CrossRef Medline
11. Lammie GA, Brannan F, Slattery J, et al. **Nonhypertensive cerebral small-vessel disease: an autopsy study.** *Stroke* 1997;8:2222–29 CrossRef Medline
12. Martinez-Ramirez S, Greenberg SM, Viswanathan A. **Cerebral microbleeds: overview and implications in cognitive impairment.** *Alzheimer's Res Ther* 2014;6:1–7 CrossRef Medline
13. Martinez-Ramirez S, Pontes-Neto OM, Dumas AP, et al. **Topography of dilated perivascular spaces in subjects from a memory clinic cohort.** *Neurology* 2013;80:1551–56 CrossRef Medline
14. Greenberg SM, Charidimou A. **Diagnosis of cerebral amyloid angiopathy evolution of the Boston criteria.** *Stroke* 2018;49:491–97 CrossRef Medline
15. Grinberg LT, Thal DR. **Vascular pathology in the aged human brain.** *Acta Neuropathol* 2010;119:277–90 CrossRef Medline
16. Schreiber S, Bueche CZ, Garz C, et al. **The pathologic cascade of cerebrovascular lesions in SHRSP: Is erythrocyte accumulation an early phase.** *J Cereb Blood Flow Metab* 2012;32:278–90 CrossRef Medline
17. Jandke S, Garz C, Schwanke D, et al. **The association between hypertensive arteriopathy and cerebral amyloid angiopathy in spontaneously hypertensive stroke-prone rats.** *Brain Pathol* 2018;28:844–59 CrossRef Medline
18. Shi Y, Thrippleton MJ, Blair GW, et al. **Small vessel disease is associated with altered cerebrovascular pulsatility but not resting cerebral blood flow.** *J Cereb Blood Flow Metab* 2018;40:85–99 CrossRef Medline
19. Mitchell GF. **Effects of central arterial aging on the structure and function of the peripheral vasculature: implications for end-organ damage.** *J Appl Physiol* 2008;53:234–41 CrossRef Medline
20. Mestre H, Kostrikov S, Mehta RI, et al. **Perivascular spaces, glymphatic dysfunction, and small vessel disease.** *Clin Sci (Lond)* 2017;131:2257–74 CrossRef Medline
21. Bouvy WH, Geurts LJ, Kuijff HJ, et al. **Assessment of blood flow velocity and pulsatility in cerebral perforating arteries with 7-T quantitative flow MRI.** *NMR Biomed* 2016;29:1295–1304 CrossRef Medline
22. Geurts L, Biessels GJ, Luijten P, et al. **Better and faster velocity pulsatility assessment in cerebral white matter perforating arteries with 7T quantitative flow MRI through improved slice profile, acquisition scheme, and postprocessing.** *Magn Reson Med* 2017;79:1473–82 CrossRef Medline
23. Schnerr RS, Jansen JFA, Uludag K, et al. **Pulsatility of lenticulostriate arteries assessed by 7 Tesla flow MRI: measurement, reproducibility, and applicability to aging effect.** *Front Physiol* 2017;8:96 CrossRef Medline
24. Mitchell GF, Van Buchem MA, Sigurdsson S, et al. **Arterial stiffness, pressure and flow pulsatility and brain structure and function: the Age, Gene/Environment Susceptibility-Reykjavik Study.** *Brain* 2011;134:3398–3407 CrossRef Medline
25. Hughes TM, Kuller LH, Barinas-Mitchell EJ, et al. **Pulse wave velocity is associated with incident dementia and amyloid deposition in the brains of elderly adults.** *Neurology* 2013;81:1711–18 CrossRef Medline
26. King KS, Chen KX, Hulsey KM, et al. **White matter hyperintensities: use of aortic arch pulse wave velocity to predict volume independent of other cardiovascular risk factors.** *Radiology* 2013;267:709–17 CrossRef Medline
27. Geurts LJ, Zwanenburg JJ, Klijn CJ, et al. **Higher pulsatility in cerebral perforating arteries in patients with small vessel disease related stroke: a 7T MRI study.** *Stroke* 2019;50:62–68 CrossRef Medline
28. Javadi U, Pennine C, Hospitals A, et al. **The Microbleed Anatomical Rating Scale (MARS): reliability of a tool to map brain microbleeds.** *Neurology* 2009;73:1759–66 CrossRef Medline
29. Wardlaw JM. **What is a lacune?** *Stroke* 2008;39:2921–22 CrossRef Medline
30. Potter GM, Chappell FM, Morris Z, et al. **Cerebral perivascular spaces visible on magnetic resonance imaging: development of a qualitative rating scale and its observer reliability.** *Cerebrovasc Dis* 2015;39:224–31 CrossRef Medline
31. Linn J, Halpin A, Demaerel P, et al. **Prevalence of superficial siderosis in patients with cerebral amyloid angiopathy.** *Neurology* 2010;74:1346–50 CrossRef Medline
32. Tsai HH, Pasi M, Tsai LK, et al. **Microangiopathy underlying mixed-location intracerebral hemorrhages/microbleeds: a PiB-PET study.** *Neurology* 2019;92:E774–81 CrossRef Medline
33. Düzel E, Acosta-Cabronero J, Berron D, et al. **European Ultra-high-Field Imaging Network for Neurodegenerative Diseases (EUFIND).** *Alzheimers Dement (Amst)* 2019;11:538–49 CrossRef Medline
34. Arts T, Siero JCW, Biessels GJ, et al. **Automated assessment of cerebral arterial perforator function on 7T MRI.** *J Magn Reson Imaging* 2021;53:234–41 CrossRef Medline
35. Zarrinkoob L, Ambarki K, Wahlin A, et al. **Aging alters the dampening of pulsatile blood flow in cerebral arteries.** *J Cereb Blood Flow Metab* 2016;36:1519–27 CrossRef Medline
36. Safar ME. **Arterial aging-hemodynamic changes and therapeutic options.** *Nat Rev Cardiol* 2010;7:442–49 CrossRef Medline
37. Kang C, Park C, Han J, et al. **Imaging and analysis of lenticulostriate arteries using 7.0-Tesla.** *Magn Reson Med* 2009;61:136–44 CrossRef Medline
38. Tzourio C, Lévy C, Dufouil C, et al. **Low cerebral blood flow velocity and risk of white matter hyperintensities.** *Ann Neurol* 2001;49:411–91 CrossRef Medline
39. Promjunyakul N, Lahna D, Kaye JA, et al. **Characterizing the white matter hyperintensity penumbra with cerebral blood flow measures.** *NeuroImage Clin* 2015;8:224–29 CrossRef Medline
40. Ten Dam VH, Van Den Heuvel DJ, De Craen AJ, et al. **Decline in total cerebral blood flow is linked with increase in periventricular but not deep white matter hyperintensities.** *Radiology* 2007;243:198–203 CrossRef Medline
41. Webb AJS, Simoni M, Mazzucco S, et al. **Increased cerebral arterial pulsatility in patients with leukoaraiosis: arterial stiffness enhances transmission of aortic pulsatility.** *Stroke* 2012;43:2631–36 CrossRef
42. Wardlaw JM, Smith C, Dichgans M. **Small vessel disease: mechanisms and clinical implications.** *Lancet Neurol* 2019;18:684–96 CrossRef Medline
43. Iliff JJ, Nedergaard M, Lee H, et al. **Brain-wide pathway for waste clearance captured by contrast-enhanced MRI.** *J Clin Invest* 2013;123:1299–1309 CrossRef Medline
44. Diem AK, Sharp MM, Gatherer M, et al. **Arterial pulsations cannot drive intramural periarterial drainage: significance for A β drainage.** *Front Neurosci* 2017;11:475–79 CrossRef Medline
45. Austin PC, Tu JV, Daly PA, et al. **The use of quantile regression in health care research: A case study examining gender differences in the timeliness of thrombolytic therapy.** *Stat Med* 2005;24:791–816 CrossRef Medline
46. Arts T, Onkenhout LP, et al. **Non-invasive assessment of damping of blood flow velocity pulsatility in cerebral arteries with MRI.** *J Magn Reson Imaging* 2021 Nov 18. [Epub ahead of print] CrossRef Medline

Identification of Small, Regularly Shaped Cerebral Aneurysms Prone to Rupture

 S.F. Salimi Ashkezari,  F. Mut,  M. Slawski,  C.M. Jimenez,  A.M. Robertson, and  J.R. Czebrak



ABSTRACT

BACKGROUND AND PURPOSE: Many small, regularly shaped cerebral aneurysms rupture; however, they usually receive a low score based on current risk-assessment methods. Our goal was to identify patient and aneurysm characteristics associated with rupture of small, regularly shaped aneurysms and to develop and validate predictive models of rupture in this aneurysm subpopulation.

MATERIALS AND METHODS: Cross-sectional data from 1079 aneurysms smaller than 7 mm with regular shapes (without blebs) were used to train predictive models for aneurysm rupture using machine learning methods. These models were based on the patient population, aneurysm location, and hemodynamic and geometric characteristics derived from image-based computational fluid dynamics models. An independent data set with 102 small, regularly shaped aneurysms was used for validation.

RESULTS: Adverse hemodynamic environments characterized by strong, concentrated inflow jets, high speed, complex and unstable flow patterns, and concentrated, oscillatory, and heterogeneous wall shear stress patterns were associated with rupture in small, regularly shaped aneurysms. Additionally, ruptured aneurysms were larger and more elongated than unruptured aneurysms in this subset. A total of 5 hemodynamic and 6 geometric parameters along with aneurysm location, multiplicity, and morphology, were used as predictive variables. The best machine learning rupture prediction-model achieved a good performance with an area under the curve of 0.84 on the external validation data set.

CONCLUSIONS: This study demonstrated the potential of using predictive machine learning models based on aneurysm-specific hemodynamic, geometric, and anatomic characteristics for identifying small, regularly shaped aneurysms prone to rupture.

ABBREVIATIONS: AUC = area under the curve; FI score = harmonic mean of precision and recall; FPR = false-positive rate; PHASES = Population, Hypertension, Age, Size, Earlier subarachnoid hemorrhage, and Site; PPV = positive predictive value; ROC = receiver operating characteristic; SVM = support vector machine; TPR = true-positive rate; WSS = wall shear stress

Cerebral aneurysms are a common vascular disease affecting about 2%–5% of the general population.^{1,2} Many studies have focused on identifying risk factors for the rupture of cerebral aneurysms.^{3–5} Aneurysm size and shape irregularity determined by the presence of blebs have been identified as risk factors for future aneurysm rupture.^{6–8} In addition, risk-scoring scales such

as Population, Hypertension, Age, Size, Earlier subarachnoid hemorrhage, and Site (PHASES)⁵ assign a higher risk of rupture to aneurysms larger than 7 mm or aneurysms that have blebs.

However, it is well-known that a large number of aneurysms presenting with rupture are small (<7mm),^{9,10} and many of them have regular shapes and do not have any blebs or daughter sacs. Thus, these aneurysms would, in general, receive a low score for rupture risk based on the current scales, leading to undertreatment and unnecessary patient mortality and morbidity. Therefore, it would be of great importance to identify those small, regularly shaped aneurysms that are prone to rupture to recommend them for treatment and prevent devastating consequences, while, at the same time, minimizing the number of unnecessary interventions.


Thus, the objective of this study was to identify patient and aneurysm characteristics associated with the rupture of small, regularly shaped aneurysms, train machine learning models using those characteristics to identify rupture-prone aneurysms in this important subpopulation, and evaluate the predictive performance

Received October 26, 2021; accepted after revision January 20, 2022.

From the Departments of Bioengineering (S.F.S.A., F.M., J.R.C.), Statistics (M.S.), and Mechanical Engineering (J.R.C.), George Mason University, Fairfax, Virginia; Neurosurgery Department (C.M.J.), University of Antioquia, Medellin, Colombia; and Departments of Mechanical Engineering and Material Science (A.M.R.) and Bioengineering (A.M.R.), University of Pittsburgh, Pittsburgh, Pennsylvania.

This work was supported by the National Institutes of Health grant R01NS097457.

Please address correspondence to Seyedeh Fatemeh Salimi Ashkezari, PhD, Bioengineering Department, Volgenau School of Engineering, George Mason University, 4400 University Dr, Fairfax, VA 22030; e-mail: ssalimia@gmu.edu

 Indicates open access to non-subscribers at www.ajnr.org

 Indicates article with online supplemental data.

<http://dx.doi.org/10.3174/ajnr.A7470>

of the trained models on an external data set to assess their potential clinical utility.

MATERIALS AND METHODS

Overview of Methodology

This was a cross-sectional study that used several data sets generated from populations from multiple geographic regions. The analysis was restricted to small (<7mm), regularly shaped aneurysms (ie, without blebs). The study was conducted in 3 steps: 1) identify the distinguishing characteristics between ruptured and unruptured small, regularly shaped aneurysms, 2) develop predictive models of rupture using machine learning techniques, and 3) validate the model performance using a separate independent data set from different hospitals. To achieve these goals, we used 2 independent cross-sectional data sets. The first data set was used for identifying differences between ruptured and unruptured small, regularly shaped aneurysms and to train the predictive models. The second data set was used as an external data set to validate the predictions of these models and determine their predictive power and generalizability. Protocols for consent, data handling, and analysis were approved by the institutional review boards at the University of Pittsburgh and George Mason University.

Patients and Data

The first data set used for machine learning model development and internal cross-validation (training set) had a total of 1079 aneurysms in 764 patients. These aneurysms corresponded to patients referred for diagnostic angiography and imaged with 3D rotational angiography or CTA. This set included data from different populations, including the United States, South America, Europe other than Finland, Finland, and Japan. Of these aneurysms, 197 were ruptured (18.3%) and the remaining 882 aneurysms (81.7%) were unruptured. Patients ranged from 12 to 90 years of age, with a mean of 56.4 years. There were 570 (75%) females and 194 (25%) males, and the mean aneurysm size was 4.1 mm (range, 1.1–6.9 mm). Multiple aneurysms were present in 344 patients (45%).

The second data set (validation set) contained 102 aneurysms in 63 patients selected for surgical clipping and imaged with 3D rotational angiography or CTA before surgery. This set contained data from the United States and Finland populations. Of these aneurysms, 14 were ruptured (13.7%) and the remaining 88 aneurysms (86.3%) were unruptured. The average patient age was 53.3 years (median, 54 years; range, 25–69 years). There were 49 (78%) women and 14 (22%) men, and the mean aneurysm size was 4.4 mm (range, 1.3–6.9 mm). Multiple aneurysms were present in 23 patients (37%). For this study, de-identified vascular geometries and patient demographic information were obtained from our data base. The details about these data sets are summarized in the Online Supplemental Data.

Aneurysm Characterization

Patient-specific 3D vascular models were constructed for all aneurysms in the training and testing sets from the available 3D rotational angiography or CTA images as previously described.¹¹ To characterize the hemodynamic environment of the aneurysm,

we performed computational fluid dynamics simulations. Similar to previous studies,^{12,13} blood was modeled as a Newtonian incompressible fluid with a density of 1.0 g/cm³ and viscosity of 0.04 Poise, and the unsteady Navier-Stokes equations were numerically solved using finite elements. Vascular walls were approximated as rigid, and pulsatile inflow conditions were imposed by scaling a representative flow waveform with an empiric law relating flow rate and cross-sectional vessel area in internal carotid and vertebral arteries. Outflow conditions were imposed by dividing flows consistent with the Murray law. Simulations were performed for 2 cardiac cycles with a heart-beat rate of 60 beats per minute using 100 time-steps per cardiac cycle, and data from the second cycle were used to characterize the flow conditions in the aneurysm.

To characterize the aneurysm hemodynamics and geometry, we computed 15 flow variables and 10 geometric parameters defined on the aneurysm region.^{14,15} Additionally, the aneurysm anatomic characteristics (location, morphology, and multiplicity) and patient demographics (population, sex, and age) were described by 6 categorical variables (numeric in the case of age).

Postprocessing and Construction of Rupture-Predictive Models

Patient and aneurysm characteristics associated with rupture of small, regularly shaped aneurysms were identified in a data set 1 by performing contingency table analysis and the Pearson χ^2 test for categorical variables. For continuous variables, tests for differences in the median of the 2 populations defined by the rupture status were performed via the 2-sample unpaired Wilcoxon (Mann-Whitney) test. All statistical analyses and machine learning modeling were performed in R statistical and computing software (<http://www.r-project.org/>). Comparisons between multiple groups were adjusted using the Benjamini-Hochberg method, and associations were considered significant with $P < .05$ after adjustment.

Various machine learning methods for supervised classification were used to identify the best predictive power. These included logistic regression, support vector machine (SVM), K-nearest neighbor, random forest, and bagging or bootstrap aggregating. Data from all 1079 aneurysms (no missing data) of the first data set were used for model training.

The columns of the feature matrix of the continuous predictor variables were standardized so that the attributes would have a mean value of zero and an SD of 1. Categorical variables were encoded as dummy variables. One hundred repetitions of nested 10-fold (internal) cross-validation, yielding 100 random partitions of the original training sample, were used to train the models, estimate the tuning parameters, and identify the important predictor variables. In this step, data set 1 was split into training and testing subsets for each of the 10 folds, and the optimal value of each tuning parameter related to the training process was determined via a grid search to achieve the largest area under the curve (AUC) of the receiver operating characteristic (ROC). The 100 results were combined (averaged) to produce a single estimation.

Feature Selection

To identify features to be used to predict rupture in aneurysms, we performed the recursive feature elimination¹⁶ technique.

Table 1: Summary of evaluation metrics for machine learning predictive models during repeated internal 10-fold cross-validation

Model	AUC (mean) (maximum)	TPR (mean) (maximum)	FPR (mean) (minimum)	Misclassification Error (mean) (minimum)
BG	0.84 (0.91)	0.75 (0.84)	0.23 (0.18)	0.23 (0.14)
RF	0.84 (0.92)	0.78 (0.89)	0.25 (0.17)	0.25 (0.16)
SVM	0.85 (0.90)	0.82 (0.95)	0.26 (0.16)	0.23 (0.17)
KNN	0.82 (0.90)	0.74 (0.90)	0.23 (0.14)	0.23 (0.15)
LR	0.83 (0.92)	0.73 (0.95)	0.23 (0.15)	0.24 (0.16)

Note:—AUC indicates area under the curve; BG, bagging or bootstrap aggregating; FPR, false-positive rate; KNN, K-nearest neighbor; LR, logistic regression; RF, random forest; SVM, support vector machine; TPR, true-positive rate.

Briefly, an initial model was built on the basis of the entire set of predictors, and an importance score was computed for each predictor. Then, the least important predictors were recursively removed while maintaining the overall model accuracy. The optimal subset of features was then used to train the final model.

Because only about 20% of small, regularly shaped cerebral aneurysms rupture, the data sets are unbalanced, negatively impacting the model fitting and performance. To deal with this problem during the internal cross-validation of the model training process, we used a down-sampling approach, in which data from most classes (unruptured aneurysms) were randomly removed to achieve a balanced class distribution and consequently mitigate this issue.

Model Performance and Validation

First, the performance of the different machine learning models of aneurysm rupture was evaluated internally (ie, on the same training data set) and compared. For this purpose, the AUC of the ROC, the true-positive rate (TPR), the false-positive rate (FPR), and the misclassification error were calculated. Pair-wise comparisons of these performance metrics between machine learning models were performed using the built-in summary function of the caret package available in R (based on a 1-sample *t* test) to find differences in the performance of various models and to determine whether these differences were statistically significant.

Second, the predictive models were externally validated on the independent validation data set 2 containing data from 102 aneurysms that were not used during training, parameter tuning, and model selection. In addition to the AUC, the accuracy of the model was assessed in terms of the true-positive rate (TPR or recall), FPR, positive predictive value (PPV or precision), negative predictive value, harmonic mean of precision and recall (F1 score), and balanced accuracy.

RESULTS

Patient and Aneurysm Characteristics Associated with Rupture

Statistical comparisons between patient and aneurysm characteristics among ruptured and unruptured small, regularly shaped aneurysms are presented in the Online Supplemental Data. Aneurysm rupture was significantly associated with patient sex (the ratio of males to females was higher in the ruptured group compared with the unruptured group, $P = .01$), age (patients with ruptured aneurysms were, in general, younger, $P = .003$), and population (the Finnish population had a higher proportion of ruptured aneurysms compared with the US and European populations, $P < .001$). In addition, aneurysm rupture was significantly associated with aneurysm multiplicity (most ruptured aneurysms

were single aneurysms, $P < .001$), morphology (ratio of bifurcation to lateral aneurysm was higher in the ruptured group, $P < .001$), and location (the anterior communicating artery was the location with the higher proportion of ruptured aneurysms, $P < .01$).

Hemodynamic and geometric differences between ruptured and unruptured small, regularly shaped aneurysms are presented in the Online Supplemental Data. As shown in these data, most of the hemodynamic and geometric variables were significantly different between the 2 groups of aneurysms, even after adjustment for multiple testing.

Hemodynamically, ruptured aneurysms had stronger (Q, $P = .02$) and more concentrated inflow jets (ICI, $P = .002$) and more complex (corelen, $P < .001$) and unstable (podent, $P < .001$) flow patterns than unruptured aneurysms. They also had larger maximum wall shear stress (WSSmax) ($P < .001$; MaxWSSnorm, $P = .003$), more concentrated (SCI, $P < .001$) and oscillatory (OSImax, $P < .001$; OSImean, $P < .001$) WSS distribution, and a larger number of critical points of the WSS field (nr.critical, $P < .001$).

Geometrically, ruptured aneurysms were larger (Asize, $P < .001$; SR, $P < .001$; GAA, $P < .001$), more elongated (AR, $P < .001$; VOR, $P < .001$; BF, $P < .001$), and had larger shape distortion (CR, $P < .001$; NSI, $P < .001$; UI, $P < .001$) than unruptured aneurysms in this subpopulation.

Variables Retained in the Model

Thirty-one variables were used to build the models and select the optimal set of predictive features. The final model retained the following 14 predictive variables from the 3 different domains: 1) hemodynamic: corelen, WSS, OSImax, OSImean, nr.critical; 2) geometric: Asize, SR, AR, VOR, BF, NSI; and 3) aneurysm: location, multiplicity, and morphology. As illustrated in the Online Supplemental Data, accuracy reached the maximum level when 14 variables were retained in the model, with a noticeable decrease in accuracy beyond 14 variables. See the Online Supplemental Data for the complete list of the variables considered and retained.

Performance of Different Predictive Models

The best predictive model for internal cross-validation was the SVM, with a mean AUC = 0.85, TPR = 0.82, FPR = 0.26, and misclassification error = 0.23 (see Table 1 for performance metrics for all machine learning models considered, and the Online Supplemental Data to visualize the spread of their AUC, sensitivity, and specificity). Pair-wise comparisons of different performance metrics among machine learning models are presented in the Online Supplemental Data.

Table 2: Performance measures for each machine learning model applied to the external testing data set^a

Model	AUC	TPR	FPR	PPV	NPV	F1 Score	Balanced Accuracy	Misclassification Error
BG	0.74	0.71	0.35	0.24	0.93	0.36	0.68	0.34
RF	0.76	0.71	0.32	0.26	0.94	0.38	0.70	0.32
SVM	0.84	0.93	0.35	0.30	0.98	0.45	0.79	0.31
KNN	0.76	0.79	0.36	0.26	0.95	0.39	0.71	0.34
LR	0.77	0.86	0.37	0.27	0.96	0.41	0.74	0.34

Note:—NPV indicates negative predictive value, the number of true-negatives divided by the number of true- and false-negatives; AUC, area under curve; FPR, false-positive rate (1-specificity = number of false-positives divided by all negatives); PPV, positive predictive value (precision = number of true-positives divided by number of true- and false-positives); TPR, true-positive rate (sensitivity or recall = number of true-positives divided by all positives).

^a $F1 = 2 \times PPV \times TPR / (PPV + TPR)$ is the harmonic mean of precision and recall. Balanced accuracy is accuracy accounting for class imbalance $[(sensitivity + specificity) / 2]$. Misclassification error is the number of incorrect classifications divided by sample size.

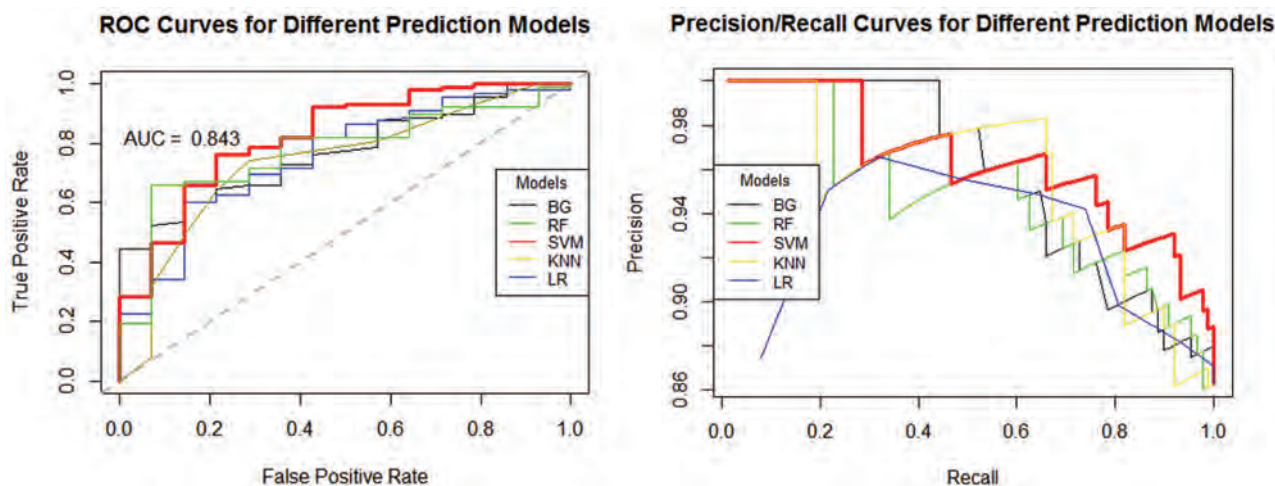


FIG 1. Performance of different machine learning models on an independent, external validation data set: A, ROC curves. B, Precision/recall curves. The best performance is achieved by the SVM model (red curves). BG indicates bagging or bootstrap aggregating; RF, random forest; SVM, support vector machine; KNN, K-nearest neighbor; LR, logistic regression.

External Validation

Table 2 presents the performance of different machine learning classifiers when applied to the independent external testing data set. It can be seen that the best performance was achieved by the SVM model, with consistently the largest AUC = 0.84 (95% CI, 0.80–0.89), TPR = 0.93, PPV = 0.30, NPV = 0.98, F1 score = 0.45, and balanced accuracy = 0.79, and the smallest misclassification error = 0.31. However, the random forest model had the smallest FPR = 0.32, slightly smaller compared with FPR = 0.35 of the SVM model. The performance of different machine learning models on the external data set is graphically presented in Fig 1, which shows the ROC and the precision/recall curves.

These results suggest that the SVM model was able to correctly identify 93% of small, regularly shaped aneurysms that ruptured. On the other hand, 35% of unruptured aneurysms were identified as at risk of rupture, which may result in overtreatment for these lower-risk aneurysms. Of all the aneurysms classified as unruptured, 98% were correctly classified. This finding indicates that the model is generalizable to independent data sets from different centers.

The most important variables ($n=14$) for discriminating between small, regularly shaped aneurysms prone to rupture and aneurysms less likely to rupture were determined using an algorithm that excludes variables from the model, one at a time, and

ranks the importance of the excluded variable on the basis of the decrement in the AUC of the ROC (as the measure of variable importance), in which a larger decrement indicates a more important feature. The most important variables (Fig 2) comprised geometric shape and size factors, flow complexity, and WSS parameters, as well as aneurysm multiplicity.

Examples of aneurysms from the external validation data set that were correctly classified by the SVM model are illustrated in the Online Supplemental Data. The upper panel of the Online Supplemental Data shows a small (<7mm) and regularly, shaped ruptured aneurysm at the anterior communicating artery. Visualizations illustrate the hemodynamic environment characterized by a strong inflow jet, elevated WSS, and a complex flow structure. The SVM model assigned a probability of 92% to this aneurysm being ruptured. The lower panel shows an unruptured, small, regularly shaped aneurysm at the anterior communicating artery and its hemodynamics characterized by a slow, smooth, and simple flow pattern with uniformly low WSS. This aneurysm was assigned a probability of 90% of not being ruptured. The upper panel of the Online Supplemental Data shows a small, regularly shaped ruptured aneurysm at the MCA and its hemodynamics environment characterized by a strong inflow jet, elevated and heterogeneous WSS, and a complex flow structure. The SVM model assigned a probability of 88% of this aneurysm being

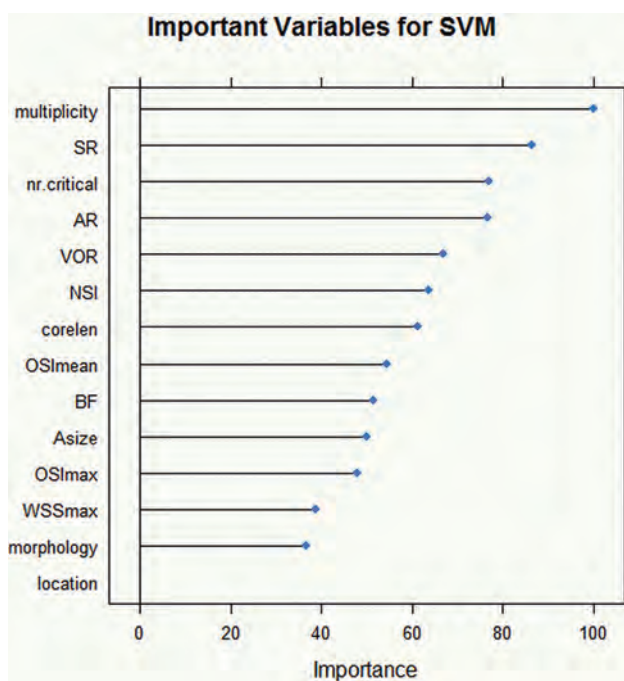


FIG 2. Variable importance for the SVM model applied to the validation data set. Variables are ordered from top to bottom according to their importance determined by the AUC of the ROC as the measure of variable importance. See the Online Supplemental Data for an explanation of the terms.

ruptured. The lower panel shows an unruptured small, regularly shaped aneurysm at the MCA and its hemodynamics, characterized by a simple flow pattern with fairly uniform WSS. This aneurysm was assigned a probability of 86% of not being ruptured. These examples highlight the generalizability of the predictive model.

DISCUSSION

The focus of this study was to identify patient and aneurysm characteristics associated with rupture of small and regularly shaped aneurysms; because this is a cross-sectional study, it is not the authors' intention to establish causal associations. Several patient and aneurysm characteristics were different between ruptured and unruptured aneurysms of this subset. In particular, our results indicate that when restricting the analysis to small aneurysms (<7mm) without blebs, ruptured aneurysms have higher flow conditions characterized by high, concentrated inflow jets; complex, unstable flow patterns; and concentrated, complex, and oscillatory WSS distribution compared with unruptured aneurysms. Additionally, ruptured aneurysms were larger and more elongated and had larger shape distortion than unruptured aneurysms in this subpopulation. Furthermore, aneurysm rupture was significantly associated with patient sex, age, population, as well as aneurysm multiplicity, morphology, and location.

Machine learning models based on patient and aneurysm characteristics are capable of identifying rupture-prone small, regularly shaped aneurysms with an accuracy of approximately 79%, a sensitivity of 93%, and a specificity of 65%. This feature is important to improve the management of patients presenting

with small, regularly shaped aneurysms. To interpret the meaning of these numbers, one should consider, for example, that in a sample of 100 small, regularly shaped aneurysms, approximately 18 would rupture (based on a rupture rate of 17.6% from our data base, which, of course, is higher than the annual rupture rates reported from highly selected series of longitudinally followed aneurysms¹⁷). On one extreme, one could decide to treat all aneurysms. In this case, all hemorrhages would presumably be avoided, but the expected number of complications would be approximately 10, assuming a 10% risk of complications.^{18,19} On the other extreme, if one decided not to treat any of these small, regularly shaped aneurysms, there would be no treatment complications, but a total of 18 hemorrhages. Even recognizing the inaccuracies of the predictive model presented here, which would correctly identify 17 of the 18 aneurysms prone to rupture and thus avoid their bleeding and misidentify as potentially risky another 29 that would probably not need intervention, this method could be useful for clinicians. For instance, with the use of the machine learning model, the number of expected treatment complications would be around 5 and the expected number of ruptures would be around 1, with a reduction in the total number of treatments to about 46 compared with the 100 treatments if one decided to treat everybody. Considering the high complication rate of unruptured cerebral aneurysm intervention, around 10% by any method, added to the low rupture rate of small, regularly shaped aneurysms, it is very important to identify those patients with aneurysms that rarely rupture for whom the intervention is probably unnecessary and thus the number of avoidable complications that lead to brain damage. These complications also have an impact on the health system because it is well-known that one of the most expensive items in attending cerebral aneurysms, both socially and economically, is the treatment of perioperative complications, which would be minimized.

Machine learning algorithms have recently gained attention for assessing rupture risk of cerebral aneurysms. One study²⁰ used 12 morphologic features in addition to clinical and anatomic characteristics to predict aneurysm stability in a sample of 420 aneurysms of <8 mm (without excluding aneurysms with blebs) from a single institution and found an aneurysm irregularity metric to be the most important predictor. Although our models incorporate hemodynamic features and did not include some of their clinical parameters (eg, hyperlipidemia), the results are consistent and the predictive power in internal cross-validation is similar (AUC = 0.85 for both). Furthermore, our external validation indicates that our models are generalizable to other populations. Another study²¹ used cross-sectional data of 374 aneurysms <8 mm (18% of which were ruptured) from a single center to build machine learning models of rupture based on patient demographics, life behaviors, clinical histories, lipid profiles, and aneurysm morphology. Their predictive power in internal 10-fold cross-validation was slightly higher than ours (AUC = 0.88) and significantly higher than the PHASES score (as expected). While our findings are consistent with this study in that aneurysm irregularity, location, multiplicity, and size ratio are important predictors, 1 important difference is that our study considered only aneurysms without blebs, while in this other study, most ruptured aneurysms had blebs.

Another recent study²² proposed the use of fluid-structure interaction for aneurysm risk assessment, by first estimating regions of thin walls from computational fluid dynamics analysis and then using fluid-structure interaction to estimate wall strain for varying wall stiffness. Although this work made several important assumptions and was based on a small (but longitudinal) sample from a single institution, it proposes an intriguing approach. Our models included several hemodynamic features that were used in this study for estimating local wall thinning, which subsequently affects wall strain and rupture risk, and thus are expected to be important predictors as shown in our study. Additionally, more advanced machine learning and artificial intelligence algorithms have also been used to predict treatment outcomes after aneurysm clipping²³ and for the detection and measurement of aneurysms on MR images,^{24,25} showing that these methods are quite effective for multivariate prediction in a wide variety of applications but need careful interpretation.

We believe that ultimately, the aneurysm risk assessment should be conducted in stages. For example, in the first stage, aneurysm size, shape irregularity, and patient characteristics (as in PHASES⁵ or unruptured intracranial aneurysm treatment score [UIATS]⁴) could be used to pick up the most dangerous aneurysms. In the second stage, additional anatomic, geometric, and hemodynamic parameters derived from precise diagnostic angiography images (3D DSA or CTA) could be used to identify rupture-prone aneurysms within the small, regularly shaped subset as in the current study. Perhaps in a third stage, further characteristics related to the status of the aneurysm wall (for example derived from MR vessel wall imaging and/or aneurysm wall-enhancement images) could be used to further identify unstable aneurysms that should be recommended for immediate treatment and those that could be safely monitored without treatment. Thus, aneurysm evaluation would be performed by first applying the existing scales based on demographics and basic imaging; second, performing a more in-depth aneurysm-specific analysis of shape and flow; and finally, studying the aneurysm wall with additional specialized imaging.

The current study has several limitations. In addition to the usual limitations of the computational fluid dynamics modeling approach (Newtonian flow, rigid walls, estimated flow rates, and so forth), in this study, the sample size was limited and there were only 14 ruptured, small, regularly shaped aneurysms in the external validation data set. Also, to deal with the inherent imbalance in the training data set, we performed down-sampling in the cross-validation process. Moreover, the internal and external validations were performed using retrospective cross-sectional data sets. A recent study²⁶ showed that geometric and hemodynamic characteristics were not significantly different between unstable (growing or symptomatic) and already ruptured aneurysms but were significantly different from unruptured aneurysms, thus providing support to the assumption that predictive models based on cross-sectional data are useful to identify aneurysms at risk of destabilization and rupture. Nevertheless, further evaluation and validation with longitudinal data sets are required and will be the focus of future studies. Finally, in the construction of the predictive models of this study, important clinical variables that have been previously

recognized as rupture risk factors such as hypertension, smoking, hyperlipidemia, and family background were omitted, possibly inducing some biases in the present work.

CONCLUSIONS

Hemodynamic conditions characterized by strong, concentrated inflow jets; complex, unstable flow patterns; and concentrated and oscillatory WSS patterns are associated with aneurysm rupture in small, regularly shaped cerebral aneurysms. Additionally, ruptured aneurysms are larger, more elongated, and have larger shape distortion than unruptured aneurysms in this subset. Predictive models based on aneurysm characteristics are capable of identifying small, regularly shaped aneurysms prone to rupture. This is an important finding because we could potentially understand which parameters predispose cerebral aneurysms in the subpopulation of small, regularly shaped aneurysms to rupture, and the findings could lead to improved patient selection for treatment or monitoring.

Disclosure forms provided by the authors are available with the full text and PDF of this article at www.ajnr.org.

REFERENCES

1. Rinkel GJ, Djibuti M, Algra A, et al. **Prevalence and risk of rupture of intracranial aneurysms: a systematic review.** *Stroke* 1998;29:251–56 CrossRef Medline
2. Agarwal N, Gala NB, Choudhry OJ, et al. **Prevalence of asymptomatic incidental aneurysms: a review of 2685 computed tomographic angiograms.** *World Neurosurg* 2014;82:1086–90 CrossRef Medline
3. Qian Y, Takao H, Umezumi M, et al. **Risk analysis of unruptured aneurysms using computational fluid dynamics technology: preliminary results.** *AJNR Am J Neuroradiol* 2011;32:1948–55 CrossRef Medline
4. Etminan N, Brown RD, Beseoglu K, et al. **The unruptured intracranial aneurysm treatment score: a multidisciplinary consensus.** *Neurology* 2015;85:881–89 CrossRef Medline
5. Greving JP, Wermer MJ, Brown RD Jr, et al. **Development of the PHASES score for prediction of risk of rupture of intracranial aneurysms: a pooled analysis of six prospective cohort studies.** *Lancet Neurol* 2014;13:59–66 CrossRef Medline
6. Beck J, Rohde S, El Beltagy M, et al. **Difference in configuration of ruptured and unruptured intracranial aneurysms determined by biplanar digital subtraction angiography.** *Acta Neurochir (Wien)* 2003;145:861–65; discussion 865 CrossRef Medline
7. Raghavan ML, Ma B, Harbaugh RE. **Quantified aneurysm shape and rupture risk.** *J Neurosurg* 2005;102:355–62 CrossRef Medline
8. Björkman J, Frösen J, Tähtinen O, et al. **Irregular shape identifies ruptured intracranial aneurysm in subarachnoid hemorrhage patients with multiple aneurysms.** *Stroke* 2017;48:1986–89 CrossRef Medline
9. Kim BJ, Kang HG, Kwun BD, et al. **Small versus large ruptured intracranial aneurysm: concerns with the site of aneurysm.** *Cerebrovasc Dis* 2017;43:139–44 CrossRef Medline
10. Joo SW, Lee SI, Noh SJ, et al. **What is the significance of a large number of ruptured aneurysms smaller than 7 mm in diameter?** *J Korean Neurosurg Soc* 2009;45:85–89 CrossRef Medline
11. Cebral JR, Castro MA, Appanaboyina S, et al. **Efficient pipeline for image-based patient-specific analysis of cerebral aneurysm hemodynamics: technique and sensitivity.** *IEEE Trans Med Imaging* 2005;24:457–67 CrossRef Medline
12. Mut F, Aubry R, Löhner R, et al. **Fast numerical solutions of patient-specific blood flows in 3D arterial systems.** *Int J Numer Method Biomed Eng* 2010;26:73–85 CrossRef Medline
13. Cebral JR, Mut F, Gade P, et al. **Combining data from multiple sources to study mechanisms of aneurysm disease: tools and**

- techniques. *Int J Numer Method Biomed Eng* 2018;34:e3133 CrossRef Medline
14. Mut F, Löhner R, Chien A, et al. **Computational hemodynamics framework for the analysis of cerebral aneurysms.** *Int J Numer Method Biomed Eng* 2011;27:822–39 CrossRef Medline
 15. Ma B, Harbaugh RE, Raghavan ML. **Three-dimensional geometrical characterization of cerebral aneurysms.** *Ann Biomed Eng* 2004;32:264–73 CrossRef Medline
 16. Guyon I, Weston J, Barnhill S, et al. **Gene selection for cancer classification using support vector machines.** *Machine Learning* 2002;46:389–422 CrossRef
 17. Ikawa F, Morita A, Tominari S, et al. **Rupture risk of small unruptured cerebral aneurysms.** *J Neurosurg* 2020;132:69–78 CrossRef Medline
 18. Kotowski M, Naggara O, Darsaut TE, et al. **Safety and occlusion rates of surgical treatment of unruptured intracranial aneurysms: a systematic review and meta-analysis of the literature from 1990 to 2011.** *J Neurol Neurosurg Psychiatry* 2013;84:42–48 CrossRef Medline
 19. Naggara ON, Lecler A, Oppenheim C, et al. **Endovascular treatment of intracranial unruptured aneurysms: a systematic review of the literature on safety with emphasis on subgroup analyses.** *Radiology* 2012;263:828–35 CrossRef Medline
 20. Liu Q, Jiang P, Jiang Y, et al. **Prediction of aneurysm stability using a machine learning model based on PyRadiomics-derived morphological features.** *Stroke* 2019;50:2314–21 CrossRef Medline
 21. Ou C, Liu J, Qian Y, et al. **Rupture risk assessment for cerebral aneurysm using interpretable machine learning on multidimensional data.** *Front Neurol* 2020;11:570181 CrossRef Medline
 22. Cho KC, Yang H, Kim JJ, et al. **Prediction of rupture risk in cerebral aneurysms by comparing clinical cases with fluid–structure interaction analyses.** *Sci Rep* 2020;10:1–8 CrossRef Medline
 23. Ban VS, El Ahmadi TY, Aoun SG, et al. **Prediction of outcomes for ruptured aneurysm surgery: the Southwestern aneurysm severity index.** *Stroke* 2019;50:595–601 CrossRef Medline
 24. Nakao T, Hanaoka S, Nomura Y, et al. **Deep neural network-based computer-assisted detection of cerebral aneurysms in MR angiography.** *J Magn Reson Imaging* 2018;47:948–53 CrossRef Medline
 25. Stember JN, Chang P, Stember DM, et al. **Convolutional neural networks for the detection and measurement of cerebral aneurysms on magnetic resonance angiography.** *J Digit Imaging* 2019;32:808–15 CrossRef Medline
 26. Chung BJ, Mut F, Putman CM, et al. **Identification of hostile hemodynamics and geometries of cerebral aneurysms: a case-control study.** *AJNR Am J Neuroradiol* 2018;39:1860–66 CrossRef Medline

Follow-up of Intracranial Aneurysms Treated by Flow Diverters: Evaluation of Parent Artery Patency Using 3D-T1 Gradient Recalled-Echo Imaging with 2-Point Dixon in Combination with 3D-TOF-MRA with Compressed Sensing

J. Burel, E. Gerardin, M. Vannier, A. Curado, M Verdalle-Cazes, N. Magne, M. Lefebvre, and C. Papagiannaki



ABSTRACT

BACKGROUND AND PURPOSE: MRA assessment of parent artery patency after flow-diverter placement is complicated by imaging artifacts produced by these devices. The purpose of this study was to assess the accuracy of liver acquisition with volume acceleration-flex technique (LAVA-Flex) MRA in combination with 3D-TOF with HyperSense MRA for the evaluation of parent vessel status after intracranial flow-diverter placement.

MATERIALS AND METHODS: Fifty-six patients treated by flow diversion and followed with both DSA and 3T MRA between November 2020 and August 2021 were included. All patients were evaluated for parent artery patency using the same imaging protocol (DSA, noncontrast MRA including 3D-TOF with HyperSense and LAVA-Flex, and contrast-enhanced MRA, including time-resolved imaging of contrast kinetics MRA and delayed contrast-enhanced MRA).

RESULTS: With DSA as a criterion standard to evaluate the patency of the parent vessel, noncontrast MRA had a good specificity (0.83) and positive predictive value (0.65), better than contrast-enhanced MRA (0.55 and 0.41, respectively). Both had excellent sensitivity and negative predictive value: noncontrast MRA, 0.93 and 0.97, respectively; contrast-enhanced MRA, 0.93 and 0.96, respectively. Specificity and positive predictive value tended to be lower for patients treated with additional devices than for those treated with flow diverters exclusively and for patients treated with a specific type of flow diverter.

CONCLUSIONS: Noncontrast MRA can be used for noninvasive follow-up of intracranial aneurysms treated by flow diverters. The combined use of LAVA-Flex and 3D-TOF with HyperSense sequences allows monitoring the status of the parent artery and aneurysm occlusion.

ABBREVIATIONS: CE-MRA = contrast-enhanced MRA; FD = flow diverter; LAVA-Flex = liver acquisition with volume acceleration-flex technique; NC-MRA = noncontrast MRA; NPV = negative predictive value; PPV = positive predictive value; TRICKS = time-resolved imaging of contrast kinetics; VA = vertebral artery

Flow Diverters (FDs) were initially developed to treat wide-neck large and giant ICA aneurysms only amenable to surgical trap with or without a bypass or endovascular vessel sacrifice, but they have rapidly increased in use.¹⁻⁴ Due to the characteristics of these devices, a careful radiologic follow-up is required to assess the status of the aneurysmal occlusion and the patency of the parent artery.⁵

The rate of complete aneurysm occlusion after flow-diverter treatment varies among series, and it gradually increases with

time due to remodeling of the parent vessel.^{6,7} Kallmes et al⁸ performed a pooled analysis of 3 large studies, with a total of 1091 patients included. The complete occlusion rates were 75.0%, 85.5%, 93.4%, and 95.2% at 6 months and 1, 3, and 5 years, respectively; the overall retreatment rate was low, 3.0%. These retreatments almost exclusively concern aneurysms that persist despite FD placement, with aneurysmal recanalization being exceptional.^{9,10} Thus, an aneurysm treated by a flow diverter whose complete occlusion has been proved is generally considered permanently occluded.^{8,11-14} Hence, once this occlusion has been obtained, whether it is observed by DSA or MRA (with or without injection of contrast media),¹⁵⁻¹⁸ long-term parent artery patency and parenchymal complications are the essential elements to monitor, preferably with noninvasive imaging.

MR imaging is the criterion standard for evaluating potential ischemic and hemorrhagic complications after FD placement and

Received November 5, 2021; accepted after revision January 3, 2022.

From the Departments of Radiology (J.B., E.G., A.C., M.V.-C., N.M., M.L., C.P.) and Biostatistics (M.V.), Rouen University Hospital, Rouen, Normandie, France.

Please address correspondence to Julien Burel, MD, Rouen University Hospital, 37 Boulevard Gambetta, Rouen 76031; e-mail: julien.burel@chu-rouen.fr

Indicates article with online supplemental data.

<http://dx.doi.org/10.3174/ajnr.A7448>

can also identify aneurysm enlargement, aneurysm wall enhancement, and perianeurysmal edema.¹⁹ DSA is the criterion standard for the evaluation of aneurysm occlusion, but 3D-TOF-MRA and CE-MRA have excellent diagnostic accuracy for the aneurysm remnant and can be used in follow-up.^{15-18,20} DSA is also the criterion standard for the evaluation of parent vessel patency after treatment by a FD, due to its unsurpassed spatial resolution and its insusceptibility to metal artifacts. However, DSA is invasive and has potential complications, either of the puncture site or neurologic.²¹ Regarding the evaluation of parent artery patency, the performance of conventional MRA sequences was initially considered insufficient.^{15,16} Recently, Oishi et al⁵ and Shao et al²² evaluated the performance of Silent MRA (GE Healthcare) and 3D-T1 sampling perfection with application-optimized contrasts by using different flip angle evolution (SPACE sequence; Siemens), respectively, to assess the parent artery status after FD placement. The results were good, but the sequences used took several minutes (12 minutes 13 seconds and 8 minutes 29 seconds, respectively) to acquire and were consequently more susceptible to motion artifacts due to swallowing or gross body movement. In addition, the 3D-T1 SPACE sequence could not be used to study aneurysmal occlusion; therefore, an additional 3D-TOF sequence was necessary.

The liver acquisition with volume acceleration-flex technique (LAVA-Flex) sequence, initially developed for liver imaging, is now used in other imaging fields. Regarding neurovascular imaging, Irie et al²³ concluded that LAVA-Flex MRA could provide information similar to TOF-MRA for assessing the cervical carotid bifurcation while reducing scan time by one-fifth. To our knowledge, the use of this sequence for the analysis of intracranial FDs or any type of intracranial stent has not been evaluated. The purpose of this study was to assess the accuracy of LAVA-Flex MRA in combination with 3D-TOF with HyperSense MRA (GE Healthcare) for the evaluation of parent artery patency after intracranial FD placement.

MATERIALS AND METHODS

Patient and FD Characteristics

All patients treated with FDs at our institution and followed with both MRA and DSA were prospectively included in a data base. Patients who underwent both DSA and 3T MRA within a maximum interval of 4 weeks, between November 2020 and August 2021, were included. Exclusion criteria were patients with a contraindication to MR imaging, patients who refused to undergo examinations (MR imaging or DSA), and those who did not undergo one or more of the 4 MRA sequences listed below. The Online Supplemental Data summarize the main technical characteristics of the devices used and evaluated in this study.

DSA Technique

Intra-arterial DSA was performed with a biplane angiographic system (Allura Xper; Philips Healthcare). By means of transfemoral 4F catheterization, selective injections of the ICA or vertebral artery (VA) were performed according to the FD location. Standard anterior-posterior and lateral projections were routinely acquired. For the ICA, 8 mL of nonionic contrast agent (iodixanol, 320-mg iodine/mL, Visipaque 320; GE Healthcare) were

injected with a velocity of 4 mL/s. For the VA, 6 mL was injected with a velocity of 3 mL/s. Rotational 3D angiography and selected oblique projections were performed for additional confirmation of findings. All acquired DSA images were converted to internationally compatible DICOM files; then the converted files were transferred to our server through a PACS.

MRA Technique

MRA examinations were performed on a 3T MR imaging system (Discovery MR750; GE Healthcare) using a 32-channel head coil. MR imaging protocol included axial FLAIR, 2 noncontrast MRA (NC-MRA) sequences (LAVA-Flex and 3D-TOF with HyperSense), and 2 contrast-enhanced MRA (CE-MRA) sequences (time-resolved imaging of contrast kinetics [TRICKS] and a delayed 3D spoiled gradient-echo sequence). TRICKS MRA was performed after the injection of a gadolinium-based contrast agent (gadobutrol, Gadovist; Bayer HealthCare) prescribed at 0.1-mmol/kg and 1-mL/s injection rates, followed immediately by 20–30 mL of normal saline flush at 1 mL/s. An MR fluoroscopic triggering technique was used. The temporal resolution was 1.7 s/frame. The delayed CE-MRA sequence was initiated immediately after acquisition of the TRICKS MRA without application of additional contrast media. Scan parameters of NC-MRA sequences and CE-MRA sequences are summarized in the Online Supplemental Data.

Image Analysis

Studies from all patients were placed in an anonymized folder on the PACS, with NC-MRA (LAVA-Flex MRA and 3D-TOF-MRA with HyperSense), CE-MRA (TRICKS MRA and delayed CE-MRA), and DSA studies forming 3 anonymized folders. The entire original acquired data set, including both source images (mask, subtracted, and unsubtracted images) and standard reformats (MIP and MPR) for each technique, was made available for review when evaluating that technique. LAVA-Flex MRA and 3D-TOF-MRA with HyperSense were evaluated together to form the NC-MRA evaluation of parent artery patency, and TRICKS MRA and delayed CE-MRA were evaluated together to form the CE-MRA evaluation of parent artery patency. NC-MRA, CE-MRA, and DSA were evaluated separately without knowledge of the MRA or DSA examination results, by 1 interventional neuro-radiologist and 1 diagnostic neuroradiologist (both MD-PhD, with >15 years' experience). The location of the FDs to be evaluated was provided to the readers. In case of disagreement, consensus was found between the 2 radiologists.

The patency status of the parent artery was evaluated as no change in the parent artery diameter (patent), focal or diffuse narrowing of the parent artery (stenosis), or parent artery occlusion. A simplified 2-grade scale was used to assess the patency of the parent artery, in which the parent artery was classified as normal or pathologic (stenosis or occlusion). An example of each technique for 1 patient is shown in the Online Supplemental Data.

Statistical Analysis

Quantitative variables are reported as mean (SD) and median (range), while qualitative variables are reported as number and percentage. Interobserver and intermodality agreement was calculated using the Cohen κ . The interpretation of κ was as follows: $\kappa < 0$,

Table 1: Evaluation of parent artery patency (n = 56)

	NC-MRA	CE-MRA	DSA
Three-grade scale			
Patent	36 (64.3%)	24 (42.9%)	42 (75.0%)
Stenosis	19 (33.9%)	31 (55.4%)	13 (23.2%)
Occlusion	1 (1.8%)	1 (1.8%)	1 (1.8%)
Simplified 2-grade scale			
Patent	36 (64.3%)	24 (42.9%)	42 (75.0%)
Stenosis or occlusion	20 (35.7%)	32 (57.1%)	14 (25.0%)

Table 2: Four-fold table of NC-MRA using consensus evaluation for NC-MRA and DSA

	Consensus Evaluation for DSA	
	Pathologic (Stenosis or Occlusion)	Normal (Patent)
Consensus Evaluation for NC-MRA		
Pathologic (stenosis or occlusion)	13	7
Normal (patent)	1	35

no agreement; $\kappa = 0-0.19$, poor agreement; $\kappa = 0.20-0.39$, fair agreement; $\kappa = 0.40-0.59$, moderate agreement; $\kappa = 0.60-0.79$, substantial agreement; and $\kappa = 0.80-1.00$, almost perfect agreement.²⁴ Contingency tables were used to summarize the relationships: NC-MRA versus DSA and CE-MRA versus DSA, using the consensus evaluation. With DSA as a criterion standard to evaluate the patency of the parent artery, the sensitivity, specificity, negative predictive value (NPV), and positive predictive value (PPV) of NC-MRA and CE-MRA were calculated for the whole population, using the consensus evaluation with corresponding 95% confidence intervals. For NC-MRA, these calculations were also made for each separate device, for patients treated with FDs exclusively and those treated with additional devices (coils, Woven EndoBridge [WEB; MicroVention], surgical clips). Comparison between possible receiver operating characteristic curves was not performed due to relatively small samples. All analyses were performed using SAS software, Version 9.4 (SAS Institute).

RESULTS

Fifty-six patients were included, 44 women (78.6%) and 12 men (21.4%), with a mean age of 57.8 (SD, 10.2) years (range, 25–79 years). Fifty-two of the 56 patients (92.9%) were treated with 1 FD; and 4 patients (7.1%), with 2 partially overlapping FDs in the same treatment. Twenty-eight of the 56 patients (50.0%) were treated with a Pipeline Shield FD (Medtronic); 19 (33.9%), with a Surpass Evolve FD (Stryker Neurovascular); and 9 (16.1%), with a Silk Vista Baby FD (Balt Extrusion). Twenty-two patients (39.3%) were treated with FDs exclusively; 32 (57.1%), with additional coils; 1, with a prior surgical clip (1.8%); and 1 (1.8%), with a WEB device. The anatomic distribution of FDs was as follows: intracranial ICA and/or M1 segment of the MCA ($n = 39$); intracranial VA, basilar artery, and/or the P1 segment of the posterior cerebral artery ($n = 7$); anterior communicating artery complex ($n = 6$); and more distal vessels ($n = 4$).

When we evaluated the status of the parent artery, interobserver agreement was 0.66 for NC-MRA, 0.67 for CE-MRA, and

Table 3: Four-fold table of CE-MRA using consensus evaluation for CE-MRA and DSA

	Consensus Evaluation for DSA	
	Pathologic (Stenosis or Occlusion)	Normal (Patent)
Consensus Evaluation for CE-MRA		
Pathologic (stenosis or occlusion)	13	19
Normal (patent)	1	23

1 for DSA. By means of the simplified 2-grade scale, κ was 0.65 for NC-MRA, 0.69 for CE-MRA, and 1 for DSA.

Table 1 shows the results of the assessment of parent artery patency with NC-MRA, CE-MRA, and DSA. Only 1 parent artery classified as patent on NC-MRA was classified as stenosis on DSA due to intimal hyperplasia (ie, 1 false-negative). Among the arteries classified as stenosis or occlusion on NC-MRA ($n = 20$), 7 were patent on DSA (ie, 7 false-positives). There were 35 true-negatives and 13 true-positives. By means of CE-MRA, 1 parent artery classified as patent was classified as stenosis on DSA (ie, 1 false-negative, which was the same for NC-MRA). Among the arteries classified as stenosis or occlusion on CE-MRA ($n = 32$), 19 were patent on DSA (ie, 19 false-positives). There were 23 true-negatives and 13 true-positives. Tables 2 and 3 present the corresponding 4-fold tables of these results.

By means of the 3-grade scale, intermodality agreement was 0.67 for NC-MRA/DSA and 0.35 for CE-MRA/DSA. With the simplified 2-grade scale, κ was 0.67 for NC-MRA/DSA and 0.33 for CE-MRA/DSA.

NC-MRA had a good specificity (0.83; 95% CI, 0.69–0.93) and PPV (0.65; 95% CI, 0.41–0.85), better than CE-MRA (0.55; 95% CI, 0.39–0.70; and 0.41; 95% CI, 0.24–0.59, respectively). Both had excellent sensitivity and NPV: 0.93; 95% CI, 0.66–1.00; and 0.97; 95% CI, 0.85–1.00, respectively, for NC-MRA and 0.93; 95% CI, 0.66–1.00; and 0.96; 95% CI, 0.79–1.00, respectively, for CE-MRA. Sensitivity, specificity, NPV, and PPV of NC-MRA for each separate device for patients treated with FD exclusively and those treated with an additional device are shown in Table 4.

DISCUSSION

Currently, 3D-TOF-MRA is the most frequently used noninvasive follow-up method for intracranial aneurysms treated using endovascular techniques.²⁰ However, for patients who underwent flow diversion, the magnetic and radiofrequency shielding causes a signal loss in the stent implantation area and often manifests as a false in-stent stenosis or interruption and, consequently, has poor specificity and PPV. To reduce these metallic artifacts, Oishi et al⁵ and Shao et al²² used, respectively, Silent MRA and 3D-T1 SPACE to assess the parent artery status. Regarding the patency of the stented arteries after FD treatment, these sequences were more accurate compared with 3D-TOF-MRA, but they were time-consuming and, consequently, more susceptible to motion artifacts. To reduce the duration of the sequences and reduce the possible motion artifacts and the total duration of the MR imaging examination procedure, we have optimized 2 sequences, which we use together: a 3D-TOF sequence with HyperSense and

Table 4: Diagnostic accuracies for parent artery patency of NC-MRA for each separate device, for patients treated with FD exclusively and those treated with additional device

	Pipeline Shield (n = 28)	Surpass Evolve (n = 19)	Silk Vista Baby (n = 9)	FD Exclusively (n = 22)	Additional Device (n = 34)
Specificity (95% CI)	0.96 (0.78–1.00)	0.57 (0.29–0.82)	1 (0.48–1.00)	0.87 (0.60–0.98)	0.81 (0.62–0.94)
PPV (95% CI)	0.80 (0.28–0.99)	0.45 (0.17–0.77)	1 (0.40–1.00)	0.78 (0.40–0.97)	0.55 (0.23–0.83)
Sensitivity (95% CI)	0.80 (0.28–0.99)	1 (0.48–1.00)	1 (0.40–1.00)	1 (0.59–1.00)	0.86 (0.42–1.00)
NPV (95% CI)	0.96 (0.78–1.00)	1 (0.63–1.00)	1 (0.48–1.00)	1 (0.75–1.00)	0.96 (0.78–1.00)

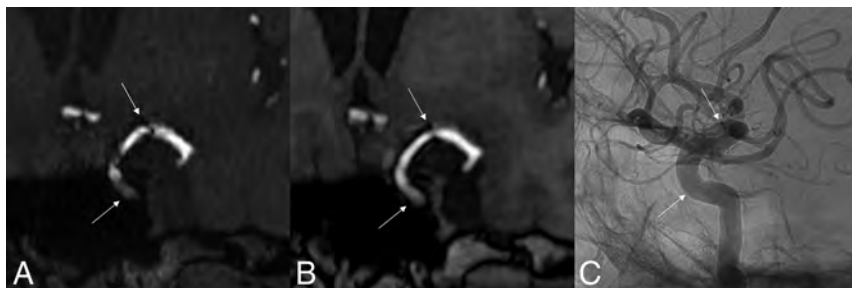


FIG 1. 3D-TOF with HyperSense MRA (A), LAVA-Flex MRA (B), and DSA (C) of a 61-year-old woman treated with a 4 × 25 Surpass Evolve FD located from the left ICA to the left MCA. There is a significant reduction in metal artifacts on the LAVA-Flex (OutPhase) sequence, which shows the absence of in-stent stenosis, confirmed by DSA. Note that there is not exactly the same projection between MRA and DSA. *White arrows* indicate the proximal and distal ends of the FDs.

a LAVA-Flex sequence, both without injection of a contrast agent. The LAVA-Flex sequence allows better study of the flow inside the stent, whereas the 3D-TOF sequence remains necessary to study aneurysmal occlusion because the LAVA-Flex sequence has not proved its effectiveness for this purpose.

Apart from increasing the signal-to-noise ratio, especially intravascular, the compressed sensing technique HyperSense allows a substantial reduction in the acquisition time of the 3D-TOF sequence. Ours had a total acquisition time of 2 minutes 59 seconds. This sequence can also be used to evaluate aneurysmal occlusion, analyze other arteries, but also, when artifacts are low, to evaluate the patency of the parent artery. The LAVA-Flex sequence allows, with a particularly short acquisition time of 1 minute 57 seconds, a 3D-T1-weighted sequence that is less sensitive to metallic artifacts, in particular on the out of phase sequence due to a shorter TE (Fig 1), with, however, a weaker intravascular signal due to an entry section phenomenon less marked than the 3D-TOF with HyperSense sequence. This can be explained by the shorter TR of the LAVA-Flex sequence compared with the 3D-TOF sequence; however, this short TR results in a remarkably decreased acquisition time, without hindering the in-stent flow analysis. MIP reformats of LAVA-Flex MRA are useful to evaluate the caliber of the parent vessel but must always be analyzed in conjunction with the native sections because the selection of the most intense voxels by the MIP algorithm hinders the visualization of the stent, whose signal is low. The total acquisition time for these 2 sequences was, therefore, 4 minutes 56 seconds, more than 2 times shorter than Silent MRA or 3D-T1 SPACE combined with 3D-TOF.

In this study, the joint use of 3D-TOF with HyperSense MRA and LAVA-Flex MRA allowed us to obtain a NC-MRA specificity of 0.83 (95% CI, 0.69–0.93) and a PPV of 0.65 (95% CI, 0.41–0.85) (Fig 2), which were better than those of CE-MRA (0.55; 95% CI, 0.39–

0.70; and 0.41; 95% CI, 0.24–0.59, respectively) in the evaluation of the parent artery patency. This result can be explained by an analysis of the TRICKS MRA sequence generally using background-subtracted volumes, which do not permit stent visualization, as well as the use of a delayed-MRA sequence, and not an arterial CE-MRA sequence. Finally, the absence of a contrast-enhanced 3D-T1-weighted sequence can also partially explain these results. With NC-MRA and CE-MRA, we had only 1 false-negative result, which can probably be explained by the delay between MR imaging and arteriography, 4 weeks for this patient, who had

stopped the dual antiplatelet therapy on his own after the MR imaging examination, 3 months after FD placement at the M1–M2 junction. Thus, the in-stent stenosis could have developed in the meantime. The sensitivity and NPV remained excellent for NC-MRA (0.93; 95% CI, 0.66–1.00; and 0.97; 95% CI, 0.85–1.00, respectively) and CE-MRA (0.93; 95% CI, 0.66–1.00; and 0.96; 95% CI, 0.79–1.00, respectively).

The specificity and PPV tended to be lower for Pipeline Shield FDs and even lower for Surpass Evolve FDs, probably due to more pronounced metallic artifacts (Fig 3). Unlike the criterion standard DSA, MRA is susceptible to the dissimilarities between flow diverters. Halitcan et al¹⁵ suggested that the key factor was the alloy used for the construction of the FDs, with nitinol-based devices being responsible for fewer metallic artifacts. While we agree that this factor influences the extent of artifacts, the marked difference between the artifacts created by Pipeline Shield FDs and Surpass Evolve FDs, which are both cobalt-chromium devices, suggests that other important factors were probably involved, such as the number of wires composing the FD combined with the thickness of the wire. Indeed, Surpass Evolve FDs are made of 64 wires (except for 2.5 mm diameter FD), while Pipeline Shield FDs are made of 48 wires, with an equivalent wire thickness (~28 and ~30 μm, respectively). In addition, the tungsten used in combination with platinum for the visibility of cobalt-chromium devices used in this study (while nitinol devices used only platinum) may also play a role.

It is important to keep in mind the shortcomings of each FD in MR imaging when interpreting the parent artery patency, so as not to erroneously conclude in-stent stenosis. Specificity and PPV tended to be lower for patients treated with additional devices than for those treated with FDs exclusively, an outcome expected due to the additional artifacts created by coils, the WEB, or surgical clips. Indeed, these artifacts can appear as false stenosis (ie, false-positives),

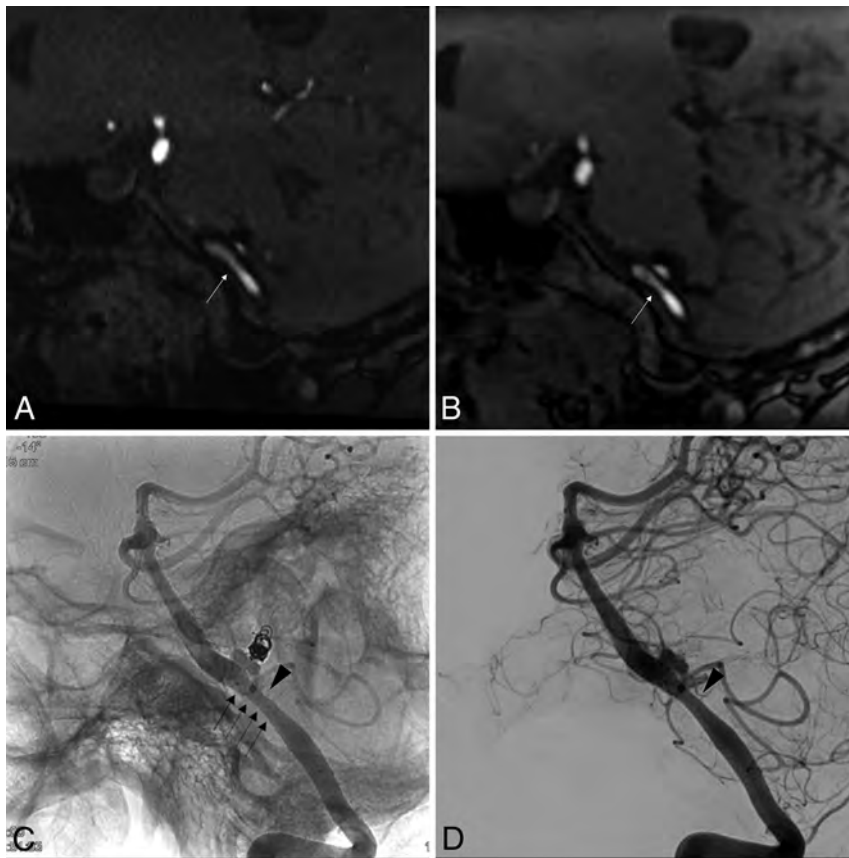


FIG 2. In-stent stenosis in a 50-year-old woman treated with a 5×15 Surpass Evolve FD placed in the left VA. This was a complementary embolization of a left PICA aneurysm, initially revealed by a subarachnoid hemorrhage 10 years earlier and treated by coiling at that time. 3D-TOF with HyperSense MRA (A) and LAVA-Flex MRA (Outphase) (B) demonstrates moderate in-stent stenosis (white arrows) predominating a few millimeters upstream of the neck of the still patent aneurysm, 6 months after placement of the FD. Confirmation of a moderate in-stent stenosis (black arrowhead) on angiography without (C) and with (D) digital subtraction. The black arrows show the limits of the FD metallic mesh.

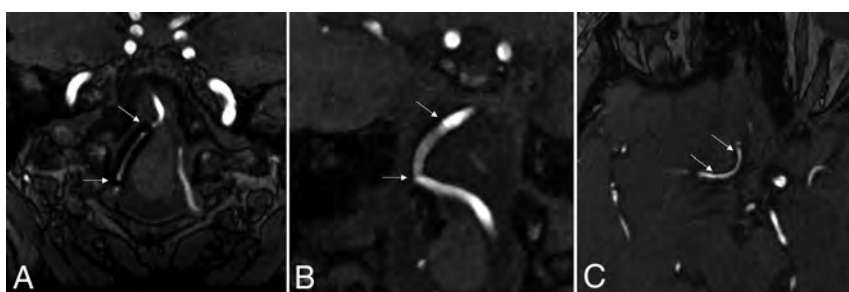


FIG 3. 3D-TOF with HyperSense MRA comparison of artifacts created by the 3 types of FDs used in our study. A, A 68-year-old woman treated with a Surpass Evolve FD (3.25×17 mm) located in the right VA. B, A 61-year-old woman treated with a Pipeline Shield FD (3.5×18 mm) located from the left VA to the basilar artery. C, A 52-year-old woman treated with a Silk Vista Baby FD (2.5×20 mm) located in the right anterior cerebral artery (A1–A2). The extent of the metallic artifacts is large for the Surpass Evolve FD, small for the Pipeline Shield FD, and minimal for the Silk Vista Baby FD. White arrows indicate the proximal and distal ends of the FDs.

thus reducing specificity and PPV. MR imaging is essential for the evaluation of potential ischemic and hemorrhagic complications after FD placement and is a relatively reliable screening test for in-

stant stenosis because of its excellent sensitivity and NPV. However, DSA remains the criterion standard in parent artery patency evaluation, especially when additional material like coils or surgical clips is used. It, thus, appears useful to systematically perform NC-MRA sequences in addition to classic parenchymal sequences to evaluate in-stent flow. Ideally, an initial concomitant DSA control would indicate any false-positive or false-negative results, which could serve as reference in the long-term follow-up of intracranial stent evaluation with NC-MRA.

Our study has some limitations: First, the small number of patients ($n = 56$) included. However, this number is comparable with that in the other 2 main studies focused on the analysis of the patency of the parent artery (40 for Shao et al²² and 78 for Oishi et al⁵). Besides, the sample size for each kind of FD is small, possibly introducing systematic error. Second, MR imaging and DSA were not systematically performed on the same day, with a maximum interval of 4 weeks and, therefore, may not reflect the exact same conditions concerning parent vessel status. Third, CTA was not evaluated in our study, notably for patients treated with FDs exclusively for whom it could be a valid option. Although it shares the risks of iodinated contrast media and ionizing radiation of DSA, it is a noninvasive examination that does not share the potential risks of puncture site and neurologic complications. Fourth, interobserver agreement ranged from 0.6 to 0.79 for the NC-MRA and CE-MRA, corresponding to “substantial agreement” and not “almost perfect agreement.”²⁴ These differences mainly concerned the analysis of Surpass Evolve FDs, which produce more pronounced metallic artifacts than the other FDs studied, thus making interpretation more difficult, especially in the presence of additional material like coils and clips.

CONCLUSIONS

NC-MRA can be used for noninvasive especially long-term follow-up of intracranial aneurysms treated by FDs. The combined use of LAVA-Flex and 3D-TOF with HyperSense sequences is accurate compared with DSA and allows

monitoring the status of the parent artery and aneurysmal occlusion. These two sequences could be useful tools, especially in the long- and very-long-term follow-up of these devices. The total acquisition time with these 2 sequences is reduced by at least half compared with Silent MRA or 3D-T1 SPACE combined with 3D-TOF. Specificity and PPV depend on the type of FD and whether patients are treated with additional devices (coils, intrasaccular flow disruptors, surgical clips).

Disclosure forms provided by the authors are available with the full text and PDF of this article at www.ajnr.org.

REFERENCES

- Nelson PK, Lylyk P, Szikora I, et al. **The Pipeline Embolization Device for the intracranial treatment of aneurysms trial.** *AJNR Am J Neuroradiol* 2011;32:34–40 CrossRef Medline
- Kallmes DF, Hanel R, Lopes D, et al. **International retrospective study of the Pipeline Embolization Device: a multicenter aneurysm treatment study.** *AJNR Am J Neuroradiol* 2015;36:108–15 CrossRef Medline
- Brinjikji W, Murad MH, Lanzino G, et al. **Endovascular treatment of intracranial aneurysms with flow diverters: a meta-analysis.** *Stroke* 2013;44:442–47 CrossRef Medline
- Dandapat S, Mendez-Ruiz A, Martinez-Galdamez M, et al. **Review of current intracranial aneurysm flow diversion technology and clinical use.** *J Neurointerv Surg* 2021;13:54–62 CrossRef Medline
- Oishi H, Fujii T, Suzuki M, et al. **Usefulness of silent MR angiography for intracranial aneurysms treated with a flow-diverter device.** *AJNR Am J Neuroradiol* 2019;40:808–14 CrossRef Medline
- O'Kelly CJ, Spears J, Chow M, et al. **Canadian experience with the Pipeline Embolization Device for repair of unruptured intracranial aneurysms.** *AJNR Am J Neuroradiol* 2013;34:381–87 CrossRef Medline
- Briganti F, Napoli M, Leone G, et al. **Treatment of intracranial aneurysms by flow diverter devices: long-term results from a single center.** *Eur J Radiol* 2014;83:1683–90 CrossRef Medline
- Kallmes DF, Brinjikji W, Cekirge S, et al. **Safety and efficacy of the Pipeline embolization device for treatment of intracranial aneurysms: a pooled analysis of 3 large studies.** *J Neurosurg* 2017;127:775–80 CrossRef Medline
- Zhang X, Lv N, Wang C, et al. **Late recurrence of a completely occluded large intracranial aneurysm treated with a Tubridge flow diverter.** *Neurointerv Surg* 2017;9:e6 CrossRef Medline
- Trivelato FP, Ulhoa AC, Rezende MT, et al. **Recurrence of a totally occluded aneurysm after treatment with a Pipeline Embolization Device.** *BMJ Case Rep* 2018;2018:bcr-2018013842 CrossRef Medline
- Soize S, Gawlitza M, Raoult H, et al. **Imaging follow-up of intracranial aneurysms treated by endovascular means: why, when, and how?** *Stroke* 2016;47:1407–12 CrossRef Medline
- Gupta R, Ogilvy CS, Moore JM, et al. **Proposal of a follow-up imaging strategy following Pipeline flow diversion treatment of intracranial aneurysms.** *J Neurosurg* 2018;131:32–39 CrossRef Medline
- Becske T, Brinjikji W, Potts MB, et al. **Long-term clinical and angiographic outcomes following Pipeline Embolization Device treatment of complex internal carotid artery aneurysms: five-year Results of the Pipeline for Uncoilable or Failed Aneurysms Trial.** *Neurosurgery* 2017;80:40–48 CrossRef Medline
- Deutschmann HA, Wehrschuetz M, Augustin M, et al. **Long-term follow-up after treatment of intracranial aneurysms with the Pipeline Embolization Device: results from a single center.** *AJNR Am J Neuroradiol* 2012;33:481–86 CrossRef Medline
- Halitcan B, Bige S, Sinan B, et al. **The implications of magnetic resonance angiography artifacts caused by different types of intracranial flow diverters.** *J Cardiovasc Magn Reson* 2021;23:69 CrossRef Medline
- Attali J, Benaissa A, Soize S, et al. **Follow-up of intracranial aneurysms treated by flow diverter: comparison of three-dimensional time-of-flight MR angiography (3D-TOF-MRA) and contrast-enhanced MR angiography (CE-MRA) sequences with digital subtraction angiography as the gold standard.** *J Neurointerv Surg* 2016;8:81–86 CrossRef Medline
- Boddu SR, Tong FC, Dehkharghani S, et al. **Contrast-enhanced time-resolved MRA for follow-up of intracranial aneurysms treated with the Pipeline Embolization Device.** *AJNR Am J Neuroradiol* 2014;35:2112–18 CrossRef Medline
- Patzig M, Forbrig R, Ertl L, et al. **Intracranial aneurysms treated by flow-diverting stents: long-term follow-up with contrast-enhanced magnetic resonance angiography.** *Cardiovasc Intervent Radiol* 2017;40:1713–22 CrossRef Medline
- McGuinness BJ, Memon S, Hope JK. **Prospective study of early MRI appearances following flow-diverting stent placement for intracranial aneurysms.** *AJNR Am J Neuroradiol* 2015;36:943–48 CrossRef Medline
- Ahmed SU, Mocco J, Zhang X, et al. **MRA versus DSA for the follow-up imaging of intracranial aneurysms treated using endovascular techniques: a meta-analysis.** *J Neurointerv Surg* 2019;11:1009–14 CrossRef Medline
- Kaufmann TJ, Huston J, Mandrekar JN, et al. **Complications of diagnostic cerebral angiography: evaluation of 19,826 consecutive patients.** *Radiology* 2007;243:812–19 CrossRef Medline
- Shao Q, Wu Q, Li Q, et al. **Usefulness of 3D T1-SPACE in combination with 3D-TOF MRA for follow-up evaluation of intracranial aneurysms treated with Pipeline Embolization Devices.** *Front Neurol* 2020;11:542493 CrossRef Medline
- Irie R, Amemiya S, Ueyama T, et al. **Accelerated acquisition of carotid MR angiography using 3D gradient-echo imaging with two-point Dixon.** *Neuroradiology* 2020;62:1345–49 CrossRef Medline
- Landis JR, Koch GG. **The measurement of observer agreement for categorical data.** *Biometrics* 1977;33:159–74 CrossRef Medline

Safety, Efficacy, and Durability of Stent-Assisted Coiling Treatment of M2 (Insular) Segment MCA Aneurysms

 K. Aydin,  M. Berdikhojayev,  F. Cay,  M. Barburolu,  S. Nurzhan,  S. Aygun,  S. Sencer, and  A. Arat



ABSTRACT

BACKGROUND AND PURPOSE: Most distal MCA aneurysms are located within the insular segment, which lies between the limen insulae and circular sulcus. However, experience is limited in the microsurgical and endovascular management of insular segment MCA aneurysms. In this multicenter retrospective case series, we aimed to investigate the safety, efficacy, and durability of stent-assisted coiling for treatment of insular segment MCA aneurysms.

MATERIALS AND METHODS: A retrospective review was performed to identify patients with insular MCA aneurysms that were treated with stent-assisted coiling. The technical success of the procedures and the initial and follow-up clinical and angiographic outcomes were assessed. Periprocedural and delayed complications were reviewed.

RESULTS: Twenty-seven aneurysms in 27 patients with a mean age of 53.3 (SD,11.3) years were included. The mean size of the aneurysms was 6.3 (SD 2.6) mm. Endovascular procedures were successfully performed in all patients. Immediate postprocedural angiography revealed complete aneurysm occlusions in 81.5%. Periprocedural complications developed in 7.4% without causing permanent morbidity. A delayed thromboembolic complication resulted in a minor permanent morbidity in 1 patient (3.7%). There was no mortality. The mean duration of angiographic follow-up was 19.5 (SD, 9.8) months. The last follow-up examinations showed complete occlusion in 92.6%. During the follow-up period, none of the treated aneurysms showed recanalization.

CONCLUSIONS: The results of this study demonstrate that stent-assisted coiling with a low-profile self-expandable stent is a feasible and relatively safe technique for endovascular treatment of insular segment complex MCA aneurysms. Additionally, it provides an effective and durable treatment for insular MCA aneurysms.

MCA aneurysms constitute 18%–20% of all intracranial aneurysms.^{1,2} Most MCA aneurysms are located at the bifurcation or trifurcation of the MCA in the proximal Sylvian fissure. Only 1.1%–6% of MCA aneurysms are located distal to the MCA bifurcation.^{3–8} Most distal MCA aneurysms are located in the distal Sylvian fissure and along the insular branches that run between the limen insulae and circular sulcus. Because these are relatively rare vascular lesions, experience is limited regarding the microsurgical or endovascular management of insular segment MCA aneurysms.^{3,4,8,9} The microsurgical treatment of distal MCA aneurysms is demanding compared with those located

at the bifurcation. Because insular segment MCA aneurysms are embedded in the insular sulci, deep in the Sylvian cistern, it may be difficult to identify and access them during microsurgery.^{3,8} Endovascular treatment of insular segment MCA aneurysms has not been specifically studied previously.⁹

Because the greatest branching of the MCA occurs in the insular segment, protection of the MCA branches supplying eloquent cortical regions is important during microsurgery or endovascular treatment. The stent-assisted coiling technique has been developed for the endovascular treatment of wide-neck intracranial aneurysms.^{10,11} Self-expandable stents dedicated to intracranial use have enabled the coiling of wide-neck and complex bifurcation aneurysms. Deployment of a stent into a bifurcation creates a scaffold to protect the vessels during the coiling of a complex bifurcation aneurysm. The risk of vessel trauma during the catheterization and the navigation into small-sized insular branches are technical and safety concerns for endovascular treatment of insular segment MCA aneurysms. The introduction of low-profile self-expandable stents has been revolutionary in the endovascular surgery of intracranial aneurysms. Low-profile stents can be delivered through microcatheters with an internal

Received December 10, 2021; accepted after revision January 17, 2022.

From the Department of Interventional Neuroradiology (K.A., S.A.), Koç University Hospital, Topkapi, Istanbul, Turkey; Department of Neuroradiology (K.A., M. Barburolu, S.S.), Istanbul Faculty of Medicine, Capa, Istanbul University, Istanbul, Turkey; Department of Neurosurgery (M. Berdikhojayev, S.N.), JSC Central Hospital, Almaty City, Kazakhstan; and Department of Radiology (F.C., A.A.), Hacettepe University Medical School, Hacettepe Hospitals, Sıhhiye, Ankara, Turkey.

Please address correspondence to Kubilay Aydin, MD, Koç University Hospital, Department of Interventional Neuroradiology, 34010 Topkapi, Istanbul, Turkey; e-mail: dr.aydink@gmail.com

<http://dx.doi.org/10.3174/ajnr.A7461>

diameter of 0.0165 inches, which facilitates the safe catheterization and easy navigation in small-sized vessels.¹¹⁻¹⁵ Moreover, low-profile stents can be implanted in arteries with diameters as small as 0.8 mm.^{12,13} Thus, the introduction of low-profile self-expandable stents has expanded the scope of the endovascular surgery to include the treatment of aneurysms located distal to the circle of Willis.

In this multicenter retrospective study, we aimed to investigate the feasibility, safety, and efficacy of the stent-assisted coiling procedure using low-profile self-expandable stents for the treatment of insular segment MCA aneurysms. We also assessed the long-term clinical and angiographic outcomes.

MATERIALS AND METHODS

Study Design

After we obtained the local ethics committee approval of Istanbul Faculty of Medicine, a multicenter retrospective review was performed to identify patients with an insular segment MCA aneurysm treated with the stent-assisted coiling technique between January 2016 and January 2021. Stent-assisted coiling was performed in the treatment of aneurysms with a dome/neck ratio of <2 or a neck diameter of >4 mm, a sac morphology not suitable for primary coiling or recanalized aneurysms after primary coiling or balloon-assisted coiling. For the definition of the insular segment, the MCA was divided into 4 anatomic segments as described by Gibo et al.¹⁶ The sphenoidal or horizontal (M1) segment begins from the internal carotid bifurcation and terminates at the site of a 90° turn called the genu. The insular (M2) segment begins at the genu and ends at the circular sulcus of the insula. On the basis of this anatomic classification, the MCA aneurysms located between the MCA genu and circular sulcus were defined as insular segment (M2) aneurysms and were included in this study.

The medical records and radiologic images of the patients with insular aneurysms were collected. Three experienced endovascular surgeons (K.A., M. Berdikhojaye, and A.A.) assessed the surgery reports, medical charts, and radiologic images of the patients. Patient demographics and presenting symptoms, the size of the aneurysms, treatment history, technical and clinical complications, and the degree of aneurysm occlusion were recorded. Patient consent was not sought for this retrospective study.

Endovascular Procedures

Patients were pretreated with 75 mg of clopidogrel and 300 mg of aspirin daily for at least 5 days before the operation. Platelet function tests were performed before the operation (Multiplate Analyzer [Roche] or VerifyNow [Accumetrics]). Patients with a poor response to clopidogrel (area under curve of >52 or platelet inhibition ratio of $<40\%$) were switched to prasugrel with a starting daily dosage of 10 mg or ticagrelor with a starting daily dosage of 2×90 mg. Endovascular procedures were performed with the patient under general anesthesia. Systemic anticoagulation was initiated at the beginning of the procedure with a bolus dose of 50- to 70-IU/kg heparin. The bolus dose was followed by an infusion to maintain an activated clotting time between 250 and 280 seconds during the operation. A 6F guiding sheath (Neuron

MAX [Penumbra], AXS Infinity LS [Stryker]) or a 7F guiding catheter (Fubuki [Asahi Intecc Medical]) was positioned in the distal cervical segment of the ICA. A bolus dose of 2 mg of nimodipine diluted in 140 mL of 0.9% NaCl solution was infused through the guiding sheath for 10 minutes to prevent vasospasms during the procedure. The insular branch arising from the neck of the aneurysm (stem artery or cortical branch) was catheterized with a stent delivery 0.017-inch microcatheter (Headway-17 [MicroVention], Vasco 10 [Balt], or SL-10 [Stryker Neurovascular]). Another 0.017-inch microcatheter was jailed inside the aneurysm sac (Headway 17 or Echelon 10 [Medtronic]) for coiling if the plan was to implant a braided stent.

A low-profile self-expandable braided or laser-cut open-cell stent was deployed into the insular branch, extending proximally to the related MCA trunk or the sphenoidal (M1) segment of the MCA. Following the sealing of the aneurysm neck with the implanted stent, the aneurysm sac was coiled using bare platinum coils. In some cases in which we used a low-profile open-cell stent, the stent delivery catheter was used for coiling after the deployment of the stent. Dual antiplatelet treatment was continued for 3–6 months after the endovascular procedure, and the patients were switched to 100 mg of aspirin thereafter.

Complications

Any intraprocedural adverse event that caused the failure or modification of the stent-assisted coiling procedure was defined as a technical complication regardless of whether it resulted in clinical symptoms. Complications that developed during the procedure or within 7 days following the procedure were defined as periprocedural complications. Complications that developed >7 days after the procedure were considered delayed complications.

Angiographic Follow-up

Immediate postprocedural DSA images were obtained to assess the aneurysm occlusion status according to the Raymond-Roy classification.¹⁷ The first follow-up DSA examinations were performed 6–15 months after the procedures. A second follow-up DSA was performed between 24 and 36 months postoperatively. The follow-up DSA images were evaluated by 3 experienced surgeons to assess the filling status of the aneurysms, patency of parent vessels, and the development of in-stent stenosis. On the follow-up imaging, progressive thrombosis was defined as an improvement in the Raymond-Roy classification. Recanalization was defined as a deterioration in the Raymond-Roy classification.

Clinical Follow-up

The patients' neurologic statuses were evaluated using the mRS before the endovascular procedure, at discharge, and during the clinical follow-up. The first clinical follow-up was performed 1–2 months after discharge. Additional clinical follow-ups were performed during every angiographic follow-up.

Statistical Analysis

The descriptive statistical analyses in this study were performed using SPSS Statistics 21.0 (IBM). Continuous variables were reported as mean (SD). Categorical variables were reported as proportions.

Table 1: Summary of the patient demographics and aneurysm characteristics

Demographics	
Mean age (yr)	53.3 (SD, 11.3)
Sex	
Female	19 (70.4%)
Male	8 (29.6%)
Aneurysm location	
Right superior MCA trunk	6 (22.2%)
Right inferior MCA trunk	8 (29.6%)
Left superior MCA trunk	9 (33.3%)
Left inferior MCA trunk	4 (14.8%)
Aneurysm size (maximal diameter)	
2–4 mm	7 (25.9%)
5–7 mm	14 (51.9%)
8–12 mm	5 (18.5%)
13–15 mm	1 (3.7%)
Aneurysm neck diameter (mm) ^a	3.8 (SD, 1.1) (2.1–6.7)
Diameter of the artery at the proximal end of stent (mm) ^a	2.1 (SD, 0.22) (1.7–2.8)
Diameter of the artery at the distal end of stent (mm) ^a	1.6 (SD, 0.17) (1.3–2.0)

^a Data are given as the mean value (SD) (minimum-maximum values).

Table 2: Stents used in the endovascular procedures

Deployed Stent	No. of Patients
LEO Baby (Balt)	20 (74.1%)
Neuroform Atlas (Stryker)	5 (18.5%)
LVIS EVO (MicroVention)	1 (3.7%)
Accero (Accandis)	1 (3.7%)

RESULTS

Patients and Aneurysms

Twenty-seven patients (19 women, 70.4%) with an insular segment MCA aneurysm were included in this study. The mean age of the patients was 53.3 (SD, 11.3) years (range, 34–70 years). The mean size of the aneurysms was 6.3 (SD, 2.6) mm (range, 3–15 mm) (Table 1). All aneurysms had a saccular morphology. One of the 27 aneurysms had ruptured 16 weeks before the endovascular treatment, and the patient with the ruptured aneurysm was referred to JSC Central Hospital (Almaty City) center for endovascular treatment. Another patient had a recanalized aneurysm that had been treated previously with a primary coiling procedure. The preoperative mRS score of 26 patients was zero. The preoperative mRS score of 1 patient was 2 due to the recent subarachnoid hemorrhage.

Immediate Angiographic Results

In most of the patients (81.5%), a self-expandable nitinol braided stent was implanted (Table 2 and Fig 1). A laser-cut open-cell stent was implanted in 5 patients (18.5%). The immediate postprocedural DSA images revealed complete aneurysm occlusion in 22 patients (81.5%) and a neck remnant in 4 patients (14.8%). In 1 patient (3.7%), the aneurysm sac was intentionally partially coiled to maintain the patency of a stem artery that was filling from the superior-medial wall of the aneurysm sac (Fig 2).

Complications

Catheterization of side branches and the aneurysm sac, stent deployment, and coiling procedures were successfully completed

in all patients. We did not have any technical complications. There was no mortality in this study. A delayed thromboembolic complication resulted in minor permanent morbidity in 1 patient (3.7%).

Periprocedural complications developed in 2 patients (7.4%) without causing permanent morbidity. The intraprocedural control DSA images of one of the patients revealed the development and formation of an in-stent thrombus, and in this patient, an intra-arterial bolus infusion of 25 µg/kg of tirofiban through the microcatheter achieved complete resolution of the thrombus. The periprocedural complication in this patient did not cause any symptoms, and the follow-up MR imaging performed 48 hours after the endovascular procedure did not reveal any ischemic lesion. The mRS score of this patient was zero at discharge. Another patient developed hemiparesis 6 hours after the completion of the endovascular procedure. An emergency DSA revealed an occlusion of the branch that was jailed by the deployed stent. An intra-arterial infusion of tirofiban through a 0.017-inch microcatheter achieved a resolution of the thrombus and complete patency of the side branch. The mRS score of this patient was zero at 1-month follow-up, and she remained asymptomatic on further follow-up. We also observed a delayed thromboembolic complication in another patient (3.7%). This patient developed dysphasia 2 weeks after the treatment of a left insular MCA aneurysm that was located in the territory of the superior trunk. Cranial MR imaging of this patient revealed an infarction with a diameter of 2 cm in the cortex of the left frontal operculum. The patient's dysphasia regressed considerably during the following 8 weeks, and the mRS score at the last follow-up was 1.

Follow-up

All patients underwent at least 1 follow-up DSA examination. The mean angiographic follow-up duration was 19.5 (SD, 9.8) months (range, 6–36 months). Fifteen patients (55.6%) underwent 2 follow-up DSAs, and the remaining 12 patients had only 1 follow-up angiography. The final follow-up angiography revealed complete occlusion of the aneurysms in 25 patients (92.6%) and neck filling in 2 patients (7.4%) (Fig 3). None of the treated aneurysms showed recanalization. One aneurysm with a residual sac filling found on the immediate postprocedural DSA eventually progressed to complete occlusion, which was seen on the 36-month second follow-up angiography (Fig 2). Another aneurysm with a neck filling on the immediate postprocedural DSA progressed to complete occlusion on the first follow-up DSA performed 7 months after the endovascular procedure. Two aneurysms that had a residual filling of the neck on the immediate postprocedural DSA remained stable on the first follow-up angiographies that were performed 6 and 9 months after the endovascular procedures. No patient required retreatment.

Twenty-five patients had mRS scores of zero at the final clinical follow-up. One patient had a preprocedural mRS score of 2 that did not change during the follow-up period. One patient who developed a delayed ischemic complication had an mRS score of 1 at the final clinical follow-up.

DISCUSSION

Among MCA aneurysms, insular segment aneurysms have been analyzed within the context of distal MCA aneurysms. Insular

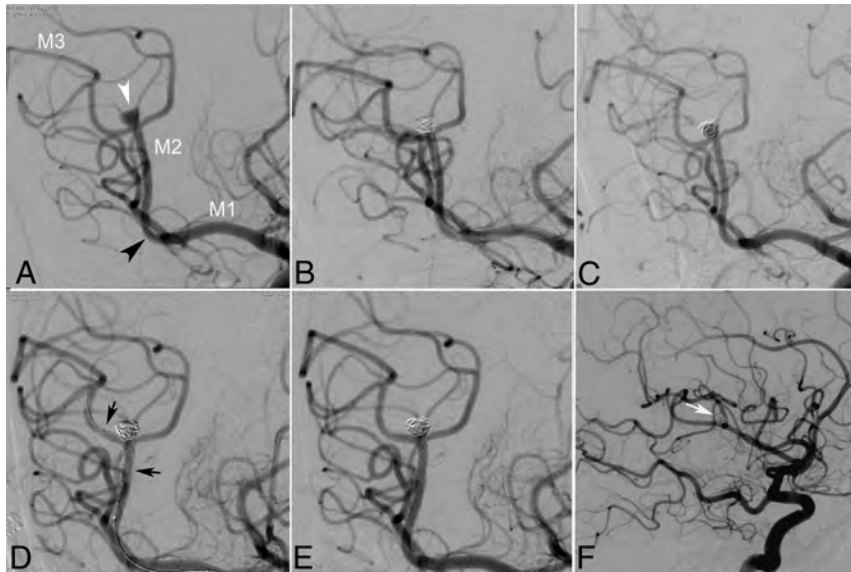


FIG 1. An adult patient with a recurrent right insular segment MCA aneurysm. *A*, DSA image shows a saccular aneurysm located distal to the MCA genu (*arrowhead*) in the insular segment of the right MCA. Two cortical branches arise from its neck. *B*, Postprocedural DSA image after the primary coiling procedure reveals complete occlusion of the aneurysm. *C*, Follow-up DSA after the primary coiling shows coil compaction and recanalization of the sac. *D*, The immediate postprocedural DSA image that was obtained following the stent-assisted coiling shows complete occlusion of the aneurysm. A self-expandable stent is deployed into one of the cortical branches (*arrows*). *E* and *F*, 36-month follow-up DSA images demonstrate the stable occlusion of the aneurysm (*white arrow*) and the patency of the cortical branches arising from its neck.

segment aneurysms constitute most distal MCA aneurysms.¹⁸ Microsurgical management of insular segment MCA aneurysms remains demanding. The difficulty in localizing these aneurysms deep in the Sylvian cistern requires navigation using special techniques. Furthermore, because they frequently have a complex morphology, the microsurgical management of these insular aneurysms often necessitates trapping and bypass.^{3,18} Although insular segment MCA aneurysms were included in the previous case series presenting the endovascular results of distal intracranial aneurysms, there has not been a prior report focusing on the endovascular treatment of insular aneurysms. This may also be related to the reluctance of performing endovascular treatment in distal, tortuous arteries with an eloquent supply.

Endovascular surgery has long been considered unfavorable for MCA aneurysms on the basis of their complex neck morphology incorporating the MCA branches, the complexity of the anatomy of the MCA branches that are difficult to decipher on 2D angiography images, and the requirement for catheterization of the distal and small-sized MCA branches.^{5,7,19} However, in the past decade, the advances in 3D angiography and the improvements in the microcatheter, coil, and stent technologies, especially introduction of low-profile self-expandable stents, have expanded the scope of endovascular surgery to include the treatment of complex intracranial aneurysms located distal to the circle of Willis.^{13,20,21} 3D angiographic imaging techniques have facilitated the deciphering of the complex anatomic relationships between the neck of MCA aneurysms and the incorporating MCA branches. Improvements in the hydrophilic coating and microcatheter design technologies

have introduced the low-profile microcatheters with enhanced flexibility and have allowed less traumatic and easier navigation in small-sized, distal, tortuous vessels. Last, low-profile, self-expandable stents have enabled the coiling of wide-neck aneurysms located in small-sized distal vessels.

The major bifurcation of the MCA gives rise to 2 or 3 trunks. The insular segment of the MCA includes the trunks that lie on and supply the insula. The greatest branching of the MCA occurs at the anterior part of the insula, which is distal to the genu.¹⁶ Six to 11 stem arteries arise from the trunks, and each stem artery gives rise to 1–5 cortical arteries. Therefore, there are many bifurcation points in the insular segment, and the insular segment MCA aneurysms usually arise from these bifurcations. Therefore, insular segment MCA aneurysms frequently have a complex neck morphology that incorporates the stem arteries or proximal parts of the cortical branches. The protection of the incorporating branches is a technical concern for the treatment of insular segment aneurysms. In our cases, we used low-profile, self-expandable stents to protect the incorporating branches during coiling of insular segment aneurysms. In the current study, the stent deployment and coiling procedures were successfully completed in all patients. We did not observe any technical complications. Thus, the results of the current study demonstrate that stent-assisted coiling with low-profile, self-expandable stents is a feasible technique for the endovascular treatment of insular segment MCA aneurysms.

In the current study, coiling with the assistance of a low-profile stent achieved immediate postprocedural complete aneurysm occlusion in 81.5% of patients. We observed a complete aneurysm occlusion rate of 92.6% during a mean follow-up period of 19.5 months. The angiographic results of the current study indicate that stent-assisted coiling provides an effective and durable treatment for MCA aneurysms located within the M2 segment. In a meta-analysis, Brinjikji et al²² included 12 case series to investigate the angiographic outcomes of the MCA aneurysms treated with various endovascular methods. Approximately 50% of the aneurysms had been ruptured. They found that 82.4% of the MCA aneurysms were completely occluded during an immediate postprocedural angiographic follow-up. However, 9.6% of the aneurysms showed recanalization that required retreatment during the follow-up period. Most aneurysms included in this meta-analysis had been treated by primary coiling, and in only 20.4% of the cases had adjunctive endovascular devices such as stents been used. Several studies have demonstrated that the recurrence risk of aneurysms treated with stent-assisted coiling is lower than that of aneurysms treated with simple coiling or

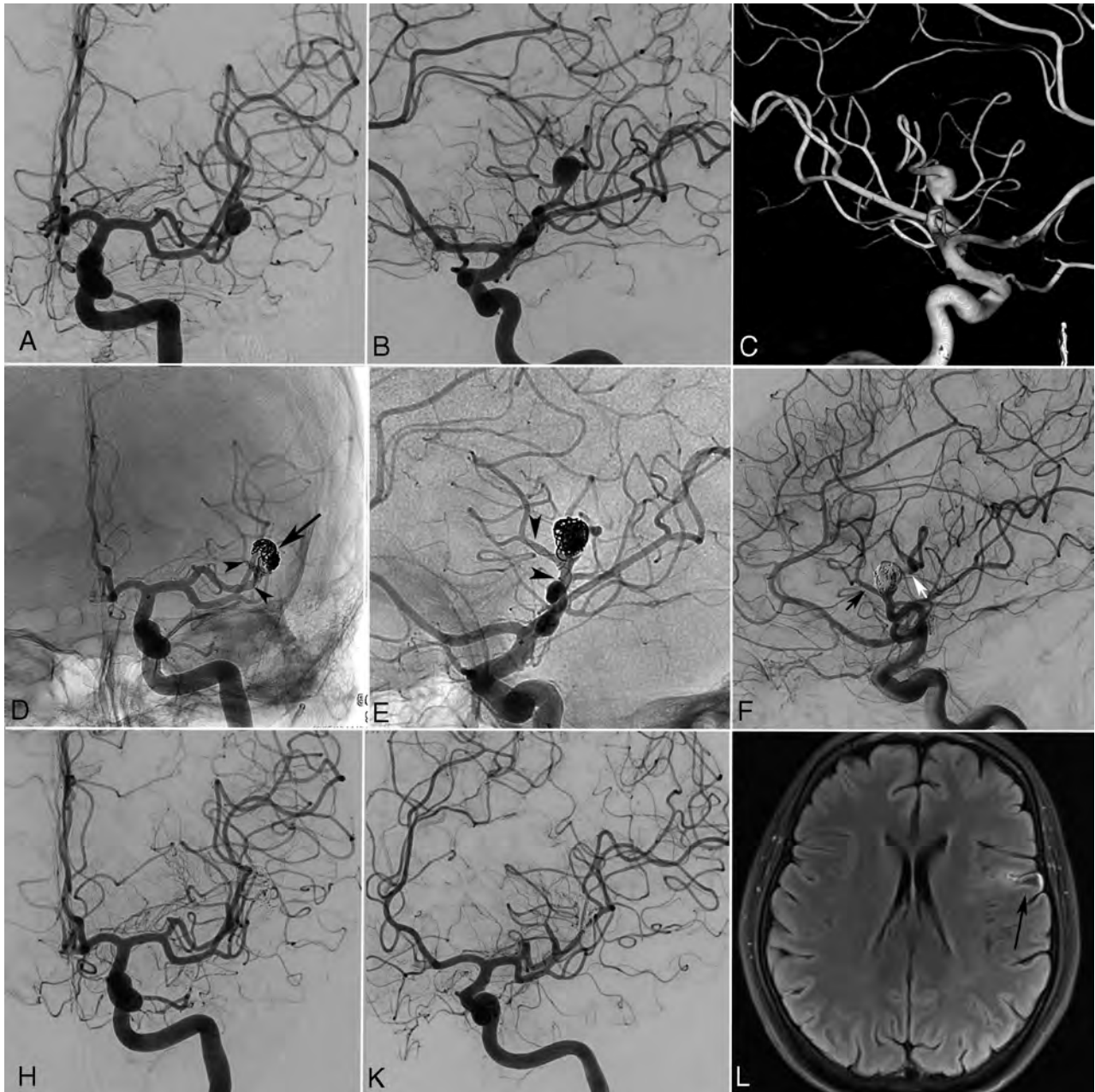


FIG 2. An adult patient with a left insular segment MCA aneurysm. A–C, Preprocedural DSA and 3D reconstructed angiography images show an insular segment MCA aneurysm with a very complex morphology. Two cortical stem arteries of the superior trunk originate from the neck and the superior-medial wall of the aneurysm sac. D and E, Immediate postprocedural nonsubtracted angiography images show the deployment of a self-expandable braided stent (*arrowheads*) into the stem artery that arises from the neck, extending proximally to the superior trunk. The sac of the aneurysm is partially coiled. Only the lateral compartment of the aneurysm sac is coiled to sustain the patency of the stem artery arising from the superior-medial wall of the sac. The *arrow* shows the coil mesh inside the aneurysm sac. F, Immediate postprocedural DSA image shows the patency of 2 stem arteries that arise from the neck (*black arrow*) and sac of the aneurysm (*white arrow*). H and K, Thirty-six-month follow-up DSA images demonstrate complete occlusion of the aneurysm. L, Follow-up MR image (FLAIR) shows a small cortical infarction (*arrow*) in the left frontal operculum. The mRS score of the patient was 1 during the clinical follow-up.

balloon-remodeling techniques.^{23,24} In an animal study, Raymond et al²⁴ showed that stent-assisted coiling provided more stable treatment than simple coiling. Deployment of a self-expandable stent into the parent artery provides a mechanical scaffold that assists in achieving a dense coil mesh inside the aneurysm sac, which prevents recanalization. Furthermore, self-expandable stents have hemodynamic effects that remodel the

arterial blood flow in the parent artery and reduce the hemodynamic stress on the aneurysm neck. Therefore, the flow-remodeling effect of the stents promotes the thrombosis of aneurysms and prevents recanalization.

Johnson et al²⁵ investigated the angiographic and clinical outcomes of 100 MCA aneurysms treated with a stent-assisted coiling technique using laser-cut self-expandable stents. In this study,

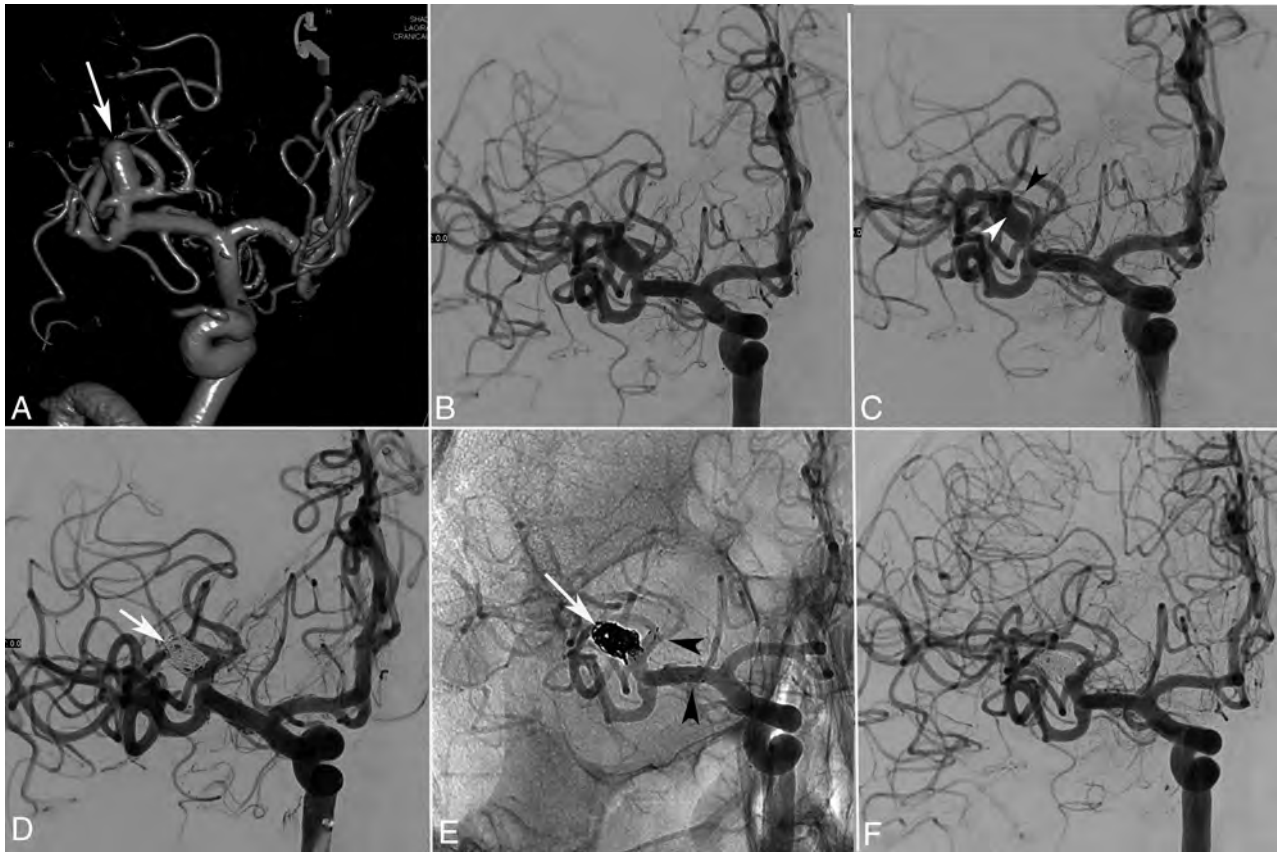


FIG 3. A 35-year-old male patient with a right insular segment MCA aneurysm. *A* and *B*, Preprocedural 3D-reconstructed angiography and DSA images show a wide-neck saccular aneurysm (*arrow*) located at the superior trunk of the right MCA. Three stem arteries arise from the aneurysm neck. *C*, Intraprocedural DSA shows that one of the branches arising from the aneurysm neck is catheterized for stent placement (*black arrowhead*) and another microcatheter is jailed inside the aneurysm for coiling (*white arrowhead*). *D* and *E*, Immediate postprocedural DSA and nonsubtracted angiography images show that the aneurysm is coiled (*white arrow*) after the deployment of an open-cell self-expandable Neuroform Atlas stent into one of the stem arteries arising from the neck, which extends proximally to the superior trunk (*arrowheads*). *F*, A 24-month follow-up DSA image demonstrates the complete occlusion of the aneurysm and patency of all the MCA branches.

only 5% of the aneurysms were ruptured. They found a complete aneurysm occlusion rate of 90.4% at the 6-month angiographic follow-up. The retreatment rate was 4.7%. In a recent study, Hanel et al²⁶ investigated the angiographic and clinical outcomes of patients with MCA aneurysms that were treated with stent-assisted coiling using laser-cut open-cell stents. In their study, most aneurysms were located at the MCA bifurcation, and only 8.6% were located within the insular segment. They reported a complete aneurysm occlusion rate of 80.8% at the end of a 12-month follow-up period, whereas 5.7% of their patients were retreated.

The long-term angiographic outcomes of the current study are slightly better than those of previous endovascular studies that have reported the results of MCA aneurysms. In our study, 2 aneurysms with partial neck and sac filling at the immediate postprocedural angiography progressed to complete occlusion during the follow-up period. None of the aneurysms recanalized or required retreatment. In most of our cases, we used self-expandable braided stents. Compared with self-expanding laser-cut stents, braided stents have a lower porosity and higher metal coverage ratios. The relatively high mesh density of braided stents provides a relatively high flow-diversion capacity.²⁷ The high flow-

diversion capacity of the braided stents lowers the risk of recanalization and enables the progressive thrombosis of partially coiled aneurysms. The use of self-expandable braided stents in most of our cases might have contributed to the favorable angiographic outcomes in our series. All aneurysms except 1 were unruptured in our study. The rupture status of the aneurysms might have also contributed to the good angiographic and clinical outcomes in our patients.

Microsurgical treatment of unruptured insular segment MCA aneurysms has not been specifically studied previously. A standard or modified pterional approach reportedly suffices for the surgical treatment of insular aneurysms.³ The surgical results of insular MCA aneurysms are similar to those of bifurcation aneurysms.¹⁸ Therefore, for practical purposes, the results of microsurgery for insular segment aneurysms can be analyzed within the context of MCA bifurcation aneurysms. In a large case series including 716 patients with 750 unruptured MCA aneurysms, Nussbaum et al²⁸ demonstrated that microsurgery achieved complete aneurysm occlusion in 92% of their cases. In another large case series, Rodriguez-Hernandez et al⁷ investigated the results of microsurgery for ruptured and unruptured MCA aneurysms. They reported a postoperative complete aneurysm occlusion rate

of 98.3%. None of their patients required retreatment during a mean follow-up period of 3.9 years. Although the follow-up period of the current study is considerably shorter, the long-term angiographic outcomes of our patients are comparable with the results of patients with MCA aneurysms treated with microsurgery in previous studies.

The safety of stent-assisted coiling treatment for MCA bifurcation aneurysms has been demonstrated in previous studies. Vendrell et al²⁹ assessed the angiographic and clinical outcomes of 49 patients with 52 MCA aneurysms treated with a stent-assisted coiling procedure. They reported a procedure-related morbidity rate of 3.8%. Johnson et al²⁵ reported a morbidity rate of 1% and a mortality rate of 1% for the stent-assisted coiling procedure used to treat MCA aneurysms. In a recent study, Hanel et al²⁶ reported a permanent morbidity rate of 8.5% after Neuroform Atlas stent-assisted coiling of MCA aneurysms.

No mortality was observed in the current study. We observed asymptomatic intraprocedural and delayed thromboembolic complications in 2 patients (11.1%). These complications resulted in a minor morbidity in 1 patient (3.7%). Nussbaum et al²⁸ reported a 2.8% treatment-related complication rate after the microsurgical treatment of unruptured MCA aneurysms. The morbidity rate of the current study is comparable with the morbidity rates that had been previously reported for MCA aneurysms treated with stent-assisted coiling or microsurgical clipping. The favorable clinical outcomes in the current study demonstrate that stent-assisted coiling is a relatively safe treatment method for MCA aneurysms located within the insular segment.

The main safety concern of stent-assisted coiling treatment for insular segment complex MCA aneurysms might be the necessity of catheterizing small-sized distal arteries. The maneuvers for catheterization and navigation in small-sized insular branches with rigid microcatheters may produce a potential risk of vessel injury. To decrease this risk, we used low-profile microcatheters with soft distal tips for both stent delivery and coiling, and we did not experience any vessel injury induced by the catheterization maneuvers.

The risk of thromboembolic complications produced by the implantation of stents into small-sized vessels might be another concern. Introduction of low-profile self-expandable stents has been a major step in the evolution of endovascular aneurysm surgery. Several previous studies demonstrated the feasibility and safety of implantation of these low-profile stents into small-sized distal arteries.^{12,13} In a recent study, Kim et al³⁰ investigated the safety of stent-assisted coiling of unruptured aneurysms using low-profile stents in small-sized vessels. They found a procedure-related morbidity in 4.5% without mortality. To reduce the risk of thromboembolic complications, we performed preoperative thrombocyte function tests to ensure sufficient antiaggregant activity levels in our patients. Furthermore, precise control of blood pressure and activated clotting time during the entire endovascular procedure might reduce the risk of intraprocedural thromboembolic events. Prevention of catheter-induced vasospasm is another important issue for the avoidance of intraprocedural thromboembolic complications. Intra-arterial nimodipine infusion during the endovascular operation impedes microcatheter-induced vasospasm.

There are some limitations of the current study. The main limitation of this study is the retrospective nature of the study design. Unblinded authors were the individuals who evaluated the postprocedural and follow-up angiographic images of this study. The decision for endovascular therapy in each case was made by the institutional neurovascular teams. Therefore, the effects of a selection bias cannot be excluded from the results of this study. Other limitations are the small number of patients and the relatively short angiographic follow-up duration. Because of the small number of patients, we could not investigate the potential effects of the stent types on the angiographic outcomes. Furthermore, the current study investigated the outcomes of insular segment MCA aneurysms. The results of this study cannot be generalized for distal MCA aneurysms located at the opercular (M3) or cortical (M4) segments.

CONCLUSIONS

The results of this retrospective case series demonstrate that stent-assisted coiling with a low-profile self-expandable stent is a feasible and relatively safe technique for endovascular treatment of insular segment MCA aneurysms. Additionally, it provides an effective and durable treatment for insular segment MCA aneurysms.

Disclosure forms provided by the authors are available with the full text and PDF of this article at www.ajnr.org.

REFERENCES

1. Sundt TM, Kobayashi S, Fode NC, et al. **Results and complications of surgical management of 809 intracranial aneurysms in 722 cases.** *J Neurosurg* 1982;56:753–65 CrossRef Medline
2. Heros RC, Fritsch MJ. **Surgical management of middle cerebral artery aneurysms.** *Neurosurgery* 2001;48:780–85 CrossRef Medline
3. Dashti R, Hernesniemi J, Niemela M, et al. **Microneurosurgical management of distal middle cerebral artery aneurysms.** *Surg Neurol* 2007;67:553–63 CrossRef Medline
4. Horiuchi T, Tanaka Y, Takasawa H, et al. **Ruptured distal middle cerebral artery aneurysms.** *J Neurosurg* 2004;100:384–88 CrossRef Medline
5. Rinne J, Hernesniemi J, Niskanen M, et al. **Analysis of 561 patients with 690 middle cerebral artery aneurysms: anatomical and clinical features as correlated to management outcome.** *Neurosurgery* 1996;38:2–11 CrossRef Medline
6. Yasargil MG. *Microneurosurgery*. Vol 1. Thieme; 1984:279–349
7. Rodriguez-Hernandez A, Sughrue ME, Akhavan S, et al. **Current management of middle cerebral artery aneurysms: surgical results with a “Clip First” policy.** *Neurosurgery* 2013;72:415–27 CrossRef Medline
8. Rodriguez-Hernandez A, Lawton MT. **Flash fluorescence with indocyanine green videoangiography to identify the recipient artery for bypass with distal middle cerebral artery aneurysms: operative technique.** *Neurosurgery* 2012;70:209–20 CrossRef Medline
9. Baltacıoğlu F, Cekirge S, Saatci I, et al. **Distal middle cerebral artery aneurysms: endovascular treatment results with literature review.** *Interv Neuroradiol* 2002;8:399–407 CrossRef Medline
10. Akpek S, Arat A, Morsi H, et al. **Self-expandable stent-assisted coiling of wide-necked intracranial aneurysms: a single-center experience.** *AJNR Am J Neuroradiol* 2005;26:1223–31 Medline
11. Pötin M, Blanc R, Spelle L, et al. **Stent-assisted coiling of intracranial aneurysms: clinical and angiographic results in 216 consecutive aneurysms.** *Stroke* 2010;41:110–15 CrossRef Medline
12. Aydin K, Arat A, Sencer S, et al. **Stent-assisted coiling of wide-neck intracranial aneurysms using low-profile LEO Baby stents: initial**

- and midterm results.** *AJNR Am J Neuroradiol* 2015;36:1934–41 CrossRef Medline
13. Cay F, Peker A, Arat A. **Stent-assisted coiling of cerebral aneurysms with the Neuroform Atlas stent.** *Interv Neuroradiol* 2018;24:263–69 CrossRef Medline
 14. Möhlenbruch M, Herweh C, Behrens L, et al. **The LVIS Jr. micro-stent to assist coil embolization of wide-neck intracranial aneurysms: clinical study to assess safety and efficacy.** *Neuroradiology* 2014;56:389–95 CrossRef Medline
 15. Ten Brinck MF, de Vries J, Bartels RH, et al. **NeuroForm Atlas stent-assisted coiling: preliminary results.** *Neurosurgery* 2019;84:179–89 CrossRef Medline
 16. Gibo H, Carver CC, Rhoton AL Jr, et al. **Microsurgical anatomy of the middle cerebral artery.** *J Neurosurg* 1981;54:151–69 CrossRef Medline
 17. Raymond J, Roy D. **Safety and efficacy of endovascular treatment of acutely ruptured aneurysms.** *Neurosurgery* 1997;41:1235–45 CrossRef Medline
 18. Calvacante T, Derrey S, Curey S, et al. **Distal middle cerebral artery aneurysm: a proposition of microsurgical management.** *Neurochirurgie* 2013;59:121–27 CrossRef Medline
 19. Alreshidi M, Cote DJ, Dasenbrock HH, et al. **Coiling versus microsurgical clipping in the treatment of unruptured middle cerebral artery aneurysms: a meta-analysis.** *Neurosurgery* 2018;83:879–89 CrossRef Medline
 20. Vollherbst DF, Berlis A, Maurer C, et al. **Periprocedural safety and feasibility of the new LVIS EVO device for stent-assisted coiling of intracranial aneurysms: an observational multicenter study.** *AJNR Am J Neuroradiol* 2021;42:319–26 CrossRef Medline
 21. Aydin K, Stracke CP, Barbuoglu M, et al. **Long-term outcomes of wide-necked intracranial bifurcation aneurysms treated with T-stent-assisted coiling.** *J Neurosurg* 2021;134:39–48 CrossRef Medline
 22. Brinjikji W, Lanzino G, Cloft HJ, et al. **Endovascular treatment of middle cerebral artery aneurysms: a systematic review and single-center series.** *Neurosurgery* 2011;68:397–402 CrossRef Medline
 23. Chalouhi N, Starke RM, Koltz MT, et al. **Stent-assisted coiling versus balloon remodeling of wide-neck aneurysms: comparison of angiographic outcomes.** *AJNR Am J Neuroradiol* 2013;34:1987–92 CrossRef Medline
 24. Raymond J, Darsaut TE, Bing F, et al. **Stent-assisted coiling of bifurcation aneurysms may improve endovascular treatment: a critical evaluation in an experimental model.** *AJNR Am J Neuroradiol* 2013;34:570–76 CrossRef Medline
 25. Johnson AK, Heiferman DM, Lopes DK. **Stent-assisted coiling of 100 middle cerebral artery aneurysms.** *J Neurosurg* 2013;118:950–55 CrossRef Medline
 26. Hanel RA, Yoon N, Sauvageau E, et al. **Neuroform Atlas stent for treatment of middle cerebral artery aneurysms: 1-year outcomes from Neuroform Atlas Stent Pivotal Trial.** *Neurosurg* 2021;89:102–08 CrossRef Medline
 27. Aydin K, Barbuoglu M, Sencer S, et al. **Diversion with low-profile braided stents for the treatment of very small or uncoilable intracranial aneurysms at or distal to the circle of Willis.** *AJNR Am J Neuroradiol* 2017;38:2131–36 CrossRef Medline
 28. Nussbaum ES, Madison MT, Goddard JK, et al. **Microsurgical treatment of unruptured middle cerebral artery aneurysms: a large, contemporary experience.** *J Neurosurg* 2018 Jun 1 [Epub ahead of print] CrossRef Medline
 29. Vendrell JF, Costalat V, Brunel H, et al. **Stent-assisted coiling of complex middle cerebral artery aneurysms: initial and midterm results.** *AJNR Am J Neuroradiol* 2011;32:259–63 CrossRef Medline
 30. Kim J, Han HJ, Lee W, et al. **Safety of stent-assisted coiling of unruptured intracranial aneurysms using low-profile stents in small parent arteries.** *AJNR Am J Neuroradiol* 2021;42:1621–26 CrossRef Medline

A Meta-analysis of Combined Aspiration Catheter and Stent Retriever versus Stent Retriever Alone for Large-Vessel Occlusion Ischemic Stroke

 D.A. Schartz,  N.R. Ellens,  G.S. Kohli,  S.M.K. Akkipeddi,  G.P. Colby,  T. Bhalla,  T.K. Mattingly, and  M.T. Bender

ABSTRACT

BACKGROUND: The efficacy of combined aspiration catheter and stent retriever compared with stent retriever alone for the treatment of large-vessel occlusion acute ischemic stroke is unclear.

PURPOSE: Our aim was to conduct a systematic literature review and meta-analysis on several metrics of efficacy comparing aspiration catheter and stent retriever with stent retriever alone.

DATA SOURCES: MEDLINE and the Cochrane Library Databases were searched. Randomized controlled trials and case-control and cohort studies were included.

STUDY SELECTION: Ten comparative studies were included detailing a combined 1495 patients with aspiration catheter and stent retriever and 1864 with stent retrievers alone.

DATA ANALYSIS: Data on first pass effect (TICI 2b/2c/3 after first pass), final successful reperfusion (modified TICI $\geq 2b$), and 90-day functional independence (mRS ≤ 2) were collected. Meta-analysis was performed using a random-effects model.

DATA SYNTHESIS: There was a pooled composite first pass effect of 40.8% (611/1495) versus 32.6% (608/1864) for aspiration catheter and stent retriever and stent retriever alone, respectively ($P < .0001$). Similarly, on a meta-analysis, aspiration catheter and stent retriever were associated with a higher first pass effect compared with stent retriever alone (OR = 1.63; 95% CI, 1.20–2.21; $P = .002$; $I^2 = 72\%$). There was no significant difference in composite rates of successful reperfusion between aspiration catheter and stent retriever (72.8%, 867/1190) and stent retriever alone (70.8%, 931/1314) ($P = .27$) or on meta-analysis (OR = 1.31; CI, 0.81–2.12; $P = .27$; $I^2 = 82\%$). No difference was found between aspiration catheter and stent retriever and stent retriever alone on 90-day functional independence (OR = 1.02; 95% CI, 0.77–1.36; $P = .88$; $I^2 = 40\%$).

LIMITATIONS: This study is limited by high interstudy heterogeneity.

CONCLUSIONS: On meta-analysis, aspiration catheter and stent retriever are associated with a superior first pass effect compared with stent retriever alone, but they are not associated with statistically different final reperfusion or functional independence.

ABBREVIATIONS: AIS = acute ischemic stroke; ASR = combined aspiration catheter and stent retriever; BGC = balloon-guide catheter; eTICI = expanded TICI; mTICI = modified TICI; FPE = first pass effect; LVO = large-vessel occlusion; SR = stent retriever

There are several different techniques used for the endovascular treatment of acute ischemic stroke (AIS) secondary to large-vessel occlusion (LVO), including mechanical thrombectomy via a stent retriever (SR), direct contact aspiration using a large-bore

intermediate catheter, and a combined approach using a contact aspiration catheter with a stent retriever (ASR). SR is a well-established, safe technique for AIS and often results in high rates of successful recanalization.¹ Similarly, contact aspiration is a commonly used technique. The Contact Aspiration vs Stent Retriever for Successful Revascularization (ASTER) trial compared contact aspiration with SR alone and found no significant difference in final reperfusion or first pass effect (FPE) between the 2 methods.² FPE is an increasingly used metric, expressed as the achievement of complete recanalization with a single use/pass of a thrombectomy device.³

Recent studies have also investigated the efficacy of ASR, which theoretically should synergize the positive thromboembolic

Received November 9, 2021; accepted after revision January 11, 2022.

From the Departments of Imaging Sciences (D.A.S.) and Neurosurgery (N.R.E., G.S.K., S.M.K.A., T.B., T.K.M., M.T.B.), University of Rochester Medical Center, Rochester, New York; and Department of Neurological Surgery (G.P.C.), University of California Los Angeles, Los Angeles, California.

Please address correspondence to Matthew T. Bender, MD, University of Rochester School of Medicine and Dentistry, University of Rochester Medical Center, 601 Elmwood Ave, Rochester, NY 14642; e-mail: matthew_bender@urmc.rochester.edu <http://dx.doi.org/10.3174/ajnr.A7459>

retrieval mechanisms of SR and contact aspiration. However, results have been mixed. While some studies have shown that ASR results in superior technical and clinical outcomes,⁴⁻⁶ other studies have shown no such benefits.⁷⁻⁹ The recently completed Combined Use of Contact Aspiration and the Stent Retriever Technique Versus Stent Retriever Alone for Recanalisation in Acute Cerebral Infarction (ASTER2) trial compared ASR with SR and found no difference in the final reperfusion, but multiple secondary reperfusion end points favored ASR.⁹ Thus, the efficacy of ASR compared with SR alone is unclear. The aim of this study was to complete a systematic literature review and meta-analysis to better evaluate how ASR compares with SR in LVO AIS.

MATERIALS AND METHODS

Literature Search and Eligibility Criteria

A Preferred Reporting Items for Systematic Reviews and Meta-Analysis (PRISMA)-guided systematic literature review and meta-analysis was conducted to investigate the efficacy of primary ASR versus SR alone for the treatment of LVO AIS. Institutional review board approval was not required because the data were obtained from already published studies and are publicly obtainable.

The MEDLINE and Cochrane Databases were searched up to September 2021 using the following search terms: “Aspiration Catheter” AND “Mechanical Thrombectomy” AND “Stroke,” “Aspiration Catheter” AND “Stent Retriever” AND “Stroke,” “Aspiration” AND “Stent Retriever” AND “Stroke,” “Aspiration” AND “Mechanical Thrombectomy” AND “Stroke.” The MEDLINE software removed duplicated studies between queries; results from the Cochrane Database were cross-referenced with the MEDLINE results, and duplicates were excluded. Only comparative studies with internal controls were included in this analysis (eg, directly compared efficacy metrics of ASR and SR within same study cohort). Each study from the literature search was screened on the basis of the title alone or abstract, with further reading of the article if there was uncertainty about preliminary inclusion. Studies had to be written in English for inclusion and to include >18 patients within the cohort. Both randomized controlled trials and observational studies were included in the quantitative synthesis. For inclusion, studies had to describe the use of primary combined aspiration catheter and stent retriever as a treatment technique; those that used adjunct aspiration/or SR as a rescue therapy were not included in this analysis. Similarly, for the SR studies, SR had to be used as a primary technique. After the initial screening process, all of the studies were more rigorously assessed for possible final inclusion by 2 independent reviewers for confirmation of data with disagreements settled by consensus. Inclusion of at least one of the main outcome measures described below was an additional requirement for inclusion in the meta-analysis.

Outcome Measures

Three primary outcome measures were evaluated to compare the efficacy of ASR and SR alone for ischemic stroke of the anterior circulation. FPE was measured on the basis of the internal metric for a successful first pass as dictated for each individual study, which included expanded TICI (eTICI) $\geq 2b$, eTICI $\geq 2c$, or modified TICI (mTICI) 3 only. For the sake of this study, FPE also included

modified FPE (eg, achieved mTICI 2b after the first pass) if that was what was reported as FPE in the study. In other words, some studies described modified FPE or the equivalent (eg, “successful reperfusion”) as an eTICI $\geq 2b$, while in other studies, only mTICI 2c/3 cases were considered a successful first pass. However, because they were internally controlled, both types were included in the FPE analysis. The final TICI score following endovascular intervention was used as a surrogate for successful reperfusion. Studies had to describe a final TICI score of either eTICI $\geq 2c$ or mTICI $\geq 2b$, and both were grouped and included in the successful reperfusion analysis. All studies had to delineate the exact TICI score for inclusion in this analysis and the FPE analysis. Ninety-day functional independence (mRS 0–2) was also investigated as a primary outcome. A study had to detail at least one of these outcome measures to be included in the quantitative synthesis. Subgroup analyses based on the TICI definition of the primary outcome measures of FPE and successful reperfusion were also completed. Studies that defined an outcome measure by TICI 3 and mTICI 2c/3 scores were grouped together, whereas those that defined an outcome with mTICI $\geq 2b$ were grouped together. Last, a secondary composite outcome measure included the 90-day mortality rate.

Results Synthesis and Statistical Analysis

Forest plots for each of the primary outcome measures of FPE, successful reperfusion, and 90-day functional independence were constructed with corresponding ORs. A random-effects model was used to calculate the pooled OR for each analysis using a Mantel and Haenszel method. All forest plots and corresponding statistical analyses including tests of heterogeneity were calculated using Review Manager (RevMan computer program, Version 5.4; <https://review-manager.software.informer.com/5.4/>). A χ^2 test (completed using GraphPad Prism 9 software; GraphPad Software) was used to assess statistical significance for overall composite differences in efficacy rates and secondary outcome measures.

Bias and Heterogeneity Assessments

Statistical heterogeneity was assessed using the Cochran Q statistic and described using the I^2 measure and P value. An I^2 of >50% and >75% was used as a benchmark for moderate and considerable heterogeneity, respectively. A heterogeneity P value > .10 was used to indicate statistically nonsignificant heterogeneity. An assessment of potential publication bias was also completed for each analysis using funnel plots and the Egger test, implemented using MedCalc statistical software (<https://www.medcalc.org>). An Egger test P value < .10 was used to indicate significant publication bias.

RESULTS

Systematic Literature Search

From MEDLINE and Cochrane Databases, 484 studies resulted from our search after the removal of duplicates. Two articles were found on the basis of screening references based on a supplementary literature review. Fourteen articles that potentially met the full inclusion criteria were more rigorously assessed. Four of these articles were eventually not included for the following reasons: One study did not adequately specify the TICI score from those treated, 2 studies had <18 patients in each treatment arm, and 1 study

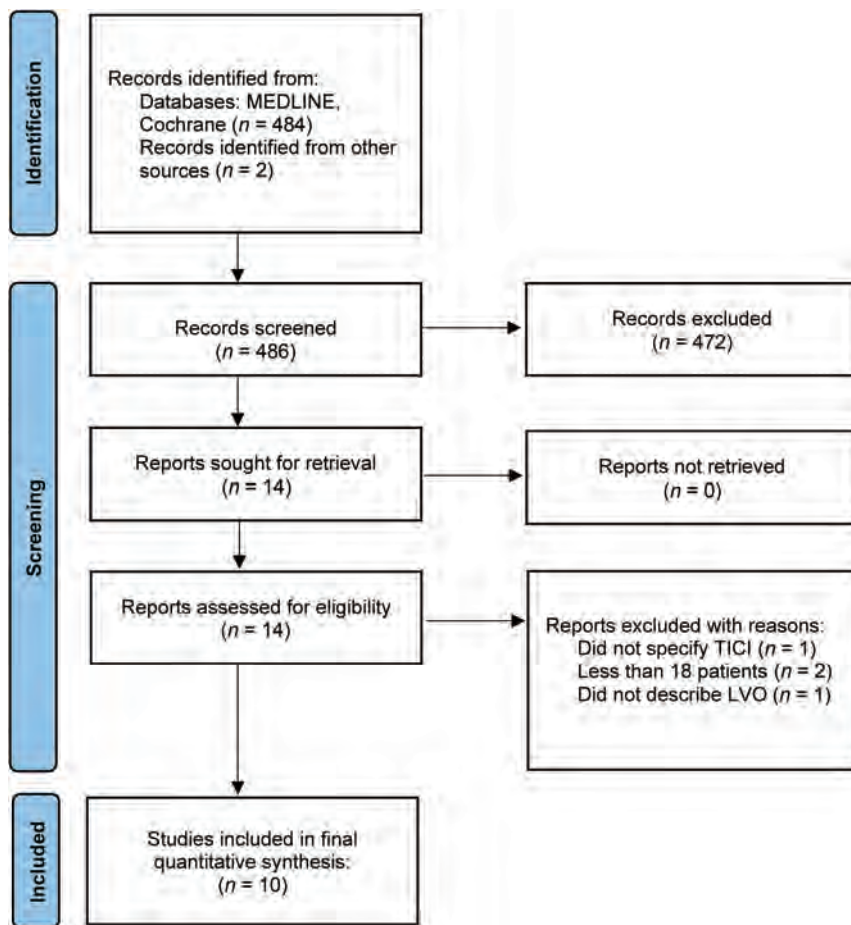


FIG 1. PRISMA literature review flow diagram.

Characteristics of studies included within quantitative synthesis

Study	Design	ASR (No.)	SR (No.)	BGC Use (No.)
Hesse et al, 2018 ¹²	Multicenter, retrospective	184	102	100
Colby et al, 2019 ¹⁰	Single center, retrospective	106	215	49.5
Hafeez et al, 2020 ¹¹	Single center, retrospective	51	57	100
Kim et al, 2020 ⁶	Single center, retrospective	42	49	100
Meder et al, 2021 ¹³	Single center, retrospective	37	33	0
Lapergue et al, 2021 ⁹	Multicenter, randomized controlled trial	203	202	93
Okuda et al, 2021 ⁵	Multicenter, retrospective	240	128	98.6
Blasco et al, 2021 ⁷	Multicenter, retrospective	128	273	100
Mohammaden et al, 2021 ⁸	Single center, prospective	165	255	100
Di Maria et al, 2021 ⁴	Multicenter, prospective	339	550	21.3

described only M2 occlusions and not LVO. As a result, 10 studies describing a total of 1495 patients having undergone ASR and 1864 having undergone SR met the final inclusion criteria for the quantitative synthesis (Fig 1).⁴⁻¹³ Of these studies, 1 was a multicenter randomized controlled trial, 1 was a multicenter prospective registry study, 4 were single-center retrospective studies, 1 was a single-center prospective study, and 3 were multicenter retrospective studies. A review of the characteristics of the included studies can be seen in the Table.

Meta-analysis

From the 10 included comparative studies, there were 1495 patients having undergone ASR and 1864 having undergone SR. The criteria for FPE were achievement of mTICI 2c/3 in 8 studies, and in 2 studies, it was defined as TICI ≥2b. Regarding FPE results, the pooled composite rates were 40.8% (611/1495) versus 32.6% (608/1864) for ASR and SR, respectively ($P < .0001$). On meta-analysis, primary ASR was also associated with a higher FPE compared with primary SR (OR = 1.63; 95% CI, 1.20–2.21; $P = .002$) (Fig 2). A subgroup analysis was completed on the basis of TICI criteria and the FPE definition. Both the mTICI 2c/3 subgroup (8 studies, 2947 patients) and the TICI ≥2b subgroup (2 studies, 412 patients) significantly favored ASR over SR with an OR of 1.47 (95% CI, 1.04–2.07; $P = .03$) and 1.63 (95% CI, 1.20–2.21; $P < .0001$), respectively (Fig 2).

Successful final reperfusion was defined as mTICI ≥2b in 7/9 (1698 patients) of the included studies, and as mTICI 2c/3 in the other 2/9 studies (806 patients). There was no significant difference in composite rates between ASR (72.8%, 867/1190) and SR (70.8%, 931/1314) ($P = .27$) regarding successful reperfusion. This was similarly the case on a meta-analysis comparing ASR and SR (OR = 1.31; 95% CI, 0.81–2.12; $P = .27$) (Fig 3). However, on subgroup analysis based on the TICI score reperfusion definition, ASR had a significantly higher odds of achieving successful final reperfusion when defined as mTICI ≥2b compared with SR alone (OR = 1.64; 95% CI, 1.04–2.50; $P = .03$), whereas in studies that defined reperfusion as mTICI 2c/3, there was no difference between ASR and SR (OR = 0.72; 95% CI, 0.22–2.39; $P = .59$) (Fig 3).

For the last main outcome measure of functional independence (ie, 90-day mRS of 0–2), there was no significant difference in reported composite rates between ASR (42.5%, 293/690) and SR (45.9%, 360/784) ($P = .19$), which was also the same on the meta-analysis (OR = 1.02; 95% CI, 0.77–1.36; $P = .88$; $I^2 = 40\%$) (Fig 4). The 90-day mortality rates from those studies that reported it were also investigated. Overall, the composite mortality rates between ASR and SR were not significant at 17.9% (117/651) versus 16.8% (132/787), respectively ($P = .58$).

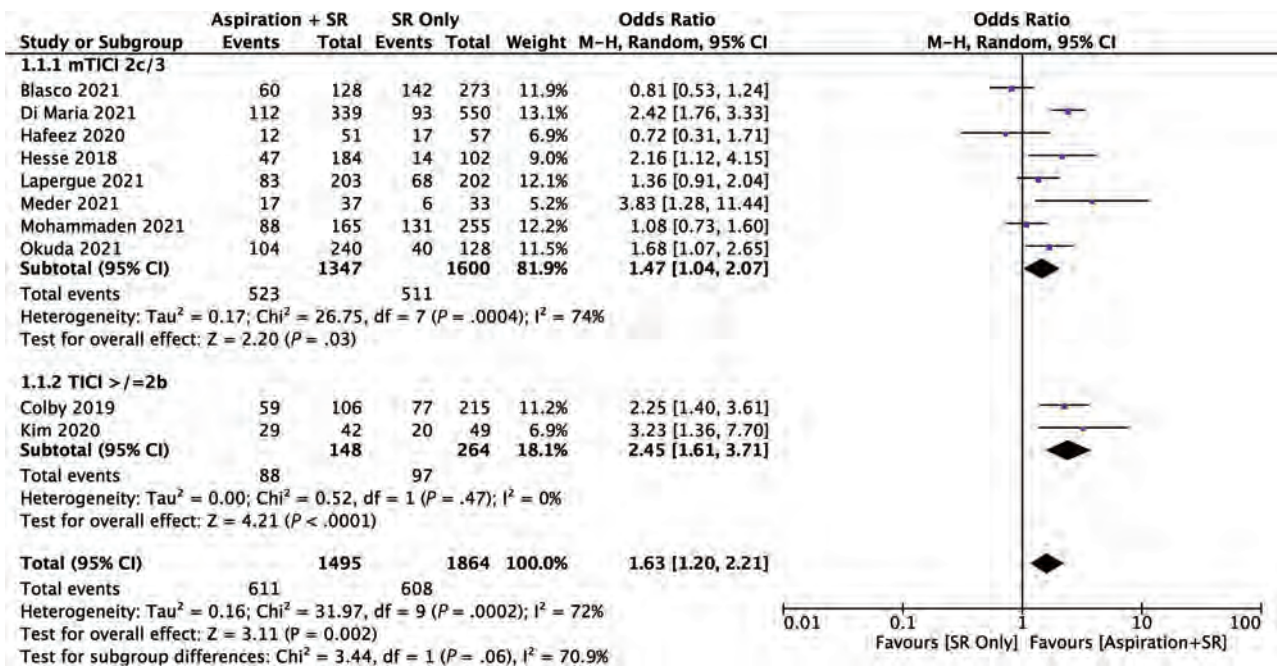


FIG 2. Forest plot for FPE analysis. M-H indicates Mantel and Haenszel.

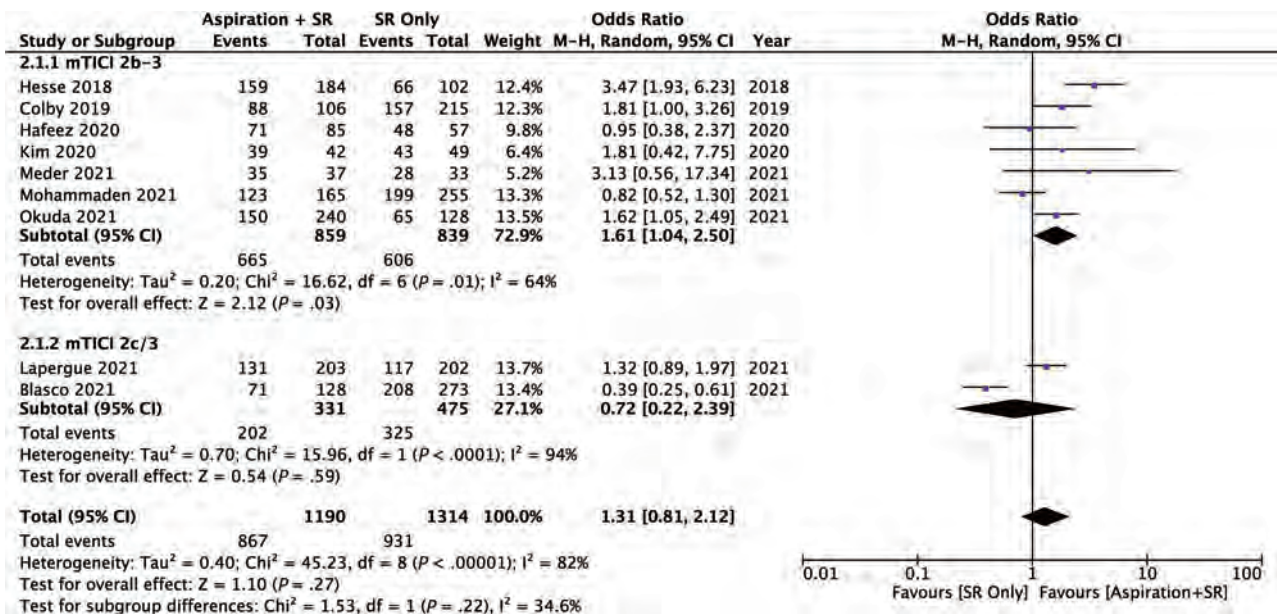


FIG 3. Forest plot for final reperfusion analysis. M-H indicates Mantel and Haenszel.

Assessment of Heterogeneity and Bias

An assessment of interstudy heterogeneity among the included studies was completed and described using the I² and heterogeneity P values. For the primary FPE analysis, there was moderate heterogeneity among the included studies (I² = 72%, P = .0002). Regarding the successful recanalization analysis, there was considerable interstudy heterogeneity (I² = 82%, P < .001). There was nonsignificant low heterogeneity among the studies included in the functional outcome analysis (I² = 40%, P = .88). The Egger test was used to assess potential publication bias for the primary outcome measures. Significant publication bias was found

in the functional independence analysis (P = .05). There was no significant publication bias in the FPE analysis (P = .75) or the reperfusion analysis (P = .68).

DISCUSSION

This was the first meta-analysis to evaluate the efficacy between ASR compared with SR alone for the treatment of AIS. The current literature comprises retrospective studies and a single randomized controlled trial. On pooled quantitative synthesis, ASR was associated with a superior first pass success rate (OR =

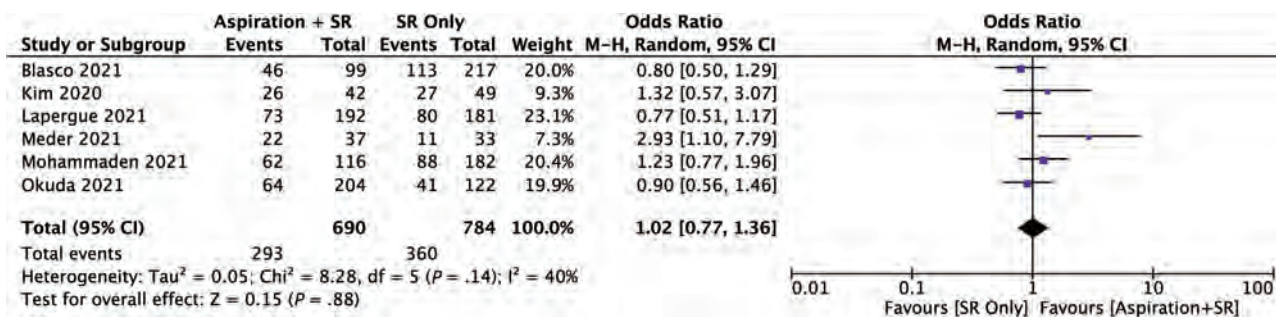


FIG 4. Forest plot for functional independence (90-day mRS of 0–2). M-H indicates Mantel and Haenszel.

1.63, $P = .002$). However, there was no significant difference between ASR and SR regarding final reperfusion, functional independence, or 90-day mortality.

The headlines emerging from randomized trials suggest similar final reperfusion with varying technical approaches to endovascular thrombectomy. The ASTER randomized clinical trial compared primary contact aspiration with primary SR and found no difference in final successful revascularization rates.² The recent ASTER2 randomized controlled trial similarly investigated the efficacy of ASR versus SR alone and also found no difference in final reperfusion rates of eTICI $\geq 2c$ (64.5% versus 57.9%, $P = .17$).⁹ However, the absolute difference of 6.6% in ASTER2 did exceed the minimal clinically important differences, believed to be between 3.1% and 5%.¹⁴ The authors acknowledged that a treatment effect of 15% was expected, so ASTER2 may have simply been underpowered.

Although the primary end point did not, several relevant secondary end points in ASTER2 favored ASR over SR alone. ASR was superior at achieving eTICI 2b/2c/3 (86.2% versus 72.3%, $P < .001$) and eTICI 2c/3 (59.6% versus 49.5%, $P = .04$) after the assigned initial intervention alone, which could be repeated up to 3 times.⁹ There was a trend toward improved FPE with ASR (40.9% versus 33.7% eTICI 2c/3, $P = .12$; 53.7% versus 44.6% eTICI 2b50/2c/3, $P = .06$), though this did not reach statistical significance. An additional study of 1832 patients found that combined thrombectomy and thromboaspiration resulted in a superior FPE compared with SR alone, and in those patients in whom FPE was achieved, a significantly better outcome and 90-day mortality result was observed.⁴ In the present meta-analysis, no difference in final reperfusion was observed ($P = .27$), but achievement of TICI 2b/2c/3 after first pass was superior in the ASR group (OR = 1.63, Fig 2). However, while there was no significant difference in final reperfusion overall, subgroup analysis based on the reperfusion definition revealed that ASR was superior at achieving mTICI 2b/3 (OR = 1.61, $P = .03$). Given that there was no significant difference in mTICI 2c/3 (Fig 3), this finding seems to suggest that the mTICI 2b/3 subgroup result was likely due to a higher proportion of mTICI 2b final reperfusion.

There has been a movement toward making FPE the primary outcome of trials of endovascular thrombectomy. This has largely been on the basis of reduced complications associated with fewer passes¹⁵ and superior outcomes if complete reperfusion is achieved after the first pass.¹⁶ FPE also has statistical advantages:

Outcomes that are evenly distributed between good and bad are more sensitive in demonstrating the salutary and detrimental effects of procedural variation. A previous meta-analysis showed that FPE and modified FPE rates after endovascular thrombectomy generally were 28% and 45%, respectively.¹⁷ Final reperfusion in most LVO series was $\geq 80\%$, which may limit the ability to detect differences resulting from technical variation.¹⁸ Moreover, final reperfusion is necessarily reported as intention-to-treat, given the technical crossover that occurs in second, third, and subsequent passes. FPE, by contrast, more closely represents the results of a single embolectomy technique. ASTER2 required 3 attempts with identical techniques,⁹ though in retrospective series crossover occurs in as high as 30%–45% of cases.^{5,7}

Given that ASR is associated with superior FPE and that FPE is associated with better outcomes, it was surprising that ASR was not also associated with superior clinical results on the meta-analysis. A possible explanation is that many studies, including ASTER2, required the use of a balloon-guide catheter (BGC) in both treatment arms.^{5,9} BGCs arrest flow, reducing clot fragmentation and distal emboli.¹⁹ Mechanistic overlap was observed from the introduction of intermediate aspiration catheters: Kurre et al²⁰ reported a reduction (14.6% to 3.3%) of distal emboli by adding an intermediate aspiration catheter to the SR without the use of a BGC. Bourcier et al²¹ showed that a BGC does not confer better reperfusion and clinical outcomes compared with no BGC when used with combined SR and contact aspiration. Given the overlapping mechanism of a BGC and distal aspiration, it is plausible that the requirement of BGCs in studies comparing ASR and SR functionally diluted the effect of the intermediate aspiration catheter. This possibility could explain why the ASTER2 trial did not achieve a significant difference in final reperfusion, and why it may have been underpowered. Additionally, the outcome measure we investigated was 90-day mRS, but it is possible that the outcome differences between ASR and SR are more granular—that is, they may be limited to short-term issues and complications that resolve by day 90: temporary physical deficits, prolonged hospital stay, increased discharge to rehabilitation facilities, and/or higher procedural costs because rescue techniques may be required. These possibilities are an avenue for future studies and should be considered in future trial design.

This study has several limitations. First, there is a degree of heterogeneity in regard to the embolectomy technique, including the required use of a BGC, which may function as a confounding variable. Most studies in the analysis required or primarily used a

BGC with their technique,^{5-9,11} whereas in some studies, it was more variable or did not necessitate a BGC for inclusion in the analysis.^{4,10,13} Additionally, there has been only 1 randomized controlled trial to date; thus, the data in the literature are limited to single or multicenter retrospective/prospective analyses, which are prone to biases inherent to their study design. Furthermore, the definition of FPE and final reperfusion varied among studies: Some defined them as achievement of mTICI 2c/3, and others, as reaching eTICI $\geq 2b$. Although we included only comparative studies with internal controls and completed subgroup analysis based on outcome definition to compensate for this difference, the results should still be interpreted within this context.

An additional limitation is that this study compared only 2 techniques without association with any other variables that could alter their efficacy. For example, clot composition was not considered but has been shown to influence FPE in thrombectomy.²² Similarly, this study did not account for the presence of a positive susceptibility vessel sign, which has also been shown to predict and influence the success of thrombectomy.²³ In fact, the ongoing Vesair Balloon Confirmatory Trial (VECTOR) is investigating how positive susceptibility vessel sign occlusions might influence the efficacy of a first-line SR combined with contact aspiration versus contact aspiration alone.²⁴ Moreover, thrombus positioning was also not considered even though thromboaspiration success has been shown to be influenced by the interface angle between the clot and thrombectomy device.²⁵ Last, we also observed a moderate-to-considerable degree of inter-study heterogeneity within the FPE and recanalization analyses, likely, in part, due to the aforementioned limitations. Thus, the results described here should be interpreted with these considerations.

CONCLUSIONS

The current literature indicates that ASR results in a superior FPE compared with SR alone. Despite no significant difference in final recanalization overall, subgroup analysis suggests that ASR may result in superior final reperfusion when defined as mTICI $\geq 2b$. Nonetheless, there was no significant difference in functional outcomes between the 2 techniques. Further research should focus on variables that account for differences between ASR and SR, such as the use of a BGC, among others.

Disclosure forms provided by the authors are available with the full text and PDF of this article at www.ajnr.org.

REFERENCES

- Goyal M, Menon BK, van Zwam WH, et al. **Endovascular thrombectomy after large-vessel ischaemic stroke: a meta-analysis of individual patient data from five randomised trials.** *Lancet* 2016;387:1723–31 CrossRef Medline
- Lapergue B, Blanc R, Gory B, et al; ASTER Trial Investigators. **Effect of endovascular contact aspiration vs stent retriever on revascularization in patients with acute ischemic stroke and large vessel occlusion: the ASTER randomized clinical trial.** *JAMA* 2017;318:443–52 CrossRef Medline
- Zaidat OO, Castonguay AC, Linfante I, et al. **First pass effect: a new measure for stroke thrombectomy devices.** *Stroke* 2018;49:660–66 CrossRef Medline
- Di Maria F, Kyheng M, Consoli A, et al; ETIS Investigators. **Identifying the predictors of first-pass effect and its influence on clinical outcome in the setting of endovascular thrombectomy for acute ischemic stroke: results from a multicentric prospective registry.** *Int J Stroke* 2021;16:20–28 CrossRef Medline
- Okuda T, Arimura K, Matsuo R, et al; QNET Investigators. **Efficacy of combined use of a stent retriever and aspiration catheter in mechanical thrombectomy for acute ischemic stroke.** *J Neurointerv Surg* 2021 Sep 20. [Epub ahead of print] CrossRef Medline
- Kim SH, Lee H, Kim SB, et al. **Hybrid mechanical thrombectomy for acute ischemic stroke using an intermediate aspiration catheter and Trevo stent simultaneously.** *J Clin Neurosci* 2020;76:9–14 CrossRef Medline
- Blasco J, Puig J, López-Rueda A, et al; ROSSETTI Group. **Addition of intracranial aspiration to balloon guide catheter does not improve outcomes in large vessel occlusion anterior circulation stent retriever based thrombectomy for acute stroke.** *J Neurointerv Surg* 2021 Aug 27. [Epub ahead of print] CrossRef Medline
- Mohammaden MH, Haussen DC, Pisani L, et al. **Stent-retriever alone vs. aspiration and stent-retriever combination in large vessel occlusion stroke: a matched analysis.** *Int J Stroke* 2021 May 27. [Epub ahead of print] CrossRef Medline
- Lapergue B, Blanc R, Costalat V, et al. ASTER2 Trial Investigators. **Effect of thrombectomy with combined contact aspiration and stent retriever vs stent retriever alone on revascularization in patients with acute ischemic stroke and large vessel occlusion: the ASTER2 randomized clinical trial.** *JAMA* 2021;326:1158–69 CrossRef Medline
- Colby GP, Baharvahdat H, Mowla A, et al. **Increased success of single-pass large vessel recanalization using a combined stentriever and aspiration technique: a single institution study.** *World Neurosurg* 2019;123:e747–52 CrossRef Medline
- Hafeez MU, Kan P, Srivatsan A, et al. **Comparison of first-pass efficacy among four mechanical thrombectomy techniques: a single-center experience.** *World Neurosurg* 2020;144:e533–40 CrossRef Medline
- Hesse AC, Behme D, Kemmling A, et al. **Comparing different thrombectomy techniques in five large-volume centers: a 'real world' observational study.** *J Neurointerv Surg* 2018;10:525–29 CrossRef Medline
- Meder G, Żuchowski P, Skura W, et al. **Mechanical thrombectomy in stroke. Experience from switching from stent retriever only to stent retriever combined with aspiration catheter.** *J Clin Med* 2021;10:1802 CrossRef Medline
- Lin CJ, Saver JL. **The minimal clinically important difference for achievement of substantial reperfusion with endovascular thrombectomy devices in acute ischemic stroke treatment.** *Front Neurol* 2020;11:524220 CrossRef Medline
- García-Tornel Á, Requena M, Rubiera M, et al. **When to stop: detrimental effect of device passes in acute ischemic stroke secondary to large vessel occlusion.** *Stroke* 2019;50:1781–88 CrossRef
- Nikoubashman O, Dekeyser S, Riabikin A, et al. **True first-pass effect.** *Stroke* 2019;50:2140–46 CrossRef Medline
- Abbasi M, Liu Y, Fitzgerald S, et al. **Systematic review and meta-analysis of current rates of first pass effect by thrombectomy technique and associations with clinical outcomes.** *J Neurointerv Surg* 2021;13:212–16 CrossRef Medline
- Tsang CO, Cheung IH, Lau KK, et al. **Outcomes of stent retriever versus aspiration-first thrombectomy in ischemic stroke: a systematic review and meta-analysis.** *AJNR Am J Neuroradiol* 2018;39:2070–76 CrossRef Medline
- Chueh JY, Kühn AL, Puri AS, et al. **Reduction in distal emboli with proximal flow control during mechanical thrombectomy: a quantitative in vitro study.** *Stroke* 2013;44:1396–1401 CrossRef Medline
- Kurre W, Vorlaender K, Aguilar-Pérez M, et al. **Frequency and relevance of anterior cerebral artery embolism caused by mechanical thrombectomy of middle cerebral artery occlusion.** *AJNR Am J Neuroradiol* 2013;34:1606–11 CrossRef Medline
- Bourcier R, Marnat G, Labreuche J, et al. **Balloon guide catheter is not superior to conventional guide catheter when stent retriever**

- and contact aspiration are combined for stroke treatment.** *Neurosurgery* 2020;88:E83–90 CrossRef Medline
22. Liu Y, Brinjikji W, Abbasi M, et al. **Quantification of clot spatial heterogeneity and its impact on thrombectomy.** *J Neurointerv Surg* 2021 Dec 15. [Epub ahead of print] CrossRef Medline
23. Belachew NF, Dobrocky T, Aleman EB, et al. **SWI susceptibility vessel sign in patients undergoing mechanical thrombectomy for acute ischemic stroke.** *AJNR Am J Neuroradiol* 2021;42:1949–55 CrossRef Medline
24. Janot K, Zhu F, Kerleroux B, JENI Research Collaboration, et al. **“Adaptative endovascular strategy to the CloT MRI in large intracranial vessel occlusion” (VECTOR): study protocol of a randomized control trial.** *J Neuroradiol* 2020;47:382–85 CrossRef Medline
25. Bernava G, Rosi A, Boto J, et al. **Direct thromboaspiration efficacy for mechanical thrombectomy is related to the angle of interaction between the aspiration catheter and the clot.** *J Neurointerv Surg* 2020;12:396–400 CrossRef Medline

CT-Guided C2 Dorsal Root Ganglion Radiofrequency Ablation for the Treatment of Cervicogenic Headache: Case Series and Clinical Outcomes

J.L. Chazen, M. Roytman, E.S. Yoon, T.K. Mullen, and D.R. Lebl



ABSTRACT

SUMMARY: Cervicogenic headache is a secondary headache syndrome attributable to upper cervical spine pathology. Osteoarthritis of the lateral atlantoaxial joint with resultant C2 dorsal root ganglion irritation is an important and potentially treatable cause of cervicogenic headache. In this case series, we present 11 patients with cervicogenic headache who underwent C2 dorsal root ganglion thermal radiofrequency ablation. Radiologists should be familiar with this efficacious procedure and technical considerations to avoid complications.

ABBREVIATIONS: DRG = dorsal root ganglion; RF = radiofrequency; RFA = radiofrequency ablation; VAS = visual analog scale

Cervicogenic headache is a secondary headache syndrome attributable to upper cervical spine pathology, with an estimated prevalence of up to 4% of the general population and 20% of patients with chronic headache.¹ Due to the convergence of upper cervical segment nociceptive afferents with the trigeminal complex, pain from the upper cervical nerves may be referred to the occipital, orbital, frontal, and/or parietal regions.² Potential culprit nerves include the greater occipital nerve, lesser occipital nerve, and third occipital nerves, with the greater and lesser occipital nerves both receiving contributions from the C2 dorsal root ganglion (DRG).^{3,4} While cervicogenic headaches may occur from a variety of pathologies (including tumor, fracture, infection, and inflammatory arthritis), osteoarthritis of the lateral atlantoaxial joint with resultant C2 DRG irritation is an important and potentially treatable cause of cervicogenic headache.⁵ Image-guided pulsed or thermal radiofrequency ablation (RFA) of the C2 DRG has been described with high response rates.⁶⁻⁹ We report clinical outcomes of a series of 11 patients in whom C2 DRG thermal RFA was performed using a CT-guided technique.¹⁰

Case Series

Institutional review board approval was obtained for this retrospective case series from the Hospital for Special Surgery and

Weill Cornell Medicine IRBs. Patient characteristics and outcomes are described in the Online Supplemental Data. All 11 patients were diagnosed with cervicogenic headache after clinical evaluation and met the International Classification of Headache Disorders diagnostic criteria for having cervicogenic headache.¹¹ All patients underwent preprocedural cervical MR imaging and demonstrated asymmetric T2 hyperintense edema within the C1–C2 lateral atlantoaxial joint, ipsilateral to the site of neck and occipital distribution pain (Fig 1).

From February 2019 through October 2021, eleven C2 DRG RFAs were performed. Cases were performed by a neuroradiologist with a Certificate of Added Qualification and 9 years of postfellowship experience and a musculoskeletal radiologist with 3 years of postfellowship experience. There were 4 men and 7 women in the cohort, with a mean age of 77 (SD, 7.8) years (median, 77 years; range, 62–90 years) (Online Supplemental Data). The C2 DRG RFA procedural technique and contraindications have been described previously.¹⁰ In brief, the patient is placed supine on the CT gantry and a noncontrast scan of the craniocervical junction is acquired with a CT grid in place. All patients were offered moderate sedation for the ablation procedure. A suitable entry site to target the C2 DRG is planned at the base of C2; it is critical to place the needle below the C1 ring just above the C2 lateral mass to avoid the traversing the V3 segment of the vertebral artery. By means of intermittent CT guidance, a 22-ga radiofrequency (RF) cannula with a 5-mm active tip (Abbott) is advanced to the C2 DRG (Fig 2). A small amount of nonionic iodinated contrast can be injected to confirm the appropriate position (Fig 3). Following sensory testing at 50 Hz up to 2 V to confirm the appropriate distribution of stimulation, thermal RFA can then be performed for 90 seconds at 80° centigrade (Abbott NeuroTherm; Greyscale Medical). A C2 nerve block

Received November 26, 2021; accepted after revision January 14, 2022.

From the Departments of Radiology (J.L.C., E.S.Y.), and Orthopedics (D.R.L.), Hospital for Special Surgery, New York, New York; and Department of Radiology (M.R., T.K.M.), New York-Presbyterian Hospital/Weill Cornell Medicine, New York, New York.

Please address correspondence to J. Levi Chazen, MD, Spine Imaging, Hospital for Special Surgery, 535 E 70th St, NY, NY 10021; e-mail: chazenjl@hss.edu; @LeviChazen

Indicates article with online supplemental data.

<http://dx.doi.org/10.3174/ajnr.A7471>

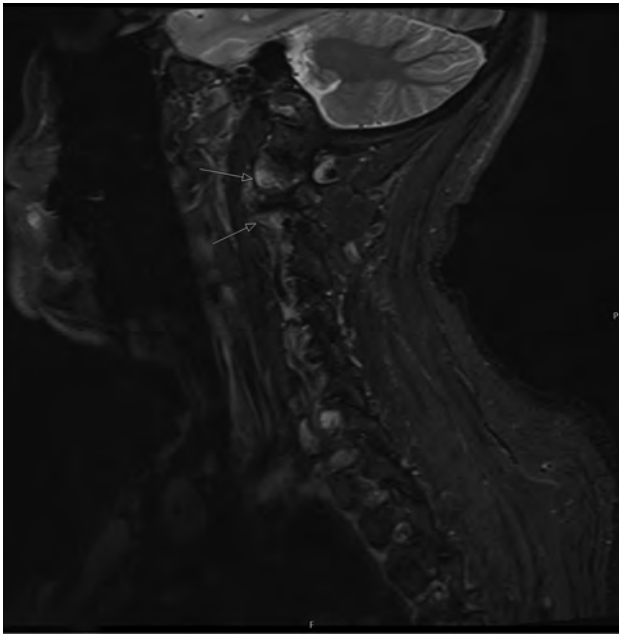


FIG 1. Sagittal STIR image (patient 11) of the cervical spine showing T2 hyperintense bone marrow edema (arrows) in the lateral atlantoaxial (C1–C2) articulation.

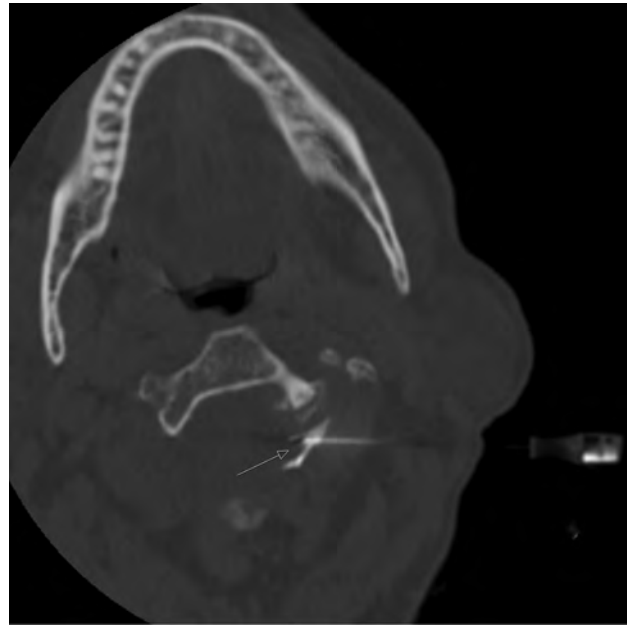


FIG 3. Intraprocedural axial CT image (patient 8) showing contrast injection surrounding the left the C2 DRG (arrow).

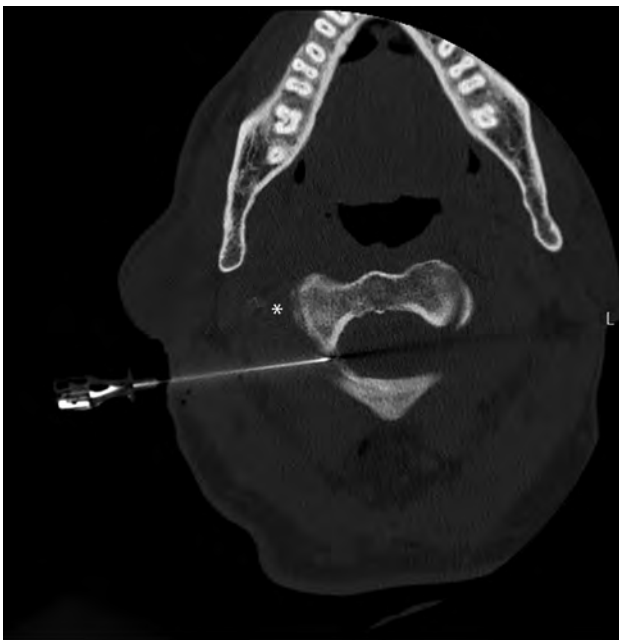


FIG 2. Intraprocedural axial CT image (patient 10) showing placement of a 22-ga RFA cannula at the expected location of the C2 DRG. The needle tip lies just above the C2 pedicle. The vertebral artery is safely located lateral to the C2 vertebral body at this level (asterisk).

is then performed using a 1:1 mixture of 1 mL preservative-free dexamethasone, 10 mg/mL, and 0.5% bupivacaine; the needle is removed and sterile dressing applied. Patients are observed for 1 hour and discharged home.

The mean preprocedural visual analog scale (VAS) pain score was 8 of 10. The mean postprocedural pain score was 2 of 10. (Table) There was a statistically significant reduction in the mean

Patient outcome

	Age (Yr)	Female	VAS Pre-Ablation	VAS Post-Ablation	VAS Reduction ^a
Mean	77	64%	8.2	1.9	77%
SD	7.8		1.7	1.6	

^a Statistically significant reduction in mean VAS as determined by the Wilcoxon signed-rank test ($P < .05$).

VAS score as determined by a 2-tailed Wilcoxon signed-rank test ($P = .003$). There were no major procedural complications. Three of 11 patients reported paresthesia in the occipital distribution with numbness and tingling. The mean follow-up was 10.4 months (range, 1–33 months). Most patients reduced or ceased the use of oral analgesics and reported improvement in lifestyle activities. All patients reported that they would undergo the procedure again if pain symptoms returned.

DISCUSSION

Cervicogenic headache can have a variety of causes, and an accurate diagnosis is required to guide management.¹² Significant overlap exists between cervicogenic headaches and other primary and secondary headache disorders, including migraine headache, tension-type headache, and occipital neuralgia.² Occipital neuralgia, another secondary headache syndrome with occipital pain as a key feature, differs from cervicogenic headaches in that it is characterized by paroxysmal shooting or stabbing pain over the posterior scalp, typically radiating from the suboccipital region toward the vertex.⁴ In this cohort, patients were screened using cervical MR imaging and only considered for ablation if C1–C2 lateral mass bone marrow edema was present ipsilateral to the site of occipital distribution pain.

Patients with cervicogenic headaches may respond to local anesthetic blockade of the occipital nerves (greater occipital nerve,

third occipital nerve, or both). The C2 DRG is the principal nerve root that contributes to the greater and lesser occipital nerves, providing an ideal target for ablation, because it only provides sensory innervation.^{13,14}

Patients should be considered for C2 DRG RFA if they present with cervicogenic headaches and have failed conservative treatment options, including physical therapy and medication therapy. Diagnostic injections may be performed to exclude a peripheral occipital nerve entrapment. MR imaging of the cervical spine should be performed to evaluate the facet joints and upper cervical nerve roots. In the authors' experience, a C2 nerve block without RFA does not provide sustained clinical relief, and the authors do not require a C2 block before performing C2 RFA. However, it is not unreasonable to consider a C2 anesthetic block to confirm the pain generator in cases in which it may be unclear.

Pre- or intra-procedural CT angiography may be performed to ensure a safe procedural approach. Vascular injury and vascular variants have been reported.^{15,16} The authors do not routinely perform vascular imaging before or during C2 ablation. However, pre-procedural cervical MR imaging was always reviewed with attention to the vertebral artery and branch vessel flow voids.

Conventional (thermal) RFA generates sustained high temperature surrounding the active tip of an insulated cannula, resulting in neurodestruction. Pulsed RF is an alternative to thermal RF and has advantages, including a decreased potential for local thermal injury and a decreased incidence of post-procedural inflammation. However, pulsed RF is typically less efficacious than thermal ablation, with patients experiencing a shorter duration of pain relief, often necessitating repeat procedures.¹⁷

Periprocedural inflammation can cause significant pain and may be distressing for patients. C2 RFA was followed by a C2 DRG nerve block in our cohort using a nonparticulate steroid mixed with a long-acting anesthetic (1 mL of preservative-free dexamethasone, 10 mg/mL, and 0.5% bupivacaine). Clinical improvement of pain may take 2–4 weeks after the ablation but appears to be durable with thermal RFA. None of the patients in this case series had recurrent symptoms during the study period.

No major complications were encountered. No patients in this cohort went on to surgical fusion during the study period. Adverse effects from the procedure include numbness and paresthesia in the occipital distribution. However, all patients indicated they would undergo the procedure again if symptoms returned and numbness did not negatively impact quality of life. Potential risks include intra-arterial or intrathecal puncture and injection of medication, CSF leak, spinal cord puncture, and vertebral artery injury with a risk of stroke.¹⁸

Surgical C1–C2 fusion may be considered for patients who fail or have a suboptimal clinical response to C2 RFA. In refractory cases of severe degenerative arthropathy of the C1–C2 articulation, a technique for surgical fusion was described by Goel and Laheri¹⁹ and popularized by Harms et al.²⁰ Patients with severe degenerative atlantoaxial arthropathy often have already lost a significant amount of cervical spine rotational motion, making surgical fusion for pain relief a viable option. In addition to the

benefit of the elimination of motion around the C2 DRG, direct surgical decompression may be performed; however, nerve root compression is often dynamic. Implantation of cervical interfacet spacers into the C1–C2 joint has been described as a technique for indirect decompression (restoration of C2 foraminal height) with successful results.²¹

In conclusion, CT-guided C2 RFA appears to be a safe and efficacious procedure for the treatment of cervicogenic headache in patients with C1–C2 lateral mass bone marrow edema and ipsilateral symptomatology. Further prospective study is necessary to fully elucidate the durability of this intervention and compare it with alternative treatment options.

Disclosure forms provided by the authors are available with the full text and PDF of this article at www.ajnr.org.

REFERENCES

1. Haldeman S, Dagenais S. **Cervicogenic headaches: a critical review.** *Spine J* 2001;1:31–46 CrossRef Medline
2. Blumenfeld A, Siavoshi S. **The challenges of cervicogenic headache.** *Curr Pain Headache Rep* 2018;22:47 CrossRef Medline
3. Janjua MB, Zhou PL, Greenfield JP, et al. **C2 and greater occipital nerve: the anatomic and functional implications in spinal surgery.** *Cureus* 2017;9:e1074 CrossRef Medline
4. Barmherzig R, Kingston W. **Occipital neuralgia and cervicogenic headache: diagnosis and management.** *Curr Neurol Neurosci Rep* 2019;19:20 CrossRef Medline
5. Bogduk N, Govind J. **Cervicogenic headache: an assessment of the evidence on clinical diagnosis, invasive tests, and treatment.** *Lancet Neurol* 2009;8:959–68 CrossRef Medline
6. Grandhi RK, Kaye AD, Abd-Elsayed A. **Systematic review of radiofrequency ablation and pulsed radiofrequency for management of cervicogenic headaches.** *Curr Pain Headache Rep* 2018;22:18 CrossRef Medline
7. Nagar VR, BIRTHI P, Grider JS, et al. **Systematic review of radiofrequency ablation and pulsed radiofrequency for management of cervicogenic headache.** *Pain Physician* 2015;18:109–30 CrossRef Medline
8. Lee HJ, Cho HH, Nahm FS, et al. **Pulsed radiofrequency ablation of the C2 dorsal root ganglion using a posterior approach for treating cervicogenic headache: a retrospective chart review.** *Headache* 2020;60:2463–72 CrossRef Medline
9. Hamer JF, Purath TA. **Response of cervicogenic headaches and occipital neuralgia to radiofrequency ablation of the C2 dorsal root ganglion and/or third occipital nerve.** *Headache* 2014;54:500–10 CrossRef Medline
10. Chazen JL, Ebani EJ, Virk M, et al. **CT-guided block and radiofrequency ablation of the C2 dorsal root ganglion for cervicogenic headache.** *AJNR Am J Neuroradiol* 2019;40:1433–36 CrossRef Medline
11. Olesen J. **International classification of headache disorders.** *Lancet Neurol* 2018;17:396–97 CrossRef Medline
12. Fredriksen TA, Antonaci F, Sjaastad O. **Cervicogenic headache: too important to be left un-diagnosed.** *J Headache Pain* 2015;16:6 CrossRef Medline
13. Shimohata K, Hasegawa K, Onodera O, et al. **The clinical features, risk factors, and surgical treatment of cervicogenic headache in patients with cervical spine disorders requiring surgery.** *Headache* 2017;57:1109–17 CrossRef Medline
14. Esposito MF, Malayil R, Hanes M, et al. **Unique characteristics of the dorsal root ganglion as a target for neuromodulation.** *Pain Med* 2019;20:S23–30 CrossRef Medline
15. Brinjikji W, Cloft H, Kallmes DF. **Anatomy of the posterior inferior cerebellar artery: relevance for C1–C2 puncture procedures.** *Clin Anat* 2009;22:319–23 CrossRef Medline

16. Katoh Y, Itoh T, Tsuji H, et al. **Complications of lateral C1-2 puncture myelography.** *Spine (Phila Pa 1976)* 1990;15:1085–87 CrossRef Medline
17. Zhang J, Shi DS, Wang R. **Pulsed radiofrequency of the second cervical ganglion (C2) for the treatment of cervicogenic headache.** *J Headache Pain* 2011;12:569–71 CrossRef Medline
18. Daniels SP, Schweitzer AD, Baidya R, et al. **The lateral C1-C2 puncture: indications, technique, and potential complications.** *AJR Am J Roentgenol* 2019;212:431–42 CrossRef Medline
19. Goel A, Laheri V. **Plate and screw fixation for atlanto-axial subluxation.** *Acta Neurochir (Wien)* 1994;129:47–53 CrossRef Medline
20. Harms J, Melcher RP. **Posterior C1-C2 fusion with polyaxial screw and rod fixation.** *Spine (Phila Pa 1976)* 2001;26:2467–71 CrossRef Medline
21. Cofano F, Sciarrone GJ, Pecoraro MF, et al. **Cervical interfacet spacers to promote indirect decompression and enhance fusion in degenerative spine: a review.** *World Neurosurg* 2019;126:447–52 CrossRef Medline

A New Frontier in Temporal Bone Imaging: Photon-Counting Detector CT Demonstrates Superior Visualization of Critical Anatomic Structures at Reduced Radiation Dose

J.C. Benson, K. Rajendran, J.I. Lane, F.E. Diehn, N.M. Weber, J.E. Thorne, N.B. Larson, J.G. Fletcher, C.H. McCollough, and S. Leng



ABSTRACT

BACKGROUND AND PURPOSE: Photon-counting detector CT is a new technology with a limiting spatial resolution of $\leq 150 \mu\text{m}$. In vivo comparisons between photon-counting detector CT and conventional energy-integrating detector CT are needed to determine the clinical impact of photon counting-detector CT in temporal bone imaging.

MATERIALS AND METHODS: Prospectively recruited patients underwent temporal bone CT examinations on an investigational photon-counting detector CT system after clinically indicated temporal bone energy-integrating detector CT. Photon-counting detector CT images were obtained at an average 31% lower dose compared with those obtained on the energy-integrating detector CT scanner. Reconstructed images were evaluated in axial, coronal, and Pöschl planes using the smallest available section thickness on each system (0.4 mm on energy-integrating detector CT; 0.2 mm on photon-counting detector CT). Two blinded neuroradiologists compared images side-by-side and scored them using a 5-point Likert scale. A post hoc reassignment of readers' scores was performed so that the scores reflected photon-counting detector CT performance relative to energy-integrating detector CT.

RESULTS: Thirteen patients were enrolled, resulting in 26 image sets (left and right sides). The average patient age was 63.6 [SD, 13.4] years; 7 were women. Images from the photon-counting detector CT scanner were significantly preferred by the readers in all reconstructed planes ($P < .001$). Photon-counting detector CT was rated superior for the evaluation of all individual anatomic structures, with the oval window (4.79) and incudostapedial joint (4.75) receiving the highest scores on a Likert scale of 1–5.

CONCLUSIONS: Temporal bone CT images obtained on a photon-counting detector CT scanner were rated as having superior spatial resolution and better critical structure visualization than those obtained on a conventional energy-integrating detector scanner, even with a substantial dose reduction.

ABBREVIATIONS: EID = energy-integrating detector; PCD = photon-counting detector

Photon-counting detector (PCD) CT is an emerging technology that has substantial promise in improving clinical imaging.^{1,2} Conventional CT scanners are equipped with energy-integrating detectors (EIDs) that use a scintillator to convert x-rays into visible light, which a photodiode converts to an electric signal. EID-CT requires the use of septa between detector elements, which limit spatial resolution.³ One CT manufacturer increased the available

spatial resolution of the system by using attenuating filters to reduce the effective pixel aperture;⁴ this use results in a decreased geometric dose efficiency, which requires an increase in the radiation dose to achieve the same noise level as an image without an attenuating filter (at lower spatial resolution). PCDs, conversely, directly transform photons into electric signal and record each individual photon and do not require septa between detector elements or the use of attenuating filters.⁵ Hence, PCDs allow more dose-efficient high-spatial-resolution imaging.^{6,7} In addition, the PCD assigns uniform weighting to each detected photon irrespective of its energy,⁸ which results in an improved SNR. PCD-CT also provides decreased beam-hardening artifacts^{9,10} and reduced electronic noise.^{1,11}

Zhou et al¹² have previously demonstrated, in a cadaver study, that the lack of attenuating filters with PCD-CT can result in an approximately 50% dose reduction if other acquisition parameters are kept unchanged. PCD-CT can also improve visualization of key anatomic structures, which may improve clinical

Received December 18, 2021; accepted after revision January 9, 2022.

From the Departments of Radiology (J.C.B., K.R., J.I.L., F.E.D., N.M.W., J.E.T., J.G.F., C.H.M., S.L.) and Quantitative Health Sciences (N.B.L.), Mayo Clinic, Rochester, Minnesota.

J.C. Benson and K. Rajendran contributed equally to this work.

Drs McCollough and Fletcher receive industry funding to their institution from Siemens, which includes in-kind support for the evaluated equipment.

Please address correspondence to John C. Benson, MD, Department of Radiology, Mayo Clinic, 200 First St SW, Rochester, MN 55905; e-mail: BensonJohn3@mayo.edu

Indicates article with online supplemental data.

<http://dx.doi.org/10.3174/ajnr.A7452>

diagnoses. On the basis of preliminary work,¹³ we designed a temporal bone PCD-CT protocol that uses up to 31% lower radiation dose and a reconstruction kernel with 35% higher cutoff spatial frequency compared with EID-CT with an attenuating filter, and a 0.2-mm section thickness, which is half of that used at EID-CT (0.4 mm). The purposes of this pilot study were to compare the capabilities of a PCD-CT system with EID-CT with an attenuating filter for temporal bone imaging and to provide examples of PCD-CT temporal bone imaging in patients with clinical indications.

MATERIALS AND METHODS

Patient Cohort

Patients referred for a clinically indicated temporal bone CT examination scanned using EID-CT scanners were prospectively recruited to undergo a research temporal bone CT scan on an investigational PCD-CT system. Written informed consent was obtained from all participants for this Health Insurance Portability and Accountability Act-compliant, institutional review board-approved study (Mayo Clinic, Rochester, MN, USA). Relevant clinical data, including but not limited to temporal bone surgical history and findings on the clinical EID-CT, were abstracted from the electronic medical record.

CT Protocol

EID-CT scans were performed on a third-generation EID-CT system (SOMATOM Force; Siemens) using a ultra-high-resolution mode (120 kV; mean volume CT dose index = 51.5 [SD, 3.8] mGy; pitch = 0.35, rotation time = 1 second), according to our routine clinical protocol, which uses a Ur77 reconstruction kernel and 0.4-mm section thickness (the minimal section thickness for this CT system).¹¹ The ultra-high-resolution protocol uses an attenuating filter.

The research PCD-CT scan was performed on an investigational PCD-CT system (SOMATOM Count Plus; Siemens; 120 kV, mean volume CT dose index = 35.6 [SD, 1.7] mGy, pitch = 1.0–1.2, rotation time = 1 second) using the high-resolution mode (120 × 0.2 mm collimation) with a dedicated sharp Hr84 kernel and the smallest section thickness of 0.2 mm that is not possible on the EID-CT system. The in-plane detector pixel size of the PCD-CT system is 0.275 mm,^{3,14,15} which translates to 0.151 mm at the isocenter. PCD-CT scans were performed at a 31% lower radiation dose compared with EID-CT (mean volume CT dose index = 35.6 versus 51.5 mGy). The dose-reduction factor for PCD-CT was determined by using phantom experiments and previously reported data¹³ that showed lower image noise on PCD-CT relative to EID-CT when the section thickness and kernel are matched between the 2 systems.

Image Review

CT images were reconstructed in axial, coronal, and Pöschl planes using the smallest available section thickness (0.2 mm for PCD-CT and 0.4 mm for EID-CT). Two neuroradiologists, each with >10 years of experience (J.I.L. and F.E.D.), independently evaluated paired PCD-CT and EID-CT images on a 2-monitor workstation (syngo via; Siemens).

The images on the viewing workstation were arranged in 2 rows of 3 panels on each of the 2 monitors, with a subject's right temporal bone on the left monitor and the left temporal bone on the right monitor. Axial, coronal, and Pöschl plane images from EID-CT or PCD-CT were randomly assigned to either the upper or lower row, with all information relating to the scanner type, acquisition settings, or image-reconstruction parameters hidden from the reader. For each temporal bone side, readers were instructed to compare the upper and lower rows for each imaging plane, evaluating the visualization of each of 7 critical anatomic structures. Readers were allowed to pan and zoom as needed, as well as to double-click on any image so that it filled the monitor for closer inspection.

Specific directions were provided regarding the plane that should be used to evaluate each anatomic structure: axial plane, round window, incudomalleolar joint, modiolus; coronal plane, oval window, scutum; Pöschl plane, modiolus; incudostapedial joint. If present, ossicular prostheses were evaluated in the best visualized plane.

Images on the lower row were scored using a 5-point Likert scale: 1 = inferior resolution with degraded visualization, 2 = slightly inferior resolution without affecting visualization, 3 = equivalent resolution and visualization, 4 = slightly superior resolution without affecting visualization, and 5 = superior spatial resolution with improved visualization. Readers were encouraged to make free text comments. After all anatomic structures were scored, an overall image-quality score considering image sharpness, noise level, and artifacts was provided using the 5-point Likert scale.

Additional oblique reformatted images were created by a non-reader neuroradiologist (J.C.B.) to demonstrate certain anatomic structures: the ossicles, ossicular prostheses, and otosclerosis. These images were not used by the readers as part of the formal side-by-side PCD-to-EID comparison and, therefore, were not scored; they were created for illustrative purposes only.

Statistical Analysis

The Likert visualization scores of anatomic structures and the overall image-quality scores for each temporal bone reflected the comparative image quality, with a score of 3 indicating equivalent image quality between the scored (lower) image and the reference (upper) image. Scores of 1 and 5 represented cases in which one scanner type demonstrated definite improvement in spatial resolution and visualization or image quality relative to the other scanner type. Post hoc, the scores were reassigned such that they reflected PCD-CT impressions relative to clinical routine EID-CT.

The mean scores for the 2 readers were calculated for each evaluated critical structure. A 1-sample Wilcoxon rank-sum test of the overall image quality score was performed to test for significant asymmetry of the Likert scores with respect to a score of 3 (equivalence) using the mean scores of the readers. Comparisons were performed for individual readers and anatomic structures in each plane and across readers and structures. No adjustment was performed for the left and right temporal bones in the same patient. A *P* value ≤ .05 was considered significant under a 2-

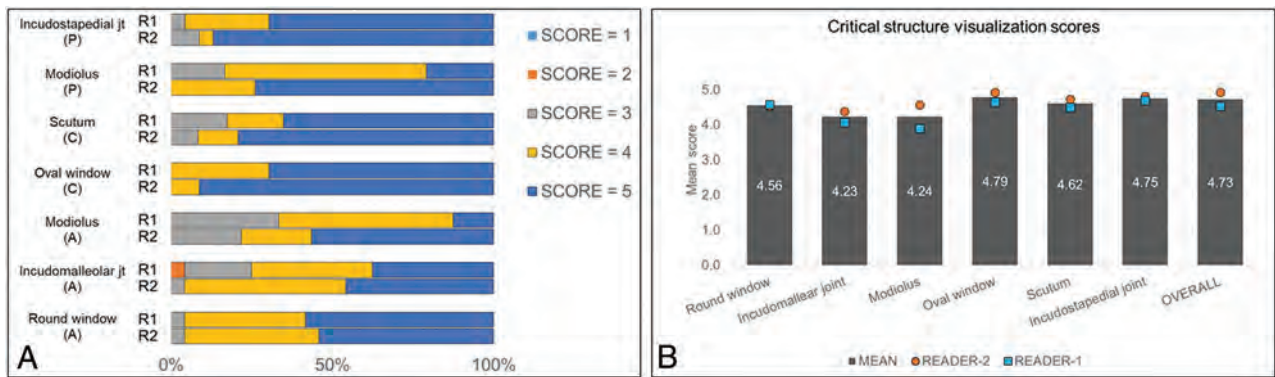


FIG 1. Readers' score distribution for spatial resolution and visualization of critical anatomic structures in different reformatted planes (A) and mean readers' scores for individual anatomic structures and overall image quality (B). All scores were based on a 5-point Likert scale, comparing PCD-CT with EID-CT: 1=inferior resolution with degraded visualization, 2=slightly inferior resolution without affecting visualization, 3=equivalent resolution and visualization, 4=slightly superior resolution without affecting visualization, and 5=superior spatial resolution with improved visualization.

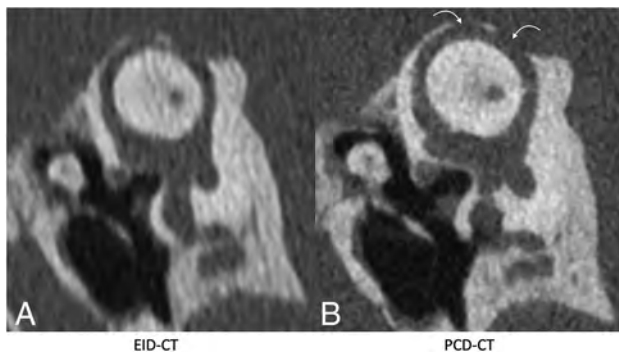


FIG 2. Pöschl reformatted images in a patient with superior semicircular canal dehiscence, shown on EID-CT (left) and PCD-CT (right) images. The PCD-CT image (B) clearly demonstrates 2 discrete regions of dehiscence (curved arrows). These regions are also identifiable on conventional EID-CT (A), though the intact adjacent bone is less well-visualized. The integrity of the roof of the superior semicircular canal was not formally evaluated in the readers' study but is shown for illustrative purposes.

sided alternative. Matlab, Version r2015b (MathWorks), was used for statistical analysis.

RESULTS

Thirteen patients underwent a clinically indicated temporal bone scan using the ultra-high-resolution mode of EID-CT followed by an investigational PCD-CT scan, yielding 26 temporal bone datasets (including the left and right temporal bones) for comparison. The average age was 63.6 [SD, 13.4] years; 7 patients were women (Online Supplemental Data). The clinical indications for the CT examinations were hearing loss in 10 patients, ear fullness with concern for eustachian tube dysfunction in 1 patient, and otitis media with a perforated tympanic membrane in 1 patient. Two patients had a stapes prosthesis in place from a prior surgery; 1 patient was status post resection of a vestibular schwannoma.

Figure 1 shows the neuroradiologists' comparison ratings for PCD-CT relative to EID-CT for each of the 7 critical anatomic

structures. For PCD-CT images assessed by reader one, 47% of the images received a score of five, 39% received a score of 4, and 13% received a score of 3. Reader 1 gave a score of 2 for the incudomalleolar joint (slightly inferior resolution without affecting visualization) for 1 of 182 PCD-CT images and noted the presence of artifacts in the free text comment. For PCD-CT images assessed by reader two, 71% of the images received a score of five, 22% received a score of 4, and 7% received a score of 3.

Of the evaluated critical structures, the oval window received the highest mean reader score (4.79), followed by the incudostapedial joint (4.75). Additionally, the visualization of semicircular canal dehiscence was substantially enhanced on the PCD-CT Pöschl reformats as illustrated in Fig 2.

For overall image quality, PCD-CT received a mean score of 4.92 (SD, 0.27) for reader 1, and 4.54 (SD, 0.50) for reader 2, with PCD-CT found to be significantly better than EID-CT for overall image quality ($P < .001$). In 3 of 13 patients, the readers commented about the presence of minor artifacts (windmill effect in 1 patient) and slightly higher image noise (in 2 patients) on PCD-CT images; however, this did not substantially impact the visualization of critical structures (the PCD-CT overall image-quality score in these patients was ≥ 4 from both readers).

Images reformatted in oblique planes for illustrative purposes are shown in Figs 3–6. These images show the ability of PCD-CT to improve the visualization of ossicular anatomy (Fig 3), providing a more direct assessment of the incudostapedial joint (Fig 4), the anatomic relationship between a stapes piston and nearby structures (Fig 5), and the relationship between the anterior crus of the stapes and an area of otosclerosis (Fig 6).

DISCUSSION

This study represents one of the first in vivo, side-by-side comparisons of PCD-CT and EID-CT in temporal bone imaging. The results and the illustrative cases convincingly demonstrate the benefit of PCD-CT with 0.2-mm image thickness relative to an EID-CT with 0.4-mm image thickness for temporal bone imaging. In addition, a 31% decrease in the radiation dose was achieved due to the differences in the technologies. The 2 readers

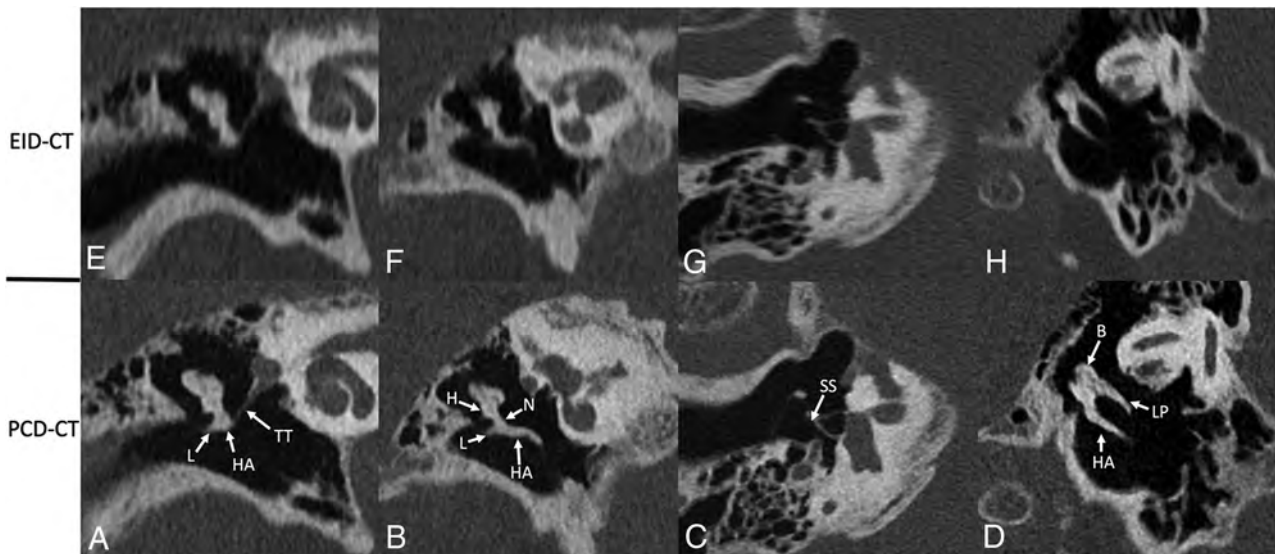


FIG 3. Ossicular anatomy, shown on conventional EID-CT (*upper row*) and PCD-CT (*lower row*). Reformatted images along the plane of the tensor tympani (*A and E*) demonstrate the tensor tympani (TT) extending to the upper handle of the malleus (HA); the lateral process (L) of the malleus is also clearly visible. An image reformatted along the long plane of the malleus (*B and F*) shows its handle (HA), lateral process (L), neck (N), and head (H). An image reformatted along the length of the stapes (*C and G*) clearly demonstrates the suprastructure (SS) and both crura. A “molar tooth” reformatted image (*D and H*) shows the HA of the malleus, as well as the body (B) and long process (LP) of the incus. These additional reformatted images were generated by a nonreviewer radiologist to demonstrate certain anatomic features but were not used by the readers to score image quality.

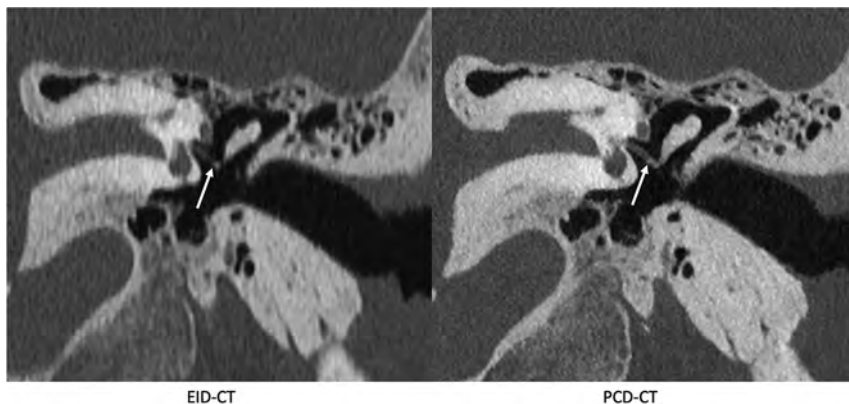


FIG 4. The incudostapedial joint (*arrows*), shown on EID-CT (*left*) and PCD-CT (*right*) images. The joint was one of several anatomic structures specifically graded using a 5-point Likert score, with higher scores favoring the quality of the PCD-CT images. The images reformatted in this plane were generated by a nonreviewer radiologist to demonstrate certain anatomic features but were not used by the readers to score image quality.

rated the PCD-CT images to be considerably sharper in multiple planes of reconstruction than those from the EID-CT scanner, which consequently improved critical structure visualization.

Prior studies have demonstrated noise reduction for temporal bone imaging using PCD-CT, as well as the radiologists’ preference for PCD-CT images relative to EID-CT with an attenuating filter.^{12,16,17} Leng et al⁵ compared PCD-CT images with EID-CT images in a limited number of patients, covering examples from lung, joint, vascular, and temporal bone examinations. The authors reported a 21% noise reduction on PCD-CT temporal bone images, though only a single axial-plane image is shown as an example. A study using cadavers reported a 29% dose reduction in

temporal bone imaging on a PCD-CT scanner, though also without reformatted examples.¹⁶ These previous studies evaluated temporal bone images in axial planes at 0.25 mm, while the current study used a 0.2-mm section thickness in reformatted planes. The current study also demonstrated a 31% lower dose on PCD-CT relative to EID-CT. Further dose reduction could be achieved using a tin filter,^{17,18} which was not available on the PCD-CT system at the time of this investigation.

On the basis of our results, we anticipate that PCD-CT will be especially advantageous in temporal bone imaging because precise evaluation of the anatomically complex region often requires optimized reformatted imaging at a high spatial resolution.¹⁹ As shown in the illustrative cases of this pilot study, certain disease entities such as otosclerosis and superior semicircular canal dehiscence are much better demonstrated on PCD-CT images. In addition, the investigated PCD-CT technology will likely lead to improved evaluation of the ossicles in various planes due to reduced partial volume averaging enabled by the 0.2-mm section thickness. This improvement will allow better visualization of ossicular anomalies, postoperative changes related to ossicular prostheses, and the integrity of the incudostapedial articulation, among other aspects of temporal bone anatomy and postoperative findings.

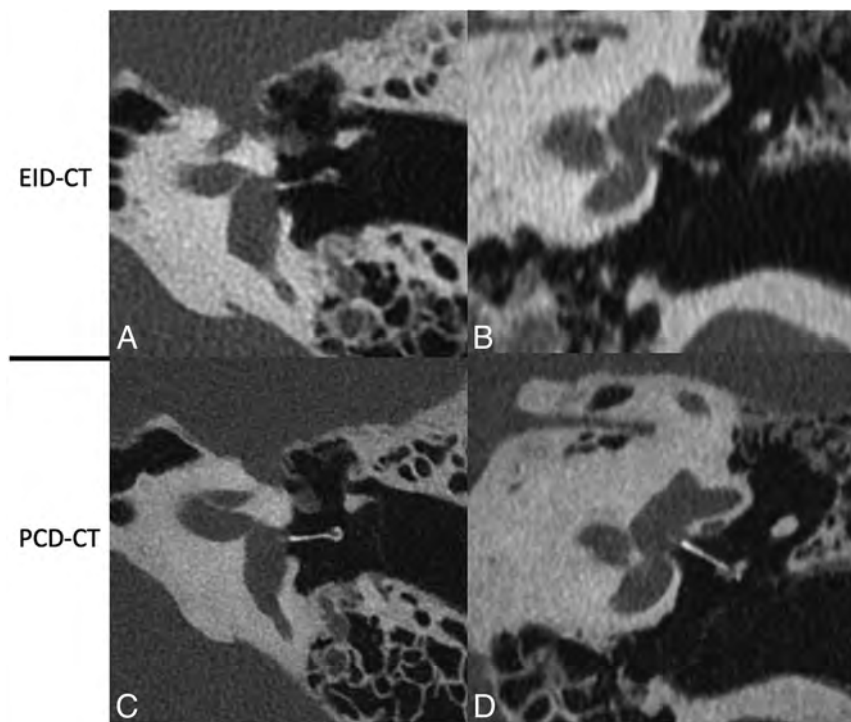


FIG 5. A stapes piston prosthesis shown on EID-CT (upper row) and PCD-CT (lower row) images. The prosthesis is shown on oblique axial (A and C) and oblique coronal (B and D) reformats along the plane of the piston. In both planes, the stapes prosthesis was better delineated on PCD-CT due to reduced partial volume averaging from 0.2 mm sections. These additional reformatted images were generated by a nonreviewer radiologist to demonstrate certain anatomic features but were not used by the readers to score image quality.

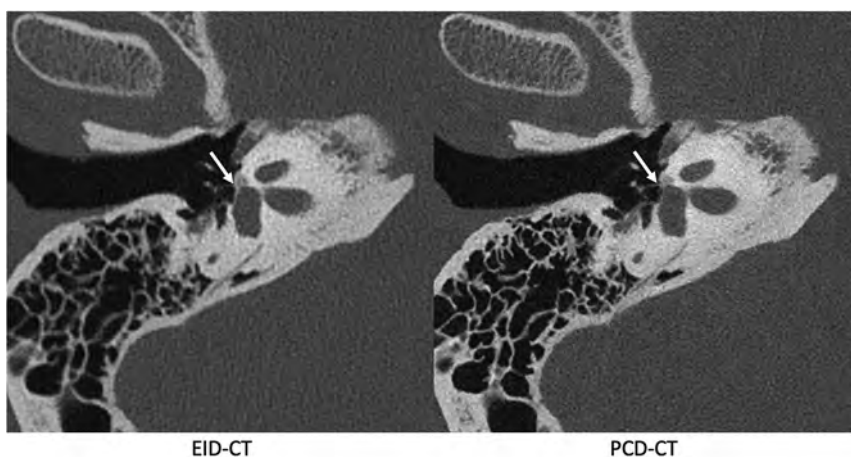


FIG 6. Images reformatted along the long axis of the stapes in a patient with fenestral otosclerosis shown on EID-CT (left) and conventional PCD-CT (right) images. The arrow points to the insertion of the anterior crus of the stapes into the region involved by otosclerosis. These additional reformatted images were generated by a nonreviewer radiologist to demonstrate certain anatomic features but were not used by the readers to score image quality.

The study had limitations. First, no independent reference standard was used in the readers' study for diagnostic truth. Instead, side-by-side blinded comparisons of PCD-CT and EID-CT images were performed, with scores assigned to 1 of the 2 modalities to assess the relative performance for image spatial resolution and visualization of critical structures. Because our primary

goal

in this study was to demonstrate improved spatial resolution and visualization from PCD-CT by leveraging sharper reconstruction kernels and a smaller section thickness (0.2 mm) not possible or available on EID-CT, we did not pursue aggressive dose-reduction strategies. Nonetheless, the overall image-quality score that reflects both image noise (a function of radiation dose) and sharpness showed that both readers favored PCD-CT images despite a 31% dose reduction.

CONCLUSIONS

The results of this patient study together with prior phantom and cadaveric studies suggest that PCD-CT offers substantial advantages over EID-CT with an attenuating filter for imaging the temporal bone. Temporal bone imaging seems particularly likely to benefit from the advantages of PCD-CT, given the submillimeter size of important anatomic structures.

ACKNOWLEDGMENTS

The authors thank Holly Kasten, Yong Lee, and Boleyn Andrist for patient recruitment and scanning and Elisabeth Shanblatt, PhD, for scanner support.

Disclosure forms provided by the authors are available with the full text and PDF of this article at www.ajnr.org.

REFERENCES

1. Willemink MJ, Persson M, Pourmorteza A, et al. **Photon-counting CT: technical principles and clinical prospects.** *Radiology* 2018;289:293–12 CrossRef Medline
2. Pourmorteza A, Symons R, Sandfort V, et al. **Abdominal imaging with contrast-enhanced photon-counting CT: first human experience.** *Radiology* 2016;279:239–45 CrossRef Medline
3. Flohr T, Petersilka M, Henning A, et al. **Photon-counting CT review.** *Phys Med* 2020;79:126–36 CrossRef Medline
4. Flohr TG, Stierstorfer K, Suss C, et al. **Novel ultrahigh resolution data acquisition and image reconstruction for multi-detector row CT.** *Med Phys* May 2007;34:1712–23 CrossRef Medline
5. Leng S, Rajendran K, Gong H, et al. **150- μ m spatial resolution using photon-counting detector computed tomography technology: technical performance and first patient images.** *Invest Radiol* 2018;53:655–62 CrossRef Medline

6. Danielsson M, Persson M, Sjolín M. **Photon-counting x-ray detectors for CT.** *Phys Med Biol* 2021;66:03TR01 CrossRef Medline
7. Mannil M, Hicketier T, von Spiczak J, et al. **Photon-counting CT: high-resolution imaging of coronary stents.** *Invest Radiol* 2018;53:143–49 CrossRef Medline
8. Schmidt TG. **Optimal “image-based” weighting for energy-resolved CT.** *Med Phys* 2009;36:3018–27 CrossRef Medline
9. Do TD, Sawall S, Heinze S, et al. **A semi-automated quantitative comparison of metal artifact reduction in photon-counting computed tomography by energy-selective thresholding.** *Sci Rep* 2020;10:21099 CrossRef Medline
10. Zhou W, Bartlett DJ, Diehn FE, et al. **Reduction of metal artifacts and improvement in dose efficiency using photon-counting detector computed tomography and tin filtration.** *Invest Radiol* 2019;54:204–11 CrossRef Medline
11. Yu Z, Leng S, Kappler S, et al. **Noise performance of low-dose CT: comparison between an energy integrating detector and a photon counting detector using a whole-body research photon counting CT scanner.** *J Med Imaging (Bellingham)* 2016;3:043503 CrossRef Medline
12. Zhou W, Lane JI, Carlson ML, et al. **Comparison of a photon-counting-detector CT with an energy-integrating-detector CT for temporal bone imaging: a cadaveric study.** *AJNR Am J Neuroradiol* 2018;39:1733–38 CrossRef Medline
13. Rajendran K, Petersilka M, Henning A, et al. **Full filed-of-view, high-resolution, photon-counting detector CT: technical assistant and initial patient experience.** *Phys Med Biol* 2021;66:20 CrossRef Medline
14. Ferda J, Vendiš T, Flohr T, et al. **Computed tomography with a full FOV photon-counting detector in a clinical setting, the first experience.** *Eur J Radiol* 2021;137:109614 CrossRef Medline
15. Grunz JP, Huflage H, Heidenreich JF, et al. **Image quality assessment for clinical cadmium telluride-based photon-counting computed tomography detector in cadaveric wrist imaging.** *Int Radiol* 2021;56:785–90 CrossRef Medline
16. Leng S, Yu Z, Halaweish A, et al. **Dose-efficient ultrahigh-resolution scan mode using a photon counting detector computed tomography system.** *J Med Imaging (Bellingham)* 2016;3:043504 CrossRef Medline
17. Rajendran K, Voss BA, Zhou W, et al. **Dose reduction for sinus and temporal bone imaging using photon-counting detector CT with an additional tin filter.** *Invest Radiol* 2020;55:91–100 CrossRef Medline
18. Kim CR, Jeon JY. **Radiation dose and image conspicuity comparison between conventional 120kVp and 150kVp with spectral beam shaping for temporal bone CT.** *Eur J Radiol* 2018;102:68–73 CrossRef Medline
19. Juliano AF. **Cross-sectional imaging of the ear and temporal bone.** *Head Neck Pathol* 2018;12:302–20 CrossRef Medline

Prediction of Wound Failure in Patients with Head and Neck Cancer Treated with Free Flap Reconstruction: Utility of CT Perfusion and MR Perfusion in the Early Postoperative Period

Y. Ota, A.G. Moore, M.E. Spector, K. Casper, C. Stucken, K. Malloy, R. Lobo, A. Baba, and A. Srinivasan



ABSTRACT

BACKGROUND AND PURPOSE: Free flap reconstruction in patients with head and neck cancer carries a risk of postoperative complications, and radiologic predictive factors have been limited. The aim of this study was to assess the factors that predict free flap reconstruction failure using CT and MR perfusion.

MATERIALS AND METHODS: This single-center prospective study included 24 patients (mean age, 62.7 [SD, 9.0] years; 16 men) who had free flap reconstruction from January 2016 to May 2018. CT perfusion and dynamic contrast-enhanced MR imaging with conventional CT and MR imaging were performed between 2 and 4 days after the free flap surgery, and the wound assessments within 14 days after the surgery were conducted by the surgical team. The parameters of CT perfusion and dynamic contrast-enhanced MR imaging with conventional imaging findings and patient demographics were compared between the patients with successful free flap reconstruction and those with wound failure as appropriate. $P < .05$ was considered significant.

RESULTS: There were 19 patients with successful free flap reconstruction and no wound complications (mean age, 63.9 [SD, 9.5] years; 14 men), while 5 patients had wound failure (mean age, 58.0 [SD, 5.7] years; 2 men). Blood flow, blood volume, MTT, and time maximum intensity projection ($P = .007, .007, .015,$ and $.004,$ respectively) in CT perfusion, and fractional plasma volume, volume transfer constant, peak enhancement, and time to maximum enhancement ($P = .006, .039, .004,$ and $.04,$ respectively) in dynamic contrast-enhanced MR imaging were significantly different between the 2 groups.

CONCLUSIONS: CT perfusion and dynamic contrast-enhanced MR imaging are both promising imaging techniques to predict wound complications after head and neck free flap reconstruction.

ABBREVIATIONS: AIF = arterial input function; DCE = dynamic contrast-enhanced; EES = extravascular extracellular space; IQR = interquartile range; K_{ep} = rate transfer constant between EES and blood plasma per minute; K^{trans} = volume transfer constant between EES and blood plasma per minute; SCC = squamous cell carcinoma; TME = time to maximum enhancement; tMIP = time maximum intensity projection; V_e = EES volume per unit tissue volume; V_p = fractional plasma volume

Head and neck cancer continues to carry a high risk of morbidity and mortality despite major advances in the fields of oncology and surgery.¹⁻³ One of the most impactful advances has been the ability to perform extensive surgical dissection followed by

microvascular free tissue transfer.⁴ Free flap viability with careful wound management is the key in the overall success of the procedure. Within the first 2 weeks after the operation, the flap is perfused solely by the anastomosed microvascular bed before endothelialization, inosculation of the anastomosis flap, and neoangiogenesis; thus, it is at highest risk for vascular thrombosis resulting in flap failure.⁵ Multiple large studies have determined a combined 10%–40% risk of wound complications such as partial flap necrosis, wound breakdown, and fistula, with approximately 10% requiring surgical exploration in the setting of decreased viability.⁶⁻⁸ Several studies have assessed the presurgical risk profile for the subsequent development of wound complications in head and neck free flaps such as diabetes, smoking history, preoperative radiation and chemotherapy history, and prolonged surgery time.⁹⁻¹¹

A variety of techniques has been used to assess and monitor the perfusion of free flaps,¹² and Doppler ultrasound and skin paddle monitor have become the most popular methods. However, these

Received September 27, 2021; accepted after revision January 8, 2022.

From the Division of Neuroradiology (Y.O., R.L., A.B., A.S.), Department of Radiology, and Department of Otolaryngology (M.E.S., K.C., C.S., K.M.), University of Michigan, Ann Arbor, Michigan; and Department of Radiology (A.G.M.), Western Michigan University, Kalamazoo, Michigan.

This work received funding from the American Society of Head and Neck Radiology under the William N. Hanafee MD Research Grant and from the Internal Seed Grant of the Department of Radiology at the University of Michigan.

Please address correspondence to Ashok Srinivasan, MD, Division of Neuroradiology, Department of Radiology, B2-A209UH, University of Michigan, Michigan Medicine, 1500 E Medical Center Dr, Ann Arbor, MI, 48109; e-mail: ashoks@med.umich.edu

Indicates open access to non-subscribers at www.ajnr.org

Indicates article with online supplemental data.

<http://dx.doi.org/10.3174/ajnr.A7458>

methods assess only superficial vasculature and are not suitable for the assessment of the deep tissue vasculature. A single study assessed the role of CTA in the diagnosis of pedicle vascular stenosis in patients with head and neck microvascular free flap reconstruction and showed a sensitivity of 63% for detecting vascular pedicle stenosis.¹³ While CTA can provide additional information for clinicians to use in the monitoring of flap viability, CTA cannot assess microperfusion alterations that play a crucial role in flap viability. During the early postoperative period when the flap vascularity is solely dependent on the microvascular anastomoses, noninvasive tissue-level perfusion imaging may provide predictive information for the development of wound failure and may also be used for risk-stratification and treatment protocols. The perfusion technique has been used for the assessment of microperfusion for disease differentiation and treatment-response prediction in the head and neck.¹⁴⁻¹⁷ However, there are no studies in the literature using CT and MR perfusion for the assessment of head and neck free flap viability in the early postoperative period.

Our study was, therefore, designed to assess predictive factors for the development of wound complications in patients undergoing free flap reconstruction using CT and MR perfusion.

MATERIALS AND METHODS

The institutional review board of University of Michigan approved this prospective single-center research study, and informed consent for participation in this research was obtained from all participants. Data were acquired in compliance with all applicable Health Insurance Portability and Accountability Act regulations.

Study Population

We initially enrolled 38 patients at our institution from January 2016 to May 2018, according to the inclusion and exclusion criteria listed below.

Inclusion criteria were as follows:

1. Patients in the early postoperative period (days 2–4) following free flap reconstruction for head and neck malignancy, non-functional larynx, or other complications due to previous radiation therapy
2. Patients considered clinically at high risk for decreased tissue viability, defined as patients with a history of head and neck radiation
3. Patients who signed informed consent prior to imaging.

Exclusion criteria were as follows:

1. Patients who tested positive for pregnancy
2. Patients who were younger than 18 years of age
3. Patients with contraindications to MRI due to noncompatible devices such as cardiac pacemakers, other implanted electronic devices, metallic prostheses, or ferromagnetic prostheses (eg, pins in artificial joints and surgical pins/clips)
4. Patients with contraindications to CT with IV contrast or to gadolinium administration.

Patient eligibility was confirmed with our inclusion and exclusion criteria, and patients were approached for enrollment in the study before their operation. While 38 patients consented before their operation, 14 patients dropped out of the study on the day

of their scheduled scans. All patients were maintained in a reverse Trendelenburg position during the postoperative period in their recovery beds to help reduce facial and neck swelling; among the total 38 patients, the 14 patients who dropped out were unsure if they could lie flat for longer than 5 minutes to tolerate the CT perfusion and/or dynamic contrast-enhanced (DCE)-MR imaging scans. Therefore, the final inclusion in our study was 24 participants (mean age, 62.7 [SD, 9.0] years; 16 men) who had free flap reconstruction and postsurgery imaging.

Determination of Wound Failure

Patients were hospitalized following their operation at the discretion of the head and neck surgeon. The wound was examined twice per day by the surgical team, and the status of the wound was electronically recorded for documentation. Free flap viability was checked every hour for the first 24 hours, every 2 hours for the second 24 hours, every 4 hours for postoperative third-to-seventh day, and every 8 hours after the seventh postoperative day. The free flap was assessed by a variety of methods, including skin paddle evaluation when applicable and external Doppler ultrasound for the main anastomotic pedicle. The patients were discharged after confirmation of a general condition of stability and absence of wound complications. The patients returned to the outpatient clinic to have the wound checked 1 week after discharge.

Wound failure was assessed by the surgical team during the hospitalization period and at the first postoperative appointment. Wound failure was considered “positive” by the following definitions: total flap loss, partial flap loss, wound dehiscence (separation of skin edges), native skin breakdown, and the presence of a pharyngocutaneous fistula or the conditions requiring re-operation such as venous congestion and ecchymosis of a free flap.

Imaging Protocol

All imaging was obtained within 2–4 days following the operation during the inpatient admission phase.

CT Perfusion Protocol. Axial images were obtained on a 64-section MDCT scanner (HD750; GE Healthcare) following the administration of 75 mL of iopamidol injection (Isovue 300; Bracco) at a 5-mm section thickness, 40-mm z-axis coverage, 50-second scan duration, 5-second start delay, and 1-second delay between images. Conventional CT images at 1.25-mm section thickness were then obtained for the entire neck 35 seconds after the administration of an additional 75 mL of iopamidol.

DCE-MR Imaging Protocol. Following the acquisition of precontrast T1WI and T2WI through the ROI at 3-mm section thickness on a 3T magnet (Ingenia; Philips Healthcare), a DCE-MR imaging sequence was performed using 3D T1-weighted fast-field echo. The parameters of 3D T1 fast-field echo were as follows: TR = 4.6 ms; TE = 1.86 ms; flip angles = 5°, 10°, 15°, 20°, and 30°; section thickness = 2.5 mm; FOV = 240 × 240 mm²; voxel size = 1.0 × 1.0 × 5.0 mm³; NEX = 1; number of slices per dynamic scan = 48; temporal resolution = 8.4 seconds; and total acquisition time = 4 minutes and 13 seconds, using a 16-channel Neurovascular Array Coil (Medrad) with the administration of gadobenate dimeglumine contrast (MultiHance; Bracco Diagnostics). An intravenous bolus of 20 mL of gadobenate

dimeglumine was administered using a power injector with a flow rate of 5.0 mL/s through a peripheral arm vein, followed by a 20-mL saline flush. These techniques were performed for all patients at a single center (University of Michigan).

The CT and MR imaging were both completed on the same day for all patients. The MR imaging was completed before the CT. While the entire free flap was covered on the DCE-MR imaging acquisition in the z-axis, only the central 4 cm demonstrating the region of anastomosis was covered on the CT perfusion acquisition. At the time of implementation of the study, we did not have the shuttle mode available on all the CT scanners running on the MDCT scanner platform at our institution, which could have increased our z-axis coverage to 8 cm. Hence, we elected to keep the z-axis coverage to the standard 4 cm on these research scans to avoid introducing more heterogeneity in the protocols.

Data Analysis

Patient Demographics. The patient demographics were reviewed from the electronic medical record and included the following information: age, sex, history of diabetes, history of chronic kidney disease, history of hypertension, body mass index, the original pathology and its staging, types of surgeries, history of radiation and chemotherapy, types of free flap, ischemia time (the time from disconnection of the free flap to the time to connect the flap to vessels in the neck), and wound infections.

Conventional Imaging Characteristics. All conventional CT and MR images were reviewed by a board-certified radiologist with 7 years of experience in neuroradiology and a board-certified otolaryngologist with 14 years of experience. They were aware of patients' demographics but blinded to whether the patients experienced postoperative complications. With consensus, they evaluated imaging characteristics using the following metrics:

1. Fluid collections in the postsurgical area, evaluated on CT and T2WI, recorded as binary variables (yes/no), and defined as a low-density area on CT and a hyperintense area on T2WI
2. Pedicle vascular structures within the free flap, evaluated on postcontrast CT, recorded as binary variables (yes/no), and defined as enhanced linear or tortuous structures on postcontrast CT and T1WI. The presence of venous thrombosis was recorded if present and recognized.

CT Perfusion Analysis. All analyses in CT perfusion were performed using commercially available software (Olea Sphere, Version 3.0; Olea Medical). The radiologist with 7 years' experience and the otolaryngologist with 14 years' experience manually placed 5 separate ROIs on postcontrast head and neck CT scans with consensus and transferred them to the perfusion maps. The ROIs were carefully placed in the junctional areas of the free flap in the head and neck, avoiding placement of the ROIs in fluid collections or in the areas where streak or other artifacts degraded the imaging quality. These were not restricted to 1 axial section, were based on the orientation of the flap, and covered 1–3 axial slices in all patients. The values of generated CT perfusion parameters (blood volume, blood flow, TTP, time-to-maximum, MTT, and time maximum intensity projection (tMIP) of the 5 ROIs were averaged. We had decided to measure 5 separate ROIs because of

the need to identify different areas of the free flap that may be affected differentially by perfusion abnormalities. An arterial input function (AIF) was calculated automatically using cluster analysis techniques, and deconvolution of the AIF was performed with a time-insensitive block-circulant singular-value decomposition.¹⁸ While this process was automated, the corresponding density time curves that demonstrated a rapid increase in density with sharp peaks were deemed appropriate and accurate for analysis.

DCE-MR Imaging Analysis. All quantitative analyses in DCE-MR imaging were performed using the OleaSphere 3.0 software permeability module, which is based on the extended Tofts model, by which pixel-based parameter maps are calculated from time-intensity curves. The radiologist with 7 years' experience and the otolaryngologist with 14 years' experience manually placed 5 separate ROIs on the conventional T1 postcontrast images and transferred them to the permeability maps with consensus. The ROIs were carefully placed in the junctional areas of the free flap in the head and neck, avoiding placement in fat tissues and fluid collections or in the areas where susceptibility artifacts from blood products or surgical clips degraded the imaging quality. Similar to the CT perfusion analysis, these were not restricted to 1 axial section, were based on the orientation of the flap, and covered 1–3 axial slices in all patients. The calculated quantitative parameters were fractional plasma volume (V_p), extravascular extracellular space (EES) volume per unit tissue volume (V_e), the volume transfer constant between EES and blood plasma per minute (K^{trans}), and the rate transfer constant between EES and blood plasma per minute (K_{ep}).

Semiquantitative analysis was also performed using the same ROIs described above with the Olea Sphere 3.0 software permeability module. The averaged signal intensity within the ROIs was plotted against time, and time-intensity curves were constructed. The following parameters were calculated on a pixel-by-pixel basis from time-intensity curves: area under curve (the relative quantity of contrast agent across time), peak enhancement (maximum concentration of contrast agent), wash-in (velocity of enhancement), washout (velocity of enhancement loss), maximum signal-enhancement ratio, and time to maximum enhancement (TME). The values of DCE-MR imaging quantitative and semiquantitative parameters of the 5 ROIs were averaged. The AIF was individually computed, and AIF curves with a rapid increase in signal enhancement and a sharp peak followed by minimal temporal noises were chosen for DCE analysis. Representative cases of the group with successful flap reconstruction and the group with wound failure are shown in Figs 1 and 2.

Statistical Analysis

This cohort was divided into 2 groups: the group with successful free flap reconstruction (group I) and the group with any type of wound failure (group II, defined as total flap loss, partial flap loss, wound dehiscence [separation of skin edges], native skin breakdown, the presence of pharyngocutaneous fistula, or a condition that needed a re-operation such as venous congestion and ecchymosis of a free flap).

As for the patient demographics and conventional imaging characteristics, age was compared using an unpaired *t* test, and body mass index and ischemia time were compared using the

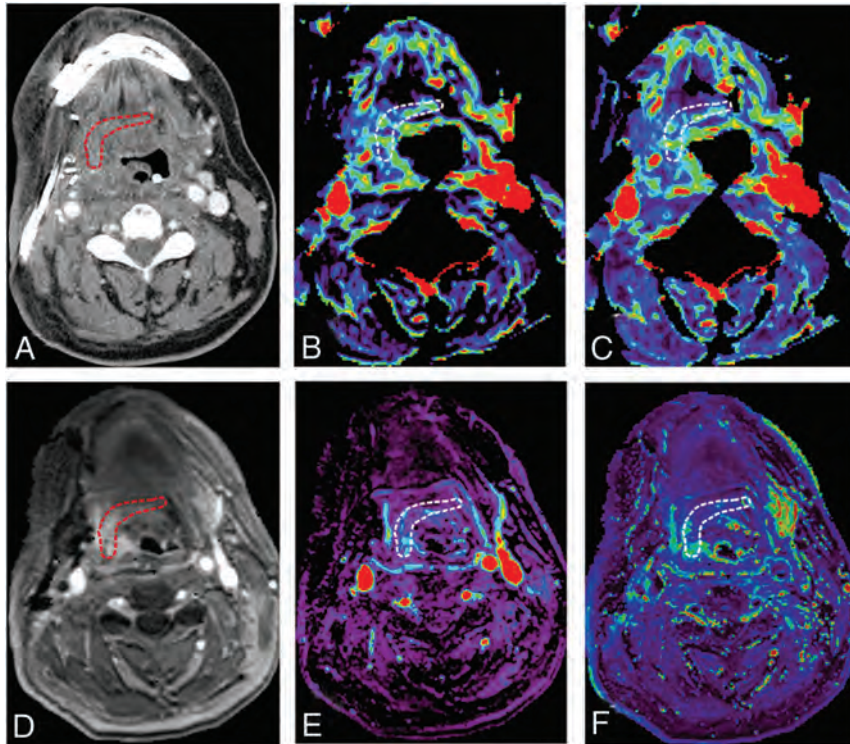


FIG 1. A 49-year-old male with tonsillar squamous cell carcinoma was treated with glossectomy, mandibulotomy, and neck dissection. An anterolateral thigh free flap was utilized for treatment of the soft tissue defect. No wound failure was observed. DCE-MR imaging and CT perfusion were performed 3 days after the surgery. **A**, An ROI is placed within the junctional area of the free flap on contrast enhanced CT. **B**, Blood volume (mL/100 ml) and **C**, blood flow (mL/100 ml/min) are calculated and are 7.67 mL/100 ml, 29.7 mL/100 ml/min, respectively. **D**, An ROI is placed on the permeability map within the junctional area of the free flap and DCE-MR imaging parameters are calculated. **E**, Vp and **F**, K^{trans} (minute⁻¹) are 0.17 and 0.19 (minute⁻¹), respectively. Red and white circled areas represent region of interests.

Mann-Whitney *U* test. Binary or categorical variables such as sex, history of diabetes, history of chronic kidney disease, history of hypertension, history of radiation and chemotherapy therapy, the presence of wound infections, fluid collections in the postsurgical areas, and pedicle vascular structures were compared using the Fisher exact test between 2 groups.

As for CT perfusion parameters (blood volume, blood flow, TTP, time-to-maximum, MTT, and tMIP) and DCE-MR imaging parameters (Vp, Ve, K^{trans} , Kep, area under curve, peak enhancement, wash-in, washout, maximum signal-enhancement ratio, and TME), these were compared using the Mann-Whitney *U* test and are described as median (interquartile range [IQR]).

For values that showed statistically significant differences in CT perfusion parameters and DCE-MR imaging parameters, the optimal cutoff values in receiver operating characteristic analysis were determined as a value to maximize the Youden index (sensitivity + specificity - 1). The diagnostic performances (sensitivity, specificity, positive predictive value, negative predictive value, and accuracy) were calculated on the basis of the cutoff values.

All statistical calculations were conducted with R statistical and computing software (Version 4.1.1; <http://www.r-project.org>) in this study. Variables with $P < .05$ were considered statistically significant.

RESULTS

Group I was composed of 19 patients (mean age, 63.9 [SD, 9.5] years; 14 men), and group II had 5 patients (mean age, 58.0 [SD, 5.7] years; 2 men). Group II consisted of 1 case of partial flap loss, 3 cases of pharyngocutaneous fistula, and 1 case of venous congestion and ecchymosis of a free flap with a reoperation.

The partial flap loss occurred 11 days after the operation; pharyngocutaneous fistula, 7, 9, and 10 days after the surgery; and venous congestion, 2 days after the surgery.

The types of free flap were anterolateral thigh free flaps (18/24), radial forearm free flap (1/24), latissimus dorsi free flap (2/24), gastro-omental free flap and split thickness skin graft (1/24), and scapula free flap with latissimus dorsi (2/24). Three anterolateral thigh free flaps and 2 scapula free flaps with the latissimus resulted in wound failure.

The original pathologies were all irradiated previously. The indications for free flap reconstruction were recurrence of the following pathologies or complications of radiation therapy: supraglottic squamous cell carcinoma (SCC) (7/24), recurrent glottic SCC (6/24), a nonfunctional larynx due to previous radiation therapy (4/24), osteoradionecrosis due to previous

radiation therapy (1/24), pharyngocutaneous fistula due to previous radiation therapy (1/24), recurrent tongue SCC (1/24), recurrent hypopharyngeal SCC (1/24), recurrent tonsillar SCC (1/24), oral cavity SCC (1/24), and soft palate SCC (1/24).

There was no significant difference in numeric or categorical variables in the patient demographics between the 2 groups. The patient demographics are shown in the Online Supplemental Data and Table 1. For conventional imaging characteristics, there were no significant differences in fluid collections or pedicle vascular structures between the 2 groups ($P = .38$ and $.14$).

CT Perfusion

CT perfusion was performed at a median of 3 days after the operations (IQR, 2–4 days). Blood flow, blood volume, and tMIP were significantly higher in group I than group II (blood flow: median, 39.1 mL/100 mL/min [IQR, 27.9–45.6 mL/100 mL/min] versus 16.8 mL/100 mL/min [IQR, 14.0–17.1 mL/100 mL/min]; $P = .007$; blood volume: median, 7.67 mL/100 mL [IQR, 6.4–10.7 mL/100 mL] versus 4.58 mL/100 mL [IQR, 4.37–5.10 mL/100 mL]; $P = .007$; tMIP: median, 15.1 [IQR, 14.1–17.2] versus 6.78 [IQR, 4.81–8.74]; $P = .004$, respectively). MTT was significantly shorter in group I than in group II (MTT: median, 13.9 seconds [IQR, 12.9–15.6 seconds] versus 16.7 seconds [IQR, 16.5–17.0 seconds];

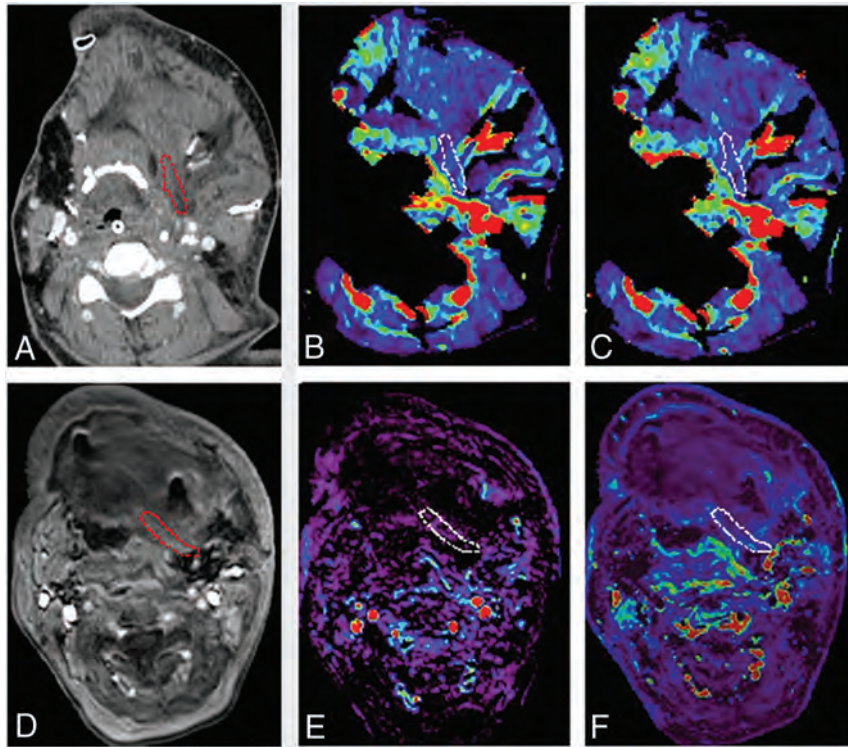


FIG 2. A 52-year-old woman with oral cavity squamous cell carcinoma was treated with mandibulectomy, glossectomy, tracheostomy, and neck dissection. A scapula free flap with latissimus dorsi was used to cover the soft tissue defect. The complication of venous congestion and ecchymosis was observed 2 days after the surgery. *A*, An ROI is placed within the junctional area of the free flap on contrast enhanced CT. *B*, Blood volume (mL/100 ml) and *C*, blood flow (mL/100 ml/min) are calculated and are 4.17 mL/100 ml and 11.3 mL/100 ml/min, respectively. *D*, An ROI is placed on the permeability map within the junctional area of the free flap and DCE-MR imaging parameters are calculated. *E*, Vp and *F*, K^{trans} (minute⁻¹) are 0.03 and 0.15 (minute⁻¹), respectively. Red and white circled areas represent region of interests.

Table 1: Demographic and imaging characteristics differences between the 2 groups^a

	Group I	Group II	P Value
No. of patients	19	5	NA
Sex (male/female)	14:5	2:3	.29
Age (yr)	63.9 (SD, 9.5)	58.0 (SD, 5.7)	.20
BMI (kg/m ²)	24.1 (22.4–29.3)	21.1 (16.1–24.7)	.14
History of smoking	17/19	5/5	1
History of HT	4/19	2/5	.57
History of DM	1/19	2/5	.10
History of previous radiation	19/19	5/5	1
History of previous chemotherapy	13/19	4/5	1
Ischemia time (mins)	60 (45–95)	105 (90–109)	.34
Presence of wound infection	1/19	3/5	.10
Presence of fluid collection	7/19	1/5	.38
Presence of pedicle vascular structure	7/19	4/5	.14
		(Venous thrombosis: 1/5)	

Note:—NA indicates not applicable; BMI, body mass index; HT, hypertension; DM, diabetes mellitus.

^a Groups I and II represent the group with successful free flap reconstruction and the group with wound failure, respectively. Values were described as mean (SD) or median (IQR).

$P = .015$). TTP and time-to-maximum were not significantly different (TTP: median, 32.3 seconds [IQR, 30.6–36.5 seconds] versus 32.6 seconds [IQR, 32.5–33.9 seconds]; $P = .84$; time-to-maximum: median, 7.39 seconds [IQR, 6.29–10.8 seconds] versus 9.04 seconds [IQR, 8.44–10.3 seconds]; $P = .42$). Blood

flow, blood volume, MTT, and tMIP showed areas under the curve ranging from 0.96 to 0.98 between the 2 groups. The mean size of ROIs was 46.3 cm². Two patients in group I and 2 patients in group II were unable to undergo CT perfusion due to their inability to lie still for the examination.

MR Perfusion

DCE-MR imaging was performed at a median 3 days after the operations (IQR, 2–4 days). Vp, K^{trans} , and peak enhancement were higher in group I than in group II (Vp: median, 0.11 [IQR, 0.06–0.15] versus 0.03 [IQR, 0.026–0.04]; $P = .006$; K^{trans} : median, 0.21 minute⁻¹ [IQR, 0.18–0.27 minute⁻¹] versus 0.15 minute⁻¹ [IQR, 0.12–0.16 minute⁻¹]; $P = .039$; peak enhancement: median, 257 [IQR, 167–275] versus 79 [IQR, 76.6–90.7]; $P = .004$). TME was shorter in group I than in group II (TME: median, 102 seconds [IQR, 77.3–118 seconds] versus 143 seconds [IQR, 137–150 seconds]; $P = .04$). Ve, Kep, area under curve, wash-in, washout, and maximum signal-enhancement ratio were not significantly different (Ve: median, 0.37 [IQR, 0.27–0.53] versus 0.28 [IQR, 0.24–0.31]; $P = .35$; Kep: median, 0.56 [IQR, 0.46–0.74] versus 0.56 [IQR, 0.54–0.58]; $P = .97$; area under curve: 6.76×10^3 [IQR, 4.55–11.7 $\times 10^3$] versus 4.76×10^3 [IQR, 4.48–4.80 $\times 10^3$]; $P = .49$; wash-in: 0.99 [IQR, 0.36–2.60] versus 1.97 [IQR, 0.31–3.15]; $P = .78$; washout: median, 0.16 [IQR, 0.08–1.08] versus 0.65 [IQR, 0.63–3.25]; $P = .09$; maximum signal-enhancement ratio: median, 97.1 [76.1–141.5] versus 86.9 [74.1–87.5]; $P = .50$).

Vp, K^{trans} , peak enhancement, and TME showed the areas under the curve ranging from 0.81 to 0.92 between the 2 groups. The ROI mean size was 43.1 cm². Three patients in group I were unable to undergo MR perfusion due to their inability to lie still for the examination. A pulsed input pattern was observed in the AIF curves in all patients in CT perfusion and DCE-MR imaging. The diagnostic performances of CT perfusion and DCE-MR imaging parameters are shown in the Table 2 and Figs 3 and 4. The distribution of CT perfusion and DCE-MR imaging parameters is shown in the Online Supplemental Data.

Table 2: Diagnostic performance of CT perfusion and DCE-MR imaging in the prediction of wound failure after head and neck free flap reconstruction

	Blood Flow (mL/100 mL/min)	Blood Volume (mL/100 mL)	MTT (Sec)	tMIP	Vp	K^{trans} (min ⁻¹)	Peak Enhancement	TME (Sec)
Cutoff	17.3	5.62	16.1	10.7	0.06	0.15	155	113
Sensitivity	1	1	1	1	1	0.80	1	1
Specificity	0.94	0.88	0.88	0.94	0.81	0.94	0.81	0.69
PPV	0.75	0.60	0.60	0.75	0.63	0.80	0.63	0.50
NPV	1	1	1	1	1	0.94	1	1
Accuracy	0.95	0.90	0.90	0.95	0.86	0.91	0.86	0.76
AUC	0.96	0.96	0.96	0.98	0.92	0.82	0.91	0.81

Note:—PPV indicates positive predictive value; NPV, negative predictive value; AUC, area under the curve.

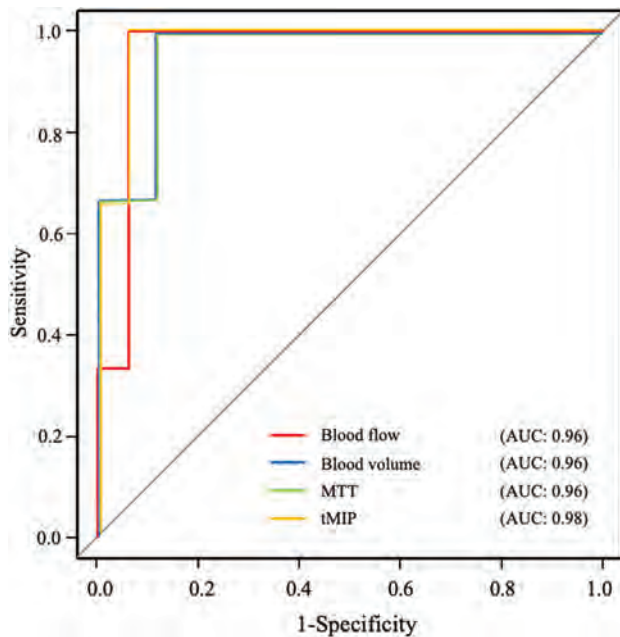


FIG 3. Receiver operating characteristic curves of CT perfusion parameters that showed statistically significant differences between groups I and II. AUC indicates area under the curve.

DISCUSSION

Our study aimed to assess the utility of CT perfusion and DCE-MR imaging for predicting wound failure after free flap reconstructive head and neck surgery. While patient demographics and conventional imaging characteristics were unable to identify any differences between group I and group II, CT perfusion and DCE-MR imaging showed significant differences between the 2 groups in multiple parameters, with the receiver operating characteristics demonstrating diagnostic performances ranging from an area under the curve of 0.81 to 0.98. A direct comparison of the results from the 2 techniques was, however, not feasible due to the small sample size.

Prior studies have shown some risk factors related to wound failure such as a history of smoking, hypertension, elevated creatinine levels, wound infection, and chemoradiation therapy.⁹⁻¹¹ While the occurrence of wound failure was relatively high (5/24) in our study, none of the patient demographics or conventional imaging features related to the presence or absence of fluid collection and pedicle vascular structures were predictive of wound failure. In only 1 case with flap failure was there an identifiable venous thrombosis, which was thought to be the cause of the free flap

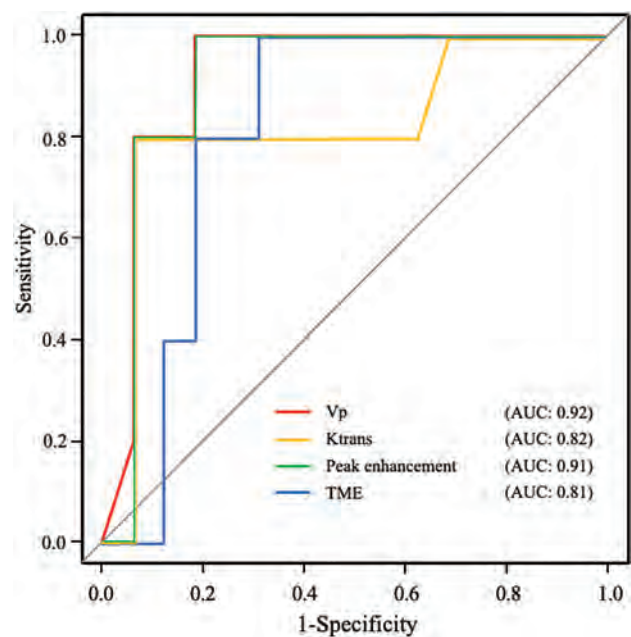


FIG 4. Receiver operating characteristic curves of DCE-MR imaging parameters that showed statistically significant differences between groups I and II. AUC indicates area under the curve.

ischemia.¹⁹ This low detectivity of venous thrombosis in our cohort may be related to the difficulty in identifying venous thrombosis due to early timing of the CT/MR imaging acquisition and the relatively smaller venous outflow anatomy compared with the larger arterial pedicle. To maximize our chances of identifying advanced imaging-based parameters that could be helpful for the prediction of wound failure (and reduce the chances of having very few wound failures in our outcomes data set that would skew the results significantly), we had selected a group of patients who were considered at baseline as high risk for decreased tissue viability due to a prior history of chemoradiation (which causes chronic radiation-induced ischemia and has been identified as the most important determinant factor of wound failure).¹⁰

As for CT perfusion, blood flow, blood volume, and tMIP were significantly lower and MTT was longer in the group with wound failure (group II) than in the group with successful free flap reconstruction (group I). These results may suggest that the vasculature in the junctional areas within the free flap in the head and neck is less anastomosed and perfused in group II than in group I in the early postoperative stage (2–4 days). Regarding DCE-MR imaging

parameters, Vp and K^{trans} were significantly lower in group II than in group I. Similar to CT perfusion results, these may also indicate reduced microperfusion and permeability in group II. Moreover, TME and peak enhancement, which are based on the time-intensity curve and can represent local perfusion alterations, were also different between the 2 groups: Group II showed lower peak enhancement with a longer TME than group I. This finding is consistent with the results of Vp and K^{trans} and likely implies a prolonged transit of a smaller amount of contrast in hypoperfused free flaps.

One prior study using MR perfusion for postoperative monitoring showed an optimal detectivity of reduced blood flow after the operation in cutaneous, subcutaneous, and muscle tissue areas including 10 patients with tissue defects in various body regions.²⁰ Our study specifically focused on head and neck free flaps and was able to show the utility of both CT perfusion and MR perfusion in identifying an early postoperative hypoperfused state that may be a risk factor for wound failure. Together, these findings suggest that patients who have normal perfusion parameters on CT /MR imaging in the early postoperative period, as our study showed, may be candidates for early discharge from hospitalization or could return to a normal diet earlier than patients with abnormal parameters.

Our study has several limitations. While this study was prospective, it included only a relatively small population from a single institution, and some patients were unable to undergo CT or MR perfusion. However, even with the relatively small numbers, we were able to identify differences in CT and MR perfusion between the 2 groups studied. We were not able to compare the predictive performance between CT perfusion and DCE-MR imaging due to the small number of patients in this pilot study. Larger trials that incorporate more patients would be needed to study which of the 2 modalities (CT versus MR perfusion) is more robust and which of the parameters in each technique provides the best differentiation of the 2 groups. Second, we were unable to measure the perfusion in the entire free flap because a very large number or area of ROIs would be needed to cover all slices that contained the free flap. However, we mitigated this potential bias by focusing on the junctional area of the free flap that is most likely to fail after an operation and used 5 separate ROIs in all patients to cover as much of the junction as possible. Last, there was a significant drop-out of patients from the study after enrollment due to their perceived inability to lie flat for the scans; this could be an impediment in routinely performing these scans for all postoperative patients, and some may require general anesthesia to tolerate the scans.

CONCLUSIONS

Parameters derived from CT perfusion and DCE-MR imaging can both serve as imaging biomarkers to predict wound complications after head and neck free flap reconstruction.

Disclosure forms provided by the authors are available with the full text and PDF of this article at www.ajnr.org.

REFERENCES

1. Wang Y, Wang M, Tang Y, et al. **Perioperative mortality of head and neck cancers.** *BMC Cancer* 2021;21:256 CrossRef Medline
2. Carvalho AL, Nishimoto IN, Califano JA, et al. **Trends in incidence and prognosis for head and neck cancer in the United States: a site-specific analysis of the SEER database.** *Int J Cancer* 2005;114:806–16 CrossRef Medline
3. Pulte D, Brenner H. **Changes in survival in head and neck cancers in the late 20th and early 21st century: a period analysis.** *Oncologist* 2010;15:994–1001 CrossRef Medline
4. Neligan PC. **Head and neck reconstruction.** *Plast Reconstr Surg* 2013;131:260e–69e CrossRef Medline
5. Yoon AP, Jones NF. **Critical time for neovascularization/angiogenesis to allow free flap survival after delayed postoperative anastomotic compromise without surgical intervention: a review of the literature.** *Microsurgery* 2016;36:604–12 CrossRef Medline
6. Simon C, Bulut C, Federspil PA, et al. **Assessment of peri- and postoperative complications and Karnofsky-performance status in head and neck cancer patients after radiation or chemoradiation that underwent surgery with regional or free-flap reconstruction for salvage, palliation, or to improve function.** *Radiat Oncol* 2011;6:109 CrossRef Medline
7. Bianchi B, Copelli C, Ferrari S, et al. **Free flaps: outcomes and complications in head and neck reconstructions.** *J Craniomaxillofac Surg* 2009;37:438–42 CrossRef Medline
8. Khouri RK, Cooley BC, Kunselman AR, et al. **A prospective study of microvascular free-flap surgery and outcome.** *Plast Reconstr Surg* 1998;102:711–21 CrossRef Medline
9. Lin PC, Kuo PJ, Kuo SCH, et al. **Risk factors associated with postoperative complications of free anterolateral thigh flap placement in patients with head and neck cancer: analysis of propensity score-matched cohorts.** *Microsurgery* 2020;40:538–44 CrossRef Medline
10. Furuta Y, Homma A, Oridate N, et al. **Surgical complications of salvage total laryngectomy following concurrent chemoradiotherapy.** *Int J Clin Oncol* 2008;13:521–27 CrossRef Medline
11. Sanati-Mehrziy P, Massenbourg BB, Rozehnal JM, et al. **Risk factors leading to free flap failure: analysis from the national surgical quality improvement program database.** *J Craniofac Surg* 2016;27:1956–64 CrossRef Medline
12. Chao AH, Lamp S. **Current approaches to free flap monitoring.** *Plast Surg Nurs* 2014;34:52–56; quiz 57–58 CrossRef Medline
13. Abdel Razek AA, Denewer AT, Hegazy MA, et al. **Role of computed tomography angiography in the diagnosis of vascular stenosis in head and neck microvascular free flap reconstruction.** *Int J Oral Maxillofac Surg* 2014;43:811–15 CrossRef Medline
14. Gaddikeri S, Gaddikeri RS, Tailor T, et al. **Dynamic contrast-enhanced MR imaging in head and neck cancer: techniques and clinical applications.** *AJNR Am J Neuroradiol* 2016;37:588–95 CrossRef Medline
15. Ota Y, Liao E, Capizzano AA, et al. **Diagnostic role of diffusion-weighted and dynamic contrast-enhanced perfusion MR imaging in paragangliomas and schwannomas in the head and neck.** *AJNR Am J Neuroradiol* 2021;42:1839–46 CrossRef Medline
16. Ota Y, Liao E, Kurokawa R, et al. **Diffusion-weighted and dynamic contrast-enhanced MRI to assess radiation therapy response for head and neck paragangliomas.** *J Neuroimaging* 2021;31:1035–43 CrossRef Medline
17. Ota Y, Liao E, Capizzano AA, et al. **MR diffusion and dynamic-contrast enhanced imaging to distinguish meningioma, paraganglioma, and schwannoma in the cerebellopontine angle and jugular foramen.** *J Neuroimaging* 2021 Dec 22. [Epub ahead of print] CrossRef Medline
18. Mouridsen K, Christensen S, Gyldensted L, et al. **Automatic selection of arterial input function using cluster analysis.** *Magn Reson Med* 2006;55:524–31 CrossRef Medline
19. McCarty JL, Corey AS, El-Deiry MW, et al. **Imaging of surgical free flaps in head and neck reconstruction.** *AJNR Am J Neuroradiol* 2019;40:5–13 CrossRef Medline
20. Lamby P, Prantl L, Fellner C, et al. **Post-operative monitoring of tissue transfers: advantages using contrast enhanced ultrasound (CEUS) and contrast enhanced MRI (ceMRI) with dynamic perfusion analysis?** *Clin Hemorheol Microcirc* 2011;48:105–17 CrossRef Medline

Revisiting CT Signs of Unilateral Vocal Fold Paralysis: A Single, Blinded Study

M.H. Bashir, C. Joyce, A. Bolduan, V. Sehgal, M. Smith, and S.J. Charous



ABSTRACT

BACKGROUND AND PURPOSE: Several CT findings are thought to be indicative of vocal cord paralysis; however, these signs have never been validated in a blinded fashion. This study attempts to compare and validate these signs and determine their accuracy in predicting vocal cord paralysis.

MATERIALS AND METHODS: A retrospective chart review was performed, and CT scans from patients with known unilateral vocal cord paralysis and known normal vocal cord movement were reviewed by 3 radiologists who were blinded to the status of the patients' laryngeal function. The scans were reviewed and scored for 8 accepted signs of vocal cord paralysis as well as for predicting a final diagnostic conclusion. Statistical analysis using odds ratios for signs and the Fleiss κ for criterion agreement among the radiologists was performed for diagnostic accuracy.

RESULTS: The presence of medial displacement of the posterior ipsilateral vocal fold margin and ipsilateral laryngeal ventricular dilation yielded the greatest positive predictive value. Other signs demonstrated high specificity, but interrater discrepancy was greater than expected and diminished the reliability of these signs in predicting vocal cord paralysis. Overall, sensitivity and negative predictive values were low.

CONCLUSIONS: Predicting vocal cord paralysis on the basis of CT findings is not as accurate or straightforward in prospectively predicting vocal cord paralysis as implied in prior studies.

ABBREVIATION: UVFP = unilateral vocal fold paralysis

Unilateral vocal fold paralysis (UVFP) is a relatively common disease process frequently seen by otolaryngologists. A definitive diagnosis of UVFP is dependent on visualization of the glottis; therefore, the exact incidence is not known.¹ Patients with UVFP most commonly present with dysphonia, dyspnea, and dysphagia, all of which may be sudden or gradual in onset.² This disease process develops as a result of injury to the vagus nerve or recurrent laryngeal nerve, a branch of the vagus nerve. Up to 40% of cases are idiopathic.³ UVFP can result from an injury at any point along the nerve as it courses from the jugular foramen to the mediastinum, around the subclavian artery on the right or the aortic arch on the left, and finally through the tracheoesophageal grooves before entering the larynx at the cricothyroid joint.

There are a variety of etiologies of UVFP, with iatrogenic injury historically being the leading cause, followed by malignancy and idiopathic, neuropathy, trauma, and inflammatory etiologies.⁴ In the absence of a history of a neck or cervical spinal operation, laryngeal trauma, or known malignancy, the standard diagnostic work-up includes CT from the skull base through the mediastinum to assess a lesion along the course of the nerve. Although cord palsy is often diagnosed clinically, up to 30% of cases may be asymptomatic and clinically unsuspected.⁵ There are many imaging signs to suggest vocal cord paralysis with varying degrees of sensitivity and specificity (Table 1).⁴⁻⁷ Representative examples of these signs are presented in Fig 1. Of note, the 3 most specific signs of cord palsy reported in the literature include dilation of the laryngeal ventricle, medial deviation and thickening of the aryepiglottic fold, and dilation of the piriform sinus.⁶

Although laryngoscopic evaluation by an otolaryngologist remains the criterion standard to establish the definitive diagnosis of vocal cord paralysis, the presence of these signs noted incidentally on CT may cause the interpreting radiologist to question vocal cord paralysis in examinations ordered for other indications. This issue may result in significant expense, psychological

Received May 3, 2021; accepted after revision January 8, 2022.

From the Department of Radiology (M.H.B., V.S.), Department of Otolaryngology (S.J.C.), Loyola University Medical Center (C.J.), Maywood, Illinois; Vanderbilt University Medical Center (A.B.), Nashville, Tennessee; and Diagnostic Imaging Alliance of Louisville (M.S.), Louisville, Kentucky.

Please address correspondence to Mariah H. Bashir, MD, Loyola University Medical Center, 2160 S. First Ave, Maywood, IL 60153; e-mail: Mariah.Bashir@lumc.edu

<http://dx.doi.org/10.3174/ajnr.A7451>

Table 1: CT signs of UVFP as previously described⁴⁻⁷

Indirect CT Signs of UVFP	
1	Dilation of the ipsilateral pyriform sinus
2	Medial rotation of the ipsilateral aryepiglottic fold
3	Thickening of the ipsilateral aryepiglottic fold
4	Dilation of the ipsilateral laryngeal ventricle
5	Medial displacement of the posterior aspect of the ipsilateral true vocal fold
6	Mushroom sign, ⁴ ipsilateral laryngeal ventricle dilation with medialization of the posterior cord margin combined with contralateral anterior subglottic air to generate a mushroom appearance on axial imaging
7	Anteromedial displacement of the ipsilateral arytenoid cartilage
8	Loss of the ipsilateral subglottic arch

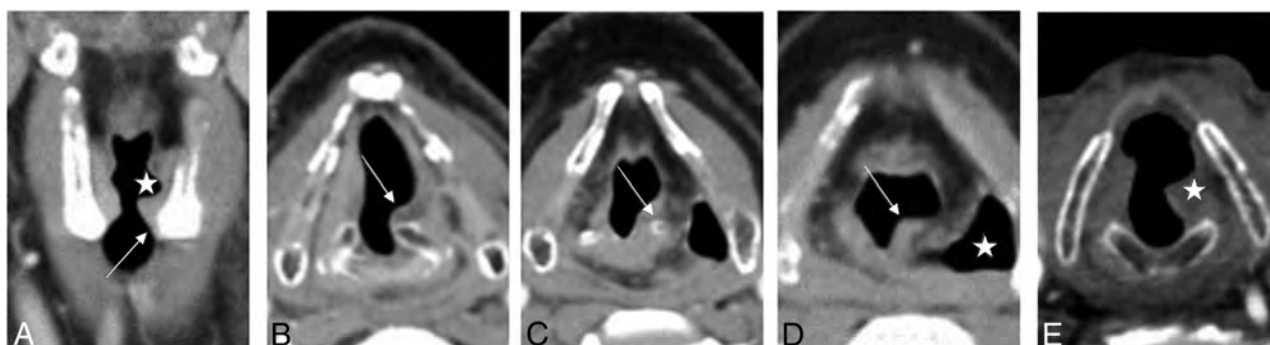


FIG 1. CT findings of UVFP images from 2 patients with proven left UVFP. *A*, Coronal CT image demonstrates dilation of the left laryngeal ventricle (*star*) and loss of the subglottic arch (*arrow*). *B*, Axial CT image demonstrates medial positioning of the left posterior vocal fold margin (*arrow*). *C*, Axial CT image demonstrates anterior positioning of the left arytenoid cartilage (*arrow*). *D*, Axial CT image demonstrates rotation and thickening of the left aryepiglottic fold and enlargement of the left pyriform sinus (*star*). *E*, Axial CT image demonstrates the mushroom sign, tilting toward the left (*star*).

stress, and physical discomfort for the patient in obtaining a definitive diagnosis through evaluation by an otolaryngologist. To our knowledge, all previous studies have evaluated the usefulness of CT signs (Table 1) in patients with a known, laryngoscopically-established diagnosis of vocal cord paralysis. This article tests the utility of these signs by blinding the interpreting radiologists to randomized CT scans of patients with and without UVFP. Thus, we attempted to identify the most useful signs for prospectively raising concern for UVFP.

MATERIALS AND METHODS

Patient Characteristics and Study Setting

A retrospective chart review of patients from Loyola University Medical Center in Maywood, Illinois between 2009 and 2019 was performed on 2 groups of patients. One group consisted of patients diagnosed with unilateral vocal cord paralysis with a confirmatory laryngoscopy performed by an attending otolaryngologist <3 months before a CT neck soft-tissue examination. Only patients with complete, unilateral vocal cord paralysis were included; patients with hypomobile vocal fold movement or bilateral vocal cord paralysis were not included. The other group consisted of patients with normal vocal cord movement, which was also confirmed on laryngoscopy by an attending otolaryngologist <3 months before a CT neck soft-tissue examination. Of note, neck CTs were performed at many institutions, given the nature of our tertiary center, and followed various protocols, but included examinations were performed with ≤3-mm section thickness, and coronal and sagittal reformats were also available.

Patients were excluded from the study if they had any of the following: prior radiation therapy to the neck, laryngeal/pharyngeal cancer, a history of laryngeal/pharyngeal trauma, a history of a laryngeal/pharyngeal operation, and intubation or a tracheostomy tube at the time of imaging. CT scans were evaluated by 3 radiologists, including 2 neuroradiologists with Certificates of Added Qualification with 5 and 22 years' experience, respectively, and 1 neuroradiology fellow. All 3 were blinded as to in which group the patient belonged. Radiologists indicated the presence and absence of each of the 8 UVFP signs as described in Table 1: 1) dilation of the ipsilateral pyriform sinus, 2) medial rotation of the ipsilateral aryepiglottic fold, 3) thickening of the ipsilateral aryepiglottic fold, 4) dilation of the ipsilateral laryngeal ventricle, 5) medial displacement of the posterior aspect of the ipsilateral true vocal fold, 6) the mushroom sign, 7) anterior displacement of the ipsilateral arytenoid cartilage, and 8) loss of the subglottic arch. The 3 radiologists met to review and discuss how to evaluate the various CT signs before the study initiation. Differences in the assessment of the presence of a criterion were resolved via consensus of the radiologists. The final radiologic diagnosis of vocal cord paralysis was based on majority consensus.

Statistical Analysis

Patient demographics were presented overall and stratified by an otolaryngologist's diagnosis of UVFP based on the laryngoscopic examination (reference standard). Variables were compared between those with and without UVFP on the basis of the laryngoscopic examination using a *t* test for age and a χ^2 test for

sex. CT scan criterion agreement among the 3 raters was assessed using the Fleiss κ . Data were summarized for each patient to determine the CT findings by a majority of radiologists, and odds ratios were estimated for the CT finding associated with the reference standard for UVFP. Measures of diagnostic accuracy (sensitivity, specificity, positive predictive value, and negative predictive value) were used as a part of the analytic approach. Combinations of CT findings were considered using best subsets logistic regression, and candidate models were compared using likelihood ratios tests. For the final chosen model, goodness of fit was assessed, and adjusted odds ratios were presented for CT findings associated with UVFP. Analyses were performed using SAS, Version 9.4 (SAS Institute).

RESULTS

A total of 147 patients met the inclusion criteria for this retrospective study. Four of these patients could not be evaluated due to the breath-hold examination ($n=2$) and motion ($n=2$). Therefore, a total of 143 patients could be analyzed. The mean age was 63 (SD, 15) years, and half were women ($n=72$, 50.3%).

Table 2: Patient characteristics by true UVFP status

	Overall ($n=143$)	UVFP ($n=104$)	No UVFP ($n=39$)	P Value
Age (mean) (SD) (yr)	62.9 (14.5)	65.5 (13.5)	56.0 (15.0)	<.001
Sex (No.) (%)				
Male	71 (49.7)	48 (46.2)	23 (59.0)	.1
Female	72 (50.3)	56 (53.8)	16 (41.0)	
Laterality (No.) (%)				
Left	76 (53.1)	76 (73.1)	—	—
Right	28 (19.6)	28 (26.9)	—	—
No paralysis	39 (27.3)	—	39 (100.0)	—

Note:— indicates not applicable.

Table 3: Agreement of radiologic diagnoses

Diagnosis	κ (95% CI)
Dilation of ipsilateral pyriform sinus	0.77 (0.68–0.86)
Medial rotation of ipsilateral aryepiglottic fold	0.66 (0.56–0.75)
Thickening of ipsilateral aryepiglottic fold	0.32 (0.17–0.47)
Anteromedial displacement of ipsilateral arytenoid cartilage	0.46 (0.34–0.57)
Medial displacement of posterior aspect of ipsilateral vocal fold	0.54 (0.42–0.65)
Mushroom sign	0.19 (0.09–0.29)
Dilation of ipsilateral laryngeal ventricle	0.50 (0.39–0.61)
Loss of subglottic arch	0.15 (0.00–0.30)
Final diagnosis of paralysis	0.58 (0.48–0.69)

Table 4: Radiologic diagnoses to predict vocal cord paralysis

	Majority Positive (No.) (%)	Sensitivity	Specificity	Positive Predictive Value	Negative Predictive Value
Dilation of ipsilateral pyriform sinus	91 (63.6%)	68.3%	48.7%	78.0%	36.5%
Medial rotation of ipsilateral aryepiglottic fold	76 (53.1%)	60.6%	66.7%	82.9%	38.8%
Thickening of ipsilateral aryepiglottic fold	19 (13.3%)	16.3%	94.9%	89.5%	29.8%
Anteromedial displacement of ipsilateral arytenoid cartilage	42 (29.4%)	36.5%	89.7%	90.5%	34.7%
Medial displacement of posterior aspect of ipsilateral vocal fold	100 (69.9%)	78.8%	53.8%	82.0%	48.8%
Mushroom sign	9 (6.3%)	7.7%	97.4%	89.9%	28.4%
Dilation of ipsilateral laryngeal ventricle	87 (60.8%)	69.2%	61.5%	82.8%	42.9%
Loss of subglottic arch	7 (4.9%)	5.8%	97.4%	85.7%	27.9%
Final diagnosis of paralysis ^a	84 (59.2%)	68.0%	64.1%	83.3%	43.0%

^a $n=142$: omitted 1 tie (1 positive, 1 negative, 1 missing value).

Those with vocal cord paralysis were older (66 [SD, 14] years versus 56 [SD, 15] years, $P<.001$), and most had paralysis on the left ($n=76$, 73.1%) (Table 2).

Agreement between raters was highest for findings of ipsilateral pyriform dilation ($\kappa=0.77$; 95% CI, 0.68–0.86) and the aryepiglottic fold medial and rotated ($\kappa=0.66$; 95% CI, 0.56–0.75), followed by medial displacement of the postsilateral cord margin ($\kappa=0.54$; 95% CI, 0.42–0.65), ipsilateral laryngeal ventricle dilation ($\kappa=0.50$; 95% CI, 0.39–0.61), and anteromedial displacement of the ipsilateral arytenoid cartilage ($\kappa=0.46$; 95% CI, 0.34–0.57). Agreement was poor-to-fair for less frequently detected findings, including aryepiglottic fold thickening ($\kappa=0.32$), the mushroom sign ($\kappa=0.19$), and subglottic arch loss ($\kappa=0.15$). The final diagnosis of UVFP had moderate agreement ($\kappa=0.58$; 95% CI, 0.48–0.69) (Table 3).

The sensitivity and specificity of the imaging criteria were evaluated on the basis of consensus of radiologists. The criteria with the highest levels of sensitivity included medial displacement of the posterior margin of the ipsilateral vocal fold (78.8%), dilation of the ipsilateral laryngeal ventricle (69.2%), and dilation of the ipsilateral pyriform sinus (68.3%). The 3 signs with the highest degree of specificity also demonstrated higher positive predictive values: mushroom sign (97.4%), loss of the subglottic arch (97.4%), and thickening of the ipsilateral aryepiglottic fold (94.9%), and anteromedial displacement of the ipsilateral arytenoid cartilage (89.7%). The negative predictive value was low across all signs. When the radiologists were asked to make a final diagnosis of UVFP based on all radiographic findings, the final diagnosis had a sensitivity of 68.0% (70/103) in detecting a UVFP and a specificity of 64.1% (25/39), with a positive predictive value of 83.3% (70/84) (presented in Tables 4 and 5, respectively). A 2-variable model that included medial displacement of the postsilateral cord margin and ipsilateral laryngeal ventricle dilation was identified

Table 5: Radiologist-versus-otolaryngologist diagnosis of vocal cord paralysis

Radiologist, Majority	Otolaryngologist	
	Vocal Cord Paralysis	No Vocal Cord Paralysis
Vocal cord paralysis	70 (49.3)	14 (9.9)
No vocal cord paralysis	33 (23.2)	25 (17.6)

Table 6: Model to predict vocal cord paralysis from radiology findings

	Odds Ratio (95% CI)	P Value
Medial displacement of posterior aspect of ipsilateral vocal fold	3.09 (1.32–7.24)	.009
Dilation of ipsilateral laryngeal ventricle	2.40 (1.03–5.5)	.04

Table 7: Predictive value by combination of positive radiology findings

	No.	Sensitivity	Specificity	PPV	NPV
CT finding					
Either finding	113	86.5%	41.0%	79.6%	53.3%
Both findings	74	61.5%	74.4%	86.5%	42.0%

Note:—PPV indicates positive predictive value; NPV, negative predictive value.

as an improvement over univariable models and the acceptable goodness of fit ($\chi^2 = 0.26$, $P = .62$). Models with additional parameters did not show statistically significant improvement. On the basis of this model, the odds of UVFP were higher for those with medial displacement of the postipsilateral cord margin (adjusted OR = 3.09; 95% CI, 1.32–7.24) and with ipsilateral laryngeal ventricle dilation (adjusted OR = 2.40; 95% CI, 1.03–5.55) (Table 6). Based on the presence of either finding, this model provides a combined sensitivity and specificity of 86.5% and 41.0%, respectively. The presence of both findings demonstrates 61.5% sensitivity and 74.4% specificity (Table 7).

DISCUSSION

This is the first study to help identify UVFP on CT prospectively, using signs established as helpful in prior studies.⁴⁻⁷ As shown in our study, agreement among the radiologists was not as high as expected, suggesting a subjectivity in the evaluation based on varying thresholds. The surprising lack of objectivity of the various other signs diminishes their usefulness in prospectively predicting vocal cord paralysis. For example, although the mushroom sign and the loss of the subglottic arch sign were the most specific, they were also rated the lowest in the radiologists' agreement. Their poor interrater reliability minimizes their usefulness (Fig 2).

In our study, the presence of medial displacement of the posterior ipsilateral vocal fold margin and ipsilateral laryngeal ventricular dilation combined yielded a positive predictive value of 87% and a specificity of 74%. These signs also had good agreement among the interpreting neuroradiologists, which is important if these signs are to be used to raise concern for UVFP and

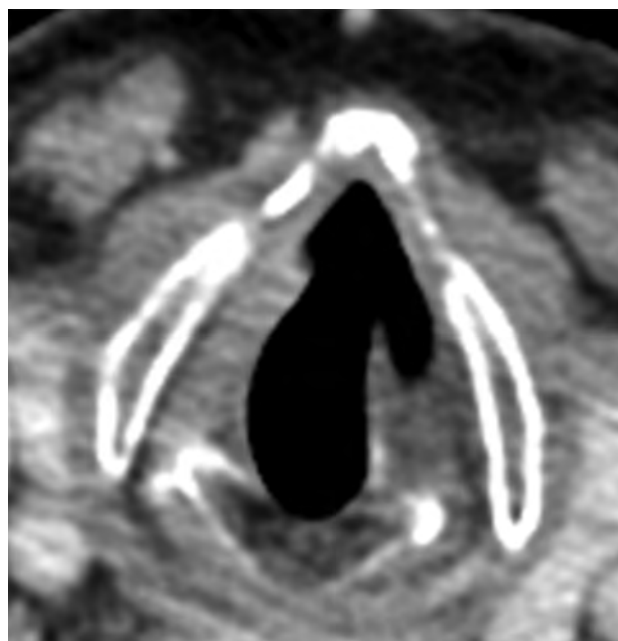


FIG 2. Radiologists' subjectivity on a single axial postcontrast CT scan demonstrates questionable findings of the mushroom sign. This was read by 2 radiologists as negative for this sign and by 1 radiologist as positive for the sign with the left side as the affected side. By laryngoscopic examination, this patient did indeed have left-sided vocal fold paralysis.

thus initiate further evaluation by an otolaryngologist. Most interesting, our findings are somewhat different from those in the study of Chin et al,⁶ in which the authors retrospectively evaluated 40 patients with the knowledge of UVCP (but did not know the laterality). While they found dilation of the laryngeal ventricle to be a very useful sign, they also found medial deviation and thickening of the aryepiglottic fold as well as dilation of the piriform sinus to be as helpful. These latter 2 signs were also helpful in our study but did not reach statistical significance.

Our study demonstrates that it is much less straightforward to prospectively raise concern for UVFP compared with interpreting examinations when a laryngoscopic diagnosis of UVFP is confirmed. If medial displacement of the posterior ipsilateral vocal fold margin and ipsilateral laryngeal ventricular dilation are present, concern should be raised for UVFP prospectively and a thorough evaluation of the course of the vagus and recurrent laryngeal nerves from the skull base through the mediastinum should be performed on the available neck CT examination. Mimics of UVFP should also be excluded when possible.⁴

Limitations to our study include uneven distribution of patients with UVFP versus healthy controls, excluding patients with bilateral vocal cord paralysis, and agreement between neuroradiologists. Despite meeting beforehand to discuss how to evaluate the various CT signs, discerning the presence or absence of some signs proved subjective in this study, largely due to varying thresholds for calling the presence of a sign for each neuroradiologist based on their own experience. Imaging findings of a high vagal nerve palsy were not included in our study. Additional, albeit less common, signs of UVFP such as subglottic fullness and a widened vallecula⁵ were also not included in our study.

CONCLUSIONS

It is not as accurate or straightforward to prospectively predict vocal cord paralysis based on CT findings as previously implied in prior studies. CT scan sensitivity and negative predictive value are low for vocal cord paralysis. Because the implied diagnosis of vocal cord paralysis necessitates further work-up, expense, and procedures, care must be taken to translate suspicious findings appropriately.

REFERENCES

1. Robinson S, Pitkäranta A. **Radiology findings in adult patients with vocal fold paralysis.** *Clin Radiology* 2006;61:863–67 CrossRef Medline
2. Williamson AJ, Shermetaro C. **Unilateral vocal cord paralysis.** *StatPearls* 2021. <http://www.ncbi.nlm.nih.gov/books/NBK535420>. Accessed March 9, 2022
3. Stimpson P, Patel R, Vaz F, et al. **Imaging strategies for investigating unilateral vocal cord palsy: how we do it.** *Clin Otolaryngol* 2011;36:266–71 CrossRef Medline
4. Paquette CM, Manos DC, Psooy BJ. **Unilateral vocal cord paralysis: a review of CT findings, mediastinal causes, and the course of the recurrent laryngeal nerves.** *Radiographics* 2012;32:721–40 CrossRef Medline
5. Kwong Y, Boddu S, Shah J. **Radiology of vocal cord palsy.** *Clin Radiol* 2012;67:1108–14 CrossRef Medline
6. Chin SC, Edelstein S, Chen CY, et al. **Using CT to localize side and level of vocal cord paralysis.** *AJR Am J Roentgenol* 2003;180:1165–70 CrossRef Medline
7. Kumar VA, Lewin JS, Ginsberg LE. **CT assessment of vocal cord medialization.** *AJNR Am J Neuroradiol* 2006;27:1643–46 Medline

Extraocular Muscle Enlargement in Growth Hormone–Secreting Pituitary Adenomas

 B. Coutu,  D.A. Alvarez,  A. Ciurej,  K. Moneymaker,  M. White,  C. Zhang, and  A. Drincic



ABSTRACT

BACKGROUND AND PURPOSE: While Graves disease is the most common cause of extraocular muscle enlargement, case reports have also associated growth hormone–secreting pituitary adenomas with this same phenomenon. We investigated the prevalence and response to treatment of extraocular muscle enlargement in patients with growth hormone–secreting pituitary adenomas.

MATERIALS AND METHODS: We retrospectively reviewed extraocular muscle sizes using MR imaging in patients with growth hormone–secreting pituitary adenomas who underwent a transsphenoidal surgical resection compared with a matched control group with nonsecreting pituitary adenomas. Descriptive and comparative statistics were used to evaluate patient characteristics and extraocular muscle sizes between the 2 groups.

RESULTS: We identified 16 patients who presented with growth hormone–secreting pituitary adenomas and underwent transsphenoidal surgical resection from 2010 to 2019. The average diameter of the extraocular muscle at the time of diagnosis for the group with growth hormone–secreting pituitary adenomas was larger than that in the control group (4.7 versus 3.8 mm, $P < .001$). Nine patients achieved insulin-like growth factor 1 level normalization at a median of 11.5 months before their most recent MR imaging evaluation. The average size of the extraocular muscles of patients who achieved a normalized insulin-like growth factor 1 was smaller compared with those that did not (difference, 0.7 mm; 95% CI, 0.3–1.2 mm; $P < .001$), approaching the size of extraocular muscle in the control group.

CONCLUSIONS: We describe a high prevalence of extraocular muscle enlargement in patients with growth hormone–secreting pituitary adenomas. Additionally, we note that the size of extraocular muscles decreased with associated improvement in the biochemical control of acromegaly.

ABBREVIATIONS: EOM = extraocular muscle; GH = growth hormone; IGF-1 = insulin-like growth factor 1; TED = thyroid eye disease; TSS = transsphenoidal surgical; ULN = upper limit of normal

Acromegaly is an uncommon disease, with an incidence of 3–4 per million per year, characterized by excessive secretion of growth hormone (GH)–inducing organomegaly.¹ A GH–secreting pituitary adenoma causes 95% of described cases of acromegaly.² The features of such disease are related to excessive growth due to elevated GH and insulin-like growth factor 1 (IGF-1). This, in turn, leads to stimulation of growth of many tissues, including skin, bone, viscera, and epithelial tissue leading to

features such as prognathism, macroglossia, goiter, arthropathy, cardiomyopathy, skin tags, and colon polyps.³

Although a rare presentation of the disease process, acromegaly is associated with clinically relevant growth of orbital structures resulting in proptosis, increased corneal thickness, and even total ophthalmoplegia.⁴ The current literature is limited to case reports describing the association between acromegaly and extraocular muscle (EOM) enlargement, which, in turn, is related to the duration of the disease process as measured by levels of GH and IGF-1.⁵ This unrecognized finding of EOM enlargement on imaging studies may lead a clinician to perform multiple diagnostic tests investigating other causes of EOM enlargement such as thyroid eye disease (TED) associated with Graves disease or other inflammatory/neoplastic processes.

There is limited knowledge regarding the prevalence of EOM enlargement in patients with GH–secreting pituitary adenomas, the correlation of IGF-1 and EOM enlargement, or the efficacy of

Received December 11, 2020; accepted after revision September 17, 2021.

From the Departments of Radiation Oncology (B.C., A.C., K.M., C.Z.), Internal Medicine, Diabetes, Endocrinology, and Metabolism Division (D.A.A., A.D.), and Radiology (M.W.), University of Nebraska Medical Center, Omaha, Nebraska.

B. Coutu and D.A. Alvarez are co-first authors.

Please address correspondence to Andjela Drincic, MD, UNMC Division of Endocrinology, 984120 Nebraska Medical Center, Omaha, NE 68198; e-mail: andjela.drincic@unmc.edu



Indicates article with online supplemental data.

<http://dx.doi.org/10.3174/ajnr.A7453>

adenoma-directed treatment to halt or reverse EOM enlargement in this patient population. We present our institutional data to contribute to the understanding of this phenomenon.

MATERIALS AND METHODS

Study Design

We undertook a single-institution retrospective review of EOM size at diagnosis and last follow-up in patients with GH-secreting adenomas as measured by MR imaging. All included patients underwent MR imaging at the time of diagnosis and routinely at follow-up as per their managing physicians. We matched these patients (1:1) with patients with nonsecretory pituitary adenomas. This study was approved by our institutional board.

Patient Selection

We included consecutive patients from 2010 to 2019 who underwent a transsphenoidal surgical (TSS) resection for a GH-secreting pituitary adenoma. Patients were excluded if they had a history of Graves disease or signs/symptoms of TED, including the presence of laboratory-detected thyroid abnormalities (elevated Free T4). Patients were excluded if they could not undergo MR imaging. We matched (1:1) a control group of patients with nonsecretory pituitary adenomas to the patients with GH-secreting adenomas on the basis of age, sex, type of definitive treatment, and date of definitive treatment. All patients in the control group had clinically nonfunctioning pituitary adenomas. Patients were not included in the control group if they had, at any point, abnormal IGF-1 levels, which may be associated with a GH-secreting adenoma or treatment-associated hypopituitarism. Standard hormonal replacement of hypopituitarism did not cause exclusion in either group.

Laboratory Evaluation

IGF-1 was evaluated using quantitative chemiluminescent immunoassay. Laboratory assessment was outsourced to ARUP Laboratories (www.aruplab.com). The IGF-1 upper limit of normal (ULN) was defined as 2 SDs above the associated laboratory value adjusted by sex and age as presented by Shimon et al.^{6,7} A corresponding z score was reported with the IGF-1 laboratory value. A z score is the number of SDs that a given result is above (positive score) or below (negative score) the age- and sex-adjusted population mean. Results that are within the IGF-1 reference interval will have a z score between -2.0 and $+2.0$. IGF-1 laboratory findings were identified as abnormal if they were outside the above-stated reference range or had an associated z score of >2.0 . A GH-secretory status of a pituitary adenoma was diagnosed per the following criteria: patients with a presenting IGF-1 of >1.2 times the ULN or between $1.0 \times$ ULN and $1.2 \times$ ULN with a serum GH nadir of $>1 \mu\text{l}$ on oral glucose tolerance testing with associated symptoms of acromegaly. IGF-1 normalization (remission) following an operation and/or salvage management was defined as $\leq 1.0 \times$ IGF-1 ULN in 2 different serum collections.

Treatment

All patient management took place at an academic medical center. Treatment decision and techniques were based on the most

current international acromegaly management guidelines,⁸ and recommendations for adjuvant and salvage therapy were as per the managing neurosurgeon, radiation oncologist, and endocrinologist. All patients underwent a TSS resection. Radiation therapy was recommended for partial resection or identification of recurrent disease and was delivered in conventional fractionation (4500–5400 cGy in 25–30 fractions) or using a stereotactic radiosurgery technique (1400–2200 cGy in 1 fraction). Indications for salvage endocrine therapy included an elevated IGF-1 level or symptoms of acromegaly. Endocrine therapy included cabergoline, somatostatin receptor ligands, and pegvisomant.

Treatment-Response Evaluation

Patients were regularly evaluated for evidence of recurrent tumor with routine follow-up MR imaging every 6–12 months according to the Endocrine Society guidelines. Laboratory evaluation included IGF-1 level, random GH level, cortisol level, thyroid levels (thyroid stimulating hormone, T3, and T4), and other pituitary hormones as indicated. The response of EOM enlargement to treatment was evaluated by comparing the patient's most recent MR imaging (following treatment completion) with their MR imaging at the time of diagnosis.

MR Imaging Technique

Patients underwent MR imaging of the sella for the initial evaluation or routine follow-up of their pituitary adenoma. MR imaging examinations were performed using 1.5T and 3T systems. The retrospective nature of the study and the various clinical setups did not allow standardization of sequences. The imaging protocols included coronal and sagittal T1-weighted image acquisitions of the pituitary gland, cavernous sinus, and orbital structures. The 2 most common protocols (encompassing 78.1% of the retrospectively reviewed MR images) were an inversion recovery protocol performed on a 1.5T system (section thickness/gap thickness = 1.0–2.0/1.0–2.0 mm; TR/TE/TI = 2000/8.7–20.0/800 ms) and a fast spin-echo protocol performed on a 3T system (section thickness/gap thickness = 2.5–3/3–3.5 mm; TR/TE = 400–500/8.4–20.0 ms).

EOM Measurement

MR images were processed with Change HealthCare Radiology Solutions, Version 12.4.1 (<https://www.changehealthcare.com/enterprise-imaging/radiology/radiology-solutions>), within which the annotation distance tool was used for measurements. The short-axis diameter of each muscle was measured at its maximum.⁹ Measurements were performed on magnified images to improve the accuracy of the measurements, with the same magnification for all MR images. A board-certified neuroradiologist (M.W.) and an endocrine fellow (D.A.A.) analyzed the images independently and were found to have concordant measurements of EOM size. Physicians performing the measurements were not blinded to individual patient factors. Measurements of the diameter of the superior oblique muscle were found to be discordant between independent measurers and across patients and were thus removed from this analysis.

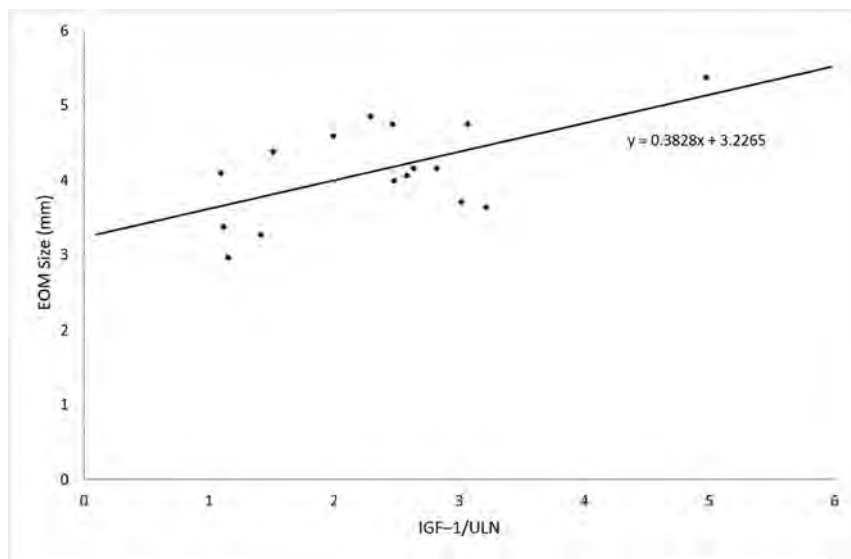


FIG 1. In patients with GH-secretory adenoma, EOM size is positively correlated with IGF-1/ULN at diagnosis. The Pearson correlation of the relationship is 0.599 ($P = .014$).

Statistical Analysis

Descriptive statistics were performed by calculating the frequencies of categorical variables and the median and range for continuous variables. Patient characteristics were compared using an independent-samples *t* test and a χ^2 test. The level of significance was set at a P value $< .05$. EOM enlargement was defined as a greater than the 95% confidence interval of the control group. Statistical analysis was performed using SPSS software, Version 26 (IBM).

RESULTS

We identified 16 patients who presented with GH-secreting pituitary adenomas who underwent TSS resection from 2010 to 2019 (Online Supplemental Data). The median patient age at the time of the operation was 44 years (range, 25–62 years). Five patients (31%) were men and 11 (69%) were women. The median IGF-1 at diagnosis was 2.15 times the upper limit of the normal (range, 1.06–3.57). The median size of the identified pituitary adenoma at diagnosis was 19.5 mm (range, 7–42 mm), with 9 patients (56%) presenting with cavernous sinus involvement and optic chiasm abutment/compression. Nine patients (56%) were identified as having pituitary adenomas that co-secreted prolactin. All patients underwent TSS resection of their adenoma, and residual disease was identified on immediate postoperative MR imaging (representing a resection of local relapsed tumor) in 12 patients (75%). No patients reported symptoms of ophthalmoplegia, orbital pain, or diplopia; however, 6 patients (37.5%) reported headaches, 2 patients (12.5%) reported epiphora, and 2 patients (12.5%) reported bitemporal hemianopsia.

At a median follow-up of 37.4 months (range, 12.5–126.0 months), 14 patients (87.5%) with GH-secreting adenomas had a normalized IGF-1 level. Four patients (25%) had a normalized IGF-1 level within 3 months of the operation without additional medical management. The median time from diagnosis to salvage therapy, including salvage radiation therapy or endocrine therapy,

was 14.7 months (range, 0–117.2 months). Twelve patients (75%) underwent salvage medical therapy including cabergoline (56%), lanreotide (50%), and pegvisomant (19%). Seven patients (44%) underwent salvage radiation therapy at a median 21.4 months (range, 4.1–117.2 months) after the operation.

The control group consisted of 16 patients matched for age and sex at the time of definitive local therapy. Compared with the patients with GH-secreting pituitary adenomas, the control group had larger pituitary adenomas at the time of diagnosis (19.5 versus 30.0 mm, $P = .02$). Consistent with the selection process, the patients with GH-secretory pituitary adenomas had a higher IGF-1/ULN (2.15 versus 0.44, $P < .01$) and a higher rate of prolactin co-secretion (56% versus 0%,

$P < .01$) than the control group. There were no differences between the GH-secretory and control groups in the rate of cavernous sinus involvement (56% versus 75%, $P = .458$), optic chiasm abutment or compression (56% versus 63%, $P = 1.00$), Resection of local relapsed tumor as defined by gross residual disease identified on immediate postoperative imaging (75% versus 56%, $P = .458$), or the rate of salvage radiation therapy (44% versus 63%, $P = .287$).

In patients with GH-secretory adenomas, the EOM size is positively correlated with IGF-1/ULN at diagnosis. The Pearson correlation of the relationship is 0.599 ($P = .014$). The average diameter of the EOM at the time of diagnosis for the group with GH-secretory pituitary adenomas was larger than that in the control group (4.7 mm; 95% CI, 4.4–4.9 mm versus 3.8 mm; 95% CI, 3.6–3.9, $P < .001$) (Fig 1). The medial rectus muscles demonstrated the greatest difference in size between the group with GH-secretory pituitary adenomas compared with the control group (difference, 1.2 mm; 95% CI, 0.7–1.6 mm; $P < .001$) (Table 1). Fourteen patients (87.5%) with GH-secretory pituitary adenomas had average EOM diameters greater than the 95% confidence interval of the control group. There was no association between cavernous sinus involvement and ipsilateral extraocular muscle enlargement (3.8 versus 3.7 mm, $P = .660$).

The median time interval from their initial MR imaging to the most recent follow-up MR imaging was 32.5 months for the GH-secretory pituitary adenoma group compared with 74.8 months for the control group ($P = .126$) (Table 1). At the time of the most recent MR imaging, all patients had undergone resection of their pituitary adenoma and 9 patients (56.3%) had met acromegaly remission criteria. Of the 9 patients who met the remission criteria, the median time from IGF-1 normalization to the most recent MR imaging was 11.5 months. At the most recent MR imaging following treatment, the enlargement of EOMs in the GH-secretory group compared with the control group persisted (4.3 mm; 95% CI, 4.0–4.4.5 mm versus 3.6 mm; 95% CI,

3.5–3.8 mm; $P < .001$). However, patients with GH-secretory pituitary adenomas overall achieved a decrease in the size of EOM from their first MR imaging to their most recent MR imaging (difference, -0.4 mm; 95% CI, -0.7 – 0.0 mm; $P = .037$) (Table 2). While the lateral and inferior rectus muscles had a decrease in size (-0.6 and -0.4 mm, respectively), the decrease in size of the superior rectus muscle did not achieve statistical significance (-0.4 mm, $P = .075$) and no decrease in the size of the medial rectus muscle was appreciated (-0.2 mm, $P = .546$).

Of the 9 patients who achieved IGF-1 normalization before their most recent MR imaging, average EOM sizes were smaller compared with the group that did not achieve IGF-1 normalization (0.7 mm; 95% CI, 0.3 – 1.2 mm; $P < .001$) (Table 3). The EOM size of patients who achieved IGF-1 normalization approached that of the control population (Fig 2). Achieving IGF-1 normalization before the most recent MR imaging was associated with a lower average IGF-1/ULN at diagnosis (difference, 0.88 ; 95% CI, 0.23 – 1.53 ; $P = .010$). Four patients

(25%) with GH-secretory pituitary adenomas experienced further growth of their EOM diameter at the time of their most recent MR imaging (relative change, 0.5 mm; range, 0.0 – 1.2 mm), of whom only 1 patient did not achieve a normalized IGF-1 by the time of the last follow-up.

DISCUSSION

This is the first study that has systematically reported the prevalence of EOM enlargement in patients with GH-secretory pituitary adenomas compared with a control group. Most patients (87.5%) with GH-secretory pituitary adenomas with or without other symptoms of acromegaly had EOM enlargement compared with the control group. Normalization of IGF-1 was associated with a decrease in EOM size. An analysis of the duration of IGF-1 normalization and the timing of follow-up imaging suggested that EOM size approaches the average size of the matched cohort, given sufficient time for biochemical control. Limited follow-up and persistent elevation of IGF-1 levels in a subset of the population with the most recent MR imaging

may limit our observation that EOM size did not decrease in the entire cohort after surgical resection. There is scant description on the prevalence and management of EOM enlargement associated with acromegaly in the published literature. Pozzo et al¹⁰ described a series of 10 patients with acromegaly, in which 8 patients had extraocular muscle enlargement identified on CT. Apart from this case series, we identified 4 published case reports of 6 patients (age range, 23–60 years) with symptomatic EOM enlargement associated with acromegaly published from 1962 to 2013. Associated symptoms at the time of presentation included proptosis, ptosis, epiphora, and lower eyelid edema. Our study contributes to the published literature of acromegaly-associated extraocular enlargement detectable by MR imaging.^{10–13}

Clinically identified EOM enlargement even in the setting of a GH-secretory pituitary adenoma has historically required an expensive and

Table 1: EOM sizes at the time of diagnosis and at time of most recent MR imaging evaluation of patients with GH-secreting pituitary adenomas compared with nonsecretory pituitary adenomas

Characteristic	GH-secretory (95% CI)	Nonsecretory (95% CI)	Difference (95% CI)	P Value
Initial size (mm)				
Superior rectus	4.7 (4.4–5.0)	4.0 (3.6–4.3)	0.7 (0.3–1.2)	.002
Medial rectus	4.8 (4.4–5.2)	3.7 (3.4–3.9)	1.2 (0.7–1.6)	<.001
Lateral rectus	4.5 (4.1–4.8)	3.6 (3.3–3.9)	0.9 (0.5–1.4)	<.001
Inferior rectus	4.8 (4.4–5.3)	4.0 (3.8–4.3)	0.8 (0.3–1.3)	.003
Average	4.7 (4.4–4.9)	3.8 (3.6–3.9)	0.9 (0.6–1.2)	<.001
Final size (mm)				
Superior rectus	4.3 (4.0–4.6)	3.9 (3.5–4.2)	0.4 (–0.1–0.9)	.088
Medial rectus	4.6 (4.3–5.0)	3.5 (3.2–3.7)	1.1 (0.8–1.6)	<.001
Lateral rectus	3.9 (3.6–4.2)	3.5 (3.2–3.7)	0.4 (0.1–0.8)	.026
Inferior rectus	4.2 (3.8–4.6)	3.7 (3.5–4.0)	0.5 (0.0–0.9)	.048
Average	4.3 (4.0–4.5)	3.6 (3.5–3.8)	0.7 (0.4–0.9)	<.001

Table 2: Change in size of EOMs with time of patients with GH-secreting pituitary adenomas

Muscle	Initial Size (95% CI)	Final Size (95% CI)	Change (95% CI)	P Value
Superior rectus (mm)	4.7 (4.4–5.0)	4.3 (4.0–4.6)	-0.4 (–0.9–0.0)	.075
Medial rectus (mm)	4.8 (4.4–5.2)	4.6 (4.3–5.0)	-0.2 (–0.7–0.4)	.546
Lateral rectus (mm)	4.5 (4.1–4.8)	3.9 (3.6–4.2)	-0.6 (–1.0–0.1)	.013
Inferior rectus (mm)	4.8 (4.4–5.3)	4.2 (3.8–4.6)	-0.7 (–1.2–0.1)	.024
Average (mm)	4.7 (4.4–4.9)	4.3 (4.0–4.5)	-0.4 (–0.7–0.0)	.037

Table 3: Patients with GH-secretory pituitary adenomas who did or did not achieve a normalized IGF-1 level before their most recent MR imaging

Characteristic	Normalized IGF-1 (95% CI) (n = 9)	Elevated IGF-1 (95% CI) (n = 7)	Difference (95% CI)	P Value
Extraocular muscle size at most recent MR imaging (mm)	3.9 (3.6–4.2)	4.7 (4.3–5.0)	0.7 (0.3–1.2)	<.001
Average IGF-1/ULN at diagnosis	1.9 (1.5–2.3)	2.8 (2.3–3.4)	0.9 (0.2–1.5)	.010
Size of pituitary adenoma (mm)	19.1 (15.9–22.3)	23.9 (17.4–30.3)	4.7 (–2.1–11.6)	.170
Average duration of elevated IGF-1 (mo)	20.4 (12.4–28.5)	39.3 (18.8–59.9)	18.9 (–2.3–40.1)	.078
Average time between initial and final MR imaging (mo)	52.8 (26.1–79.4)	39.9 (19.7–60.1)	-12.9 (–45.0–19.1)	.417

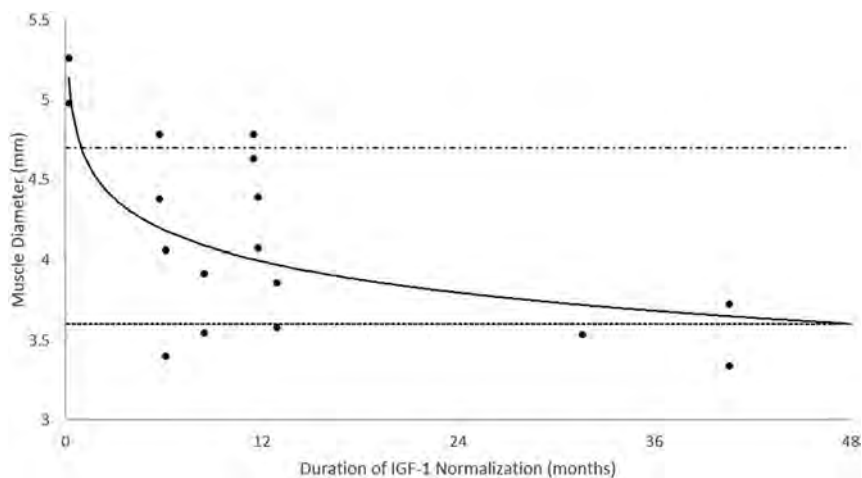


FIG 2. EOM size in patients who achieved normalization of the IGF-1 before their most recent MR imaging. The average EOM size appears to decrease as the duration (months) of IGF-1 normalization increases. The *alternating dashed/dotted line* represents the average EOM size (4.7 mm) in patients who did not achieve IGF-1 normalization before their most recent MR imaging. The *dashed line* represents that average EOM size (3.6 mm) in patients without acromegaly at the time of their most recent MR imaging.

time-consuming investigation of a differential diagnosis including TED. Our findings further support the association between EOM size and GH-secretory pituitary adenomas and suggest that beyond obtaining free T4 and thyroid-stimulating hormone measurements (which is a part of routine assessment of patients with pituitary adenomas), further evaluation of EOM enlargement may be of low clinical yield. Furthermore, our findings suggest the reversibility of the EOM size with effective adenoma-directed surgical and appropriate salvage medical management. Nevertheless, the reversibility of GH-associated organomegaly is debated because the Acromegaly Consensus Conference has reported that in patients with acromegaly, comorbidities may not remit even when full biochemical control is achieved.^{5,14,15}

Although the most common cause of EOM enlargement is Graves disease-associated TED, our study demonstrates a high prevalence of EOM among patients with GH-secretory pituitary adenomas. A retrospective analysis of 60 patients with nonthyroidal enlarged EOMs performed by Patrinely et al¹⁶ demonstrated that only 3% of the cases were caused by acromegaly. However, the pathophysiology of EOM enlargement is largely understudied. In TED, overexpression of the insulin-like growth factor 1 receptor in fibroblasts and T-cells may lead to overactivation of T-cells playing an important part in the development of EOM enlargement across disease processes. It is hypothesized that IGF-1 promotes inflammation by cytokine activation and hyaluronic acid deposition, which causes edema and enlargement of the EOM. This process might also explain the EOM enlargement phenomenon that we identified in GH-secretory pituitary adenomas. To this point, the use of a novel medication recently approved for clinically active TED, teprotzumab, an insulin-like growth factor 1 receptor inhibitor, has demonstrated clinical improvement in diplopia and proptosis compared with a placebo, further confirming the importance of insulin-like growth factor 1 receptor expression and activity in such disease.¹⁷

In our study, we describe EOM enlargement in patients with GH-secretory pituitary adenomas relative to a control group, given the lack of normative measurements of orbital structures by MR imaging. Ozgen^{8,18} proposed criteria for the diameters of normal EOMs on MR imaging, with a proposed normal mean for diameters of the EOM as follows: medial rectus, 4.0 mm; lateral rectus, 3.7 mm; superior group, 4.4 mm; inferior rectus, 4.8 mm; and superior oblique, 3.2 mm. Measurements were similar to previously proposed normative measurements of the EOM by CT imaging.¹⁸ However, EOM measurements can differ depending on race and the measurement technique. Our average measurements of the control group's lateral rectus muscles (lateral rectus, 3.6 mm; 95% CI, 3.3–3.9 mm) were less than the proposed normal means.

We recognize that our study has limitations. The retrospective nature and limited number of patients and short follow-up period limit the wide application of these results. We limited our analysis to objective radiologic findings rather than clinical findings, including measured proptosis and self-reported patient symptoms, which may have greater clinical implications. Furthermore, patients were evaluated using variable MR imaging protocols, not all of which included thin slices through the EOM. Finally, follow-up of the cohort of patients with abnormal IGF-1 levels may reveal further normalization of EOM size beyond what is reported in this study. Despite these limitations, we believe that this study contributes to our understanding of the effects of acromegaly on EOM thickness and both the incidence and reversibility of this finding.

CONCLUSIONS

Notwithstanding the limitations of this study, we identified a strong association between EOM enlargement and the GH-secretory status of pituitary adenomas. We conclude that further investigation of alternative causes of EOM enlargement may be of limited clinical utility in this population. Our data also suggest the potential reversibility of EOM enlargement with pituitary adenoma-directed treatment with salvage management indicated on the basis of IGF-1 elevation. These findings warrant further investigation with larger observation studies because they might assist in patient care and reduce the cost of extraneous testing.



















Disclosures: Andjela Drincic—UNRELATED: Board Membership: Corcept Therapeutics/WellCare, Comments: Advisory Board for Corcept Therapeutics on Cushing disease (it was >2 years ago), advisory board for WellCare (Medicaid) for population health related to diabetes management; Grants/Grants Pending: Toyota, Comments: grant for research on diabetes and driving*; Travel/Accommodations/Meeting Expenses Unrelated to Activities Listed: Corcept paid travel money for Principal Investigator-related travel cost for the Cushing trial*; Other: I serve on the Endocrine Society writing committee for inpatient diabetes (no monetary compensation) and the Endocrine Society Special

Program Committee developing educational activities (no monetary compensation) and was elected to the Pituitary Society Centers of Excellence Committee (no monetary compensation); I am a Principal Investigator for clinical trial in acromegaly with Chiasma (no personal financial gain) and for Cushing medication with Corcept. *Money paid to the institution.

REFERENCES

1. Holdaway IM, Rajasoorya C. **Epidemiology of acromegaly.** *Pituitary* 1999;2:29–41 CrossRef Medline
2. Vilar L, Vilar CF, Lyra R, et al. **Acromegaly: clinical features at diagnosis.** *Pituitary* 2017;20:22–32 CrossRef Medline
3. Giustina A, Bronstein MD, Chanson P, et al. **Staging and managing patients with acromegaly in clinical practice: baseline data from the SAGIT® validation study.** *Pituitary* 2019;22:476–87 CrossRef Medline
4. Lacey B, Chang W, Rootman J. **Nonthyroid causes of extraocular muscle disease.** *Surv Ophthalmol* 1999;44:187–213 CrossRef Medline
5. Zafar A, Jordan DR. **Enlarged extraocular muscles as the presenting feature of acromegaly.** *Ophthalmic Plast Reconstr Surg* 2004;20:334–36 CrossRef Medline
6. Shimon I, Adnan Z, Gorshtein A, et al. **Efficacy and safety of long-acting pasireotide in patients with somatostatin-resistant acromegaly: a multicenter study.** *Endocrine* 2018;62:448–55 CrossRef Medline
7. Van Esdonk MJ, van Zutphen EJ, Roelfsema F, et al. **How are growth hormone and insulin-like growth factor-1 reported as markers for drug effectiveness in clinical acromegaly research? A comprehensive methodologic review.** *Pituitary* 2018;21:310–22 CrossRef Medline
8. Giustina A, Barkan A, Beckers A, et al. **A consensus on the diagnosis and treatment of acromegaly comorbidities: an update.** *J Clin Endocrinol Metab* 2020;105:dgz096 CrossRef Medline
9. Ozgen A, Aydingöz U. **Normative measurements of orbital structures using MRI.** *J Comput Assist Tomogr* 2000;24:493–96 CrossRef Medline
10. Pozzo G, Boschi MC. **Extraocular muscle enlargement in acromegaly.** *J Comput Assist Tomogr* 1982;6:706–707 CrossRef Medline
11. Heireman S, Delaey C, Claerhout I, et al. **Restrictive extraocular myopathy: a presenting feature of acromegaly.** *Indian J Ophthalmol* 2011;59:517–19 CrossRef Medline
12. Mehra M, Mohsin M, Sharma P, et al. **Epiphora and proptosis as a presenting complaint in acromegaly: report of two cases with review of literature.** *Indian J Endocrinol Metab* 2013;17(Suppl 1): S149–51 CrossRef Medline
13. Schwarz F, der Kinderen PJ, Houtstra-Lanz M. **Exophthalmos-producing activity in the serum and in the pituitary of patients with Cushing's syndrome and acromegaly.** *J Clin Endocrinol Metab* 1962;22:718–25 CrossRef Medline
14. Geraedts VJ, Andela CD, Stalla GK, et al. **Predictors of quality of life in acromegaly: No consensus on biochemical parameters.** *Front Endocrinol (Lausanne)* 2017;8:40 CrossRef Medline
15. Kyriakakis N, Lynch J, Gilbey SG, et al. **Impaired quality of life in patients with treated acromegaly despite long-term biochemically stable disease: results from a 5-years prospective study.** *Clin Endocrinol (Oxf)* 2017;86:806–15 CrossRef Medline
16. Patrinely JR, Osborn AG, Anderson RL, et al. **Computed tomographic features of nonthyroid extraocular muscle enlargement.** *Ophthalmology* 1989;96:1038–47 CrossRef Medline
17. Douglas RS, Kahaly GJ, Patel A, et al. **Teprotumumab for the treatment of active thyroid eye disease.** *N Engl J Med* 2020;382:341–52 CrossRef Medline
18. Ozgen A, Ariyurek M. **Normative measurements of orbital structures using CT.** *AJR Am J Roentgenol* 1998;170:1093–96 CrossRef Medline

Radiomics Can Distinguish Pediatric Supratentorial Embryonal Tumors, High-Grade Gliomas, and Ependymomas

 M. Zhang,  L. Tam,  J. Wright,  M. Mohammadzadeh,  M. Han,  E. Chen,  M. Wagner,  J. Nemalka,  H. Lai,  A. Eghbal,  C.Y. Ho,  R.M. Lober,  S.H. Cheshier,  N.A. Vitanza,  G.A. Grant,  L.M. Prolo,  K.W. Yeom, and  A. Jaju



ABSTRACT

BACKGROUND AND PURPOSE: Pediatric supratentorial tumors such as embryonal tumors, high-grade gliomas, and ependymomas are difficult to distinguish by histopathology and imaging because of overlapping features. We applied machine learning to uncover MR imaging–based radiomics phenotypes that can differentiate these tumor types.

MATERIALS AND METHODS: Our retrospective cohort of 231 patients from 7 participating institutions had 50 embryonal tumors, 127 high-grade gliomas, and 54 ependymomas. For each tumor volume, we extracted 900 Image Biomarker Standardization Initiative–based PyRadiomics features from T2-weighted and gadolinium-enhanced T1-weighted images. A reduced feature set was obtained by sparse regression analysis and was used as input for 6 candidate classifier models. Training and test sets were randomly allocated from the total cohort in a 75:25 ratio.

RESULTS: The final classifier model for embryonal tumor-versus-high-grade gliomas identified 23 features with an area under the curve of 0.98; the sensitivity, specificity, positive predictive value, negative predictive value, and accuracy were 0.85, 0.91, 0.79, 0.94, and 0.89, respectively. The classifier for embryonal tumor-versus-ependymomas identified 4 features with an area under the curve of 0.82; the sensitivity, specificity, positive predictive value, negative predictive value, and accuracy were 0.93, 0.69, 0.76, 0.90, and 0.81, respectively. The classifier for high-grade gliomas-versus-ependymomas identified 35 features with an area under the curve of 0.96; the sensitivity, specificity, positive predictive value, negative predictive value, and accuracy were 0.82, 0.94, 0.82, 0.94, and 0.91, respectively.

CONCLUSIONS: In this multi-institutional study, we identified distinct radiomic phenotypes that distinguish pediatric supratentorial tumors, high-grade gliomas, and ependymomas with high accuracy. Incorporation of this technique in diagnostic algorithms can improve diagnosis, risk stratification, and treatment planning.

ABBREVIATIONS: AUC = area under the curve; EP = ependymoma; GLCM = gray-level co-occurrence matrix; HGG = high-grade glioma; LR = logistic regression; NPV = negative predictive value; PNET = primitive neuroectodermal tumor; PPV = positive predictive value; WHO = World Health Organization; XGB = extreme gradient boosting; LASSO = least absolute shrinkage and selection operator

Pediatric supratentorial embryonal tumors, high-grade gliomas (HGGs), and ependymomas (EPs) can be difficult to

differentiate by both imaging and histopathology because of overlapping features.^{1,2} Given the vastly different treatment approaches and prognoses, accurate diagnosis of these entities is extremely important; however, it requires advanced immunohistochemistry and molecular analyses, which have substantial practical barriers of availability, timeliness, and cost.³⁻⁵


Embryonal tumors of the CNS are highly malignant, undifferentiated, or poorly differentiated tumors of neuroepithelial origin, a category that has continuously evolved during the past few decades, reflecting an improving understanding of tumor biology.^{1,6} The nomenclature of supratentorial HGG has also

Received September 17, 2021; accepted after revision January 25, 2022.

From the Departments of Neurosurgery (M.Z.), Stanford University School of Medicine (L.T.), Stanford, California; Department of Radiology (J.W.), Division of Pediatric Hematology/Oncology (N.A.V.), and Department of Pediatrics, Seattle Children's Hospital, Seattle, Washington; Department of Radiology (J.W.), Harborview Medical Center, Seattle, Washington; Department of Radiology (M.M.), Tehran University of Medical Sciences, Tehran, Iran; Department of Pediatrics (M.H.), Children's Hospital of Philadelphia, University of Pennsylvania, Philadelphia, Pennsylvania; Departments of Clinical Radiology & Imaging Sciences (E.C., C.Y.H.), Riley Children's Hospital, Indiana University, Indianapolis, Indiana; Department of Diagnostic Imaging (M.W.), The Hospital for Sick Children, Ontario, Canada; Division of Pediatric Neurosurgery (J.N., S.H.C.), Department of Neurosurgery, Huntsman Cancer Institute, Intermountain Healthcare Primary Children's Hospital, University of Utah School of Medicine, Salt Lake City, Utah; Department of Radiology (H.L., A.E.), CHOC Children's Hospital of Orange County California, University of California, Irvine, California; Division of Neurosurgery (R.M.L.), Dayton Children's Hospital, Dayton, Ohio; Department of Pediatrics, Wright State University Boonshoft School of Medicine, Dayton, Ohio; Departments of Radiology (K.W.Y.) and Neurosurgery (G.A.G., L.M.P.), Lucile Packard Children's Hospital, Stanford University, Palo Alto, California; and Department of Medical Imaging (A.J.), Ann and Robert H. Lurie Children's Hospital of Chicago, Northwestern University Feinberg School of Medicine, Chicago, Illinois.

K.W. Yeom and A. Jaju are co-senior authors.

Please address correspondence to Alok Jaju, MD, Department of Medical Imaging, Ann and Robert H. Lurie Children's Hospital of Chicago, 225 E. Chicago Ave, Chicago, IL 60611; e-mail: ajaju@luriechildrens.org; @alok_jaju

 Indicates article with online supplemental data.

<http://dx.doi.org/10.3174/ajnr.A7481>

changed across the years, including major updates in the 2021 World Health Organization Classification of CNS Tumors (WHO CNS5), with separation of “adult-type” and “pediatric-type” gliomas and further subgrouping based on specific genetic mutations. The term “anaplastic astrocytoma” has been discontinued, and “glioblastoma” is no longer used in the pediatric context.⁷ Supratentorial EPs have been shown to be biologically distinct from the more common infratentorial counterparts, with different cells of origin and specific genetic mutations.^{8,9} Supratentorial embryonal tumors, HGGs, and EPs all demonstrate aggressive behavior, and routine histopathology may be unreliable in accurately differentiating these tumor types.

Recent advances in machine learning and computer vision in medicine offer a new potential for precision in oncology whether it is classification of the tumor subgroup or prognosis. For example, feature extraction, such as radiomics, enables mining of high-dimensional, quantitative image features that facilitate data-driven, predictive modeling. With such approaches, computational algorithms assign probabilities for diagnoses based on quantitative analyses of tumor voxels on imaging.^{10,11} Prior studies have used various machine learning approaches to separate the different posterior fossa tumors in children, to predict the molecular subtypes for pediatric medulloblastomas and adult high-grade gliomas, and for development of prognostic biomarkers for various tumors.¹²⁻¹⁹

Here, we present a large multi-institutional cohort of pediatric supratentorial tumors for MR imaging-based radiomics analysis, in an attempt to identify quantitative imaging features and radiomic profiles that can help distinguish these tumors types.

MATERIALS AND METHODS

Study Population

We performed a multi-institutional, retrospective study after institutional review board approval (No. 51059) at participating institutions (Online Supplemental Data) with a waiver of consent. Stanford served as the host institution and executed site-specific data-use agreements. The inclusion criteria were consecutive patients with pathologically confirmed supratentorial embryonal tumors, HGGs, and EPs spanning 2003–2021, nineteen years of age or younger, and with preoperative MR imaging that included both axial T2-weighted and gadolinium-enhanced T1-weighted sequences. For this retrospective study, the original tumor type assignments were based on the older WHO classifications. The HGG group included anaplastic astrocytomas (grade III) and glioblastomas (grade IV); both terms have been discontinued in the 2021 WHO Classification. All supratentorial EPs, regardless of the pathologic grade (grade II or III), were included in the study. We excluded patients if the MR imaging was nondiagnostic or had artifacts.

Imaging Techniques

MR imaging brain scans were performed on 1.5 or 3T MR imaging scanners across centers using the following vendors: GE Healthcare, Siemens, Philips Healthcare, and Toshiba Canon Medical Systems. The T2-MR imaging sequence parameters were the following: T2 TSE clear/sensitivity encoding, T2 FSE, T2 PROPELLER, T2 BLADE (Siemens), T2 DRIVE sensitivity encoding (TR/TE = 2475.6–9622.24/80–146.048 ms); section

thickness = 1–5 mm, 0.5- or 1-mm skip; matrix ranges = 224–1024 × 256–1024. T1-MR imaging sequences comprised T1 MPRAGE, T1 axial MRI 3D brain volume, T1 fast-spoiled gradient recalled, T1 echo-spoiled gradient echo, and T1 spin-echo (section thickness = 0.8–1.2 mm; matrix = 256–512 × 256–512).

Feature Extraction and Reduction

One blinded neuroradiology attending physician (reader 1, K.W.Y.) independently segmented the volumetric whole-tumor boundary on both T2-MR imaging and T1-MR imaging, inclusive of solid, cystic, and hemorrhagic components, excluding perilesional edema. The T2-MR imaging was used as the baseline for tumor segmentation, and the ROI was manually overlaid onto the T1-MR imaging. A second blinded neuroradiology attending physician (reader 2, A. J.) confirmed tumor boundary delineation. Normalization was performed by normalizing the intensities by centering at the mean (SD), with a scaling factor of 100. Isotropic voxel resampling was performed to $1 \times 1 \times 1 \text{ mm}^3$. A bin width of 10 was used for gray-level discretization in both normalized MR images. Both the normalization and resampling elements are further detailed in the Online Supplemental Data. From each tumor volume, we extracted 1800 (900 each from T2-MR imaging and T1-MR imaging) Image Biomarker Standardization Initiative-based^{20,21} PyRadiomics features (2.2.0.post7+gac7458e; <https://aim.hms.harvard.edu/pyradiomics>) using the Quantitative Image Feature Pipeline (Online Supplemental Data).²² Extracted features underwent sparse regression analysis by a least absolute shrinkage and selection operator (LASSO) on RStudio 1.2.5033 (<https://www.rstudio.com/products/rstudio/download/>; Online Supplemental Data). We conducted feature selection from the entire cohort given our relatively small data set size and addressed this potential limitation by performing internal cross-validated LASSO (glmnet package; <https://glmnet.stanford.edu/articles/glmnet.html>) to obviate overfitting.

Binary Classifier Training and Testing

For each binary classifier model, we first conducted feature reduction using the extracted feature set and clinical variables (age at diagnosis and sex) as input. The corresponding reduced feature set was then submitted to train 6 candidate classifiers to identify the best-performing algorithm. The 6 candidate classifiers included support vector machine, logistic regression (LR), k-nearest neighbor, random forest, extreme gradient boosting (XGB), and neural net. Training and test sets were randomly allocated from the total cohort in a 75:25 ratio. The training cohort underwent resampling to correct for sample imbalance. Embryonal tumors were designated as the positive class in classifiers containing such pathologies. For the classifier between EP and HGG, EP was designated as the positive class. Optimal classifier parameters were estimated by a grid search (Online Supplemental Data). The relative influences of imaging features were calculated for the optimal classifiers, namely, feature coefficients for LR and percentage gain for tree-based classifiers.

Single-Stage Multiclass Classifier Model

To compare the performance of multiple individual binary primary models (embryonal tumor versus HGG; embryonal tumor versus EP; EP versus HGG) with that of a single multiclass model, we used

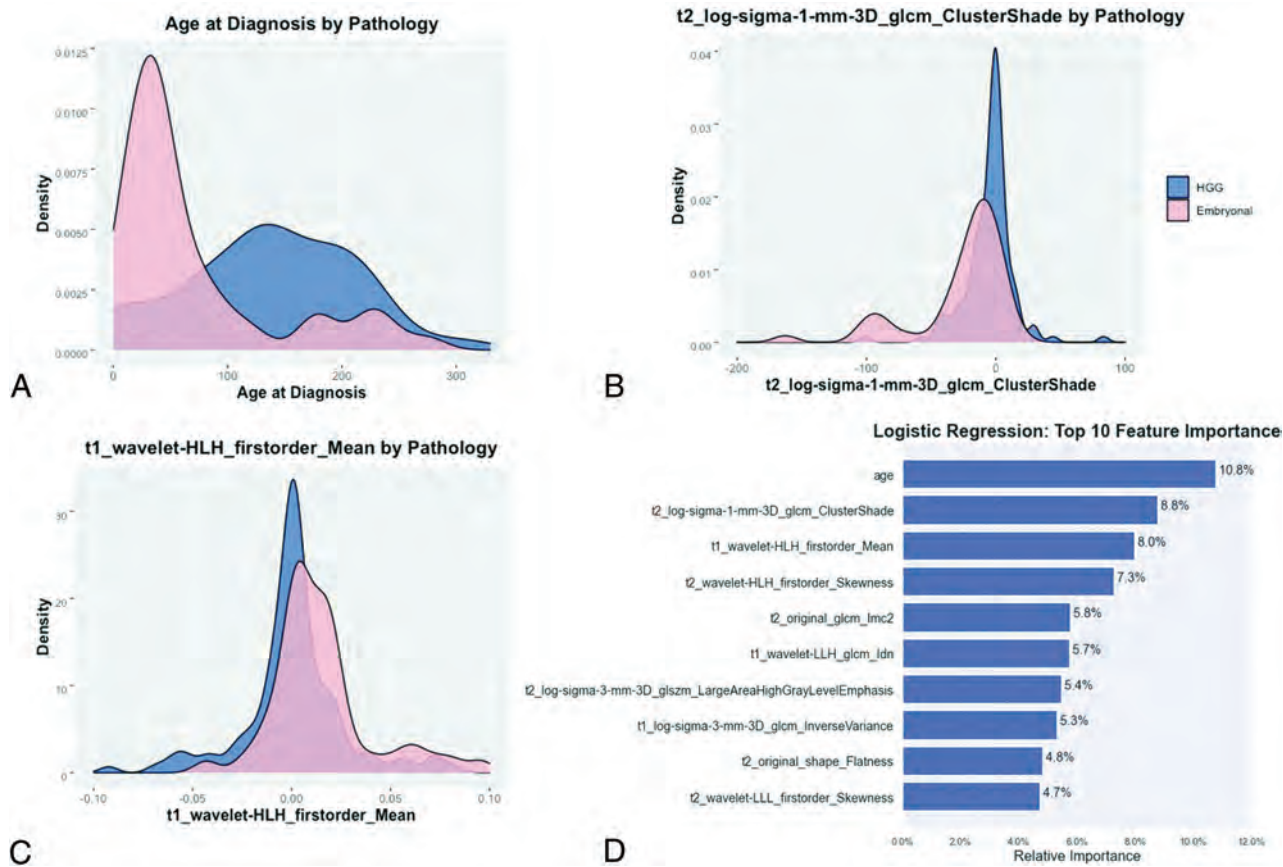


FIG 1. Density plots of the top 3 features, including age at diagnosis (A), T2-Cluster Shade (B), and T1-Mean Intensity (C). D, Bar plot measuring the relative influence as calculated by LR of the top 10 reduced features for the binary classifier trained to distinguish embryonal tumors and high-grade gliomas.

the same 6 candidate classifiers to perform a multiclass classification across the 3 tumor groups: embryonal tumor, HGG, and EP.

Statistical Analysis

A P value $< .05$ was considered statistically significant for all analyses. We calculated sensitivity, specificity, positive predictive value (PPV), negative predictive value (NPV), and area under the curve (AUC) for each classifier. The accuracy confidence interval was compared with the no-information rate, which was calculated from the prevalence of the more populous class within a binary pairing (Wald statistic). Confidence intervals were obtained by bootstrapping the test sets for 2000 random samples. Classifier development was performed using Python 3.8.5 (<https://www.python.org/downloads/release/python-385/>). Feature reduction and statistics were calculated with RStudio 1.2.503.

RESULTS

Patient Cohort

Of the 271 patients who were shared by participating sites, 231 met the final inclusion criteria. Reasons for exclusion were lack of either axial plane T2-MR imaging or T1-MR imaging or artifacts. A few patients were excluded due to infratentorial tumor location. There were 50 (21.6%) embryonal tumors, 127 (55.0%) HGGs, and 54 (23.4%) EPs, with pathologic subtypes as detailed

in the Online Supplemental Data. The mean ages at diagnosis were 69.3, 138.1, and 87.3 months, respectively.

Embryonal Tumor and High-Grade Glioma Classifier

The subsequent classifier for embryonal tumor and HGG identified 23 features (Online Supplemental Data). These features entailed 1 clinical feature (age), 9 from T1-MR imaging, and 13 from T2-MR imaging, including 6 first-order, 2 shape, and 14 textural features (8 gray-level co-occurrence matrix [GLCM], 5 gray-level size zone, 1 gray-level run length matrix). Among the 6 classifier models, LR showed highest performance (AUC = 0.98) (Online Supplemental Data) with a sensitivity, specificity, PPV, NPV, and accuracy of 0.85, 0.91, 0.79, 0.94, and 0.89, respectively. The top 3 relevant features included age, T2-cluster shade (GLCM), and T2-mean (first-order intensity, Fig 1, and Online Supplemental Data). Accuracy was significantly higher than the no-information rate ($P < .001$). Metrics from all 6 classifier models are provided in the Online Supplemental Data.

Embryonal Tumor and Ependymoma Classifier

In the binary classifier for embryonal tumor versus EP, LASSO regression identified 4 relevant Image Biomarker Standardization Initiative features, with 2 from T1-MR imaging and 2 from T2-MR imaging (Online Supplemental Data), including 3 first-order features and 1 textural feature (1 GLCM). Among the 6 classifier models,

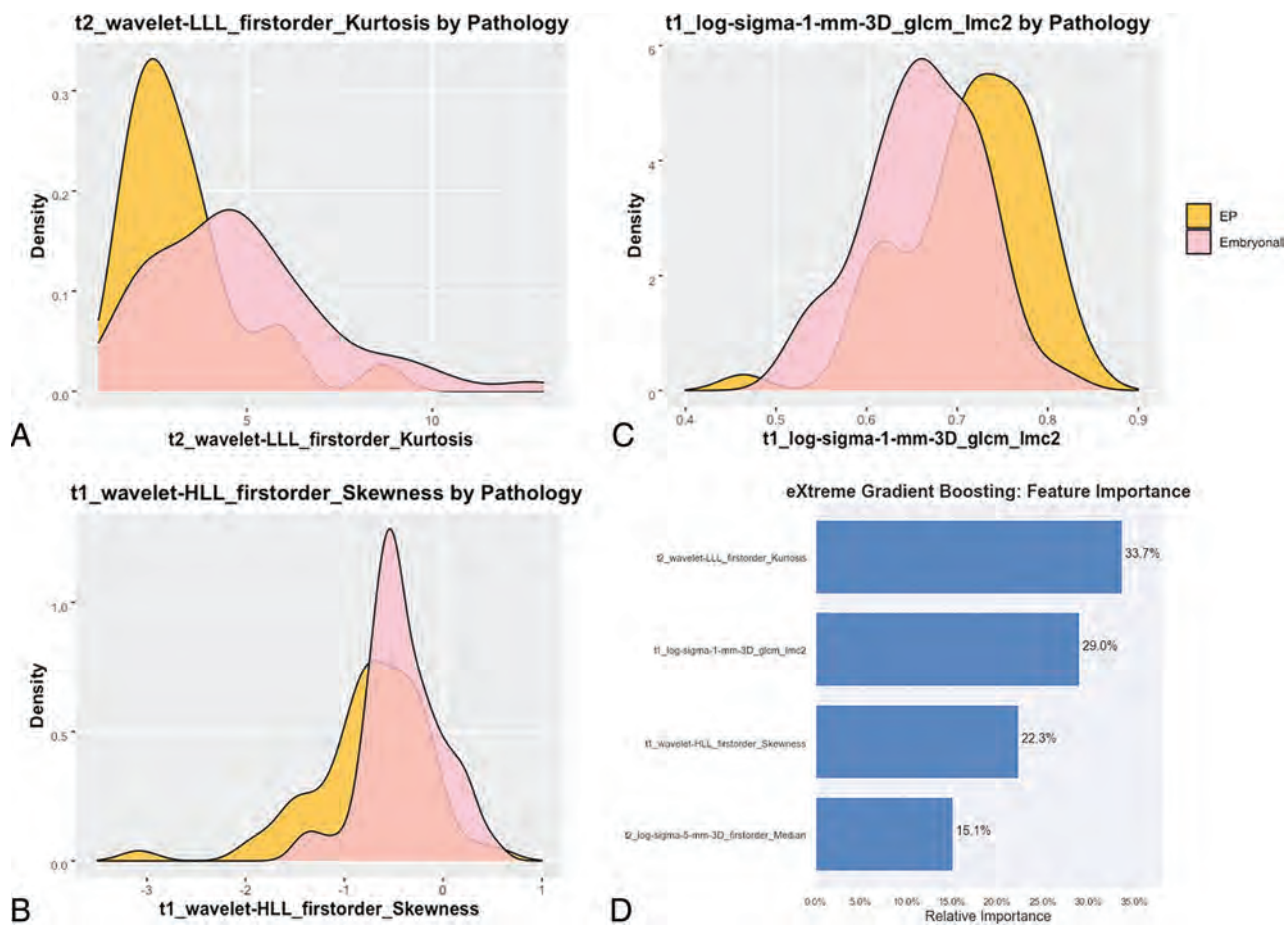


FIG 2. Density plots of the top 3 features, including T2-kurtosis (A), T1-skewness (B), and T1-information measure of correlation (C). D, Bar plot measuring the relative influence as calculated by XGB of the 4 reduced features for the binary classifier trained to distinguish embryonal tumor and ependymoma.

XGB had the best performance (AUC = 0.82) (Online Supplemental Data). The top 3 relevant features included T2-kurtosis (first-order), T1-informational measure of correlation (GLCM), and T1-skewness (first-order, Fig 2 and Online Supplemental Data). Sensitivity, specificity, PPV, NPV, and accuracy were 0.93, 0.69, 0.76, 0.90, 0.81, respectively. Accuracy was statistically greater than the no-information rate ($P = .001$). Metrics from all 6 classifier models are provided in Online Supplemental Data.

Ependymoma and High-Grade Glioma Classifier

Finally, a classifier performed for HGG and EP identified 35 features (Online Supplemental Data), including 1 clinical feature, 16 from T1-MR imaging, and 18 from T2-MR imaging, including 8 first-order, 1 shape, and 25 textural features (11 GLCM, 10 gray-level size zones, 4 gray-level run length matrix). Among the 6 classifier models, neural net showed the highest performance (AUC = 0.96) (Online Supplemental Data) with a sensitivity, specificity, PPV, NPV, and accuracy of 0.82, 0.94, 0.82, 0.94, and 0.91, respectively. The top 3 relevant features included T1-mean (first-order intensity), T1-cluster shade (GLCM), and T2-maximal correlation coefficient (GLCM, Fig 3, and Online Supplemental Data). Accuracy was statistically higher than the no-information rate ($P < .001$). Metrics from all 6 classifier models are provided in the Online Supplemental Data.

Single-Stage Embryonal Tumor, High-Grade Glioma, Ependymoma Classifier

The performance of this multiclass classifier was inferior to the above-described binary classifiers, and the metrics stemming from this model are included in the Online Supplemental Data.

DISCUSSION

In this multi-institutional study, we constructed machine learning classifiers to identify MR imaging-based radiomics phenotypes that distinguish supratentorial embryonal tumors, HGG, and EP. Our study represents the largest study to date on imaging of pediatric supratentorial tumors and the first one to apply radiomics.

Histopathologic features of embryonal tumors, HGG, and EP can overlap and require immunohistochemistry and/or molecular profiling for accurate diagnosis. Also, recent clinical trials have reported that rates of discordance between central and site pathologic review range between 28% and 38%, further highlighting the difficulties in accurate pathologic diagnosis.^{1,4,8,23} The diagnosis of embryonal tumors from other entities is particularly challenging. In the past, the histologically diagnosed category of primitive neuroectodermal tumors (CNS-PNET) was considered synonymous with embryonal tumors. However, molecular profiling using genome-

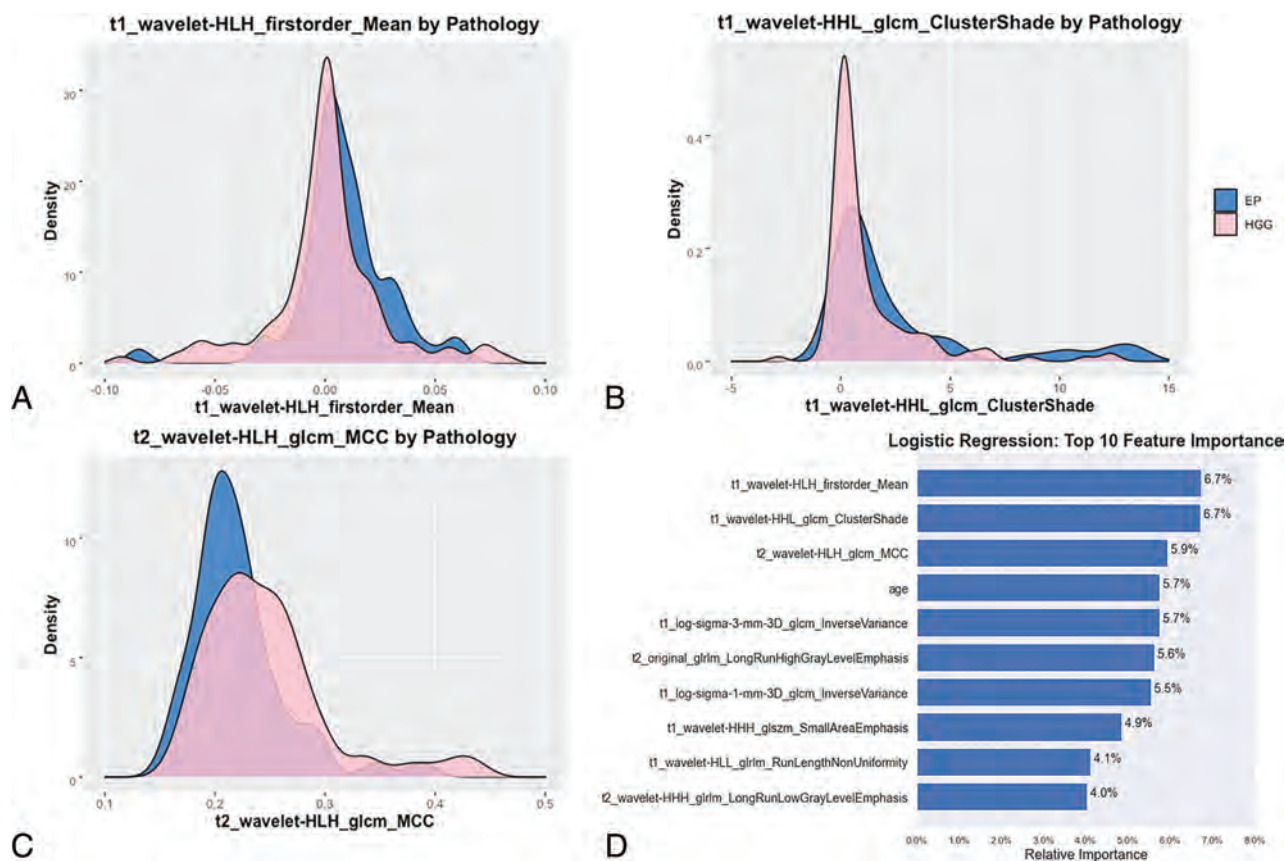


FIG 3. Density plots of the top 3 features, including T1-mean (A), T1-cluster shade (B), and T2-maximal correlation coefficient (C). D, Bar plot measuring the relative influence as calculated by LR of the top 10 reduced features for the binary classifier trained to distinguish ependymomas and high-grade gliomas.

wide DNA methylation of CNS-PNETs has revealed that this group comprises disparate entities including embryonal tumors as well as nonembryonal tumors such as HGG and EP, thereby leading to discontinuation of the term CNS-PNET in the WHO Classification.^{1,2} The supratentorial embryonal tumors include a broad group termed “CNS embryonal tumors (not otherwise specified)” and some more specific entities like embryonal tumors with multilayered rosettes.⁶ In addition to these, supratentorial embryonal tumors have traditionally included atypical teratoid/rhabdoid tumors and pineoblastomas.^{6,8} Supratentorial embryonal tumors represent approximately 15% of CNS neoplasms in children and are biologically distinct from medulloblastomas.²⁴

High-grade gliomas constitute 8%–12% of all pediatric CNS neoplasms, and one-third of these are supratentorial.^{3,25} The 2021 WHO CNS5 places adult and pediatric HGG in separate categories, which are further subdivided on the basis of a complex spectrum of genomic abnormalities.⁷ In contrast to adult-type HGGs, pediatric HGGs are typically *IDH* wild-type and demonstrate histone mutations in more than half the cases.²⁶ Ependymomas constitute 10% of all primary CNS neoplasms in children, and 40% are supratentorial with most in a parenchymal location.^{24,27,28} Supratentorial EPs are now identified as genetically distinct from infratentorial and spinal EPs; WHO CNS5 has introduced genetically defined subgroups of *ZFTA* fusion-positive and *YAP1* fusion-positive for supratentorial EPs, with the former demonstrating more aggressive clinical behavior.^{7,8}

Histopathologic grading of EPs has been controversial with regard to its reproducibility and clinical significance. Although EPs can be either grade II or III, the clinical outcome is poorly correlated with tumor grade; therefore, all EPs regardless of the grade were included in this study.²⁹

There are only a few published studies on the imaging appearance of pediatric supratentorial high-grade tumors.^{27,30–34} The only study comparing the imaging features of supratentorial embryonal tumors with other high-grade tumors (HGG and EP) concluded that it is not possible to distinguish these entities by conventional MR imaging.³⁰ A prior report compared the MR imaging findings of CNS-PNET not otherwise specified with ependymoblastomas and ependymomas, and although the authors found some differences on imaging, their conclusion was that precise distinction is not feasible.³⁵ All of these high-grade tumors have overlapping imaging appearances and typically present as large, heterogeneous, diffusion-restricting, hemispheric, or ventricular masses with variable cystic and necrotic changes. Enhancement is usually present but can vary in extent and intensity.²⁴

Our radiomic models demonstrated high predictive accuracy for each of the embryonal tumor versus HGG, embryonal tumor versus EP, and HGG versus EP classifiers. The final model for embryonal tumor versus HGG selected age as one of the dominant contributors, which is congruent with the reported propensity of embryonal tumors to occur in younger children, and HGG, in the adolescent age group.²⁴ The other 2 models selected

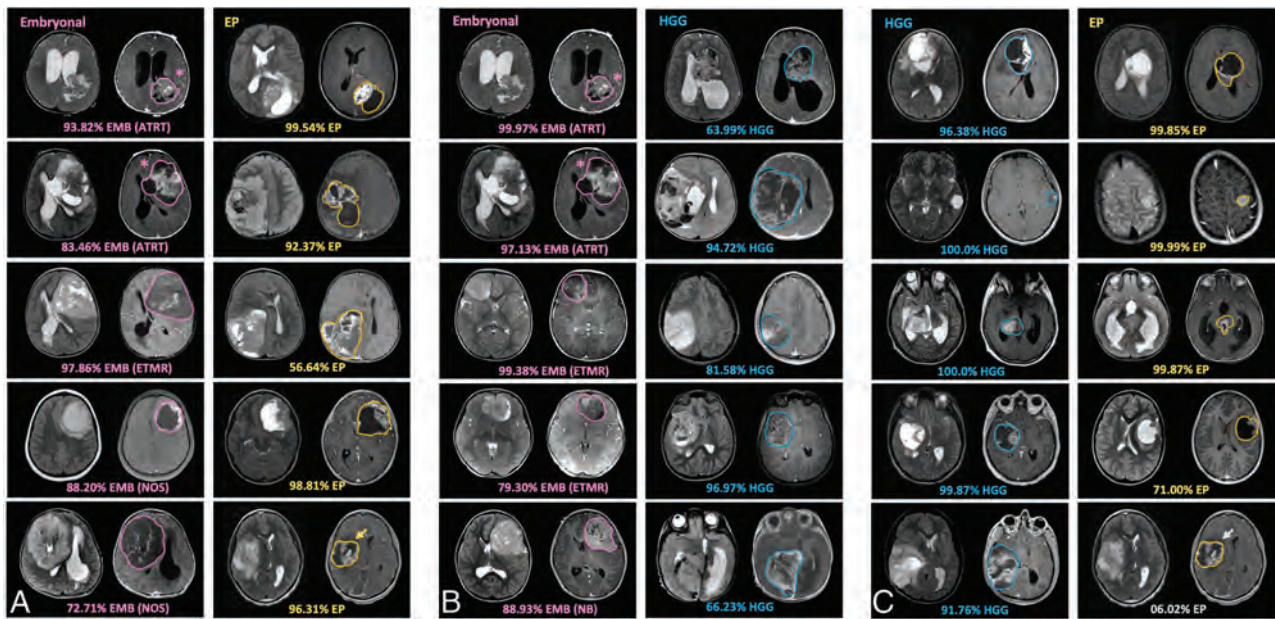


FIG 4. Examples of model-derived probability output are shown on test cohorts of supratentorial embryonal tumors (EMB), EP, and HGG that did not participate in training. Due to overlap in macroscopic features of these malignant supratentorial tumors (eg, a wide range in size, morphology, and enhancement/intensity features), independent binary classifiers that specifically targeted feature separation for EMB versus EP (A, XGB), EMB versus HGG (B, LR), and HGG versus EP (C, Neural network [NN]) were found predictive over a single multiclass classifier. Examples of the same EMB tumors that were separately submitted into XGB and LR models are shown (*asterisk*) and show strong EMB discrimination against EP and HGG, respectively. In 1 example, the same EP tumor could be distinguished from EMB (*yellow arrow*) but was not predictive against HGG (*gray arrow*). ATRT indicates atypical teratoid/rhabdoid tumors; ETMR, embryonal tumor with multi-layered rosettes; NB, CNS neuroblastoma; NOS, not otherwise specified.

purely MR imaging–based radiomic features. One of the advantages of the radiomics technique is that it allows identification of specific computational features that drive model prediction, thus offering some transparency compared with the “black box” nature of deep learning. For the embryonal tumor-versus-HGG classifier, the embryonal tumors demonstrated more balanced T2 voxel intensities around the mean intensity and were overall brighter on T1 postcontrast imaging (Fig 1). For the embryonal tumor-versus-EP classifier, the embryonal tumors demonstrated overall darker voxel intensities on T2, while EPs had more homogeneous texture on T1 postcontrast images (Fig 2). The performance of the embryonal tumor-versus-HGG model was stronger compared with the embryonal tumor-versus-EP model. For the HGG-versus-EP classifier, EPs were overall brighter with more balanced signal intensities around the mean on T1 postcontrast images and had a more “complex” texture involving a greater proportion of brighter intensities on T2-weighted images (Fig 3).

Examples of model-derived probability output are shown on test cohorts of supratentorial embryonal tumors, EP, and HGG that did not participate in training (Fig 4), showing strong discrimination for these binary classifiers. Due to overlap in macroscopic features of these malignant supratentorial tumors (eg, a wide range in size, morphology, and enhancement/intensity features), independent binary classifiers that specifically targeted feature separation for embryonal tumor versus HGG, embryonal tumor versus EP, and HGG versus EP were found predictive over a single multiclass classifier.

We note several limitations, including the small cohort size of each tumor type related to its relative rarity. Nevertheless, our

cohort represents the largest imaging study of supratentorial tumors to date with data pooled from multiple institutions. There were institutional differences in MR imaging acquisition techniques, sequence availability, and image quality; however, we identified discriminating features that are retained despite diverse imaging protocols and vendors that may facilitate future generalizability and usability across centers. While the use of an independent institution outside of training would be desirable to show model generalization, this was not feasible due to uneven distribution of the tumor types across institutions. A future larger cohort study could build on our pilot results and further examine the robustness of radiomics-based separation of these supratentorial tumors. Additional imaging sequences such as ADC and DWI, which may have predictive information, were excluded to preserve a robust sample size. We extracted radiomics features from isolated tumors and thus did not incorporate spatial relationship. Future design could consider combining radiomics and deep learning approaches that can intake whole-brain MR imaging for feature extraction and thereby assimilate tumor spatial features. While we performed intensity normalization and isotropic voxel resample, incorporation of other pre-processing steps would be desirable to further enhance the reproducibility and generalization of MR imaging–based radiomics classification.

A common limitation of radiomics lies in replicability when obscure algorithms are used for feature extraction. Thus, we used the publicly available PyRadiomics package to compute features, as defined by the Imaging Biomarker Standardization Initiative, for future reproducibility.²⁰

CONCLUSIONS

Accurate pathologic diagnosis of supratentorial tumors often requires advanced immunohistochemistry and molecular analyses. These techniques are not readily available outside a handful of brain tumor centers and can be prohibitively expensive. Also, final diagnosis may take multiple weeks and is often not available for initial surgical and treatment planning. Conventional MR imaging is also of limited utility in distinguishing these tumors. Our MR imaging–based radiomic phenotypes demonstrated high accuracy and provided a rapid, readily available tool that can help provide a more accurate imaging diagnosis or a narrower differential diagnosis. This result in conjunction with initial histopathology can be more effective in guiding the surgery, treatment planning, and prognostication and can improve the overall outcomes of these patients. In recent years, standardization of quantitative image features by the radiology and bioinformatics community now enables potential deployment of such image-derived variables with fidelity in the clinical environment across centers. Pediatric embryonal tumors, HGGs, and EPs also have a wide and complex spectrum of genomic features involving several oncogenic pathways that can further affect the therapeutic strategies, and noninvasive distinction among these would be the next frontier for machine learning–based imaging techniques.

Disclosure forms provided by the authors are available with the full text and PDF of this article at www.ajnr.org.

REFERENCES

- Hwang EI, Kool M, Burger PC, et al. **Extensive molecular and clinical heterogeneity in patients with histologically diagnosed CNS-PNET treated as a single entity: a report from the Children's Oncology Group Randomized ACNS0332 Trial.** *J Clin Oncol* 2018;36:3388–95 CrossRef
- Sturm D, Orr BA, Toprak UH, et al. **New brain tumor entities emerge from molecular classification of CNS-PNETs.** *Cell* 2016;164:1060–172 CrossRef Medline
- Braunstein S, Raleigh D, Bindra R, et al. **Pediatric high-grade glioma: current molecular landscape and therapeutic approaches.** *J Neurooncol* 2017;134:541–49 CrossRef Medline
- Jakacki RI, Burger PC, Kocak M, et al. **Outcome and prognostic factors for children with supratentorial primitive neuroectodermal tumors treated with carboplatin during radiotherapy: a report from the Children's Oncology Group.** *Pediatr Blood Cancer* 2015;62:776–83 CrossRef Medline
- Lillard JC, Venable GT, Khan NR, et al. **Pediatric supratentorial ependymoma: surgical, clinical, and molecular analysis.** *Neurosurgery* 2019;85:41–49 CrossRef Medline
- Louis DN, Perry A, Reifenberger G, et al. **The 2016 World Health Organization Classification of Tumors of the Central Nervous System: a summary.** *Acta Neuropathol* 2016;131:803–20 CrossRef Medline
- Louis DN, Perry A, Wesseling P, et al. **The 2021 WHO Classification of Tumors of the Central Nervous System: a summary.** *Neuro Oncol* 2021;23:1231–51 CrossRef Medline
- AlRayahi J, Zapotocky M, Ramaswamy V, et al. **Pediatric brain tumor genetics: what radiologists need to know.** *Radiographics* 2018;38:2102–22 CrossRef Medline
- Torre M, Alexandrescu S, Dubuc AM, et al. **Characterization of molecular signatures of supratentorial ependymomas.** *Mod Pathol* 2020;33:47–56 CrossRef Medline
- Lambin P, Leijenaar RTH, Deist TM, et al. **Radiomics: the bridge between medical imaging and personalized medicine.** *Nat Rev Clin Oncol* 2017;14:749–62 CrossRef Medline
- Napel S, Mu W, Jardim-Perassi BV, et al. **Quantitative imaging of cancer in the postgenomic era: Radio(gen)omics, deep learning, and habitats.** *Cancer* 2018;124:4633–49 CrossRef Medline
- Chaddad A, Kucharczyk MJ, Daniel P, et al. **Radiomics in glioblastoma: current status and challenges facing clinical implementation.** *Front Oncol* 2019;9:374 CrossRef Medline
- Dong J, Li L, Liang S, et al. **Differentiation between ependymoma and medulloblastoma in children with radiomics approach.** *Acad Radiol* 2021;28:318–27 CrossRef Medline
- Lohmann P, Elahmadawy MA, Gutsche R, et al. **FET PET radiomics for differentiating pseudoprogression from early tumor progression in glioma patients post-chemoradiation.** *Cancers (Basel)* 2020;12:3835 CrossRef Medline
- Park CJ, Han K, Kim H, et al. **MRI features may predict molecular features of glioblastoma in isocitrate dehydrogenase wild-type lower-grade gliomas.** *AJNR Am J Neuroradiol* 2021;42:448–56 CrossRef Medline
- Quon JL, Bala W, Chen LC, et al. **Deep learning for pediatric posterior fossa tumor detection and classification: a multi-institutional study.** *AJNR Am J Neuroradiol* 2020;41:1718–25 CrossRef Medline
- Rodriguez Gutierrez D, Awwad A, Meijer L, et al. **Metrics and textural features of MRI diffusion to improve classification of pediatric posterior fossa tumors.** *AJNR Am J Neuroradiol* 2014;35:1009–15 CrossRef Medline
- Zhang M, Wong SW, Lummus S, et al. **Radiomic phenotypes distinguish atypical teratoid/rhabdoid tumors from medulloblastoma.** *AJNR Am J Neuroradiol* 2021;42:1702–08 CrossRef Medline
- Zhou H, Hu R, Tang O, et al. **Automatic machine learning to differentiate pediatric posterior fossa tumors on routine MR imaging.** *AJNR Am J Neuroradiol* 2020;41:1279–85 CrossRef Medline
- Zwanenburg A, Vallieres M, Abdalah MA, et al. **The image biomarker standardization initiative: standardized quantitative radiomics for high-throughput image-based phenotyping.** *Radiology* 2020;295:328–38 CrossRef Medline
- van Griethuysen JJ, Fedorov A, Parmar C, et al. **Computational radiomics system to decode the radiographic phenotype.** *Cancer Res* 2017;77:e104–07 CrossRef Medline
- Mattonen SA, Gude D, Echegaray S, et al. **Quantitative imaging feature pipeline: a web-based tool for utilizing, sharing, and building image-processing pipelines.** *J Med Imaging (Bellingham)* 2020;7:042803 CrossRef Medline
- Fouladi M, Hunt DL, Pollack IF, et al. **Outcome of children with centrally reviewed low-grade gliomas treated with chemotherapy with or without radiotherapy on Children's Cancer Group high-grade glioma study CCG-945.** *Cancer* 2003;98:1243–52 CrossRef Medline
- Zamora C, Huisman TA, Izbudak I. **Supratentorial tumors in pediatric patients.** *Neuroimaging Clin N Am* 2017;27:39–67 CrossRef Medline
- Fangusaro J. **Pediatric high-grade glioma: a review and update on tumor clinical characteristics and biology.** *Front Oncol* 2012;2:105 CrossRef Medline
- Mackay A, Burford A, Carvalho D, et al. **Integrated molecular meta-analysis of 1,000 pediatric high-grade and diffuse intrinsic pontine glioma.** *Cancer Cell* 2017;32:520–37.e5 CrossRef Medline
- Mangalore S, Aryan S, Prasad C, et al. **Imaging characteristics of supratentorial ependymomas: study on a large single institutional cohort with histopathological correlation.** *Asian J Neurosurg* 2015;10:276–81 CrossRef Medline
- Reni M, Gatta G, Mazza E, et al. **Ependymoma.** *Crit Rev Oncol Hematol* 2007;63:81–89 CrossRef Medline
- Ellison DW, Kocak M, Figarella-Branger D, et al. **Histopathological grading of pediatric ependymoma: reproducibility and clinical relevance in European trial cohorts.** *J Negat Results Biomed* 2011;10:7 CrossRef Medline

30. Jaju A, Hwang EI, Kool M, et al. **MRI features of histologically diagnosed supratentorial primitive neuroectodermal tumors and pineoblastomas in correlation with molecular diagnoses and outcomes: a report from the Children's Oncology Group ACNS0332 Trial.** *AJNR Am J Neuroradiol* 2019;40:1796–1803 CrossRef Medline
31. Borja MJ, Plaza MJ, Altman N, et al. **Conventional and advanced MRI features of pediatric intracranial tumors: supratentorial tumors.** *AJR Am J Roentgenol* 2013;200:W483–503 CrossRef Medline
32. Chawla A, Emmanuel JV, Seow WT, et al. **Paediatric PNET: pre-surgical MRI features.** *Clin Radiol* 2007;62:43–52 CrossRef Medline
33. Dai AI, Backstrom JW, Burger PC, et al. **Supratentorial primitive neuroectodermal tumors of infancy: clinical and radiologic findings.** *Pediatr Neurol* 2003;29:430–34 CrossRef Medline
34. Klisch J, Husstedt H, Hennings S, et al. **Supratentorial primitive neuroectodermal tumours: diffusion-weighted MRI.** *Neuroradiology* 2000;42:393–98 CrossRef Medline
35. Nowak J, Seidel C, Pietsch T, et al. **Systematic comparison of MRI findings in pediatric ependymoblastoma with ependymoma and CNS primitive neuroectodermal tumor not otherwise specified.** *Neuro Oncol* 2015;17:1157–65 CrossRef Medline

Different from the Beginning: WM Maturity of Female and Male Extremely Preterm Neonates— A Quantitative MRI Study

V.U. Schmidbauer, M.S. Yildirim, G.O. Dovjak, K. Goeral, J. Buchmayer, M. Weber, M.C. Diogo, V. Giordano, G. Mayr-Geisl, F. Prayer, M. Stuempflen, F. Lindenlaub, V. List, S. Glatter, A. Rauscher, F. Stuhr, C. Lindner, K. Klebermass-Schrehof, A. Berger, D. Prayer, and G. Kasprlan



ABSTRACT

BACKGROUND AND PURPOSE: Former preterm born males are at higher risk for neurodevelopmental disabilities compared with female infants born at the same gestational age. This retrospective study investigated sex-related differences in the maturity of early myelinating brain regions in infants born <28 weeks' gestational age using diffusion tensor- and relaxometry-based MR imaging.

MATERIALS AND METHODS: Quantitative MR imaging sequence acquisitions were analyzed in a sample of 35 extremely preterm neonates imaged at term-equivalent ages. Quantitative MR imaging metrics (fractional anisotropy; ADC [$10^{-3}\text{mm}^2/\text{s}$]; and T1-/T2-relaxation times [ms]) of the medulla oblongata, pontine tegmentum, midbrain, and the right/left posterior limbs of the internal capsule were determined on diffusion tensor- and multidynamic, multiecho sequence-based imaging data. ANCOVA and a paired *t* test were used to compare female and male infants and to detect hemispheric developmental asymmetries.

RESULTS: Seventeen female (mean gestational age at birth: 26 + 0 [SD, 1 + 4] weeks+days) and 18 male (mean gestational age at birth: 26 + 1 [SD, 1 + 3] weeks+days) infants were enrolled in this study. Significant differences were observed in the T2-relaxation time ($P = .014$) of the pontine tegmentum, T1-relaxation time ($P = .011$)/T2-relaxation time ($P = .024$) of the midbrain, and T1-relaxation time ($P = .032$) of the left posterior limb of the internal capsule. In both sexes, fractional anisotropy ($P [\eta] < .001/P [\delta] < .001$) and ADC ($P [\eta] = .017/P [\delta] = .028$) differed significantly between the right and left posterior limbs of the internal capsule.

CONCLUSIONS: The combined use of various quantitative MR imaging metrics detects sex-related and interhemispheric differences of WM maturity. The brainstem and the left posterior limb of the internal capsule of male preterm neonates are more immature compared with those of female infants at term-equivalent ages. Sex differences in WM maturation need further attention for the personalization of neonatal brain imaging.

ABBREVIATIONS: FA = fractional anisotropy; GA = gestational age; ICC = intraclass correlation coefficient; MDME = multidynamic multiecho; PLIC = posterior limb of the internal capsule; PMA = postmenstrual age; T1R = T1-relaxation time; T2R = T2-relaxation time

Brain myelination begins prenatally and reaches completion in the third decade of life.¹ The biochemical composition of the myelin sheath causes T1- and T2-weighted MR imaging signal

intensity characteristics, which allow the radiologic evaluation of the human WM maturation.²⁻⁴

Preterm delivery interferes with regular brain maturation and leads to delays in myelin development.⁵ Since prematurity is associated with future neurologic and cognitive impairment,⁶⁻⁹ the neuroradiologic assessment of brain myelination is paramount to evaluate the risk of potential disabilities in later life. Despite MR imaging being the current standard of reference for neonatal brain imaging, subjective radiologic assessments are limited by the visually subtle effects of small myelin quantities on T1-/T2-weighted MR imaging contrasts.^{1,4,5,10} Hence, subtle myelin-related signal intensity changes may escape conventional, qualitative MR imaging evaluations.⁵

Diffusion tensor- and relaxometry-based mapping techniques provide objective, quantitative metrics for cerebral development.¹¹⁻¹³ Recent multidynamic multiecho (MDME) sequence-

Received October 2, 2021; accepted after revision January 25, 2022.

From the Department of Biomedical Imaging and Image-guided Therapy (V.U.S., M.S.Y., G.O.D., M.W., F.P., M.S., F.L., F.S., C.L., D.P., G.K.); Comprehensive Center for Pediatrics (K.G., J.B., V.G., V.L., S.G., K.K.-S., A.B.), Department of Pediatrics and Adolescent Medicine, Division of Neonatology, Pediatric Intensive Care and Neuropediatrics; and Department of Neurosurgery (G.M.-G.), Medical University of Vienna, Vienna, Austria; Department of Neuroradiology (M.C.D.), Hospital Garcia de Orta, Almada, Portugal; and Department of Pediatrics (A.R.), University of British Columbia, Vancouver, British Columbia, Canada.

Please address correspondence to Gregor Kasprlan, MD, Department of Biomedical Imaging and Image-guided Therapy, Medical University of Vienna, Waehringer Guertel 18-20, 1090 Vienna, Austria; e-mail: gregor.kasprlan@meduniwien.ac.at

Indicates article with online supplemental data.

<http://dx.doi.org/10.3174/ajnr.A7472>

Table 1: Demographics and characteristics of included neonates

	Extremely Preterm Neonates ^a (n = 35)		Unpaired T Test ^b /Fisher Exact Test ^c
	Female (n = 17)	Male (n = 18)	
Neonatal characteristics			
GA at birth (weeks + days) ^d	26 + 0, SD = 1 + 4; R = 23 + 3–27 + 6	26 + 1, SD = 1 + 3; R = 23 + 4–27 + 6	P = .787
Vaginal delivery	n = 3	n = 2	P = .658
Caesarean delivery	n = 14	n = 16	P = .658
Birth weight (g) ^d	773, SD = 250; R = 480–1500	918, SD = 241; R = 530–1300	P = .091
Singleton pregnancy	n = 10	n = 12	P = .733
Multiple pregnancy	n = 7	n = 6	P = .733
Surfactant received	n = 17	n = 18	P > .999
PMA at MR imaging (weeks + days) ^d	37 + 4, SD = 2 + 1; R = 34 + 0–43 + 4	37 + 0, SD = 1 + 2; R = 35 + 1–40 + 2	P = .283
Maternal characteristics			
Maternal age at delivery (yr) ^d	33, SD = 5; R = 22–40	30, SD = 6; R = 19–38	P = .145
Presence of pre-eclampsia	n = 5	n = 2	P = .228
Presence of GDM	n = 1	n = 0	P = .486
Presence of IAI ^e	n = 2	n = 2	P > .999
Neonatal mortality risk			
CRIB II scored ^d	11, SD = 2; R = 7–16	11, SD = 3; R = 8–17	P = .928
Neonatal diagnoses ^f			
Perinatal asphyxia ^g	n = 4	n = 6	P = .711
Patent ductus arteriosus	n = 3	n = 0	P = .104
Necrotizing enterocolitis	n = 1	n = 1	P > .999
Bronchopulmonary dysplasia	n = 3	n = 3	P > .999
Retinopathy of prematurity	n = 9	n = 7	P = .505

Note:—CRIB II indicates Clinical Risk Index for Babies II; GDM, gestational diabetes mellitus; IAI, intra-amniotic infection (chorioamnionitis).

^a Born before 28 weeks' gestation (routine MR imaging of the preterm neonatal brain at approximately term-equivalent age).

^b Applies to metric data.

^c Applies to categoric variables.

^d Data presented as mean (SD) and range (R).

^e Based on clinical presentation, placental histology, bacterial culture, and blood markers of inflammation.

^f Neonates could be represented in multiple rows (>1 condition).

^g Based on clinical presentation, Apgar scores, umbilical cord pH, and first blood gas analysis (pH, base excess, and lactate) (absence of asphyxia-induced brain injury).

acquisition strategies provide a variety of MR imaging contrasts and quantitative maps based on a single scan of <6 minutes.^{14–16} Therefore, SyMRI-based (SyntheticMR) MDME postprocessing (postprocessing time, <1 minute) makes tissue-specific T1-/T2-relaxation time (T1R/T2R) metrics available in a clinically acceptable time.¹⁶ The capability to quantify myelination in the neonatal brain using diffusion tensor parameters (fractional anisotropy [FA] and ADC) and relaxation properties (T1R and T2R) has been demonstrated in previous investigations.^{12,17}

Sex and gestational age (GA) at birth have an impact on WM maturation and on the neurodevelopmental outcome of former preterm neonates.^{5,8,17,18} Evidence suggests that male infants born before 28 weeks' gestation are at the highest risk of severe cognitive impairment.^{8,9,18,19} This investigation was conducted to prove that prematurity affects brain maturation differently in females and males at early developmental stages. Thus, diffusion tensor- and relaxometry-based mapping approaches were applied to detect sex-related maturity differences of early myelinating brain regions in a sample of former extremely preterm neonates. In addition, quantitative imaging markers were used to assess hemispheric asymmetries in brain development in both female and male infants. Relationships between diffusion tensor parameters and tissue-specific relaxation time metrics with regard to brain myelination processes were elucidated.

MATERIALS AND METHODS

Ethics Approval

The local ethics commission approved the protocol of this retrospective study. All parents/guardians provided written, informed consent for neonatal MR imaging before scanning and agreed to the scientific use of the data.

Study Sample

Between June 2017 and August 2020, brain MR imaging was performed in 73 extremely preterm infants (GA at birth: <28 + 0 [weeks + days]) at the Department of Neuroradiology of a tertiary care hospital. All infants were referred for neuroimaging by the Department of Neonatology of the same hospital. At Vienna General Hospital, Medical University of Vienna, brain MR imaging (imaging at approximately term-equivalent age) is performed routinely in former extremely preterm infants. After a review of the imaging data by 1 neonatal neuroimaging expert with 15 years' experience, all neonates with brain scans with pathologic findings were excluded from this study. Thus, only infants without intracranial pathologic brain imaging findings were included (Table 1). At the time of imaging, none of the included infants presented with neurologic symptoms.

Neonatal MR Imaging, Quantitative Sequence, and MR Imaging Data Postprocessing

Before MR imaging, infants were fed or slightly sedated (chloral hydrate, 30–50 mg/kg, or chloral hydrate, 30 mg/kg, combined

Table 2: Quantitative MR imaging sequences

	MDME	DTI
TR (ms)	3309	2435
TE (ms)	13; 100	88
Acquired voxel size (mm)	0.89 × 1.04 × 4.00	2.41 × 2.48 × 2.50
FOV (mm)	200 × 165 × 109	164 × 164 × 100
Echo-train ^a /EPI factor ^b	10	33
Pixel/Hz	1.366/159.0	5.310/40.9
Sense factor	2	2
Gap (mm)	1	0
Slice number	22	40
b-value (s/mm ²)		0/800
Directional resolution		32
Acquisition time (min)	05:24	05:26

Note.—MDME indicates multidynamic multiecho.

^a Applies to MDME sequence.

^b Applies to diffusion tensor imaging sequence.

with midazolam, 0.1 mg/kg) and bedded in a vacuum mattress. All neonates were imaged using a standardized neonatal MR imaging protocol (Online Supplemental Data) on an Ingenia (Philips Healthcare) 1.5T MR imaging system equipped with a 32-channel head coil. An axial MDME sequence and an axial diffusion tensor imaging sequence (flip angle = 90°) (Table 2) were acquired to obtain quantitative data. By applying 2 repeated acquisition phases (phase 1: saturation of 1 section by a section-selective saturation pulse [flip angle = 120°]; and phase 2: generation of a series of spin echoes for another section by section-selective excitation pulses [flip angle = 90°] and section-selective refocusing pulses [flip angle = 180°]), the MDME sequence acquires information about T1R/T2R parameters of the investigated tissue.^{16,20,21} The MDME sequence postprocessing software SyMRI (Version 11.2) was used to generate quantitative T1R-/T2R-based maps. Diffusion tensor data were postprocessed using the IntelliSpace Portal (Version 10; Philips Healthcare).

Determination of Quantitative Parameters

Diffusion tensor parameters (FA; ADC [10^{-3} mm²/s]) and tissue-specific relaxation time metrics (T1R [ms]; T2R [ms]) were quantified in infratentorial and supratentorial neonatal brain regions, which are characterized by advanced states of myelination.¹ ROI placement was performed manually on diffusion tensor-based data and SyMRI-generated maps (Fig 1) by 2 different raters (rater 1, with 3 years' experience and rater 2, with 2 years' experience with neonatal neuroimaging). To ensure maximal overlap across diffusion tensor and relaxation time measures, we conducted a multisection approach. Therefore, for each brain section of interest, 2 separate ROIs were drawn at different levels (performed by both raters in a consensus reading): medulla oblongata (ROI 1: level of the inferior olive; ROI 2: level of the dorsal column nuclei); pontine tegmentum (ROI 1: level of the locus coeruleus; ROI 2: level of the superior olive); midbrain (ROI 1: level of the superior colliculus/intercollicular area; ROI 2: level of the inferior colliculus); and right/left posterior limbs of the internal capsule (PLICs) (ROI 1: level of the foramen of Monroe; ROI 2: level of the third ventricle). On the basis of both ROI drawings for each section, the mean values of FA, ADC, T1R, and T2R were calculated. If the implementation of a multisection approach

was not possible (ie, multiple contiguous slices were not provided, poor delineability of ROIs), 2 separate measures were obtained on 1 appropriate section.

Statistical Analysis

Two groups were defined for statistical analyses: female and male neonates. SPSS Statistics for Macintosh (Version 25.0; IBM) was used for statistical analyses at a significance level of $\alpha = 5\%$ ($P < .05$). Metric data are expressed as means (SD). To summarize the overall agreement of the quantitative parameters determined by both raters, we calculated an intraclass correlation coefficient (ICC) for each ROI. ICC values ≥ 0.75 were considered strong agreement.²² In case of strong concordances, the results of rater 1 were presented. If there were no strong concordances, the results of both raters were reported. To detect differences in FA, ADC, T1R, and T2R of the medulla oblongata, pontine tegmentum, midbrain, right PLIC, and left PLIC between the groups, we performed an ANCOVA. GA at birth; mode of delivery; birth weight; singleton/multiple pregnancy; receipt of surfactant; postmenstrual age (PMA) at MR imaging; maternal age at delivery; presence of pre-eclampsia, gestational diabetes, and chorioamnionitis; Clinical Risk Index for Babies II score;²³ and neonatal diagnoses (Table 1) were defined as covariates to correct for possible confounding effects. An unpaired *t* test (metric data) and a Fisher exact test (categorical variables) were used to detect between-group differences in these variables (Table 1). A paired *t* test was used to assess differences in FA, ADC, T1R, and T2R between the right and left PLICs in both female and male infants. Within both groups, a Pearson correlation analysis was performed to detect relationships between FA and T1R, FA and T2R, ADC and T1R, and ADC and T2R. Multiple-comparison correction was waived due to the small sample size and the increased risk of type II error.²⁴

RESULTS

A total of 35/73 (48%) neonates (female: $n = 17$; mean GA at birth: 26 + 0 [SD, 1 + 4] weeks+days; mean PMA at MR imaging: 37 + 4 [SD, 2 + 1] weeks+days; male: $n = 18$, mean GA at birth: 26 + 1 [SD, 1 + 3] weeks+days; mean PMA at MR imaging: 37 + 0 [SD, 1 + 2] weeks+days) were included in this study (Table 1). The remaining 38/73 (52%) infants were not enrolled due to pathologic brain MR imaging findings (hemorrhage, $n = 35$; periventricular leukomalacia, $n = 2$; and arteriovenous malformation, $n = 1$).

ICC Analysis

For relaxation time metrics, ICC values ranged between 0.831 (95% CI, 0.249–0.948) and 0.986 (95% CI, 0.962–0.995).

For diffusion tensor parameters, ICC values ranged between 0.604 (95% CI, –0.001–0.852) and 0.994 (95% CI, 0.982–0.998). There were no strong correlations between the ADC values determined by both raters in the right/left PLICs (0.743; 95% CI, 0.270–0.908; 0.604; 95% CI, –0.001–0.852) of females and in the medulla oblongata (0.713; 95% CI, 0.068–0.902) and the pontine tegmentum (0.605; 95% CI, –0.038–0.851) of male preterm neonates (Online Supplemental Data).

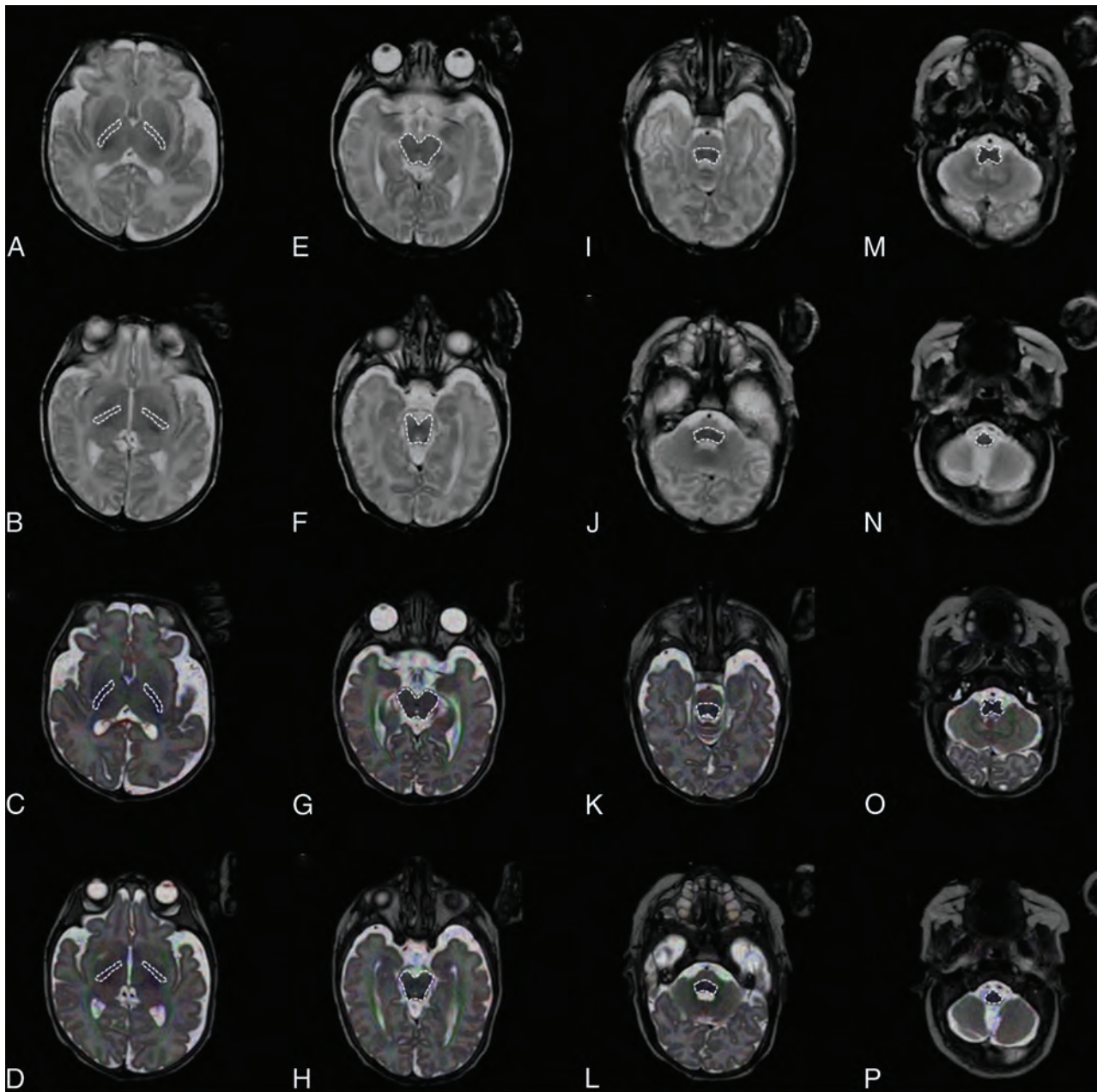


FIG 1. ROI placement is demonstrated on an SyMRI-generated T2-weighted MR imaging contrast (A, B, E, F, I, J, M, N) (TR = 4500 ms; TE = 100 ms; axial plane) and a diffusion tensor map superimposed on a T2-weighted turbo spin-echo sequence-based image (C, D, G, H, K, L, O, P) (TR = 3000 ms; TE = 140 ms; axial plane) of a female infant (GA at birth: 24 + 4 weeks + days; PMA at MR imaging: 39 + 2 weeks + days). For each investigated brain region, 2 separate ROIs were defined at different levels: right/left PLIC (ROI 1: level of the foramen of Monro [A and C]; ROI 2: level of the third ventricle [B and D]); midbrain (ROI 1: level of the superior colliculus/intercollicular area [E and G]; ROI 2: level of the inferior colliculus [F and H]); pontine tegmentum (ROI 1: level of the locus coeruleus [I and K]; ROI 2: level of the superior olive [J and L]); and medulla oblongata (ROI 1: level of the inferior olive [M and O]; ROI 2: level of the dorsal column nuclei [N and P]).

Differences between Female and Male Neonates

Significant differences between female and male infants were observed in T2R ($P = .014$) of the pontine tegmentum, T1R ($P = .011$) and T2R ($P = .024$) of the midbrain, and T1R ($P = .032$) of the left PLIC.

Based on FA ($P = .529$), ADC (rater 1: $P = .651$; rater 2: $P = .844$), T1R ($P = .073$) or T2R ($P = .099$) of the medulla oblongata; FA ($P = .464$), ADC (rater 1: $P = .100$; rater 2: $P = .581$), or T1R ($P = .124$) of the pontine tegmentum; FA ($P = .200$) or ADC ($P =$

$.828$) of the midbrain; FA ($P = .167$), ADC (rater 1: $P = .809$; rater 2: $P = .675$), T1R ($P = .073$), or T2R ($P = .226$) of the right PLIC; and FA ($P = .244$), ADC (rater 1: $P = .511$; rater 2: $P = .072$), or T2R ($P = .443$) of the left PLIC, no significant differences were observed between female and male infants (Figs 2 and 3).

Hemispheric Asymmetries of the PLIC

Female Neonates. There were significant differences in FA ($P < .001$) and ADC (rater 1: $P = .017$; rater 2: $P < .001$) of the

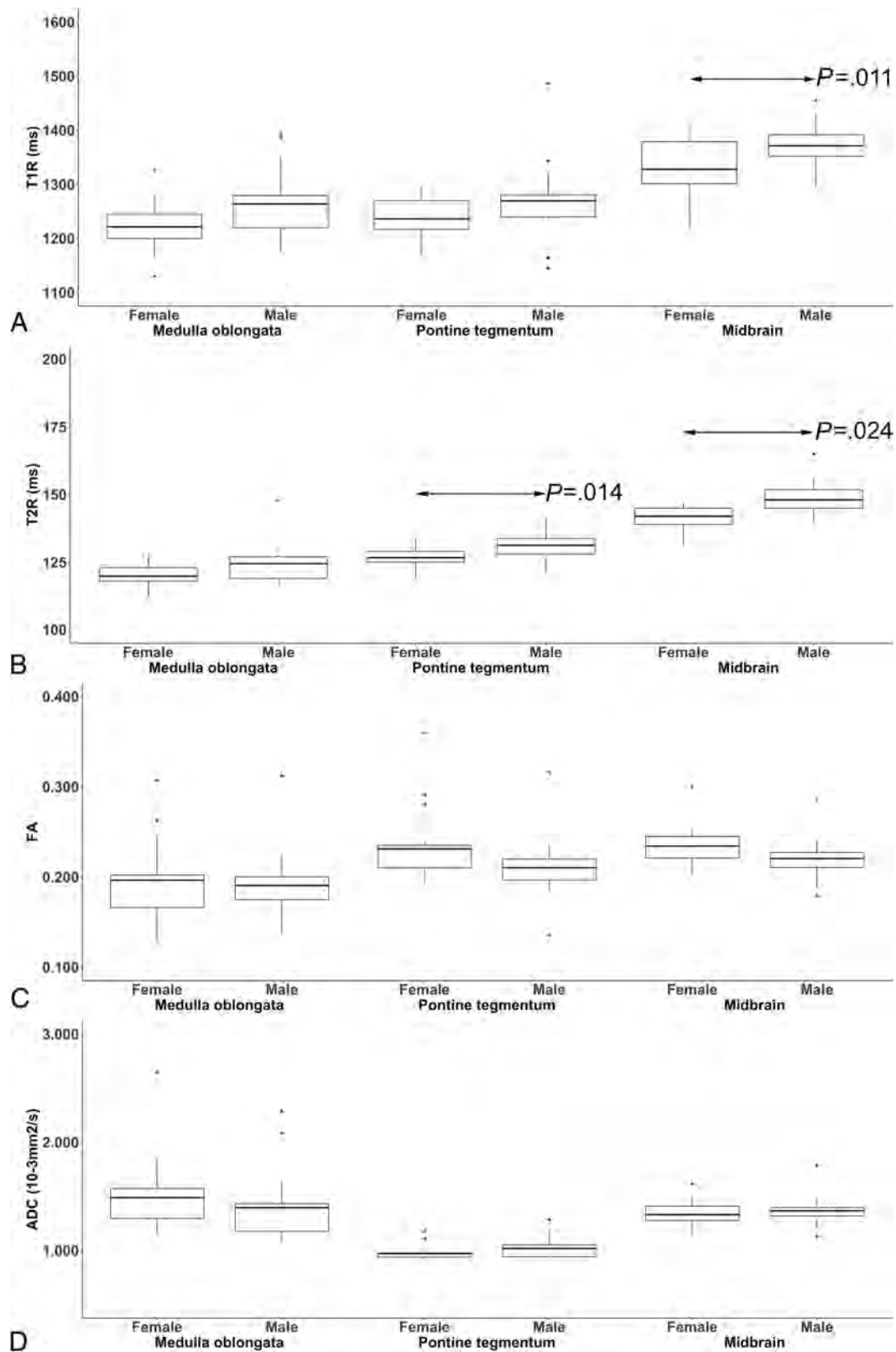


FIG 2. The boxplots show sex-related differences in T1-/T2-relaxation time metrics (ms) (A and B) and diffusion tensor parameters (FA; ADC [$10^{-3}\text{mm}^2/\text{s}$]) (C and D) (determined by rater 1 at term-equivalent ages) of the neonatal medulla oblongata, pontine tegmentum, and midbrain. The *black bar* indicates mean values. Significant differences (*arrows*) were observed in T1R ($P = .011$) of the midbrain (A), T2R ($P = .014$) of the pontine tegmentum, and T2R ($P = .024$) of the midbrain (B) between female and male neonates.

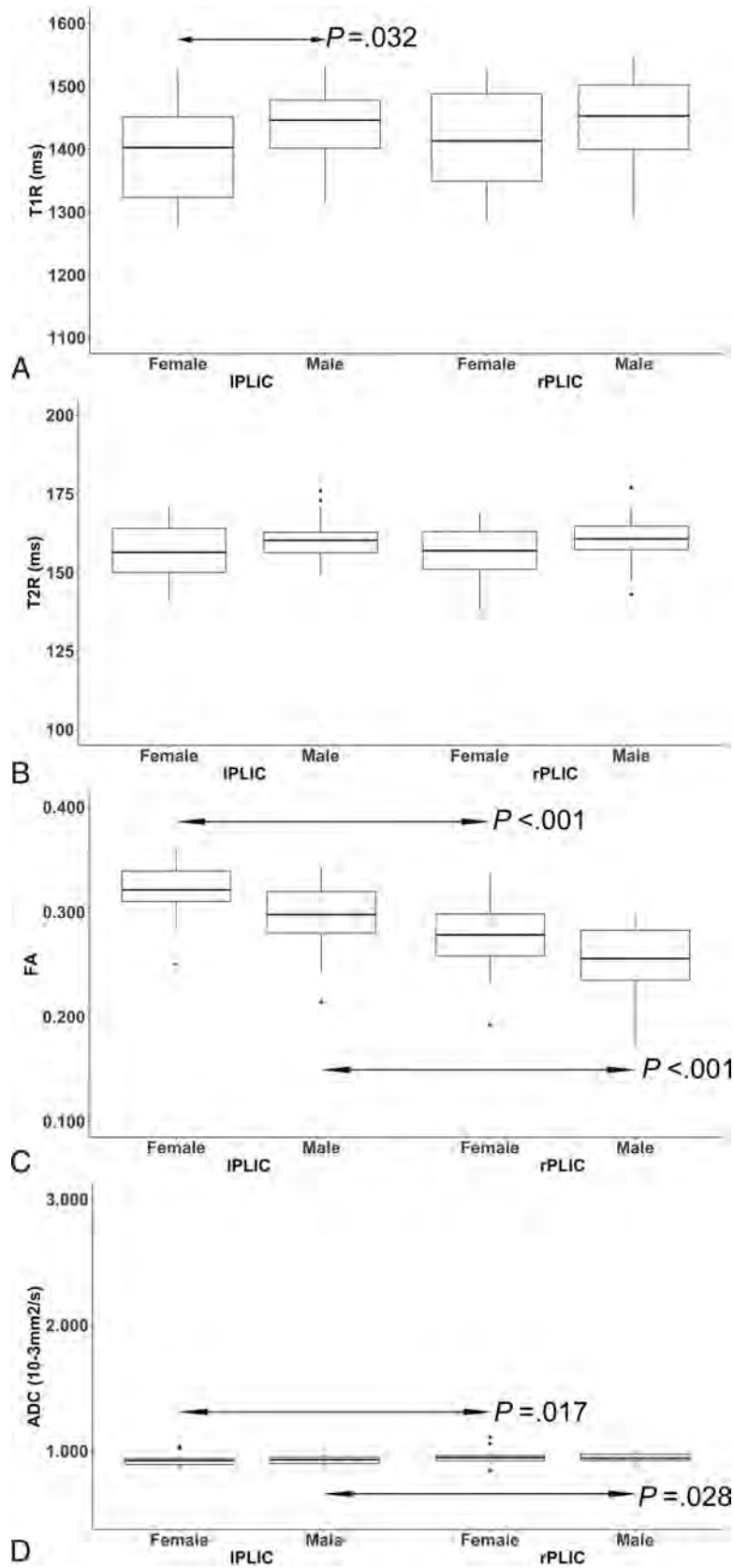


FIG 3. The boxplots show differences in T1-/T2-relaxation time metrics (ms) (A and B) and diffusion tensor parameters (FA; ADC [$10^{-3} \text{mm}^2/\text{s}$]) (C and D) (determined by rater 1 at term-equivalent ages) between both sexes and the right/left posterior limbs of the internal capsule (rPLIC/IPLIC). The *black bar* indicates mean values. Significant sex-related differences (*arrow*) were observed in T1R ($P = .032$) of the IPLIC (A). In both sexes, FA ($P [♀] < .001/P [♂] < .001$) and ADC ($P [♀] = .017; P [♂] = .028$) differed significantly (*arrows*) between the rPLIC and IPLIC (C and D).

left compared with the right PLIC, characterized by higher FA values and lower ADC values (left PLIC). The T1R ($P = .140$) and T2R metrics ($P = .563$) did not reveal significant differences between the right and left PLICs.

Male Neonates. There were significant differences in FA ($P < .001$) and ADC ($P = .028$) of the left compared with the right PLIC, characterized by higher FA values and lower ADC values (left PLIC). The T1R ($P = .162$) and T2R metrics ($P = .740$) did not reveal significant differences between the right and left PLICs (Fig 3).

Relationships between Diffusion Tensor and Relaxation Time Metrics

In female infants, there were significant correlations between the ADC and T1R values in the medulla oblongata ($r = -0.507$, $P = .038$) and the midbrain ($r = -0.516$, $P = .034$).

In male infants, there were significant correlations between the ADC and T2R values in the right ($r = 0.484$, $P = .042$) and left PLICs ($r = 0.492$, $P = .038$) (Online Supplemental Data).

DISCUSSION

This study investigated sex-related brain maturity differences at an early stage of development using quantitative MR imaging. Relaxometry-based mapping revealed a more advanced state of brainstem maturation in female compared with male extremely preterm infants at term-equivalent ages. Moreover, on the basis of T1R, myelination appeared more advanced in the left PLIC in females compared with males. Furthermore, diffusion tensor-based metrics detected advanced maturational stages of the left-sided compared with the right-sided internal capsule regions. However, diffusion tensor and relaxation parameters did not show consistent relationships, which might indicate that both modalities respond to different molecular aspects of myelinogenesis. Therefore, the combined use of diffusion tensor- and relaxation property-derived metrics detects subtle characteristics of WM maturation.

Before 30 weeks' GA, brainstem structures (brachium conjunctivum, medial longitudinal fascicle, medial lemniscus, central tegmental tract, and statoacoustic system) already show remarkable myelination, whereas the PLIC has maximum quantities of myelin supratentorially.^{1,25} The T1R decreases as premyelination processes occur.²⁶⁻²⁸ These are characterized by interactions between isolated myelin components and H₂O molecules.²⁶⁻²⁸ In the course of myelinogenesis, the entry of organic compounds into the myelin sheath results in further T1R shortening.¹ A study in an animal model proved that female sex hormones stimulate the anchoring of proteins into the myelin bilayer.²⁹ Thus, estrogen and progesterone appear to promote myelin formation. Based on T2R, there were significant differences between both sexes at the level of the pontine tegmentum and the midbrain. As opposed to T1R, T2R shortening occurs as fully developed myelin sheaths progressively tighten.²⁶⁻²⁸ Because brain myelination progresses caudally to rostrally, pronounced T2 shortening in the female brainstem appears credible, while maturity-related effects on T2R may have remained limited in supratentorial regions.¹ Although diffusion-based MR imaging has been proved to

visualize gonadal hormone-related maturity differences in WM in an animal model, the quantitative approach applied in this study did not reveal significant results.³⁰ Although ADC values decrease at the stage of premyelination,^{31,32} this parameter seems insensitive to sex-related maturity differences. In contrast to ADC metrics, the FA responds to advanced states of myelin development,³² possibly explaining the limited ability to detect reliable maturity differences between female and male preterm infants.

On the basis of diffusion tensor metrics, myelination appears more advanced in the left compared with the right PLIC in both sexes. This finding is in keeping with descriptions in the literature.²⁸ Using diffusion tensor imaging, Dubois et al^{28,33} demonstrated left-right asymmetries in the infant brain in favor of left-sided projection tracts. Because somatosensory pathways develop rapidly, extensive myelination is detectable in the PLIC at the beginning of the third trimester of pregnancy, while fully developed myelin sheaths are not detectable before 44 weeks' postconceptional age.^{25,33,34} This fact could explain the absence of considerable T2R shortening in the investigated sample. However, even though sex-related differences were observed in T1R of left-sided internal capsule regions, relaxometry-based mapping seems insensitive to hemispheric asynchronies of neonatal brain development.

Diffusion tensor and relaxation time metrics appear to characterize various aspects of myelin maturation: The T1R responds immediately to chemical bonding between H₂O molecules and myelin building blocks; the increase in membrane attenuation (ADC) and the process of axonal myelin ensheathment (FA) further result in the response of diffusion tensor parameters, whereas tightening of myelin sheaths is required for T2R shortening to occur.^{26,31,35} These assumptions are supported by the presented data, which show that diffusion tensor and relaxation time metrics are inconsistently associated.

Preterm delivery accounts for delays in myelin development.^{6,7} Our data suggest that brain myelination processes are more severely affected in former extremely preterm males than their female counterparts. The combined use of different, quantitative MR imaging modalities allows sex-related and hemispheric maturity differences to be identified noninvasively at an early stage of development. Quantitative MR imaging might enable physicians to identify infants in need of intensified support and closer follow-up at an early maturational stage and, therefore, increase their chance of favorable neurodevelopmental outcomes. However, this possibility was beyond the scope of the present investigation and needs to be addressed in the future.

This study has several limitations. Quantitative imaging markers were determined only in a limited number of brain regions. However, the investigation of sex-related characteristics of premyelinating areas was beyond the scope of this investigation. Diffusion tensor- and MDME-based imaging data differed in voxel size and section thickness. Therefore, diffusion tensor and relaxation time metrics were potentially determined on different slices. Thus, a multisection approach was conducted to ensure maximal overlap across FA/ADC and T1R/T2R measures. Even though neonates with brain scans with pathologic findings

were excluded, there were still infants with (extracranial) conditions that might impact neurodevelopment. Thus, statistical methods were applied that correct for possible confounding effects of these conditions. This study did not elaborate on the future outcomes of the preterm infants included. Nonetheless, further investigations that link developmental asynchronies/sex-related differences to the lateralization of brain functions are of highest interest. Although only homogeneous cohorts of former preterm born females and males were included in this study, the investigated sample size was small. However, our data revealed considerable sex-related maturity differences at an early stage of human brain development. Nonetheless, sex-related neurodevelopmental differences require further investigation in larger samples.

CONCLUSIONS

The combined use of diffusion tensor- and relaxometry-based mapping approaches reveals sex-related maturity differences and hemispheric asynchronies of WM maturation. Quantitative imaging markers can detect subtle characteristics of the sequential process of myelination noninvasively at an early stage of cerebral development.

Disclosure forms provided by the authors are available with the full text and PDF of this article at www.ajnr.org.

REFERENCES

- van der Knaap MS, Valk J. *Magnetic Resonance of Myelination and Myelin Disorders*. 3rd ed. Springer-Verlag; 2005
- Barkovich AJ, Kjos BO, Jackson DE, et al. **Normal maturation of the neonatal and infant brain: MR imaging at 1.5 T.** *Radiology* 1988;166:173–80 CrossRef Medline
- van der Knaap MS, Valk J. **MR imaging of the various stages of normal myelination during the first year of life.** *Neuroradiology* 1990;31:459–70 CrossRef Medline
- Porto L, Kieslich M, Yan B, et al. **Accelerated myelination associated with venous congestion.** *Eur Radiol* 2006;16:922–26 CrossRef Medline
- Schmidbauer V, Geisl G, Diogo M, et al. **SyMRI detects delayed myelination in preterm neonates.** *Eur Radiol* 2019;29:7063–72 CrossRef Medline
- Ibrahim J, Mir I, Chalak L. **Brain imaging in preterm infants <32 weeks' gestation: a clinical review and algorithm for the use of cranial ultrasound and qualitative brain MRI.** *Pediatr Res* 2018;84:799–806 CrossRef Medline
- Parikh NA. **Advanced neuroimaging and its role in predicting neurodevelopmental outcomes in very preterm infants.** *Semin Perinatol* 2016;40:530–41 CrossRef Medline
- Glass HC, Costarino AT, Stayer SA, et al. **Outcomes for extremely premature infants.** *Anesth Analg* 2015;120:1337–51 CrossRef Medline
- Marlow N, Wolke D, Bracewell MA, et al; EPICure Study Group. **Neurologic and developmental disability at six years of age after extremely preterm birth.** *N Engl J Med* 2005;352:9–19 CrossRef Medline
- Schmidbauer V, Geisl G, Cardoso Diogo M, et al. **Validity of SyMRI for assessment of the neonatal brain.** *Clin Neuroradiol* 2021;31:315–23 CrossRef Medline
- Wimberger DM, Roberts TP, Barkovich AJ, et al. **Identification of "premyelination" by diffusion-weighted MRI.** *J Comput Assist Tomogr* 1995;19:28–33 CrossRef Medline
- Qiu A, Mori S, Miller MI. **Diffusion tensor imaging for understanding brain development in early life.** *Annu Rev Psychol* 2015;66:853–76 CrossRef Medline
- Lee SM, Choi YH, You SK, et al. **Age-related changes in tissue value properties in children: simultaneous quantification of relaxation times and proton density using synthetic magnetic resonance imaging.** *Invest Radiol* 2018;53:236–45 CrossRef Medline
- McAllister A, Leach J, West H, et al. **Quantitative synthetic MRI in children: normative intracranial tissue segmentation values during development.** *AJNR Am J Neuroradiol* 2017;38:2364–72 CrossRef Medline
- Tanenbaum LN, Tsiouris AJ, Johnson AN, et al. **Synthetic MRI for clinical neuroimaging: results of the Magnetic Resonance Image Compilation (MAGiC) prospective, multicenter, multi-reader trial.** *AJNR Am J Neuroradiol* 2017;38:1103–10 CrossRef Medline
- Warntjes JB, Leinhard OD, West J, et al. **Rapid magnetic resonance quantification on the brain: optimization for clinical usage.** *Magn Reson Med* 2008;60:320–29 CrossRef Medline
- Schmidbauer V, Dovjak G, Geisl G, et al. **Impact of prematurity on the tissue properties of the neonatal brain stem: a quantitative MR approach.** *AJNR Am J Neuroradiol* 2021;42:581–89 CrossRef Medline
- Skiöld B, Alexandrou G, Padilla N, et al. **Sex differences in outcome and associations with neonatal brain morphology in extremely preterm children.** *J Pediatr* 2014;164:1012–18 CrossRef Medline
- O'Driscoll DN, McGovern M, Greene CM, et al. **Gender disparities in preterm neonatal outcomes.** *Acta Paediatr* 2018;107:1494–99 CrossRef
- Hagiwara A, Warntjes M, Hori M, et al. **SyMRI of the brain: rapid quantification of relaxation rates and proton density, with synthetic MRI, automatic brain segmentation, and myelin measurement.** *Invest Radiol* 2017;52:647–57 CrossRef Medline
- Kang KM, Choi SH, Kim H, et al. **The effect of varying slice thickness and interslice gap on T1 and T2 measured with the multidynamic multiple echo sequence.** *Magn Reson Med* 2019;81:126–33 CrossRef Medline
- Cicchetti D. **Guidelines, criteria, and rules of thumb for evaluating normed and standardized assessment instruments in psychology.** *Psychol Assess* 1994;6:284–90 CrossRef
- Bührer C, Metzke B, Obladen M. **CRIB, CRIB-II, birth weight or gestational age to assess mortality risk in very low birth weight infants?** *Acta Paediatr* 2008;97:899–903 CrossRef Medline
- Rothman KJ. **No adjustments are needed for multiple comparisons.** *Epidemiology* 1990;1:43–46 CrossRef Medline
- Yakovlev P, Lecours A. The myelogenetic cycles of regional maturation of the brain. In: Minkowski A, eds. *Regional Development of the Brain in Early Life*. Oxford: Blackwell; 1967; 3–70
- Wang S, Ledig C, Hajnal JV, et al. **Quantitative assessment of myelination patterns in preterm neonates using T2-weighted MRI.** *Sci Rep* 2019;9:12938 CrossRef Medline
- Barkovich AJ, Lyon G, Evrard P. **Formation, maturation, and disorders of white matter.** *AJNR Am J Neuroradiol* 1992;13:447–61 Medline
- Dubois J, Dehaene-Lambertz G, Kulikova S, et al. **The early development of brain white matter: a review of imaging studies in fetuses, newborns and infants.** *Neuroscience* 2014;276:48–71 CrossRef Medline
- Darling JS, Daniel JM. **Pubertal hormones mediate sex differences in levels of myelin basic protein in the orbitofrontal cortex of adult rats.** *Neuroscience* 2019;406:487–95 CrossRef Medline
- Prayer D, Roberts T, Barkovich AJ, et al. **Diffusion-weighted MRI of myelination in the rat brain following treatment with gonadal hormones.** *Neuroradiology* 1997;39:320–25 CrossRef Medline
- Dubois J, Dehaene-Lambertz G, Perrin M, et al. **Asynchrony of the early maturation of white matter bundles in healthy infants:**

- quantitative landmarks revealed noninvasively by diffusion tensor imaging.** *Hum Brain Mapp* 2008;29:14–27 CrossRef Medline
32. Woitek R, Prayer D, Weber M, et al. **Fetal diffusion tensor quantification of brainstem pathology in Chiari II malformation.** *Eur Radiol* 2016;26:1274–83 CrossRef Medline
33. Dubois J, Hertz-Pannier L, Cachia A, et al. **Structural asymmetries in the infant language and sensori-motor networks.** *Cereb Cortex* 2009;19:414–23 CrossRef Medline
34. Kinney HC, Brody BA, Kloman AS, et al. **Sequence of central nervous system myelination in human infancy, II: patterns of myelination in autopsied infants.** *J Neuropathol Exp Neurol* 1988;47:217–34 CrossRef Medline
35. Uddin MN, Figley TD, Solar KG, et al. **Comparisons between multi-component myelin water fraction, T1w/T2w ratio, and diffusion tensor imaging measures in healthy human brain structures.** *Sci Rep* 2019;9:2500 CrossRef Medline

Third Trimester Structural and Diffusion Brain Imaging after Single Intrauterine Fetal Death in Monochorionic Twins: MRI-Based Cohort Study

M. Segev, B. Djurabayev, E. Hadi, Y. Yinon, S. Rabinowicz, C. Hoffmann, and S. Shrot

ABSTRACT

BACKGROUND AND PURPOSE: Single intrauterine fetal death increases the risk of antenatal brain lesions in the surviving twin. We evaluated the prevalence of structural brain lesions, biometry, and diffusivity on routine third trimester MR imaging performed following single intrauterine fetal death.

MATERIALS AND METHODS: In a retrospective MR imaging–based cohort study, we compared 29 monochorionic twins complicated with single intrauterine fetal death (14 following laser ablation treatment for twin-to-twin transfusion syndrome, 8 following selective fetal reduction, and 7 spontaneous) with 2 control cohorts (49 singleton fetuses and 28 uncomplicated twin fetuses). All fetuses in the single intrauterine fetal death group underwent fetal brain MR imaging as a routine third trimester evaluation. Structural brain lesions were analyzed. Cerebral biometry and diffusivity were measured and compared.

RESULTS: Brain lesions consistent with the evolution of prior ischemic injury were found in 1 of 29 fetuses, not detected by ultrasound. No acute brain infarction, hemorrhage, or cortical abnormalities were found. Supratentorial biometric measurements in the single intrauterine fetal death group were significantly smaller than those in the singleton group, but not significantly different from those in the uncomplicated twin group. There were no significant differences in ADC values of the cerebral hemispheres, basal ganglia, and pons between the single intrauterine fetal death group and either control group.

CONCLUSIONS: Although smaller brain biometry was found, normal diffusivity in surviving twins suggests normal parenchymal microstructure. The rate of cerebral structural injury was relatively low in our cohort, arguing against the routine use of fetal brain MR imaging in twin pregnancies complicated with single intrauterine fetal death. Larger prospective studies are necessary to guide appropriate surveillance protocol and parental counseling in twin pregnancies complicated by single intrauterine fetal death.

ABBREVIATIONS: DC = dichorionic; fbMRI = fetal brain MRI; GA = gestational age; ICC = interclass correlation coefficient; MC = monochorionic; sIUFD = single intrauterine fetal death; TTTS = twin-to-twin transfusion syndrome; US = ultrasound

Monochorionic (MC) twin pregnancies are associated with increased perinatal morbidity and mortality compared with singleton or dichorionic (DC) pregnancies.¹ This increased risk is mainly related to placental architecture and vascular anastomoses in the MC placenta, which can result in fetal growth restriction or twin-to-twin transfusion syndrome. Single intrauterine fetal death (sIUFD) occurs in approximately 6% of twin

pregnancies.^{2,3} This risk is significantly higher, approximately 7- to 10-fold, in MC compared with DC twin pregnancies.¹ sIUFD considerably increases the surviving cotwin's risk of mortality and morbidity.⁴ This might be related to hypoperfusion of the surviving twin at the time of the cotwin's death due to placental vascular anastomoses. Up to 20% of surviving twins might experience adverse neurodevelopmental outcomes.^{2,3,5}

Prenatal identification of brain abnormalities in the surviving cotwin is critical for parental counseling. Expert neurosonography has a high sensitivity in detecting brain abnormalities.⁶ However, there is increasing evidence that fetal brain MR imaging (fbMRI) provides a more accurate diagnosis of brain abnormalities, specifically in detecting hemorrhage or acute ischemia.^{7,8} Relatively few studies have evaluated the utility of fbMRI for detecting brain abnormalities in cotwin survivors following sIUFD.⁴ These studies have described a range of patterns of cerebral abnormalities, mainly ischemic or hemorrhagic, in 9%–33% of surviving cotwins.^{9–12}

Received December 23, 2021; accepted after revision February 7, 2022.

From the Section of Neuroradiology (M.S., B.D., C.H., S.S.), Division of Diagnostic Imaging, Diagnostic Ultrasound Unit of the Institute of Obstetrical and Gynecological Imaging (E.H.), Department of Obstetrics and Gynecology, and Fetal Medicine Unit (Y.Y.), Department of Obstetrics and Gynecology, Sheba Medical Center, Ramat-Gan, Israel; Sackler School of Medicine (Y.Y., C.H., S.S.), Tel Aviv University, Tel-Aviv, Israel; and Pediatric Neurology Unit (S.R.), The Edmond and Lilly Safra Children's Hospital, Sheba Medical Center, Ramat Gan, Israel.

Please address correspondence to Shai Shrot, MD, Section of Neuroradiology, Division of Diagnostic Imaging, Sheba Medical Center, Ramat-Gan, Israel, 2 Sheba Rd, Ramat Gan, 52621 Israel; e-mail: shai.shrot@sheba.health.gov.il
<http://dx.doi.org/10.3174/ajnr.A7475>

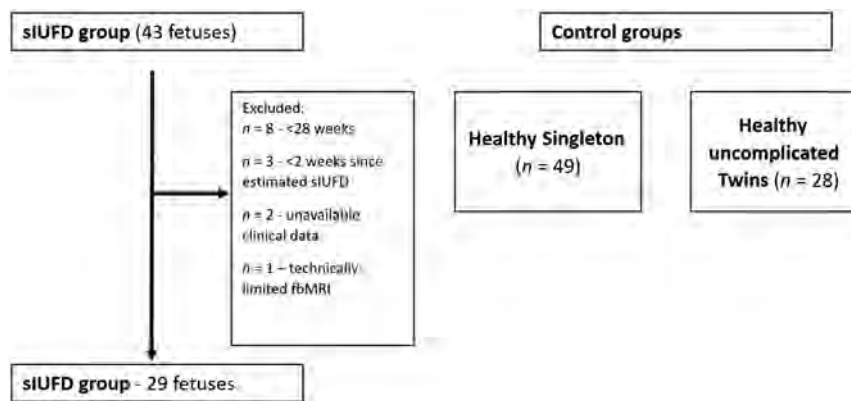


FIG 1. Study flow chart.

Relatively small cohorts, nonstandardized timing of fbMRI following the sIUFD, and lack of correlation with neurodevelopmental outcomes limit the incorporation of fbMRI into routine surveillance following sIUFD.

DWI has been shown to increase the sensitivity of structural fbMRI in diagnosing ischemic events following sIUFD, especially in the acute phase.¹³ In addition, quantitative diffusivity changes can reflect subtle structural parenchymal changes. Such changes were reported in various fetal pathologies affecting normal brain development and maturation, eg, congenital cardiac anomalies and fetal hydrocephalus.¹⁴ The effect of sIUFD on the integrity of a normal-appearing cotwin's brain, as assessed by quantitative diffusivity metrics, has not been described yet.

In Sheba Medical Center, as in other fetal medicine centers, we routinely perform a third trimester fbMRI on all MC twin fetuses following sIUFD to detect brain anomalies such as migration and proliferation disorders.¹⁵ Our objectives in the current study were to determine the utility of our practice by evaluating the prevalence of brain abnormalities as detected on surveillance third trimester fbMRI compared with a prenatal targeted ultrasound (US) and to evaluate the use of quantitative diffusivity measurements in assessing residual brain microstructural changes and brain maturation in the surviving twin following sIUFD.

MATERIALS AND METHODS

The institutional review board approved this retrospective study.

Study Design and Population

Our fetal brain imaging data base was reviewed for MC twin pregnancies following sIUFD managed in our referral center between February 2017 and June 2020. All patients in the study group underwent follow-up, which included US evaluation every 2 weeks, including targeted neurosonography. In 14 pregnancies, sIUFD occurred following laser ablation treatment for twin-to-twin transfusion syndrome (TTTS); in 8 patients, selective fetal reduction was performed; and 7 sIUFDs were spontaneous. Control groups were singleton pregnancies and uncomplicated twin pregnancies (19 were bichorionic, and 7, MC, with unavailable chorionicity data in 2 pregnancies), who had fbMRI in the same period for various indications with normal brain imaging findings. Inclusion

criteria for the sIUFD group were the following: 1) MC pregnancy, 2) documented sIUFD, 3) technically adequate third trimester fbMRI (gestational age [GA] = 28–36 weeks), and 4) fbMRI performed as a routine screening test at least 2 weeks following suspected sIUFD dating. Exclusion criteria were the following: unavailable clinical data and fbMRI performed acutely (<2 weeks) following sIUFD because of a suspected hypoxic-ischemic event in the cotwin. Inclusion criteria for control groups were singleton or uncomplicated twins with normal brain structure assessed by third trimester fbMRI with no clinical or laboratory evidence of chromosomal abnormalities or intrauterine infection.

The indications for MR imaging in the singleton control group were suspected CNS anomalies on prenatal screening US studies, not confirmed by MR imaging ($n = 20$), limb abnormalities ($n = 7$), abnormal outcome in previous pregnancies in siblings ($n = 8$), suspected abdominal vascular abnormalities ($n = 2$), polyhydramnios ($n = 2$), poor quality of a US study ($n = 1$), a maternal procedure during pregnancy ($n = 3$), recessive genetic abnormalities of the parents ($n = 1$), suspected spinal abnormality ($n = 3$), familial history of CNS abnormalities ($n = 1$), and exclusion of cerebral hemorrhage in fetal thrombocytopenia ($n = 1$). In the twins control group, one of the fetuses was chosen randomly for imaging analysis. The indications for MR imaging were suspected CNS anomalies on prenatal screening US studies in one of the fetuses or anomalies not confirmed by MR imaging ($n = 12$), mild asymmetry (<3 mm) or dilation of the lateral ventricles (<12 mm) seen on fetal US ($n = 8$), limb abnormalities ($n = 2$), abnormal outcome in previous pregnancies in siblings ($n = 2$), twins discordance ($n = 1$), and poor quality of a US study ($n = 3$). A summary of study groups is presented on Fig 1.

fbMRI

According to our protocol, all mothers had refrained from eating or drinking fluids containing sugar for 4 hours before the MR imaging examination. At our institution, a single administration of low-dose diazepam before imaging is used routinely to decrease fetal motion during the scan. Scans were obtained using a 3T MR imaging system (Ingenia 3T, Philips Healthcare, or Magnetom Prisma 3T, Siemens). Acquisition parameters for the Philips scanner were the following: a single-shot fast spin-echo T2-weighted sequence in 3 orthogonal planes, with a section thickness of 3 mm and no gap, using a flexible coil (16-channel body coil). The FOV was determined by the size of the fetal head and ranged from 230 to 290 mm. Other parameters were the following: matrix size = 224/224; TE = 90 ms; TR = approximately 2500 ms. A fast spoiled gradient-echo axial T1-weighted sequence was performed only in the axial plane (FOV = 320 mm, section thickness = 3 mm with no gap, TR = 10 ms, TE = 4.6 ms). A DWI sequence in an axial plane was then performed (FOV = 350 mm, b-value = 0 and 700 ms, section thickness = 3 mm with

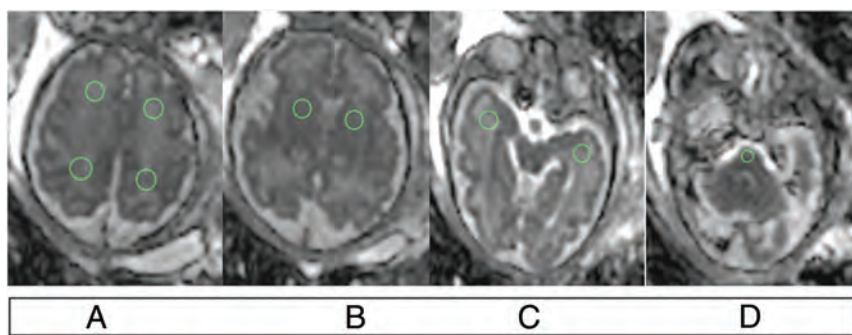


FIG 2. ROI placement on ADC map of DWI. A, Frontal and parietal lobes. B, Basal ganglia. C, Temporal lobes. D, Pons.

Table 1: Maternal and perinatal demographic and clinical features of sIUFD and control groups

	sIUFD	Singleton	Twins Control	Significance (Group 1 vs 2, Group 1 vs 3)
No.	29	49	28	
GA (mean) (wk)	30.9 (SD, 1.2)	31.5 (SD, 1.9)	31.4 (SD, 1.2)	$P = .17, P = .21$
Maternal age (mean) (yr)	31.7 (SD, 6.4)	32.3 (SD, 4.9)	33.8 (SD, 6.7)	$P = .62, P = .20$
Fetal presentation				
Head	22	38	20	$P = .53$
Breech	7	9	8	
Transverse	0	2	0	

no gap). Acquisition parameters for the Siemens scanner were the following: a HASTE T2-weighted sequence in 3 orthogonal planes (section thickness = 3 mm with no gap, using a flexible coil [16-channel body coil]). The FOV was determined by the size of the fetal head and ranged from 250 to 300 mm. Other parameters were the following: matrix size = 192/192; TE = 90 ms; TR = approximately 2500 ms. A single-shot axial T1-weighted sequence was performed only in the axial plane (FOV = 300 mm, section thickness = 3 mm with no gap, TR = 90 ms, TE = 2.35 ms). A DWI sequence in an axial plane was then performed (FOV = 256 mm, b-value = 0 and 1000 ms, section thickness = 3 mm with gaps of 0.3 mm.)

Image Analysis

Biometric measurements were read with a consensus of 2 radiologists, blinded to the clinical data (S.S., C.H.). MR imaging measurements included brain biparietal diameter (BPD), fronto-occipital diameter (FOD), length of the corpus callosum (CC), transcerebellar diameter (TCD), vermis height, vermis anteroposterior diameter, and lateral ventricle width. Fetal brain MR imaging biometry was converted to centiles using nomograms, previously published by Tilea et al.¹⁶

ADC Measurements

The acquired DWIs were transferred in DICOM format to the IntelliSpace portal, Version 10 (Philips Healthcare), and ADC maps were generated using the MR diffusion tool. To avoid inter-vendor variability in diffusivity metrics, we analyzed diffusivity data only from studies acquired on the Philips scanner (94 of 106 fbMRIs in our study). Nine circular ROIs were manually placed on

the following areas of the fetal brain (Fig 2): bilateral frontal WM, parietal WM, temporal WM, basal ganglia, and pons. ROIs ranged from 10 to 57 mm² (mean, 37.1 [SD, 12.7] mm²). ADC values were measured in the same regions of the bilateral cerebral hemisphere and basal ganglia; then, mean ADC values were calculated for each ROI. To validate the consistency of measurements and the reliability of results, 2 observers independently evaluated the first 13 consecutive fetuses (neuroradiology fellow, B.D., and a senior radiology resident, M.S.). Interobserver variability was assessed by the interclass correlation coefficient (ICC). We considered an ICC value of ≥ 0.8 as excellent agreement. ADC measurements were not available in fetuses with either degraded DWIs (ie, marked motion artifacts or field inhomogeneity) or fbMRI performed on different magnets.

Clinical Data

Demographic and clinical data included maternal age, GA at fbMRI, and fetal presentation. Clinical data for the sIUFD pregnancies included the following: sIUFD etiology (spontaneous, following laser treatment for TTTS, and following fetal reduction), the presence of TTTS, selective intrauterine growth restriction, twin anemia polycythemia sequence, and presumed GA at sIUFD.

Statistical Analysis

Categorical variables were expressed as numbers and percentages. Continuous variables were expressed as mean (SD). The distribution of continuous variables was assessed using a histogram and quantile-quantile plot. Categorical variables were compared using the χ^2 test. Continuous variables were compared using Mann-Whitney and Kruskal Wallis tests. Linear regression was used to evaluate the effect of sIUFD on ADC values. A 2-tailed $P < .05$ was considered statistically significant. Analyses were performed with SPSS (Version 25.0, 2019; IBM).

RESULTS

Study Population

MR imaging was performed in the sIUFD group at a mean GA of 30.9 (SD, 1.2) weeks, which was not significantly different from performance in the control groups. No significant differences were found in the mean maternal age or fetal presentation (Table 1).

Clinical Characteristics of the sIUFD Group

The estimated GA at sIUFD was 19.9 (SD, 4.2) weeks. TTTS was diagnosed on the prenatal US in 14 pregnancies (Quintero stage 1–2 pregnancies, stage 2–3 pregnancies, stage 3–7 pregnancies, and one pregnancy was stage 4, TTTS stage was unavailable in one pregnancy). In 6 pregnancies, selective intrauterine growth

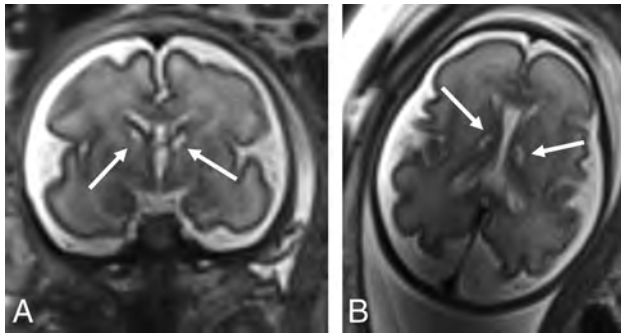


FIG 3. Coronal (A) and axial (B) T2-weighted images of a 30-week surviving twin following spontaneous sIUFD at a GA of 18 weeks, showing caudothalamic cystic changes (arrows).

restriction was found on the prenatal US, and in 2 pregnancies, a twin anemia polycythemia sequence was suspected. Post-sIUFD US did not show any major CNS abnormalities in the surviving twin (ie, infarction or hemorrhage). A minor finding of choroid plexus cyst was diagnosed in 1 fetus.

MR Imaging

fbMRI revealed a normal sulcation pattern in all surviving fetuses following sIUFD. No acute brain infarction or parenchymal hemorrhage was noted in any of the surveillance third-trimester fbMRIs performed in the sIUFD group. One fetus (~3.5% of the sIUFD group) showed bilateral caudothalamic cystic changes (Fig 3). No ventriculomegaly was observed, though 7 fetuses showed asymmetry of the lateral ventricles (compared with 5 in the singleton and 7 in the twins control groups). No cortical abnormalities, corpus callosum, septum pellucidum, or posterior fossa abnormalities were noted.

Various biometric parameters of the brain were measured in the sIUFD and control groups (Table 2). Supratentorial biometric parameters (FOD, BPD) of the sIUFD group were significantly smaller than those in the singleton group with smaller lateral ventricles. No significant differences were found in most biometric parameters between the sIUFD group and the twins control group or between the singleton and twins control groups.

ADC Analysis

DWI data were available in 22 of 29 in the sIUFD group (4 fetuses had technically degraded DWI, and fbMRI of 3 fetuses was performed on a different scanner); in 30 of 49 fetuses in the singleton cohort (12 fetuses had technically degraded DWI images, and fbMRI of 7 fetuses was performed on a different scanner); and in 15 of 28 in the twins control cohort (11 fetuses had technically degraded DWI, and fbMRI of 2 fetuses was performed on a different scanner). ADC measurements showed good-to-excellent interobserver agreement for most regions, with the ICC between 0.82 and 0.94. The ICC was considered good for the basal ganglia (ICC = 0.71).

In all groups, ADC values in supratentorial WM were higher than those in the basal ganglia and pons (Fig 4). No significant differences were found in post-sIUFD ADC values of the cerebral hemispheres (frontal, parietal, temporal lobes), basal ganglia, and pons between the sIUFD group and control groups and both

singleton and twins control groups ($P = .75, .87, .38, .41,$ and $.81$, respectively). After adjustment for GA, no significant differences were found between sIUFD and the singleton control groups or between the singleton and twins control groups for all evaluated brain regions. ADC measurements were similar in various sIUFD etiologies (spontaneous, following laser treatment of TTTS, or following fetal reduction, $P = .28-.9$ in different brain regions). The presence of TTTS on pre-sIUFD imaging did not result in significant ADC changes ($P = .36-.84$ in different brain regions).

DISCUSSION

In our retrospective cohort study, routine third trimester MR imaging showed structural brain lesions in approximately 3.5% of sIUFD pregnancies. These results are in agreement with Stirnemann et al,¹⁷ who also reported brain lesions in 5/239 (2.1%) surviving twins following TTTS treatment complicated by sIUFD. However, the incidence of brain lesions was relatively low compared with that in other studies. In a recent meta-analysis, Mackie et al⁴ described approximately 20% of abnormal brain findings on fbMRI of the surviving cotwin following sIUFD. There is a high variability of reported abnormal brain imaging findings in different cohorts, ranging from 9% to 33%.^{10,12,18,19} Such high variability might be attributed to the relatively small sIUFD cohorts, the indication for fetal brain examination, the timing of fbMRI following the sIUFD, and whether the sIUFD was spontaneous or following laser ablation or cord coagulation. Inconsistency in the definition of abnormal imaging findings such as mild ventriculomegaly or nonconclusive MR imaging findings such as suspected subependymal blood products are another reason for the incidence variability.²⁰ Early fbMRI, performed acutely (<2 weeks) following sIUFD or when postprocedural complications are noted, might also increase the sensitivity for diagnosing acute ischemia or hemorrhage, especially when DWI is performed.¹⁹ Early ischemic or hemorrhagic findings may spontaneously resolve and may not be detected later in pregnancy and at the time of third trimester follow-up.^{11,21}

Moreover, the risk of CNS injury in the surviving twin is obviously higher following spontaneous sIUFD versus sIUFD following laser therapy in which the twins have been dichorionized before the fetal death. On the other hand, the high proportion of sIUFD following laser therapy or cord coagulation in our cohort may explain the low rate of CNS injuries in the surviving twin found in our study. Termination of pregnancy performed in cases of major brain injury detected by post-sIUFD US or on fbMRI performed early might also contribute to the relatively low incidence of structural brain abnormalities detected on later third trimester fbMRI.

In our series, brain lesions found on MR imaging, ie, bilateral caudothalamic cystic changes, that were not detected on the prenatal US probably represent an evolution of earlier ischemic insult. Cerebral lesions in sIUFD pregnancies are usually ischemic or hemorrhagic. Ischemic injury includes focal encephalomalacic lesions or diffuse brain atrophy. Reparative cortical abnormalities such as polymicrogyria are a relatively common sequela of such focal ischemic insults. Intraventricular hemorrhage and resulting ventriculomegaly or periventricular venous infarction can also be found following sIUFD. Several possible

Table 2: Fetal MR imaging biometric parameters of sIUED fetuses (n = 29), singleton (n = 49), and twins control (n = 28) groups^a

	sIUED (n = 29) Mean ± SD	Singleton (n = 49) Mean ± SD	Twins Control (n = 28) Mean ± SD	Significance (P Value)		
				sIUED vs Singleton	sIUED vs Twins Control	Twins vs Singleton Controls
FOD (mm)	88.4 ± 4.4	91.5 ± 6.5	90.5 ± 4.9	.01 ^b	.09	.43
FOD (%)	50.7 ± 18.6	64.2 ± 22.0	59.9 ± 25.9	.01 ^b	.13	.46
BPD (mm)	68.0 ± 3.9	71.7 ± 6.2	70.4 ± 3.8	.00 ^b	.02 ^b	.25
BPD (%)	36.9 ± 17.6	56.9 ± 22.5	46.9 ± 24.4	.00 ^b	.08	.08
CC (mm)	36.8 ± 2.9	37.9 ± 2.4	37.4 ± 2.0	.08	.31	.39
CC (%)	38.9 ± 22.9	48.2 ± 17.5	43.2 ± 22.3	.07	.48	.32
TCD (mm)	37.8 ± 2.1	39.1 ± 3.7	38.4 ± 2.4	.05 ^b	.37	.29
TCD (%)	44.1 ± 21.0	51.7 ± 23.3	43.2 ± 23.5	.14	.88	.13
Vermian height (mm)	18.4 ± 1.2	18.4 ± 1.6	18.3 ± 1.1	.94	.84	.89
Vermian height (%)	61.6 ± 18.6	56.5 ± 20.1	57.0 ± 18.3	.27	.35	.92
Vermian_AP (mm)	11.8 ± 1.0	12.0 ± 1.2	11.6 ± 1.0	.59	.32	.12
Vermian_AP (%)	48.6 ± 19.5	46.5 ± 18.5	46.1 ± 16.8	.66	.60	.92
Average lateral ventricles	6.4 ± 1.3	7.3 ± 1.2	7.8 ± 1.6	.01 ^b	.00 ^b	.17

Note:—FOD indicates fronto-occipital diameter; BPD, biparietal diameter, CC, corpus callosum; TCD, transcerebellar diameter; AP, anterior-posterior.

^a Variables are presented as mean (SD). MR imaging centiles in fetal CNS biometry are based on Tilea et al.¹⁶

^b Statistically significant values.

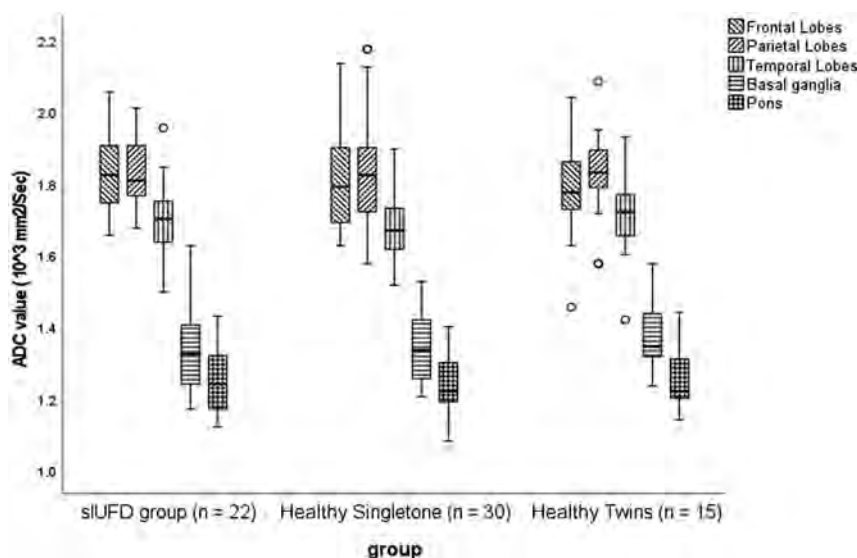


FIG 4. Boxplot of ADC values in sIUED and control groups. No significant differences were found among various areas in different study groups.

mechanisms might lead to brain injury in survivors after sIUED.²² Hypoxic-ischemic injury might result from the low-pressure vascular compartment of the fetus who died, leading to the survivor twin's hemodynamic fluctuations and low brain perfusion. Another theory relates to potential thrombi formed in the vascular compartment of the fetus who died and embolizing to the surviving twin through persisting placental anastomoses, resulting in ischemic injury.²³

Analyzing the biometric parameters of surviving fetuses following sIUED revealed that most supratentorial and infratentorial brain structures were significantly smaller than in control singleton fetuses, probably related to the underlying twin pregnancy,²⁴ though there is the possibility of an underlying pathology that affects broad regions of the developing brain in surviving twins following sIUED. Similar diffusivity values, ie, measured ADC values, found in our

study in sIUED and control groups do not support such a hypothesis. DWI enables quantitative free-water assessment in the brain parenchyma, which reflects tissue maturation. Diffusivity changes were found in various fetal pathologies affecting normal brain development and maturation, such as congenital cardiac anomalies or fetal hydrocephalus, even with normal morphologic T2-weighted fbMRI findings.^{14,25} Transient hemodynamic fluctuations following sIUED and resulting decreased brain perfusion might affect brain maturation. However, our results of similar diffusivity in the surviving twins on routine third trimester fbMRI support near-normal brain maturation, especially in the setting of normal morphologic-anatomic imaging findings.

Neurodevelopmental impairment in the surviving twin following sIUED is of great concern and affects parental counseling. Hillman et al⁸ described long-term neurodevelopmental impairment in up to 26% of twins following a single fetal death. Nevertheless, formal developmental tests were not routinely performed in most cohorts, and the age at follow-up was relatively young to detect neurodevelopmental abnormalities. The association between focal or diffuse brain injury found on pre- or postnatal imaging and adverse neurodevelopmental outcomes is also controversial. Hillman et al did not find a significant correlation between abnormal brain imaging findings and neurodevelopmental impairment, possibly related to lack of imaging, underreporting, inconsistent imaging reports, and lack of consistency in imaging timing related to delivery and development of neurologic signs.⁸ Such correlation was also not found in a recently published meta-analysis by Mackie et al.⁴ Prematurity, which is very common in twin pregnancies, especially

following sIUFD,^{8,26} probably contributes significantly to long-term neurologic morbidity,^{4,8,27} which can explain the high rate of neurodevelopmental impairment, much more than reported abnormal prenatal imaging findings. The low incidence of brain abnormalities on prenatal diagnosis is not likely to reflect the low sensitivity of prenatal imaging but is probably related to the study cohort of third trimester survivors following cotwin death with normal brain maturation and development, as suggested by normal diffusivity. Many of previously reported brain abnormal findings were also strongly associated with preterm birth, obviously apparent only on postnatal imaging.

US is the main imaging technique used on routine follow-up of twin pregnancies. It enables evaluation of fetal growth and the diagnosis of hemodynamics and MC twin complications. However, it has limited sensitivity in diagnosing ischemia, hemorrhage, or cortical malformations.^{7,11,28} Currently, fbMRI is gaining widespread acceptance as an important adjunct to US, especially in high-risk twin pregnancies. There is currently little evidence to guide the optimal timing of fbMRI (relative to the occurrence of the twin complication, including sIUFD) to improve the detection of brain insult and prognostication. In our cohort, fbMRI performed routinely in the mid-late third trimester for all surviving twins had a relatively low incidence of cerebral injury (~3.5%), which argues against routine use of fbMRI in an MC twin pregnancy complicated with sIUFD. fbMRI, performed earlier, especially following US evidence of fetal compromise (ie, intrauterine growth restriction, flow abnormalities, or abnormal brain findings), will probably have increased diagnostic ability and, similar to previous studies, will show a higher incidence of cerebral injury.^{13,29} A follow-up third trimester fbMRI is highly recommended to evaluate the sequelae of acute injury and reparative malformations in these cases of early brain injury.

The retrospective nature and the relatively small population are major limitations of our study. Study recruitment was noncontrolled, so our data describe the observed rates of brain abnormalities in third trimester routine fbMRI rather than reflecting the true prevalence of brain abnormalities. Selection bias, either related to referral to our tertiary center or for exclusion of acute complications in the sIUFD group that might result in termination/reduction due to concern for injury to the surviving fetus is an important limitation of our study. Our control cohorts of singleton and uncomplicated twins were also relatively heterogeneous and underwent fbMRI due to various indications, though in all cases, fbMRI findings were normal. Our study is also limited by the lack of correlation of fetal MR findings with neurodevelopmental outcomes. However, the high prematurity rate in this subgroup of twin pregnancies is an important confounding factor in assessing long-term outcomes. Future studies should include prospective fetal monitoring protocols, including US and fbMRI, following twin pregnancies complicated by sIUFD. Evidence-based parental counseling requires a correlation between specific brain abnormalities demonstrated on fbMRI and postnatal imaging and neurodevelopmental outcomes. Currently, such correlation is lacking in large-scale cohorts.

CONCLUSIONS

In surviving twins following sIUFD, routine third trimester fbMRI showed persistent small biometry, though normal diffusivity

suggests normal parenchymal maturation and microstructure. The rate of cerebral structural injury, not detected by US, was relatively low in our relatively small cohort (1/29, ~3.5%), which argues against routine use of fbMRI in an MC twin pregnancy complicated by sIUFD. fbMRI should be performed following sonographic evidence of a fetal compromise or brain injury. Larger prospective studies with expert fetal neurosonography and standardized timing of pre- and postnatal MR imaging, including formal neurodevelopmental assessment, are necessary to evaluate the appropriate surveillance protocol better and guide parental counseling in twin pregnancies complicated with sIUFD.

Disclosure forms provided by the authors are available with the full text and PDF of this article at www.ajnr.org.

REFERENCES

1. D'Antonio F, Thilaganathan B, Dias T, et al; Southwest Thames Obstetric Research Collaborative (STORK). **Influence of chorionicity and gestational age at single fetal loss on risk of preterm birth in twin pregnancy: analysis of STORK multiple pregnancy cohort.** *Ultrasound Obstet Gynecol* 2017;50:723–27 CrossRef Medline
2. Pharoah PO, Adi Y. **Consequences of in-utero death in a twin pregnancy.** *Lancet* 2000;355:1597–1602 CrossRef Medline
3. Saito K, Ohtsu Y, Amano K, et al. **Perinatal outcome and management of single fetal death in twin pregnancy: a case series and review.** *J Perinat Med* 1999;27:473–77 CrossRef Medline
4. Mackie FL, Rigby A, Morris RK, et al. **Prognosis of the co-twin following spontaneous single intrauterine fetal death in twin pregnancies: a systematic review and meta-analysis.** *BJOG* 2019;126:569–78 CrossRef Medline
5. Ong SS, Zamora J, Khan KS, et al. **Prognosis for the co-twin following single-twin death: a systematic review.** *BJOG* 2006;113:992–98 CrossRef Medline
6. van der Knoop BJ, Zonnenberg IA, Verbeke JIML, et al. **Additional value of advanced neurosonography and magnetic resonance imaging in fetuses at risk for brain damage.** *Ultrasound Obstet Gynecol* 2020;56:348–58 CrossRef Medline
7. Aertsen M, Van Tieghem De Ten Berghe C, Deneckere S, et al. **The prevalence of brain lesions after in utero surgery for twin-to-twin transfusion syndrome on third-trimester MRI: a retrospective cohort study.** *Eur Radiol* 2021;31:4097–4103 CrossRef Medline
8. Hillman SC, Morris RK, Kilby MD. **Co-twin prognosis after single fetal death: a systematic review and meta-analysis.** *Obstet Gynecol* 2011;118:928–40 CrossRef Medline
9. Griffiths PD, Sharrack S, Chan KL, et al. **Fetal brain injury in survivors of twin pregnancies complicated by demise of one twin as assessed by in utero MR imaging.** *Prenat Diagn* 2015;35:583–91 CrossRef Medline
10. Jelin AC, Norton ME, Bartha AI, et al. **Intracranial magnetic resonance imaging findings in the surviving fetus after spontaneous monochorionic cotwin demise.** *Am J Obstet Gynecol* 2008;199:398 e391–95 CrossRef Medline
11. Robinson A, Teoh M, Edwards A, et al. **Fetal brain injury in complicated monochorionic pregnancies: diagnostic yield of prenatal MRI following surveillance ultrasound and influence on prognostic counselling.** *Prenat Diagn* 2017;37:611–27 CrossRef Medline
12. van Klink JM, van Steenis A, Steggerda SJ, et al. **Single fetal demise in monochorionic pregnancies: incidence and patterns of cerebral injury.** *Ultrasound Obstet Gynecol* 2015;45:294–300 CrossRef Medline
13. Hoffmann C, Weisz B, Yinon Y, et al. **Diffusion MRI findings in monochorionic twin pregnancies after intrauterine fetal death.** *AJNR Am J Neuroradiol* 2013;34:212–16 CrossRef Medline
14. Schonberg N, Weisstanner C, Wiest R, et al. **The influence of various cerebral and extracerebral pathologies on apparent diffusion**

- coefficient values in the fetal brain. *J Neuroimaging* 2020;30:477–85 CrossRef Medline
15. Khalil A, Rodgers M, Baschat A, et al. **ISUOG Practice Guidelines: role of ultrasound in twin pregnancy.** *Ultrasound Obstet Gynecol* 2016;47:247–63 CrossRef Medline
 16. Tilea B, Alberti C, Adamsbaum C, et al. **Cerebral biometry in fetal magnetic resonance imaging: new reference data.** *Ultrasound Obstet Gynecol* 2009;33:173–81 CrossRef Medline
 17. Stirnemann J, Chalouhi G, Essaoui M, et al. **Fetal brain imaging following laser surgery in twin-to-twin surgery.** *BJOG* 2018;125:1186–91 CrossRef Medline
 18. Conte G, Righini A, Griffiths PD, et al. **Brain-injured survivors of monochorionic twin pregnancies complicated by single intrauterine death: MR findings in a multicenter study.** *Radiology* 2018;288:582–90 CrossRef Medline
 19. Weisz B, Hoffmann C, Ben-Baruch S, et al. **Early detection by diffusion-weighted sequence magnetic resonance imaging of severe brain lesions after fetoscopic laser coagulation for twin-twin transfusion syndrome.** *Ultrasound Obstet Gynecol* 2014;44:44–49 CrossRef Medline
 20. Hochberg A, Silber R, Avnet H, et al. **Fetal and neonatal brain lesions following laser ablation for twin-to-twin-transfusion-syndrome as detected by pre- and post-natal brain imaging.** *Prenat Diagn* 2021;41:1531–40 CrossRef Medline
 21. Shrot S, Hoffmann C, Katorza E. **Reversible parenchymal ischemic injury on fetal brain MRI following fetoscopic laser coagulation- Implication on parental counseling.** *Radiol Case Rep* 2020;15:1369–72 CrossRef Medline
 22. Shek NW, Hillman SC, Kilby MD. **Single-twin demise: pregnancy outcome.** *Best Pract Res Clin Obstet Gynaecol* 2014;28:249–63 CrossRef Medline
 23. Patten RM, Mack LA, Nyberg DA, et al. **Twin embolization syndrome: prenatal sonographic detection and significance.** *Radiology* 1989;173:685–89 CrossRef Medline
 24. Ghi T, Prefumo F, Fichera A, et al; Societa Italiana di Ecografia Ostetrica e Ginecologica Working Group on Fetal Biometric Charts. **Development of customized fetal growth charts in twins.** *Am J Obstet Gynecol* 2017;216:514 e1–17 CrossRef Medline
 25. Yaniv G, Katorza E, Bercovitz R, et al. **Region-specific changes in brain diffusivity in fetal isolated mild ventriculomegaly.** *Eur Radiol* 2016;26:840–48 CrossRef Medline
 26. Cimpoia B, Syngelaki A, Chi Mu A, et al. **Twin pregnancy with two live fetuses at 11-13 weeks: effect of one fetal death on pregnancy outcome.** *Ultrasound Obstet Gynecol* 2020;55:482–88 CrossRef Medline
 27. Lopriore E, Ortibus E, Acosta-Rojas R, et al. **Risk factors for neurodevelopment impairment in twin-twin transfusion syndrome treated with fetoscopic laser surgery.** *Obstet Gynecol* 2009;113:361–66 CrossRef Medline
 28. Griffiths PD, Bradburn M, Campbell MJ, et al. **Use of MRI in the diagnosis of fetal brain abnormalities in utero (MERIDIAN): a multicentre, prospective cohort study.** *Lancet* 2017;389:538–46 CrossRef Medline
 29. Lanna MM, Consonni D, Faiola S, et al. **Incidence of cerebral injury in monochorionic twin survivors after spontaneous single demise: long-term outcome of a large cohort.** *Fetal Diagn Ther* 2020;47:66–73 CrossRef Medline

Diagnostic Value of Sylvian Fissure Hyperechogenicity in Fetal SAH

M. Zhang, H. Wen, M. Liang, Y. Qin, Q. Zeng, D. Luo, X. Zhong, and S. Li



ABSTRACT

BACKGROUND AND PURPOSE: Fetal SAH is an intracranial malformation. The typical diagnostic features of fetal SAH in ultrasound have not been reported. This study aimed to evaluate the diagnostic value of Sylvian fissure hyperechogenicity by prenatal ultrasound in fetuses with SAH.

MATERIALS AND METHODS: The features on ultrasound and MR imaging of 10 fetuses with SAH were reviewed and summarized. The diagnostic value of the Sylvian fissure in fetal SAH by prenatal ultrasound was evaluated.

RESULTS: The typical and most obvious manifestations of SAH during the prenatal period were hyperechogenicity in the subarachnoid cavity, especially in the Sylvian fissure; all 10 cases (10/10) had such manifestations. Other manifestations included a hyperecho in other sulci (6/10), especially in the subfrontal sulcus, superior temporal sulcus, or parieto-occipital sulcus; a hyperecho in the cisterns (8/10), especially in the suprasellar cistern, posterior cranial fossa, cisterna ambiens, or quadrigeminal cistern; and a hyperecho around the anterior and posterior longitudinal fissures (2/10). Combined hemorrhage in the parenchymal layer or ventricles (9/10) was found. In addition, Doppler ultrasound showed that the peak flow velocity in the MCA increased in 6 cases (6/10).

CONCLUSIONS: The homogeneous hyperechogenicity of the Sylvian fissure is an important clue for detecting and diagnosing fetal SAH by prenatal ultrasound. A diagnostic approach has been proposed for fetal SAH, which has great significance in further prognosis.

ABBREVIATIONS: SF = Sylvian fissure; US = ultrasound

Fetal SAH is considered a finding of blood flow into the subarachnoid space after the rupture of a blood vessel at the base or on the surface of the brain. It is one of the forms of nongerminal stromal hemorrhage, with an estimated incidence of less than 0.5–0.9 per 1000 pregnancies; however, its pathogenesis remains unclear.¹ It not only causes fetal stroke, fetal brain injury, and other diseases but is closely related to postpartum epilepsy,

mental disorders, psychomotor retardation, cerebral palsy, and other neurologic disorders.² At present, few cases of fetal SAH have been reported at home and abroad.^{3–11} In addition, the diagnosis of fetal SAH by prenatal ultrasound (US) has not been mentioned at all. Ten cases of fetal SAH were detected during a 3-year period at Shenzhen Maternity & Child Healthcare Hospital. Awareness of the diagnostic criteria, especially the characteristics of ultrasound of the Sylvian fissure (SF), disease progression, combined malformations, and further prognosis, is necessary for informed prenatal counseling and obstetric management. The related literature of fetal SAH for nearly 30 years was systematically discussed in this study.

MATERIALS AND METHODS

Research Design and Patients

We detected 10 gravidas with fetal SAH undergoing routine prenatal scanning between January 2018 and April 2021. Ethics approval for this study was by the regional ethical review board in Shenzhen: approval number: SFYLS [2020] 019 (decision 2020-06-11).

Received August 25, 2021; accepted after revision January 1, 2022.

From the Department of Ultrasound (M.Z., H.W., M.L., Y.Q., Q.Z., D.L., S.L.), Shenzhen Maternity & Child Healthcare Hospital, The First School of Clinical Medicine, Southern Medical University, Shenzhen, Guangdong, China; and Department of Ultrasound (X.Z.), Xiamen Maternal Child Health Care Hospital, Xiamen, China.

This study was supported by funds from the National Nature Science Foundation of China (81771598).

Please address correspondence to Shengli Li, PhD, Shenzhen Maternity & Child Healthcare Hospital, The First School of Clinical Medicine, Southern Medical University, Hongli Rd, No. 2004, Futian Shenzhen 518028, China; e-mail: ls13530386700@126.com

Indicates open access to non-subscribers at www.ajnr.org

Indicates article with online supplemental data.

<http://dx.doi.org/10.3174/ajnr.A7449>

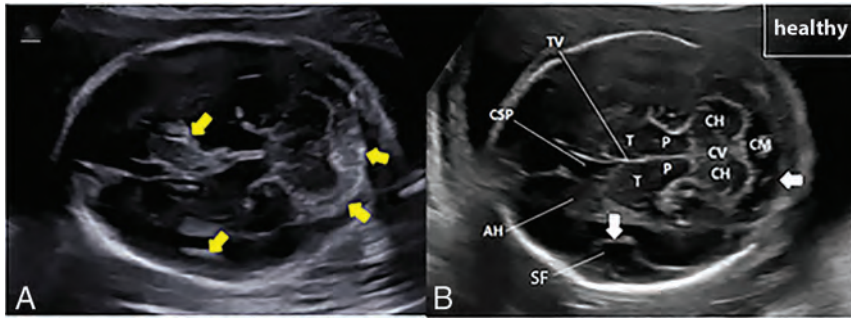


FIG 1. Transcerebellar plane of US in SAH and healthy fetuses. *A*, Echo in the subarachnoid space of fetal SAH was enhanced and widened. Hyperechoic filling could be seen in the SF; uneven strong echo masses could be seen in anterior parenchyma of the thalamus and around the ependyma; and hyperechoic filling could be seen in the posterior cranial fossa (yellow arrows). *B*, In healthy fetuses, the SF and posterior cranial fossa are homogeneous hypoechoes (white arrows). TV indicates third ventricle; CSP, cavity of septum pellucidum; AH, anterior horn of lateral ventricle; T, thalamus; P, mesencephalon; CH, cerebellar hemisphere; CV, cerebellar vermis; CM, cisterna magna.

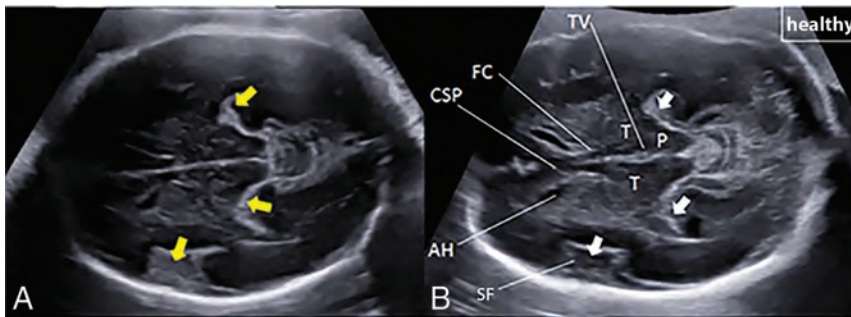


FIG 2. Transthalamic plane of US in SAH and healthy fetuses. *A*, The SF and temporal angle are filled with coarse hyperecho in the fetus with SAH (yellow arrows). *B*, In healthy fetuses, the SF is hypoechoic with narrow and sharp hyperechoic lines on both sides of the posterior midbrain (white arrows). TV indicates third ventricle; CSP, cavity of septum pellucidum; AH, anterior horn of lateral ventricle; T, thalamus; P, mesencephalon; FC, fornix column.

Materials Used

The scanning was performed by experienced radiologists using WS80A (Samsung Health) and S60 (SonoScape Health) equipped with transabdominal transducers (CA1-7A [Samsung Health]; CV1-8A [Samsung Health] and C1-6A [SonoScape Health] MHz).

Means of Confirming Diagnoses

Ultrasonic images of the fetal SAH were collected by 2 researchers, one with >20 years' experience in fetal sonography (Dr Li) and the other with only 2 years (Dr Zhang). All examinations were performed in real time, digitally stored, and documented using a commercially available system.

The routine cerebral survey included a detailed anatomic ultrasound survey of the fetal head. Fetal cerebrum views were routinely obtained in the transverse views of the thalamus plane, the lateral ventricle plane, and the cerebellum plane. If the fetal SF showed hyperechogenicity, additional views, including transverse, coronal, and sagittal sections of the fetal head from the parietal bone to the skull base, were needed to observe other cerebral sulci and cisterns dynamically, which mainly contained the superior

frontal sulcus, inferior frontal sulcus, supratemporal sulcus, inferior temporal sulcus, parieto-occipital sulcus in the sulci and the posterior cranial fossa, cisterna ambiens, and suprasellar cistern in the cisterns. If homogeneous hyperechoic or subarachnoid dilation was visualized, SAH was considered and MR imaging or genetic testing was recommended. All the screening procedures were performed on 2 sides of the brain to prevent a missed diagnosis. Furthermore, dynamic scanning was performed at the midsagittal view of the spine to obtain more findings in the subarachnoid space. At the same time, color Doppler was used to measure the peak flow velocity of the MCA to search for the possible causes of SAH.

All suspected patients were recommended for MR imaging in 2–5 days. Fetuses with an abnormal subarachnoid echo on the prenatal examination were recommended for follow-up perinatal outcome and prognosis.

Statistical Analysis

Interobserver agreement with regard to the observation of the SAH sites was determined as κ coefficients and *P* values, according to the κ methods. Statistical analyses were performed using SPSS 20.0 for Windows (IBM). Basic descriptive statistics were performed when appropriate. The diagnostic utility of SF hyperechogenicity for the diagnosis of fetal SAH was

determined by calculating the detection rate for consensus reader data.

RESULTS

Incidence

Fetal SAH was detected in 10 cases of 425,258 deliveries (0.23/10,000 deliveries) at the authors' institution between January 2018 and April 2021. The incidence was probably biased because of the diagnosis of fetal SAH that required specific expertise, and the actual incidence of SAH might be higher. The mean maternal age was 29.3 (SD, 4.3) years (range, 26–38 years). The mean gestational age at diagnosis was 28.6 (SD, 4.6) weeks (range, 23–36 weeks).

Results of Prenatal Examinations

The typical and most obvious manifestation of SAH in prenatal diagnoses was hyperechogenicity in the subarachnoid cavity, especially in the SF; all 10 cases (10/10) had such manifestations (Figs 1–3). Other manifestations included thick hyperechogenicity in the other sulci (6/10), especially in the subfrontal sulcus, superior temporal sulcus, or parieto-occipital sulcus (Figs 3 and

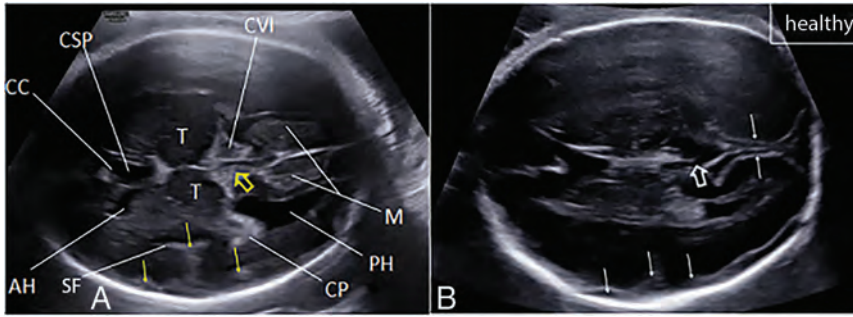


FIG 3. Transventricular plane of US in SAH and healthy fetuses. *A*, Hyperecho inside the cerebral sulci, such as the subfrontal sulcus, the SF, and the superior temporal sulcus, can be seen in the fetus with SAH, and the boundary is blurred (*small yellow arrow*). There is an enhanced echo in the cavum veli interpositi (*yellow hollow arrow*) and symmetric isoechoic or slightly hyperechoic hemorrhagic foci (M) around the parafalx anterior to the sinus confluence. Compression of the cerebral parenchyma is seen. *B*, In healthy fetuses, a clear hypoecho in the subarachnoid spaces in the SF, the superior temporal sulcus and subfrontal sulcus (*small white arrow*), and cavum veli interpositi (*white hollow arrow*); a normal cerebral falx; and no compression are observed in brain parenchyma. CC indicates corpus callosum; CSP, cavity of septum pellucidum; CVI, cavum veli interpositi; PH, posterior horn of lateral ventricle; CP, choroid plexus; AH, anterior horn of lateral ventricle; T, thalamus; M, subdural hemorrhage was suspected.

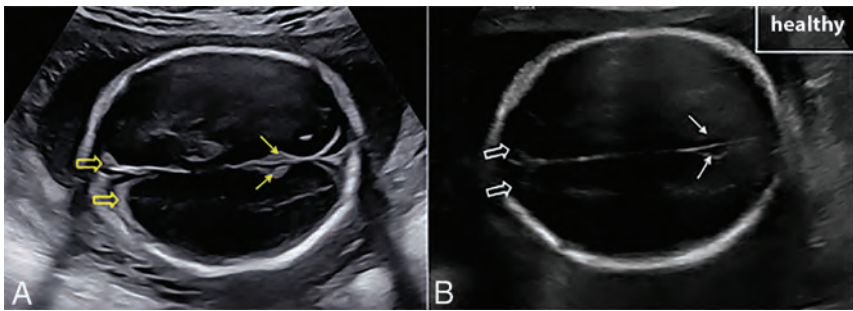


FIG 4. The transcalvarial plane of US in SAH and healthy fetuses. *A*, Abnormal hyperecho in the parieto-occipital sulcus of the fetus with SAH, with blurred boundaries (*yellow arrows*). The enhanced echo and blurred boundary between the superior sagittal sinus and the parenchyma are thickened (*yellow hollow arrows*). *B*, In healthy fetuses, only the midline of the brain is clear in the parieto-occipital sulcus, and both sides of the sulcus are filled with clear anechoic CSF (*white arrows*). The superior sagittal sinus is clearly demarcated from the pericerebral parenchyma, showing a clear isoechoic line (*white hollow arrows*).

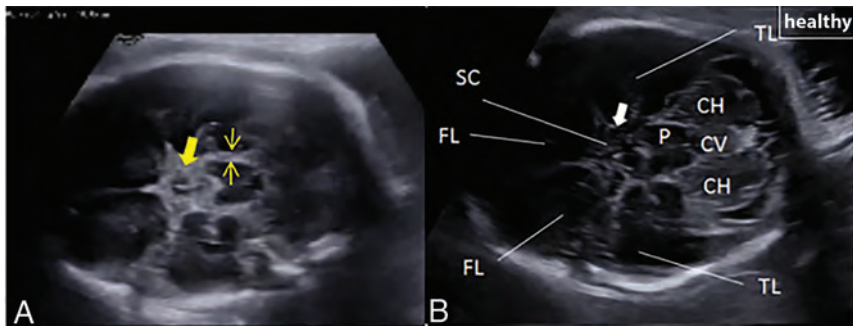


FIG 5. Transbasicranial plane of US in SAH and healthy fetuses. *A*, The suprasellar cistern and ambient cistern of the fetus with SAH show hyperecho (*yellow thick arrow*). Compared with the healthy fetus, the cistern was significantly widened and enhanced (*yellow thin arrows*). *B*, The suprasellar cistern and ambient cistern of a healthy fetus show hypoechoic or anechoic (*white arrow*). SC indicates suprasellar cistern; TL, temporal lobe; FL, frontal lobe; CV, cerebellar vermis; CH, cerebellar hemisphere; P, mesencephalon.

4); hyperecho in the cisterns (8/10), especially in the suprasellar cistern, posterior cranial fossa, cisterna ambiens, or quadrigeminal cistern (Figs 1 and 5); hyperecho around the anterior and posterior longitudinal fissures (2/10) (Figs 3 and 4); combined hemorrhage in the parenchymal layer or ventricles (9/10) (Fig 1); and the hyperechoic dilated subarachnoid space in the middle view of the spine (1/10) (Fig 6). In addition, Doppler US showed that the peak flow velocity in the MCA increased obviously in 6 cases (6/10). Using this method and diagnostic features, we found that the κ number for the assessment was high, up to 0.82 ($P < .05$). An abnormal SF was visualized in all cases by the 2 researchers with different experience (Table).

Fetuses (5/10) underwent MR imaging 2–5 days after US, and all were diagnosed with SAH. Fetuses (6/10) underwent fetal chromosomal microarray analysis, which indicated negative results. The peak flow velocity of the MCA increased in fetuses (6/10). It was >1.55 and 1.29 multiples of the median (MOM) in 4 and 2 cases, respectively; mild and severe anemia were indicated, respectively. Neither of the parents had a history of blood diseases. In cases 1 and 5, the umbilical cord was wrapped 3 times around the neck. Twin-to-twin transfusion syndrome (phase IV) was found in case 7 of twins.

Perinatal Outcome

Six pregnancies with fetal SAH were induced after prenatal counseling and confirmed by postmortem examination (Fig 7). Two cases were intrauterine death and the rest were in pregnancy. The postmortem and imaging results showed that the novel diagnostic method with SF hyperechogenicity as the main clue had reached a detection rate of 100% (10/10).

DISCUSSION

In the normal SF and other sulci, cisterns are filled with anechoic CSF. When SAH occurs, the blood rarely forms a localized or encapsulated hematoma but flows along the CSF to low-lying areas, including some brain sulci and cisterns, owing to the

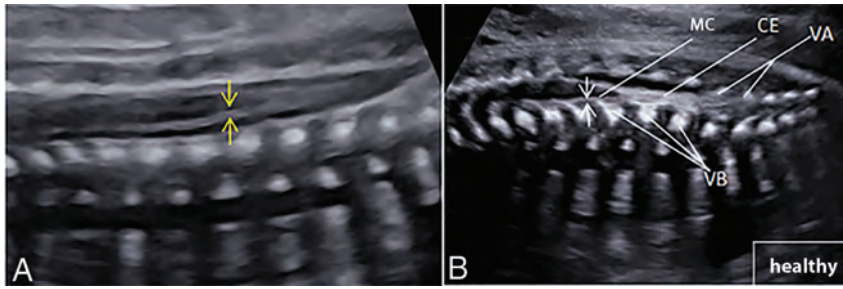


FIG 6. The midsagittal view of the spine on a sonogram in SAH and healthy fetuses. *A*, There are uniform thickening and a strong echo in the subarachnoid space between the pia mater spinalis and the arachnoid membranes of fetal SAH (yellow arrows). *B*, The normal fetal pia mater and arachnoid membrane are relatively close, forming a narrow space (white arrows). MC indicates medullary cone; CE, cauda equina; VA, vertebral arch; VB, vertebral body.

Comparison of intraobserver assessment in 10 cases

SAH Sites	Observer A	Observer B	κ (A and B)
Sylvian fissure	10	10	
Parieto-occipital sulcus	6	6	
Superior frontal sulcus	3	2	
Superior temporal sulcus	3	2	
Quadrigeminal cistern	7	6	
Posterior cranial fossa	8	7	
Suprasellar cistern	8	6	
Cisterna ambiens	8	7	
Longitudinal fissures	2	1	
Spinal subarachnoid space	1	0	
Total count	56	47	0.819 ($P < .05$)

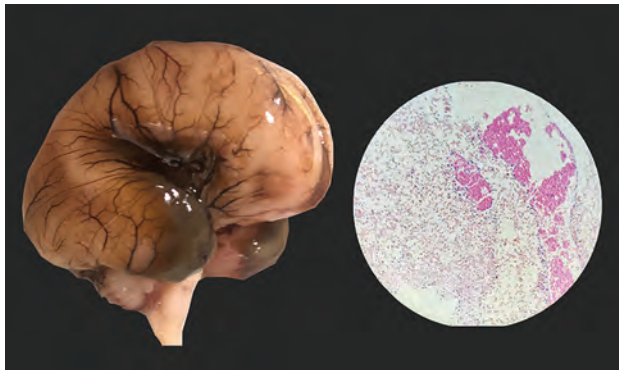


FIG 7. Postmortem examination results and pathology. Hematoceles are seen in the SF and subarachnoid space of the temporal horn. The left image shows the cerebral postmortem examination of the fetus with SAH; the right image shows large amounts of remote bleeding in the SF in pathologic findings.

influence of gravity and arterial pulsation. The factors predisposing to fetal SAH include a variety of conditions, mostly maternal trauma and fetal coagulation disorders.^{1,12} In many cases, however, the cause is not identified. Most fetal SAHs were usually considered spontaneous bleeding without a potential cause. However, previous studies¹³⁻¹⁴ reported that fetal SAH might be

related to *COL4A1* and *GATA1* gene mutations, but some reports¹⁵⁻¹⁶ had normal outcomes.

Ultrasonography is the preferred imaging method for the prenatal diagnosis of SAH. Previous findings on the capacity of ultrasound to diagnose fetal SAH have been inconsistent. In this study, the 12 cases of fetal SAH for the past 30 years were reviewed in 9 published studies (Online Supplemental Data).³⁻¹¹ However, only 2 cases were diagnosed by US due to the lack of the description of ultrasonographic characteristics and diagnostic approaches in previously published studies.^{6,10} Fetal SAH was still prone to missed diagnoses and misdiagnosis.

The SF is the earliest and largest sulcus shown on prenatal US, which can be observed at 18–20 weeks’ gestation. The parieto-occipital sulcus and cisterns also appear earlier, but they need to be visualized at the specific section and angle. The other sulci of the subarachnoid space can be displayed much later.^{17,18} For example, generally, the superior temporal sulcus and inferior frontal sulcus appear at 31 weeks’ gestation.^{17,19}

The SF is an excellent structure for diagnosing SAH. In our case, the earliest gestational age in SAH diagnosis was 23 weeks. However, theoretically, it was believed that fetal SAH could be diagnosed as early as 18 weeks according to the visualization of the SF in fetuses. The characteristics of the SF were the direct evidence indicating that SAH had occurred. Previous studies focused on the morphology of the sulci, especially the SF, to assess cortical development rather than the internal sonography of the sulci.^{19,20} In this study, the hyperechoic US features within the SF were detected as the most intuitive, which served as an essential clue to the diagnosis of fetal SAH. Furthermore, a 100% (10/10) rate of appearance of a hyperechoic SF was detected by the 2 observers in all cases. Other sulci (6/10) and cisterns (8/10) were also seen with the hyperecho in them. The analysis of detection by the 2 observers is summarized in the Table. The κ number for the 2 observers with different seniority was 0.82 ($P < .05$), which showed good repeatability and agreement on the diagnostic characteristics and methods.

In the 8 cases before 31 weeks’ gestation, only 1 case showed SAH in the superior temporal sulcus and inferior frontal sulcus because most sulci could rarely be detected before 31 weeks’ gestation.¹⁹ Therefore, a focus on the observation of the SF, parieto-occipital sulcus, and cisterns before 31 weeks was recommended. The diagnosis at the third trimester might be disturbed by SF operculization with an unclear intrafissural hyperecho. Dynamic scanning could make a multiangle observation of the SF, other sulci, and cisterns. Therefore, in SF operculization or a doubtful situation, other cerebral planes should be added dynamically besides the 3 cerebral screening axial planes when hyperechogenicity is found within the SF. The echo of the sulci and cisterns should also be observed, such as the superior temporal sulcus, parieto-occipital sulcus, posterior cranial fossa, and cisterna ambiens. Furthermore, the anterior and posterior longitudinal fissures and the spinal

subarachnoid space should also be examined for further evidence of fetal SAH. Two cases of SAH in the longitudinal fissure and 1 in the spinal subarachnoid space were detected; all these cases were associated with intraparenchymal hemorrhage, intraventricular hemorrhage, or SAH. It was recommended that the anterior and posterior longitudinal fissure and the spinal subarachnoid space of fetuses, combined with intraparenchymal hemorrhage, intraventricular hemorrhage should be visualized, not just the common sulci and cisterns in the brain. At the same time, this study and previous studies suggested that SAH was usually associated with an increased peak flow rate of the MCA, implicating different degrees of anemia in fetuses (6/10).²¹ Spectral Doppler in the MCA might help determine the cause.

However, once the SAH clot has formed, it might cause CSF obstruction and lead to chronic hydrocephalus or cerebral edema, affecting the blood supply and causing cerebral function damage, which should be well-noted in fetal SAH.

On the basis of the straightforward and intuitive diagnostic features and method, the detection rate of fetal SAH was up to 100% (10/10); the SF hyperecho was the best indicator of SAH diagnosis in prenatal US.

MR imaging should be recommended once US suggests the presence of fetal SAH. It is primarily found in the subacute phase on MR imaging, showing a high signal on T1WI and a low signal on T2WI. However, the partial volume effect and dilution of CSF with a higher partial pressure of oxygen make the detection of SAH difficult on MR imaging using conventional sequences. Uncontrolled fetal movement makes MR imaging diagnosis more challenging.

Considering the aforementioned reasons, in the present study, the US diagnosis was confirmed by MR imaging (5/10), indicating that the signal changes were seen in tiny sulci but no definite signs in the SF, leading to higher diagnostic difficulty and misdiagnosis rates compared with US for fetal SAH.

The differential diagnosis of hyperechoic or heterogeneous hyperechoic intracranial lesions includes tumor, calcification, hemangioma, and so forth. Tumors compress the adjacent brain tissue, and the mass shows little change or only gradual enlargement with time. Color Doppler can be used to explore rich blood flow.^{12,22} Calcification is mostly present as a dot or block hyperecho but with no obvious dynamic change.²³

Perinatal SAH can cause seizures, apneas, and nervous system abnormalities, such as drowsiness and bregma.²⁴⁻²⁶ Studies^{3,5} showed certain neurologic symptoms in 2 cases (2/12) with a follow-up of 4–20 months. However, most of our cases were induced (8/10); only 2 cases with the gradual absorption of bleeding had a follow-up of 1–2 months after birth with no symptoms. Some scholars^{1,2} believed that fetal SAH was rare and occurred at a relatively early gestational age, leading to a higher risk of severe sequelae or perinatal death. Previous studies and our study also demonstrated high induction (11/22) and death rates (7/22). In the neonatal period, consensus²⁴⁻²⁶ was reached that neonates with isolated SAH had a good prognosis generally, but the site and degree of bleeding were considered, too.

At present, the reported results may vary significantly due to the lack of a prenatal diagnosis and case reports of fetal SAH and insufficient follow-up data. Also, the prognosis may need to be

inferred from neonatal SAH according to the etiology and medical history for further prenatal consultation and management.

CONCLUSIONS

Fetal SAH can be diagnosed by prenatal US due to its unique sonographic characteristics. SF hyperechogenicity is recommended as a significant clue. Prenatal US is used to observe the SF and other sulci and cisterns from conventional transverse planes or in coronal and sagittal sections dynamically. If combined cerebral hemorrhage occurs, the spinal subarachnoid space and the longitudinal fissure are continuously viewed. This kind of method has great significance in assessing bleeding degrees and further prognosis. At present, case reports of fetal SAH are lacking; hence, future studies should aim to collect more cases and test the proposed novel diagnostic method for further stages.

ACKNOWLEDGMENTS

The authors are thankful to all the study participants for taking part in the study and to the team members for their support.

Disclosure forms provided by the authors are available with the full text and PDF of this article at www.ajnr.org.

REFERENCES

1. Ghi T, Simonazzi G, Perolo A, et al. **Outcome of antenatally diagnosed intracranial hemorrhage: case series and review of the literature.** *Ultrasound Obstet Gynecol* 2003;22:121–30 CrossRef Medline
2. Sanapo L, Whitehead MT, Bulas DI, et al. **Fetal intracranial hemorrhage: role of fetal MRI.** *Prenat Diagn* 2017;37:827–36 CrossRef Medline
3. Bowdler N, Faix RG, Elkins T. **Fetal skull fracture and brain injury after a maternal automobile accident: a case report.** *J Reprod Med* 1987;32:375–78 Medline
4. Govaert P, Bridger J, Wigglesworth J. **Nature of the brain lesion in fetal allo-immune thrombocytopenia.** *Dev Med Child Neurol* 1995;37:485–95 CrossRef Medline
5. Hagmann CF, Schmitt-Mechelke T, Caduff JH, et al. **Fetal intracranial injuries in a preterm infant after maternal motor vehicle accident: a case report.** *Pediatr Crit Care Med* 2004;5:396–98 CrossRef Medline
6. Kidron D, Tepper R, Beyth Y, et al. **Superficial hemosiderosis in a second trimester fetus: pathological and clinical manifestations.** *Hum Pathol* 1995;26:1038–40 CrossRef Medline
7. Nishida N, Ina S, Hata Y, et al. **Fetal closed head injuries following maternal motor vehicle accident: a clinicopathologic case report.** *Medicine (Baltimore)* 2018;97:e13133 CrossRef Medline
8. Stafford PA, Biddinger PW, Zumwalt RE. **Lethal intrauterine fetal trauma.** *Am J Obstet Gynecol* 1988;159:485–89 CrossRef Medline
9. Tattoli L, Di Vella G, Solarino B. **A case of intrauterine lethal fetal injury after attempted suicide of the mother.** *Forensic Sci Int* 2017;280:e1–e5 CrossRef Medline
10. Tongsong T, Puntachai P, Tongprasert F, et al. **Sonographic findings in an isolated widened fetal subarachnoid space.** *J Ultrasound Med* 2015;34:917–24 CrossRef Medline
11. Zanders EH, Buist FC, van Vugt JM. **Prenatal diagnosis of fetal intracranial hemorrhage at 25 weeks of gestation.** *Fetal Diagn Ther* 2003;18:324–27 CrossRef Medline
12. Putbresi B, Kennedy A. **Findings and differential diagnosis of fetal intracranial haemorrhage and fetal ischaemic brain injury: what is the role of fetal MRI?** *Br J Radiol* 2017;90:2016025 CrossRef Medline

13. Bouchghoul H, Quelin C, Loget P, et al. **Fetal cerebral hemorrhage due to X-linked GATA1 gene mutation.** *Prenat Diagn* 2018;38:772–78 CrossRef Medline
14. Kutuk MS, Balta B, Koderer H, et al. **Is there relation between COL4A1/A2 mutations and antenatally detected fetal intraventricular hemorrhage?** *Childs Nerv Syst* 2014;30:419–24 CrossRef Medline
15. Elchalal U, Yagel S, Gomori JM, et al. **Fetal intracranial hemorrhage (fetal stroke): does grade matter?** *Ultrasound Obstet Gynecol* 2005;26:233–43 CrossRef Medline
16. Martino F, Malova M, Cesaretti C, et al. **Prenatal MR imaging features of isolated cerebellar haemorrhagic lesions.** *Eur Radiol* 2016;26:2685–96 CrossRef Medline
17. Girard N, Raybaud C, Gambarelli D, et al. **Fetal brain MR imaging.** *Magn Reson Imaging Clin N Am* 2001;9:19–56, vii CrossRef Medline
18. Levine D, Barnes PD. **Cortical maturation in normal and abnormal fetuses as assessed with prenatal MR imaging.** *Radiology* 1999;210:751–58 CrossRef Medline
19. Chen X, Li SL, Luo GY, et al. **Ultrasonographic characteristics of cortical sulcus development in the human fetus between 18 and 41 weeks of gestation.** *Chin Med J (Engl)* 2017;130:920–28 CrossRef Medline
20. Guibaud L, Selleret L, Larroche JC, et al. **Abnormal Sylvian fissure on prenatal cerebral imaging: significance and correlation with neuropathological and postnatal data.** *Ultrasound Obstet Gynecol* 2008;32:50–60 CrossRef Medline
21. Mari G, Deter RL, Carpenter RL, et al. **Noninvasive diagnosis by Doppler ultrasonography of fetal anemia due to maternal red-cell alloimmunization: collaborative group for Doppler assessment of the blood velocity in anemic fetuses.** *N Engl J Med* 2000;342:9–14 CrossRef Medline
22. Bin C, Jun Z. **MRI characteristics fetal intracranial hemorrhage in 120 cases.** *Chinese Journal of Magnet Resonance Imaging* 2019;10:491–96
23. Fukuyama Y, Osawa M, Suzuki H. **Congenital progressive muscular dystrophy of the Fukuyama type: clinical, genetic and pathological considerations.** *Brain Dev* 1981;3:1–29 CrossRef Medline
24. Gupta SN, Kechli AM, Kanamalla US. **Intracranial hemorrhage in term newborns: management and outcomes.** *Pediatr Neurol* 2009;40:1–12 CrossRef Medline
25. Tan AP, Svrckova P, Cowan F, et al. **Intracranial hemorrhage in neonates: a review of etiologies, patterns and predicted clinical outcomes.** *Eur J Paediatr Neurol* 2018;22:690–717 CrossRef Medline
26. Shah NA, Wusthoff CJ. **Intracranial hemorrhage in the neonate.** *Neonatal Netw* 2016;35:67–71 CrossRef Medline

Prenatal MR Imaging Phenotype of Fetuses with Tuberous Sclerosis: An Institutional Case Series and Literature Review

S.K. Goergen and M.C. Fahey



ABSTRACT

BACKGROUND AND PURPOSE: Most patients with tuberous sclerosis complex (TSC) do not receive prenatal diagnosis. Our aim was to describe MR imaging findings to determine the following:

1. Whether normal fetal MR imaging is more common in fetuses imaged at ≤ 24 weeks' gestation compared with > 24 weeks
2. The frequency of cardiac rhabdomyoma
3. The range of MR imaging phenotypes in fetal tuberous sclerosis complex.

MATERIALS AND METHODS: Our institutional fetal MR imaging data base was searched between January 1, 2011 and June 30, 2021, for cases of TSC confirmed either by genetic testing, postnatal imaging, postmortem examination, or composite prenatal imaging findings and family history. A MEDLINE search was performed on June 8, 2021.

RESULTS: Forty-seven published cases and 4 of our own cases were identified. Normal findings on fetal MR imaging were seen at a lower gestational age (mean, 24.7 [SD, 4.5] weeks) than abnormal findings on MR imaging (mean, 30.0 [SD, 5.3] weeks) ($P = .008$). Nine of 42 patients with abnormal MR imaging findings were ≤ 24 weeks' gestation. Subependymal nodules were present in 26/45 cases (57.8%), and cortical/subcortical lesions, in 17/46 (37.0%). A foramen of Monro nodule was present in 15 cases; in 2/7 cases in which this was unilateral, it was the only abnormal cerebral finding. Cardiac rhabdomyoma was absent in 3/48 cases at the time of fetal MR imaging but was discovered later. Megalencephaly or hemimegalencephaly was observed in 3 cases.

CONCLUSIONS: Fetuses with abnormal cranial MR imaging findings were older than those with negative findings. Fetal hemimegalencephaly and megalencephaly should prompt fetal echocardiography. Cardiac rhabdomyoma was not always present at the time of fetal MR imaging.

ABBREVIATIONS: CR = cardiac rhabdomyoma; GA = gestational age; GE = ganglionic eminence; TSC = tuberous sclerosis complex; iuMR = fetal MR imaging; US = ultrasound

Tuberous sclerosis complex (TSC) is an autosomal dominant genetic disease with an incidence of 1 in 6000. Its clinical manifestations are highly variable, but symptoms include seizures, mental retardation, skin lesions, and the formation of hamartomas in multiple organs, including the heart, brain, eye, and kidney.¹ Autosomal dominant pathogenic variants in 1 of the 2 tumor-suppressor genes *TSC1* and *TSC2* are responsible for TSC,² and more than half of cases are due to spontaneous

(noninherited) mutations. Clinically unaffected parents with a child with TSC, however, have a 3% risk of recurrence in a subsequent offspring because of gonadal/germline mosaicism. It has been estimated that approximately 1% of individuals with TSC have germline^{3,4} and 15% have somatic mosaicism, likely accounting for the 20% of people meeting the diagnostic criteria for TSC who have no demonstrated genetic abnormality on peripheral blood testing.⁵ Although the presence of a pathogenic *TSC1* or *TSC2* variant is now a major diagnostic criterion for TSC, the difficulty in identifying the variant in a substantial proportion of patients with the condition underscores the importance of imaging, particularly in the prenatal and early postnatal period when cardiac and cerebral abnormalities are often the only stigmata of TSC. Additionally, prenatal and postconception genetic diagnoses of TSC in embryos and fetuses are not yet widely available within an appropriate timeframe in most settings that undertake pregnancy care. Judicious use of costly genetic

Received October 19, 2021; accepted after revision January 10, 2022.

From Monash Health Imaging and Department of Imaging (S.K.G.), and Monash Health Paediatric Neurology Unit and Department of Paediatrics (M.C.F.), Monash University, School of Clinical Sciences, Clayton, Victoria, Australia.

Please address correspondence to Stacy K. Goergen, MBBS, MCLinEpi, FRANZCR, Monash Health Imaging and Department of Imaging, Monash University, School of Clinical Sciences, 246 Clayton Rd, Clayton, Victoria 3168; e-mail: Stacy.Goergen@monashhealth.org

Indicates article with online supplemental data.

<http://dx.doi.org/10.3174/ajnr.A7455>

testing is contingent on a prenatal imaging phenotype and family history. Moreover, the early use of *mTOR* inhibitors may ameliorate the clinical course and modify the clinical and imaging phenotype. Postnatal treatment of TSC with rapamycin and antiepileptic therapy with vigabatrin are well-established; however, there have been very recent case reports of successful in utero treatment with rapamycin of affected fetuses.⁶

While identification of one or multiple cardiac rhabdomyomas is the most common reason for TSC suspected on prenatal ultrasound (US) at or after the midtrimester, up to one-third of fetuses with cardiac tumors do not have TSC.⁷ In the absence of genetic confirmation, a diagnosis of TSC requires the presence of at least 2 major or 1 major and 2 minor criteria; 2 major criteria are subependymal nodules and cortical tubers.⁵ However, fetal cranial manifestations of TSC are not confined to these 2 abnormalities despite their acknowledged importance as primary diagnostic criteria.⁸

Improved understanding of the range of abnormal fetal brain phenotypes in TSC and their variation with gestational age may help identify potentially affected fetuses earlier; triage pregnancies appropriately for more efficient and cost-effective genetic testing and prenatal surveillance with cardiac sonography when cardiac tumors are not present; and initiate intrauterine rapamycin treatment earlier when this treatment becomes more mainstream.

Aims

To report on the prenatal MR imaging findings in 4 fetuses from a single institution with TSC and review the literature on cranial abnormalities on MR imaging in fetuses with TSC to more fully describe and understand the prenatal TSC phenotype and determine whether:

1. Normal fetal MR imaging (iuMR) is reported more commonly in fetuses ≤ 24 weeks' gestation compared with > 24 weeks
2. Any cases of TSC diagnosed by iuMR had neither cardiac rhabdomyoma nor known family history at the time of iuMR.

MATERIALS AND METHODS

A data base review was conducted at our own institution to identify fetuses with a confirmed diagnosis of TSC who had iuMR during the past 10 years. A waiver of institutional review board approval for this activity and for use of these de-identified patient data for research and teaching purposes was obtained. In addition, a literature search of MEDLINE was conducted on June 8, 2021, using the following search terms: (Fetal or Fetus) and (MR imaging or Magnetic Resonance) and (tuberous sclerosis). Full-text articles were accessed for all retrieved citations, and inclusion and exclusion criteria were applied. For studies to be included, a description of iuMR findings for fetuses with TSC had to be provided and/or illustrated. Letters, case reports, short communications, and case series and other research publications were considered if they were published in English and if the diagnosis of TSC were ascertained through composite prenatal imaging findings/family history consistent with the diagnosis and/or genomic confirmation and/or postmortem/postnatal diagnosis of TSC. Reference lists of retrieved studies were scanned for potentially eligible additional studies that were not retrieved in the

original search. Studies were excluded if details of the iuMR findings in individual TSC cases could not be extracted from provided images or if

1. The imaging findings in individual cases were not described (ie, only aggregated data were reported) or
2. The gestational age of the fetus at the time of iuMR was not provided.

In addition to the literature search, we conducted an audit of our institutional iuMR data base between January 1, 2011, and June 30, 2021, and applied the same inclusion/exclusion criteria as used for the MEDLINE search.

Data Extraction

When a case was reported as having abnormal findings, the reported and/or depicted cranial imaging findings were categorized as present, absent, or not stated. "Not stated" was when the particular domain or feature was not specifically mentioned as being present or absent in the report of the case and the provided images did not permit confident confirmation of presence or absence of the finding.

The range of tabulated cranial abnormalities was determined by findings in previous case reports and on the basis of our clinical experience in our own cases. When cranial findings on iuMR for a case were reported as being normal, all domains were scored as absent. These domains were the following: foramen of Monro mass/ganglionic eminence (GE) enlargement (unilateral or bilateral), subependymal nodules, cortical or subcortical nodules, dominant hemispheric mass, hemimegalencephaly, megalencephaly, white matter signal abnormalities/transmantle sign, ventriculomegaly, and cerebellar abnormality. In addition, fetal gestational age at iuMR, the presence of cardiac tumors or renal cysts, and a positive family history were tabulated.

RESULTS

Seventy-nine primary studies were retrieved as a result of the MEDLINE search (Fig 1). An additional 2 studies meeting the inclusion criteria were identified from scanning the reference lists of the retrieved studies; a literature review and case report⁹ and a letter reporting a single case¹⁰ were identified in this way.

Four additional cases were identified following an audit of our institutional iuMR data base (Figs 2–4), 2 of which were included in a prior publication on imaging of fetal GE abnormalities,⁸ with a total of 51 cases (Fig 1). Details of included and excluded studies with full citations are provided in the Online Supplemental Data.

Twenty studies each reported the findings of a single fetus. Seven of the included studies reported imaging findings in > 1 case that met the inclusion criteria, accounting for a further 27 cases: Ulm et al¹¹ ($n = 6$), Zhou et al¹² ($n = 5$), Mühler et al¹³ ($n = 5$), Jurkiewicz et al¹⁴ ($n = 5$), Levine et al¹⁵ ($n = 2$), Prabowo¹⁶ ($n = 2$), and Sonigo et al¹⁷ ($n = 2$).

The mean gestational age (GA) for the 51 fetuses was 29.1 weeks, and the mean GA for the 4/51 new cases from our institution was 27.3 weeks. For the 9 fetuses with normal MR imaging findings, the mean GA was 24.7 (SD, 4.5) weeks, whereas for those with abnormal MR imaging findings, the mean GA was 30.0 (SD, 5.3) weeks ($P = .008$). Eleven fetuses were reported as

having a family member affected with TSC. Of 20 cases in which the field strength for the iuMR examination was reported, 2 studies were performed at 3T and the other 18 at 1.5T.

Imaging Findings

Details of the imaging findings at iuMR for individual included cases are provided in the Online Supplemental Data. These are summarized in Tables 1 and 2.

Subependymal nodules were present in 26 of 45 cases (57.8%), and cortical/subcortical lesions, in 17 of 46 (37.0%). In 8 of 19 (42.1%) cases demonstrating ventriculomegaly, only 1 had this as an isolated cerebral finding in a fetus with a GA of 26 weeks¹⁸ with cortical tubers evident on postnatal MR imaging despite sirolimus administration from 28 weeks' gestation.

A foramen of Monroe nodule was present in 15 cases; in 8 of these, it was bilateral, and in 7, unilateral. Of the 7 unilateral cases, in 2 of 7, it was the only reported abnormal cerebral finding, and in a third case, one of our own, was accompanied only by mild ventriculomegaly. However, all 3 cases were referred for iuMR due to cardiac tumor.

Megalencephaly, hemimegalencephaly, and cerebellar abnormality were very uncommon, being observed in 2/18, 1/18, and 1/18 fetuses, respectively. The fetus with cerebellar abnormality had other characteristic features of TSC, including subependymal nodules and cortical mass lesions. The cases with megalencephaly or hemimegalencephaly had ≥ 1 cardiac mass, though in 1 of the

2 cases of hemimegalencephaly previously reported from our institution as part of another study,⁸ the single cardiac ventricular rhabdomyoma became evident only when fetal echocardiography was repeated the day following the MR imaging, which had been performed due to a suspicion on prenatal US of a cerebral hemispheric mass lesion or hemorrhage.

The phenotypic manifestations of TSC in the group of fetuses of ≤ 24 weeks' gestation ($n = 9$) are of particular interest. A dominant hemispheric mass was present in 5 (55%), and this was associated with either subependymal nodules ($n = 1$) or unilateral GE enlargement. In only 2 of the 9 cases were subependymal nodules alone or unilateral GE enlargement alone identified, and in the 2 remaining cases, a combination of subependymal nodules, cortical/subcortical nodules, and a foramen of Monroe mass lesion was present.

Of 9 patients with normal fetal cranial MR imaging findings, all of whom had ≥ 1 cardiac rhabdomyoma (CR), repeat MR imaging, performed between 3 and 12 weeks later in 3 cases, demonstrated cerebral abnormalities consistent with TSC; all of these repeat studies occurred during the third trimester of pregnancy at 26–34 weeks' gestation.

Furthermore, only 3 of the 48 (6.7%) fetuses with description of the presence or absence of a cardiac mass had no sonographic evidence of a cardiac mass at the time of iuMR. In 2 of these, including the case of hemimegalencephaly from our institution, the fetus's father was known to have TSC. In all 3 cases, the CR was demonstrated on a second US performed between 1 day and 4 weeks after the iuMR at a gestational age of between 22 and 34 weeks.^{19,20}

The presence or absence of renal cysts was reported in only 3 cases, apart from the 4 from our institution, none of whom had cysts identified on US. Of these 3, only 1 had cysts and also had evidence of CR.²¹

DISCUSSION

The current review, including 4 cases from our own institution, establishes that a cardiac tumor was present at the time of iuMR in all except 3 of 51 cases of proved TSC, and in 2 of these 3 cases, the fetus's father had known TSC. This finding highlights the importance of a careful search for CR in fetuses with cranial abnormalities suggestive of TSC because CRs substantially increase the pretest probability of TSC and their absence should raise questions about the diagnosis, especially in a fetus with no family history.

Similarly, when a unilateral foramen of Monroe nodule or mass, essentially synonymous with unilateral GE enlargement, is seen as an isolated abnormality, or with only ventriculomegaly, TSC should be considered if a CR is present. Unilateral germinal matrix hemorrhage can mimic this appearance; consequently, routine performance of susceptibility-weighted imaging and fetal echocardiography can help avoid overdiagnosis of TSC, with resulting inappropriate prognostic and recurrence counseling in this situation.

The incidence of CR in patients with TSC is 50%–80%,²² with a recent

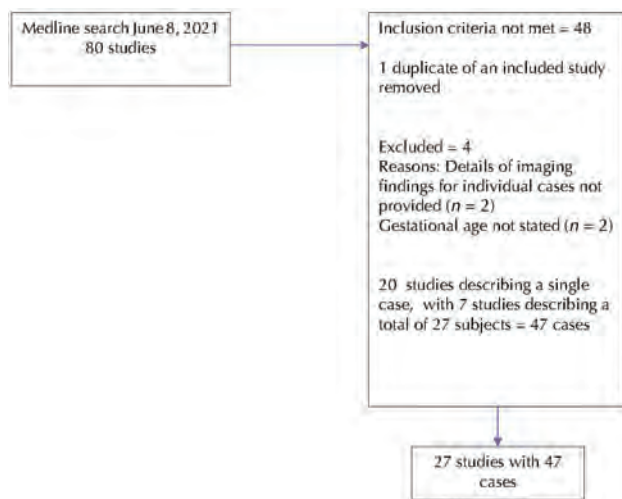


FIG 1. Case ascertainment process.

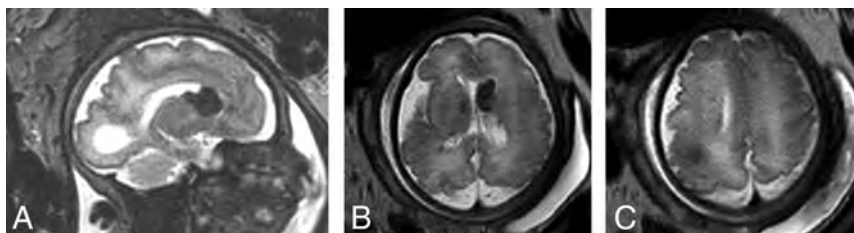


FIG 2. Thirty-two to 40 weeks' gestation. 3T, single-shot T2-weighted EPI shows the foramen of Monroe dominant nodule/enlarged GE (A and B) and cortical tuber (C).

study suggesting that only 22% of a cohort of patients with TSC had CR diagnosed prenatally. Moreover, CRs can appear late in pregnancy, most often after the midtrimester screening examination is performed.²³ Thus, it is possible that a substantial number

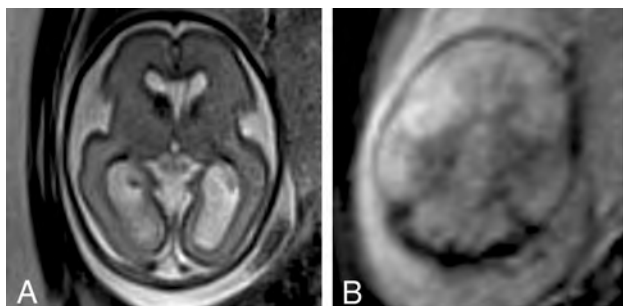


FIG 3. Twenty-five weeks' gestation. A 1.5T, single-shot T2-weighted EPI (A) shows the right foramen of Monro dominant nodule/enlarged GE and the normal GE on the left. T2*-weighted image (B) demonstrates no blood products in the mass.

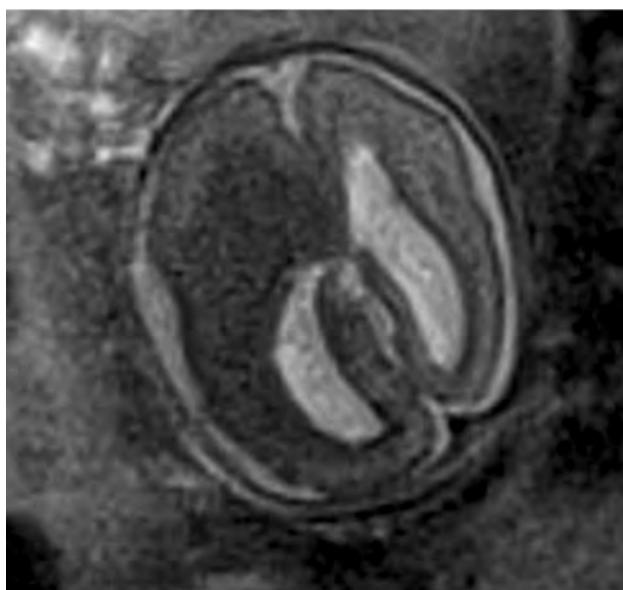


FIG 4. Twenty-two weeks' gestation. A 1.5T single-shot T2-weighted EPI demonstrates hemimegalencephaly and a dominant ipsilateral mass representing a possible coexistent subependymal giant cell astrocytoma. This was initially interpreted on screening US as a parenchymal hemorrhage. After the iuMR, dedicated fetal echocardiography the following day identified a single small rhabdomyoma.

of fetuses with TSC will not have this diagnosis suggested prenatally by the presence of CR. While intracranial manifestations of TSC on iuMR might, therefore, be the first indication of the disorder due to iuMR being more sensitive and specific than prenatal US for intracranial pathology,²⁴ this was not borne out by our literature review. This may, however, reflect selection bias in that reported cases of TSC on iuMR have been referred for MR imaging due to the identification of CR either at the midtrimester screening examination or in the third trimester as an “incidental” finding when growth, placental position, or other surveillance has occurred.

We have identified that among fetuses with proved TSC who have had iuMR, the likelihood of abnormal cranial findings varies significantly with GA. Fetuses who have abnormal findings were, on average, at 30 weeks' gestation compared with 25 weeks for fetuses with no abnormality. Interestingly, most fetuses with TSC, when the diagnosis was made at 24 weeks or earlier in gestation, demonstrated a dominant hemispheric mass, whereas only 1 fetus (11% of this early-gestation cohort) had subependymal nodules as their sole imaging manifestation. This finding makes intuitive sense because more severe “masslike” lesions would be more likely to be detected at the midtrimester screening US examination, typically performed between 19 and 21 weeks' gestation, and would manifest as a midline shift. Such masslike presentations at screening US can be misinterpreted as hemorrhage and underscore the importance of careful tertiary echocardiography and T2*-weighted iuMR for further fetal evaluation.

While association of cranial abnormalities with increasing gestation might suggest that it is better to wait to perform iuMR, 9/42 (23%) fetuses with abnormal cranial MR imaging findings were 19–24 weeks' gestation when MR imaging was performed. This timing is potentially important in jurisdictions where GA-related limitations exist on pregnancy termination. It may also be salient to the commencement of intrauterine therapy with rapamycin. When genomic testing is either unavailable or not turned around quickly enough to be clinically useful regarding counseling and therapeutic decision making, earlier diagnosis may also be important. However, “early” (<25 gestational weeks) MR imaging may be associated with a higher rate of negative findings; thus, it may be a more costly strategy if a second iuMR is performed later in pregnancy after initial negative examination.

Improvements in ultrasound equipment during the past decade and in particular the evolution of the tertiary neurosonogram using a transvaginal approach and, when possible, the sonographic window of the anterior fontanelle have dramatically improved the quality of fetal brain imaging with US. In addition,

Table 1: Cranial MR abnormalities in fetuses with TSC^a

	Foramen of Monro /GE Mass Unilateral	Foramen of Monro/GE Mass Bilateral	SEN	Cortical/ Subcortical	Dominant Hemispheric Mass	MEG	HMEG	WM Signal Abnormality	VM	Cerebellar Abnormality
Present	2	1	1	2	1	1	1	0	3	0
Absent	2	3	3	2	3	3	3	4	1	4
Not stated	0	0	0	0	0	0	0	0	0	0

Note:—SEN indicates subependymal nodules; HMEG, hemimegalencephaly; MEG, megalencephaly; VM, ventriculomegaly.

^a Local institutional cases (n = 4).

Table 2: Cranial abnormalities in fetuses with TSC: combined data from literature review and local institutional cases^a

	Foramen of Monro/GE Mass Unilateral	Foramen of Monro/GE Mass Bilateral	SEN	Cortical/ Subcortical	Dominant Hemispheric Mass	MEG	HMEG	WM Signal Abnormality	VM	Cerebellar Abnormality
Present	7	8	26	17	6	2	1	7	8	1
Absent	24	20	19	29	25	16	17	19	11	17
Not stated	20	21	4	5	20	33	33	25	32	13

Note:—SEN indicates subependymal nodules; HMEG, hemimegalencephaly; MEG, megalencephaly; VM, ventriculomegaly.

^aLocal institutional cases (n = 4).

the spatial resolution of US is superior to that of MR imaging, theoretically making subependymal nodule detection easier with US than with MR imaging. However, tertiary neurosonography remains highly operator-, patient-, and fetal position-dependent. Whether such optimized US can detect subependymal nodules in practice in fetuses at a high demographic risk of TSC when these are not demonstrable with iuMR is a question outside of the scope of the current review.

Finally, by aggregating data from multiple case reports and case series, the current study highlights some less common presentations of TSC, in particular hemimegalencephaly and megalencephaly. Because other genetic disorders, in particular other *mTOR* pathogenic variants, such as *PIK3CA*-related overgrowth spectrum disorders, are the underlying pathogenic variants in most cases of megalencephaly or hemimegalencephaly and these are almost invariably de novo mutations or, much less often, the result of germline mosaicism, distinguishing TSC-related hemimegalencephaly/megalencephaly from these more common non-TSC causes is very important. It is theorized that because activation of *TSC1* and *TSC2* is driven by upstream signals of the *PIK3/AKT* pathway, the loss-of-function pathogenic variants of *TSC1* or *TSC2* that result in clinical TSC could induce an imbalance in *PIK3/AKT* pathway functioning, producing cerebral hemispheric overgrowth.¹⁰ Hence, careful examination and re-examination of the fetal heart with tertiary fetal echocardiography are recommended in the presence of hemimegalencephaly/megalencephaly in the fetus. These will help direct genomic testing and prevent inappropriate advice regarding the utility of such testing or the likelihood of recurrence in subsequent pregnancies.

Our study has limitations, mainly due to potential selection bias in published cases driven by a prenatal US diagnosis of CR being the trigger to refer a patient for iuMR. Because it is recognized that CR may not be detectable with US until the third trimester of pregnancy and frequently not until the postnatal period, the cases included in this review are likely to provide a biased impression regarding the following:

- The likelihood of TSC being the cause for fetal cerebral abnormalities when there is no CR or family history (because the pregnancy may be terminated without a genetic diagnosis or postmortem examination)
- How early in gestation the cerebral lesions of TSC can be diagnosed with MR imaging in fetuses with high pretest risk
- How often iuMR findings are negative for cerebral lesions in fetuses with high pretest risk of TSC (because of family history of the condition) and at what gestational age, because cases with negative findings are less likely to be published.

A prospective cohort study of serial MR imaging in fetuses who are the offspring or siblings of individuals with TSC would provide a more accurate estimate of these important issues to help inform clinical practice. However, pre-implantation genetic diagnosis and/or gene panel testing for pathogenic *TSC1* and *TSC2* variants during early pregnancy may become more feasible, economical, and acceptable to patients than second trimester iuMR screening when the fetus has a high risk of the condition due to an affected sibling or parent. In addition, only a small minority of fetuses reported in this study were imaged using a 3T scanner; the reduced signal-to-noise and thus the resolution of iuMR at 1.5T may reduce the sensitivity for cerebral abnormalities in fetuses with TSC.

A further limitation of the current study is due to variable terminology used to describe iuMR imaging findings and, in particular, the general lack of routine reporting of cranial biometry. Specifically, when iuMR was said have normal findings but it was unclear whether fetal brain biometry had actually been performed, it is possible that megalencephaly with a “normal”-appearing brain may have been underrecognized. Moreover, the range of terms used to describe a mass, nodule, or swelling in the region of the foramen of Monro or GE of a fetus on MR imaging may have made the distinction among a foramen of Monro “mass,” a small hemispheric mass, and subependymal nodule in the region of the foramen of Monro an artificial one. Hence, we may have misclassified abnormalities in this region when relying on descriptive terms used in the report, mainly because their imaging appearances can overlap.

CONCLUSIONS

The current study highlights the ability of iuMR to provide the diagnosis of TSC in fetuses ≤ 24 weeks’ gestation and underscores the importance of considering the possibility of TSC when fetal megalencephaly or hemimegalencephaly or a masslike cerebral lesion are observed; these findings should trigger tertiary fetal echocardiography which, if normal, may need to be repeated later in pregnancy. Whole-exome sequencing and specific *TSC* genetic testing will be increasingly used to provide an earlier prenatal diagnosis when family history, the presence of CR, or iuMR cerebral phenotype suggests potential TSC.

ACKNOWLEDGMENTS







The authors would like to thank the families who permitted their fetuses’ imaging data to be provided in this publication.

Disclosure forms provided by the authors are available with the full text and PDF of this article at www.ajnr.org.

REFERENCES

1. Curatolo P, Maria BL. **Tuberous sclerosis.** *Handb Clin Neurol* 2013;111:323–31 CrossRef Medline
2. Crino PB, Nathanson KL, Henske EP. **The tuberous sclerosis complex.** *N Engl J Med* 2006;355:1345–56 CrossRef Medline
3. Chen L, Jiang Y, Wang J. **Fetal cardiac rhabdomyoma due to paternal mosaicism of TSC2: a case report.** *Medicine (Baltimore)* 2020;99:e21949 CrossRef Medline
4. Ehninger D. **From genes to cognition in tuberous sclerosis: implications for mTOR inhibitor-based treatment approaches.** *Neuropharmacology* 2013;68:97–105 CrossRef Medline
5. Northrup H, Krueger DA; International Tuberous Sclerosis Complex Consensus Group. **Tuberous sclerosis complex diagnostic criteria update: recommendations of the 2012 International Tuberous Sclerosis Complex Consensus Conference.** *Pediatr Neurol* 2013;49:243–54 CrossRef Medline
6. Cavalheiro S, da Costa MD, Richtmann R. **Everolimus as a possible prenatal treatment of in utero diagnosed subependymal lesions in tuberous sclerosis complex: a case report.** *Childs Nerv Syst* 2021;37:3897–99 CrossRef Medline
7. Tworetzky W, McElhinney DB, Margossian R, et al. **Association between cardiac tumors and tuberous sclerosis in the fetus and neonate.** *Am J Cardiol* 2003;92:487–89 CrossRef Medline
8. Goergen SK, Alibrahim E, Christie J, et al. **The fetus with ganglionic eminence abnormality: head size and extracranial sonographic findings predict genetic diagnoses and postnatal outcomes.** *AJNR Am J Neuroradiol* 2021;42:1528–34 CrossRef Medline
9. Wortmann SB, Reimer A, Creemers JW, et al. **Prenatal diagnosis of cerebral lesions in tuberous sclerosis complex (TSC): case report and review of the literature.** *Eur J Paediatr Neurol* 2008;12:123–26 CrossRef Medline
10. Bruet S, Francannet C, Marguet F, et al. **Prenatal diagnosis of hemimegalencephaly revealing tuberous sclerosis complex.** *Ultrasound Obstet Gynecol* 2020;55:688–89 CrossRef Medline
11. Ulm B, Muin D, Scharrer A, et al. **Prenatal ultrasound and magnetic resonance evaluation and fetal outcome in high-risk fetal tumors: a retrospective single-center cohort study over 20 years.** *Acta Obstet Gynecol Scand* 2020;99:1534–45 CrossRef Medline
12. Zhou Y, Dong SZ, Zhong YM, et al. **Prenatal and postnatal diagnosis of rhabdomyomas and tuberous sclerosis complex by ultrasound and standard MRI.** *Indian J Pediatr* 2018;85:729–37 CrossRef Medline
13. Mühler MR, Rake A, Schwabe M, et al. **Value of fetal cerebral MRI in sonographically proven cardiac rhabdomyoma.** *Pediatr Radiol* 2007;37:467–74 CrossRef Medline
14. Jurkiewicz E, Bekiesińska-Figatowska M, Romaniuk-Doroszewska A, et al. **Brain MRI in fetuses with cardiac tumours.** *Neuroradiol J* 2007;20:494–99 CrossRef Medline
15. Levine D, Barnes P, Korf B, et al. **Tuberous sclerosis in the fetus: second-trimester diagnosis of subependymal tubers with ultrafast MR imaging.** *AJR Am J Roentgenol* 2000;175:1067–69 CrossRef Medline
16. Prabowo AS, Anink JJ, Lammens M, et al. **Fetal brain lesions in tuberous sclerosis complex: TORC1 activation and inflammation.** *Brain Pathol* 2013;23:45–59 CrossRef Medline
17. Sonigo P, Elmaleh A, Brunelle E, et al. **Prenatal MRI diagnosis of fetal cerebral tuberous sclerosis.** *Pediatr Radiol* 1996;26:1–4 CrossRef Medline
18. Pluym ID, Sklansky M, Wu JY, et al. **Fetal cardiac rhabdomyomas treated with maternal sirolimus.** *Prenat Diagn* 2020;40:358–64 CrossRef Medline
19. Brackley KJ, Farndon PA, Weaver JB, et al. **Prenatal diagnosis of tuberous sclerosis with intracerebral signs at 14 weeks' gestation.** *Prenat Diagn* 1999;19:575–79 CrossRef Medline
20. Borțea CI, David VL, Stoica F, et al. **The value of imagistics in early diagnosis of tuberous sclerosis.** *Case Rep Pediatr* 2020;2020:1309184 CrossRef Medline
21. Mongrain V, van Doesburg NH, Rypens F, et al. **A case report of severe tuberous sclerosis complex detected in utero and linked to a novel duplication in the TSC2 gene.** *BMC Neurol* 2020;20:324 CrossRef Medline
22. Axt-Fliedner R, Qush H, Hendrik HJ, et al. **Prenatal diagnosis of cerebral lesions and multiple intracardiac rhabdomyomas in a fetus with tuberous sclerosis.** *J Ultrasound Med* 2001;20:63–67 CrossRef Medline
23. Gu X, Han L, Chen J, et al. **Antenatal screening and diagnosis of tuberous sclerosis complex by fetal echocardiography and targeted genomic sequencing.** *Medicine (Baltimore)* 2018;97:e0112 CrossRef Medline
24. Rossi AC, Prefumo F. **Additional value of fetal magnetic resonance imaging in the prenatal diagnosis of central nervous system anomalies: a systematic review of the literature.** *Ultrasound Obstet Gynecol* 2014;44:388–93 CrossRef Medline

Early Ultrasonic Monitoring of Brain Growth and Later Neurodevelopmental Outcome in Very Preterm Infants

 V.A.A. Beunders,  J.A. Roelants,  J. Suurland,  J. Dudink,  P. Govaert,  R.M.C. Swarte,  M.M.A. Kouwenberg-Raets,  I.K.M. Reiss,  K.F.M. Joosten, and  M.J. Vermeulen



ABSTRACT

BACKGROUND AND PURPOSE: In infants born very preterm, monitoring of early brain growth could contribute to prediction of later neurodevelopment. Therefore, our aim was to investigate associations between 2 early cranial ultrasound markers (corpus callosum–fastigium and corpus callosum length) and neurodevelopmental outcome and the added value of both markers in the prediction of neurodevelopmental outcome based on neonatal risk factors and head circumference in very preterm infants.

MATERIALS AND METHODS: This prospective observational study included 225 infants born at <30 weeks' gestational age, of whom 153 were without any brain injury on cranial ultrasound. Corpus callosum–fastigium and corpus callosum length and head circumference were measured at birth, 29 weeks' gestational age, transfer from the neonatal intensive care unit to a level II hospital, and 2 months' corrected age. We analyzed associations of brain markers and their growth with cognitive, motor, language, and behavioral outcome at 2 years' corrected age.

RESULTS: In infants without brain injury, greater corpus callosum–fastigium length at 2 months was associated with better cognitive outcome. Corpus callosum length at 2 months was positively associated with cognitive, motor, and language outcome. Faster growth of the corpus callosum length between birth and 2 months was associated with better cognitive and motor function. Prediction of neurodevelopmental outcome based on neonatal risk factors with or without head circumference was significantly improved by adding corpus callosum length.

CONCLUSIONS: Both corpus callosum–fastigium and corpus callosum length on cranial ultrasound are associated with neurodevelopmental outcome of very preterm infants without brain injury at 2 years, but only corpus callosum length shows the added clinical utility in predicting neurodevelopmental outcome.

ABBREVIATIONS: CA = corrected age; CBCL = Child Behavior Checklist; CC = corpus callosum; CCF = corpus callosum–fastigium; CUS = cranial ultrasound; GA = gestational age; HC = head circumference; IQR = interquartile range; NICU = neonatal intensive care unit

In infants born very preterm, adverse brain growth is an important predictor of later neurodevelopmental impairment.^{1,2} Therefore, monitoring early brain growth is important and requires reliable and clinically applicable markers. The most commonly used marker


in infancy is head circumference (HC), which is easily applicable in clinical care. In preterm infants however, head circumference often poorly reflects brain size due to head deformities and increased extracerebral fluid.^{3,4} Brain imaging techniques can add valuable information on the actual size of the brain. MR imaging is considered the most reliable method but is not bedside-available and is expensive, limiting the possibility of serial repeat imaging. Cranial ultrasound (CUS) can be performed more easily and, therefore, serially during a stay in the neonatal intensive care unit (NICU).⁵

Several previous studies in preterm infants linked corpus callosum (CC) length at term-equivalent age with neurodevelopmental outcome in childhood.^{6–8} Because CC length only reflects a small part of the brain, our study group introduced corpus callosum–fastigium (CCF) length as a new marker for brain growth.⁹ CCF length is measured on CUS in a standard midsagittal plane and covers a larger part of the brain than CC length, including several important brain structures such as the thalamus. The measurement

Received October 27, 2021; accepted after revision January 10, 2022.

From the Department of Pediatrics (V.A.A.B., J.A.R., P.G., R.M.C.S., I.K.M.R., M.J.V.), Division of Neonatology, Department of Child and Adolescent Psychiatry/Psychology (J.S.), Department of Pediatrics (K.F.M.J.), Intensive Care Unit, Erasmus MC Sophia Children's Hospital, University Medical Center Rotterdam, Rotterdam, the Netherlands; Department of Neonatology (J.D.), Wilhelmina Children's Hospital, University Medical Center Utrecht, Utrecht, the Netherlands; Brain Center (J.D.), University Medical Center Utrecht, Utrecht, the Netherlands; and Department of Pediatrics (M.M.A.K.-R.), Division of Neonatology, Maastricht University Medical Center, Maastricht, the Netherlands.

Please address correspondence to M.J. Vermeulen, MD, Erasmus MC - Sophia Children's Hospital, Marijn Vermeulen, PO Box 2060, 3000 CB Rotterdam, the Netherlands; e-mail: m.j.vermeulen@erasmusmc.nl

 Indicates article with online supplemental data.

<http://dx.doi.org/10.3174/ajnr.A7456>

can be performed both pre- and postnatally. We previously showed that CCF length has high reproducibility and applicability for monitoring brain growth during fetal life and a NICU stay.^{9,10} CCF length was found to be smaller in fetuses and neonates with fetal growth restriction compared with those with normal growth.^{10,11} However, the predictive value of CCF length for neurodevelopmental outcome needs further investigation.

In this study, we explored the associations between length and growth of the CCF and CC in early infancy and neurodevelopmental outcome at 2 years' corrected age (CA) in infants born very preterm, specifically in those without brain injury. We hypothesized that longer length and faster growth of the CCF and CC are associated with improved neurodevelopmental outcome and that both markers have added clinical value to the prediction of neurodevelopment compared with neonatal risk factors and head circumference.

MATERIALS AND METHODS

Participants

This study combined data of 2 comparable prospective observational cohort studies performed between 2010 and 2017 at the NICU of the Erasmus MC Sophia Children's Hospital, Rotterdam, the Netherlands. All preterm infants born between 24 and 30 weeks' gestational age (GA) and admitted to the NICU within 48 hours after birth were eligible for participation in Study A (Submarine study) or Study B (BOND study) (Online Supplemental Data).^{12,13} Infants with severe congenital or chromosomal abnormalities, perinatal asphyxia (cord blood/first postnatal pH, <7.0 and APGAR score at 5 minutes, <5), and congenital TORCH infection (toxoplasmosis, other agents, rubella, cytomegalovirus, and herpes simplex) were excluded. Parental informed consent was obtained for all participants. Both studies were approved by the medical ethics committee of the Erasmus MC Sophia Children's Hospital, University Medical Center, Rotterdam.

Maternal, obstetric, and neonatal characteristics were collected prospectively from the electronic medical record. Ethnicity was classified as non-Western if one or both parents were born in a non-Western country, and parental education level was based on both parents.¹⁴ Brain injury was diagnosed on CUS and included subependymal and intraventricular hemorrhage (grade 1–2+), cerebellar hemorrhage, stroke, and/or periventricular leukomalacia. Postnatal age was defined as days after birth with the day of birth as day 1.¹⁵

Markers of Brain Growth

CUS was routinely performed according to local clinical protocol by the attending neonatologist or an experienced researcher. The local protocol included CUS on postnatal age days 1, 2, 3, and 7, followed by weekly measurements until transfer from the NICU to a level II hospital. A MyLab 70 scanner (Esaote) with a convex neonatal probe (7.5 MHz) was used. Off-line measurements of CC length and CCF length on a standard midsagittal plane were performed using MyLab software (Esaote) by one of the researchers. As described previously in detail, CCF length (centimeters) was measured from the genu of the corpus callosum (outer border) to the fastigium, and CC length (centimeters), from genu to the splenium (outer-outer border) (Online Supplemental Data).⁹

Head circumference (centimeters) was measured during the NICU stay as part of standard care using a tape measure. Growth *z* scores were based on the Fenton Growth Charts from birth until discharge or 50 weeks' GA and on the World Health Organization growth charts thereafter.¹⁶

For this study, we used measurements of CCF length, CC length, and HC assessed at the following times: 1) birth (postnatal age, days 1–3); 2) around 29 weeks' GA (28–30 weeks); and 3) at NICU transfer to a level II hospital (limited to 30–36 weeks' GA). Growth rate (millimeters/week) of CCF length, CC length, and HC was calculated between birth and NICU transfer. To increase homogeneity in timing and the length of the growth periods, we only calculated growth rate when the first CUS was performed in the first week of life and the period between 2 measurements covered at least 14 days.

In study B, CUS and HC measurements were also performed at the routine outpatient clinic visit at a median of 6.9 weeks' CA (interquartile range [IQR], 6.1–8.3 weeks), further referred to as the 2 months' visit. In these infants, the growth rate of each marker was also calculated between birth and 2 months.

Neurodevelopmental Outcome

As part of the national neonatal follow-up program, all children were routinely invited to the outpatient clinic at 2 years' CA for physical and neurologic examinations by a neonatologist or pediatric neurologist. Trained physiotherapists and psychologists performed extensive testing of psychomotor and cognitive development using fine-motor and gross motor (summarized in a total motor score) and cognitive tests of the Bayley Scales of Infant and Toddler Development, 3rd edition (Bayley-III, Dutch edition), expressed as standard scores adjusted for CA at the moment of testing.¹⁷ Following Dutch guidelines, the Lexi list was used to evaluate expressive language development. This validated questionnaire is completed by parents to quantify the child's vocabulary with scores adjusted for CA at assessment and sex.¹⁸ For each child, parents were asked to complete the Child Behavior Checklist 1.5–5 years (CBCL 1.5–5), which is an internationally validated questionnaire examining behavioral and emotional problems.¹⁹ For this study, we used the CBCL Total Problems scale expressed in T-scores adjusted for CA at assessment and sex. Assessors and parents were unaware of CC or CCF length measurements.

Statistical Analysis

Because the presence and severity of brain injury in the neonatal period can influence both brain growth and neurodevelopmental outcome disproportionately,²⁰ we mainly focused on the large group of infants without any brain injury on neonatal CUS. To explore the value of the brain growth markers in the presence of brain injury, we performed additional exploratory analyses in the smaller and more heterogeneous group with any extent of neonatal brain injury on CUS. Relative risks for adverse outcomes were calculated comparing infants with and without brain injury.

First, we used nonparametric statistical tests for nonresponse analyses. Second, we used linear regression models to study the associations between length (at birth, 29 weeks' GA, NICU transfer, and 2 months' CA) and growth rate (between birth and

NICU transfer and between birth and 2 months) of the CCF, CC, and HC and the 4 neurodevelopmental outcomes (motor, cognitive, language, and behavior) at 2 years' CA in both groups. In the basic models, we adjusted for GA or CA at CUS assessment. The adjusted models were additionally corrected for sex, GA at birth, birth weight z score, and parental education on the basis of relevance reported in the literature.^{5,21} These 4 covariates were tested and confirmed to show either a statistical association with at least 1 of the 2 ultrasonic brain markers at 2 months and cognitive outcome or a change in the effect size of $>10\%$ after addition of the covariate to the basic model. Given the number of participants and variables in our models and to limit type I or II error, we only performed analyses when at least 40 measurements were available per analysis. For comparability of effect sizes, associations are reported by steps resembling the average IQR of each marker. We observed no significant interactions between any of the brain markers and sex.

Third, we evaluated the added clinical value of the brain markers in predicting neurodevelopmental outcome in infants without brain injury, compared with prediction based on neonatal risk factors and head circumference only. As baseline, a "basic neonatal" regression model was used for prediction of cognitive outcome. This model was recently created in a preterm population overlapping this cohort.²² This model included sex, GA at birth, combined parental education level, grade of bronchopulmonary dysplasia (no/mild/severe), treated patent ductus arteriosus (medically and surgically), brain injury, and the duration of the hospital admission. Because this analysis was performed in the group of infants without any brain injury, we did not include "brain injury" as a covariate in the basic neonatal model of the current study. Using linear hierarchical regression models and explained variances (R^2), we compared the basic neonatal model (both with and without HC) with models that additionally included any CUS markers associated with neurodevelopmental outcomes.

P values (2-tailed) $< .05$ were considered statistically significant. We calculated 95% confidence intervals for all effect estimates. Correction for multiple testing was not deemed necessary given the step-based and exploratory character of the analyses. Data were analyzed using SPSS Statistics, Version 25.0 (IBM) and R statistical and computing software (<http://www.r-project.org/>).

RESULTS

Study Population

Of 293 eligible children, 225 (77%) were included in this study (Online Supplemental Data), of whom 153 (68%) showed no brain injury on CUS during the neonatal period. Nonresponse analyses showed that included children more often were Western, had slightly higher birth weights, and encountered fewer complications during the NICU stay (data not shown). Parental, perinatal, and neonatal characteristics were mostly similar in infants with and without brain injury (Online Supplemental Data).

Markers of Brain Growth

Length and growth rate of the CC, CCF, and HC are presented in the Online Supplemental Data. The correlation of CC length and CCF length compared with HC during the NICU stay is plotted in the Online Supplemental Data. At all 4 time points, the

absolute length of all 3 markers appeared to be slightly larger in infants without brain injury compared with infants with brain injury. In both groups, the length of the CCF, CC, and HC increased with time. Also, the growth rate of CCF length, and even more so CC length, decreased after transfer from the NICU to a level II hospital (median $31^{+5} - 32^{+1}$ weeks' GA), while the growth rate of HC increased.

Neurodevelopmental and Neurologic Outcomes

Scores on the 4 neurodevelopmental tests as well as the prevalence and relative risk of neurologic complications are listed in the Online Supplemental Data. In general, outcomes were less favorable in infants with brain injury, with 11% having cerebral palsy compared with 3% (risk ratio, 3.4; 95% CI, 1.2–10.0) and 11% having visual disorders compared with 5% in those without brain injury (risk ratio, 2.1; 95% CI, 0.8–5.4). In both groups, all 4 neurodevelopmental tests showed median scores within the normal range. However, moderate or severe motor impairment was more common in those with brain injury (14% versus 5%; risk ratio, 2.7; 95% CI, 1.1–6.5).

Associations between Brain Length or Growth and Neurodevelopmental Outcome

In infants without neonatal brain injury, larger CCF length at 2 months was associated with better cognitive outcome: Every IQR (5 mm) increase in CCF length was associated with a 9.1 (95% CI, 2.4–15.8) point higher Bayley-III cognitive score (Online Supplemental Data). As for CC length, we observed a 5.9 (95% CI, 2.8–9.1) point higher Bayley-III cognitive score, a 4.6 (95% CI, 1.3–8.0) point higher total motor score, and a 6.5 (95% CI, 2.0–11.0) point higher language score for every IQR (5 mm) increase at 2 months. In addition, a 5-mm larger CC length at birth was associated with a 5.9 (95% CI, 0.4–11.4) point higher motor score. HC was also positively associated with multiple neurodevelopmental outcomes: For every IQR (20 mm) increase at 2 months, we observed a 7.2 (95% CI, 2.9–11.6) point increase in cognitive score and an 8.7 (95% CI, 2.7–14.7) point higher Lexi score.

Each IQR (0.25 mm/week) increase in the CC growth rate between birth and 2 months was associated with a 5.1 (95% CI, 0.9–9.4) point higher cognitive score and a 4.5 (95% CI, 0.1–8.9) point higher motor score. An IQR (1 mm/week) faster HC growth in this period was associated with a 5.8 (95% CI, 0.9–10.7) point higher Lexi score. We did not observe any associations between the growth rate of CCF length and neurodevelopmental outcomes. In the brain injury group, results were only available for the associations of absolute length of the CC, CCF, and HC at birth and 29 weeks' GA and neurodevelopmental outcomes, due to too-small group sizes ($n < 40$) at the other time points. None of these associations were statistically significant (Online Supplemental Data). Results of the basic models, not corrected for sex, GA at birth, birth weight z score, and parental education, are presented in the Online Supplemental Data.

Added Value of CUS Brain Markers for Outcome Prediction

In the Online Supplemental Data, we present the added values of CC and CCF length at 2 months to the prediction of the 3

associated neurodevelopmental outcomes (cognitive, motor, and language) by neonatal risk factors in infants without brain injury. Compared with the basic neonatal model with or without HC, adding CC length led to an 8.8%–9.8% increase in the explained variance (R^2) of cognitive and language outcomes ($P < .05$). There was no added value of (additionally) including CCF length in any of the models for predicting motor, cognitive and language outcomes.

DISCUSSION

In this longitudinal study of 225 infants born very preterm, larger CCF length at 2 months' CA in infants without brain injury was associated with better cognitive outcome at 2 years' CA. As for the CC, larger length at 2 months' CA and a faster growth rate from birth to 2 months were associated with higher cognitive, motor, and language scores at 2 years' CA. These associations were similar to those observed for head circumference. Prediction of neurodevelopmental outcome based on neonatal risk factors and head circumference significantly improved when CC length, but not CCF length, at 2 months was additionally taken into account.

CCF length is a new reliable marker of brain growth that captures a large part of the brain and is related to fetal growth restriction.^{10,11} We showed that in infants without brain injury, CCF length was related to cognitive outcome but had no added clinical value in the prediction of neurodevelopment. Because this is the first study to explore this association, there are no previous studies with which to compare it. The lack of predictive power may have different explanations. First, the anatomic structures that are covered by CCF length (diencephalon, thalamus, mesencephalon) are important areas of the brain, but the cerebellum and WM (as reflected by the CC) are not incorporated into CCF length. Yet these parts of the brain may be more susceptible to external factors influencing brain growth and may, therefore, be more important for outcome in this specific patient group and time period after birth.^{23,24} Second, measurement error may have played a role. However, we consider this explanation less likely because we previously showed adequate reproducibility and reliability of CCF length in a similar setting, and all measurements were performed by 2 experienced researchers.^{9,10}

The positive associations of CC length at 2 months' CA with cognitive, motor, and language outcome, and CC growth until 2 months with cognitive and motor function are in line with previous MR imaging and CUS studies and reflect the importance of the CC as the major WM pathway in the brain.^{6-8,25-27} WM is involved in different domains of neurodevelopment and is very susceptible to injury or microinjury by external factors, including neonatal complications experienced after preterm birth.²⁶ Therefore, in this specific patient group, it is likely that CC size reflects the extent of injury of the WM, which translates to later neurodevelopment. This may also explain why CC length and growth appear to be more strongly associated with neurodevelopmental outcomes than HC. Most interesting, apart from the association between CC length at birth and motor outcome, we only observed associations with outcome when CC length was measured after NICU transfer (>30 – 32 weeks' GA) and not during the NICU stay. These findings are comparable with those in the CUS studies of Anderson et al,^{26,27}

who reported a relation with the Bayley motor scores at 2 years for CC growth between 2 and 6 weeks after birth (30–34 weeks' GA), but not for CC growth in the first 2 weeks after birth in a similar preterm population. We hypothesize that in infants without brain damage, the period after the NICU stay may be more critical for neurodevelopment. This hypothesis is supported by the decrease in the CC growth rate after NICU transfer observed in this and other studies, likely due to the impact of more chronic complications like bronchopulmonary dysplasia.^{5,27-29}

None of the brain markers were associated with behavioral outcome. This finding may reflect the complex and multifactorial origin of behavior development, which hampers adequate prediction of later behavioral problems, especially at a young age. Furthermore, the CBCL 1.5–5 years used in this study is a screening questionnaire that roughly estimates problem behavior but is not suitable for diagnosis. In addition, underreporting of behavioral problems by parents might be an issue. Nonetheless, a very recent MR imaging study linked global brain abnormalities at term age with the CBCL total problems score at 2 years' CA.³⁰ An important difference compared with our study is that they used detailed and comprehensive Kidokoro scoring on MR images compared with a single CUS measure in our study.³¹

The observed associations of CC length at 2 months with neurodevelopmental outcomes were not stronger than those of HC. However, CC length at 2 months still showed significant added value in the prediction of neurodevelopment compared with prediction based on neonatal risk factors and head circumference only. These findings are the opposite of the conclusion that was drawn in a similar study of 87 very preterm infants by Perenyi et al,⁷ who stated that measuring CC length on CUS in early life had no additional clinical value. To further explore and improve the potential clinical value of CUS at 2 months in neonatal follow-up programs, future studies could explore combining different CUS brain markers (eg, CC length, CCF length, ventricular size, biparietal diameter, vermis length, and cerebellar width) with CUS injury scores to predict neurodevelopmental outcome.

Strengths and Limitations

This study is unique in studying CCF length in relation to neurodevelopment in preterm infants. The availability of longitudinally performed CUS enabled us to study brain markers both during and after NICU admission. Another strength of this study is the relatively large cohort of preterm infants without brain damage, representing a part of the NICU population in whom neurodevelopment has always been difficult to predict. Our data confirm that in those with neonatal brain injury, neurodevelopmental outcomes are less favorable.

Our study also has limitations. First, the group of infants with brain injury was too small and heterogeneous to perform reliable analyses at NICU transfer and 2 months or on growth of the CC and CCF length and HC. Also, the observed lack of associations at birth and 29 weeks' GA in this group should be interpreted with caution because these analyses also contained small numbers of ultrasounds/infant. Future studies should explore how the observed associations in infants without any brain injury hold in a large cohort of children with brain injury. Larger cohorts are also needed to disentangle which types of brain injury affect brain

growth and neurodevelopment most. Second, no CUS was performed around term-equivalent age because, per national policy, infants were transferred to a level II hospital when they were stable, most often around 30–32 weeks' gestation. Third, we were unable to correct for other psychological factors related to neurodevelopment, such as parenting or parental mental health. However, we believe that the most important perinatal, neonatal, and sociodemographic confounders have been covered. Last, the Bayley-III test is a commonly used—but-rough estimate of global neurodevelopment with limited predictive value for later intelligence quotient performance.³² Therefore, follow-up of this cohort into school age is needed.

CONCLUSIONS

This prospective study of infants born very preterm without asphyxia, severe congenital abnormalities, or infections showed the clinical benefit of 2 brain-growth markers, which can be easily measured on CUS. Especially, the CC (length and growth) but also CCF (length) at 2 months' CA were associated with various important neurodevelopmental outcomes at 2 years' CA. Furthermore, CC length but not CCF length showed a significant added clinical value to the prediction of neurodevelopment based on neonatal risk factors and head circumference.

ACKNOWLEDGMENTS

We would like to express our thanks to all children and parents for their cooperation and to Arianne Jacobse for her logistical support.

Disclosure forms provided by the authors are available with the full text and PDF of this article at www.ajnr.org.

REFERENCES

- Young JM, Powell TL, Morgan BR, et al. **Deep grey matter growth predicts neurodevelopmental outcomes in very preterm children.** *Neuroimage* 2015;111:360–68 CrossRef Medline
- Pascal A, Govaert P, Oostra A, et al. **Neurodevelopmental outcome in very preterm and very-low-birthweight infants born over the past decade: a meta-analytic review.** *Dev Med Child Neurol* 2018;60:342–55 CrossRef Medline
- Armstrong DL, Bagnall C, Harding JE, et al. **Measurement of the subarachnoid space by ultrasound in preterm infants.** *Arch Dis Child Fetal Neonatal Ed* 2002;86:F124–26 CrossRef Medline
- Kawasaki Y, Yoshida T, Matsui M, et al. **Clinical factors that affect the relationship between head circumference and brain volume in very-low-birth-weight infants.** *J Neuroimaging* 2019;29:104–10 CrossRef Medline
- Cuzzilla R, Spittle AJ, Lee KJ, et al. **Postnatal brain growth assessed by sequential cranial ultrasonography in infants born <30 weeks' gestational age.** *AJNR Am J Neuroradiol* 2018;39:1170–76 CrossRef Medline
- Park HW, Yoon HK, Han SB, et al. **Brain MRI measurements at a term-equivalent age and their relationship to neurodevelopmental outcomes.** *AJNR Am J Neuroradiol* 2014;35:599–603 CrossRef Medline
- Perenyi A, Amodio J, Katz JS, et al. **Clinical utility of corpus callosum measurements in head sonograms of preterm infants: a cohort study.** *BMJ Open* 2013;3:e002499 CrossRef Medline
- Klebermass-Schrehof K, Aumüller S, Goeral K, et al. **Biometry of the corpus callosum assessed by 3D ultrasound and its correlation to neurodevelopmental outcome in very low birth weight infants.** *J Perinatol* 2017;37:448–53 CrossRef Medline
- Roelants JA, Koning IV, Raets MM, et al. **A new ultrasound marker for bedside monitoring of preterm brain growth.** *AJNR Am J Neuroradiol* 2016;37:1516–22 CrossRef Medline
- Koning IV, Roelants JA, Groenenberg IAL, et al. **New ultrasound measurements to bridge the gap between prenatal and neonatal brain growth assessment.** *AJNR Am J Neuroradiol* 2017;38:1807–13 CrossRef Medline
- Pharande P, Krishnamurthy M, Whiteley G, et al. **Ultrasound measurements of intracranial structures in growth-restricted neonates with fetal blood flow redistribution: a pilot observational study.** *Neonatology* 2020;117:446–52 CrossRef Medline
- Raets MM, Sol JJ, Govaert P, et al. **Serial cranial US for detection of cerebral sinovenous thrombosis in preterm infants.** *Radiology* 2013;269:879–86 CrossRef Medline
- Roelants JA, Joosten KF, van der Geest BM, et al. **First week weight dip and reaching growth targets in early life in preterm infants.** *Clin Nutr* 2018;37:1526–33 CrossRef Medline
- van Houdt CA, van Wassenaer-Leemhuis AG, Oosterlaan J, et al. **Developmental outcomes of very preterm children with high parental education level.** *Early Hum Dev* 2019;133:11–17 CrossRef Medline
- Volpe J. *Neurology of the Newborn*. 5th ed. Saunders Elsevier; 2008:517–88
- Fenton TR, Kim JH. **A systematic review and meta-analysis to revise the Fenton growth chart for preterm infants.** *BMC Pediatr* 2013;13:59 CrossRef Medline
- Bayley N. *Bayley Scales of Infant and Toddler Development*. 3rd ed. San Antonio, TX: Harcourt Assessment. *Journal of Psychoeducational Assessment*; 2007 CrossRef
- Schlichting JE, van Eldrik MC, Lutje Spelberg HC, et al. *Schlichting Test for Expressive Language*. Berkhout BV; 1987
- Achenbach TM, Rescola LA. **Manual for the ASEBA Preschool Forms & Profiles**. 2000 https://www.researchgate.net/publication/243771256_Manual_for_the_ASEBA_Preschool_forms_profiles. Accessed February 19, 2020
- Kidokoro H, Anderson PJ, Doyle LW, et al. **Brain injury and altered brain growth in preterm infants: predictors and prognosis.** *Pediatrics* 2014;134:e444–53 CrossRef Medline
- Cormack BE, Harding JE, Miller SP, et al. **The influence of early nutrition on brain growth and neurodevelopment in extremely preterm babies: a narrative review.** *Nutrients* 2019;11:2029 CrossRef Medline
- Beunders VA, Vermeulen MJ, Roelants JA, et al. **Early visuospatial attention and processing and related neurodevelopmental outcome at 2 years in children born very preterm.** *Pediatr Res* 2021;90:608–16 CrossRef Medline
- Van Kooij BJ, Benders MJ, Anbeek P, et al. **Cerebellar volume and proton magnetic resonance spectroscopy at term, and neurodevelopment at 2 years of age in preterm infants.** *Dev Med Child Neurol* 2012;54:260–66 CrossRef Medline
- Campbell H, Check J, Kuban KC, et al. **Neonatal cranial ultrasound findings among infants born extremely preterm: associations with neurodevelopmental outcomes at ten years of age.** *J Pediatr* 2021;237:197–205.e4 CrossRef Medline
- Malavolti AM, Chau V, Brown-Lum M, et al. **Association between corpus callosum development on magnetic resonance imaging and diffusion tensor imaging, and neurodevelopmental outcome in neonates born very preterm.** *Dev Med Child Neurol* 2017;59:433–40 CrossRef Medline
- Anderson NG, Laurent I, Cook N, et al. **Growth rate of corpus callosum in very premature infants.** *AJNR Am J Neuroradiol* 2005;26:2685–90 Medline
- Anderson NG, Laurent I, Woodward LJ, et al. **Detection of impaired growth of the corpus callosum in premature infants.** *Pediatrics* 2006;118:951–60 CrossRef Medline

28. Huang HC, Chou HC, Tsao PN, et al. **Linear growth of corpus callosum and cerebellar vermis in very-low-birth-weight preterm infants.** *J Formos Med Assoc* 2020;119:1292–98 CrossRef Medline
29. Lee JM, Choi YH, Hong J, et al. **Bronchopulmonary dysplasia is associated with altered brain volumes and white matter microstructure in preterm infants.** *Neonatology* 2019;116:163–70 CrossRef Medline
30. Jansen L, van Steenis A, van den Berg-Huysmans AA, et al. **Associations between neonatal magnetic resonance imaging and short- and long-term neurodevelopmental outcomes in a longitudinal cohort of very preterm children.** *J Pediatr* 2021;234:46–53.e2 CrossRef Medline
31. Kidokoro H, Neil JJ, Inder TE. **New MR imaging assessment tool to define brain abnormalities in very preterm infants at term.** *AJNR Am J Neuroradiol* 2013;34:2208–14 CrossRef Medline
32. Anderson PJ, Burnett A. **Assessing developmental delay in early childhood: concerns with the Bayley-III scales.** *Clin Neuropsychol* 2017;31:371–81 CrossRef Medline

Same-Day Bilateral Decubitus CT Myelography for Detecting CSF-Venous Fistulas in Spontaneous Intracranial Hypotension

L. Carlton Jones and P.J. Goadsby



ABSTRACT

SUMMARY: Lateral decubitus CT myelography is a sensitive technique for detecting CSF-venous fistulas in patients with spontaneous intracranial hypotension. It might be necessary to perform bilateral studies to locate a fistula. We report on the feasibility of obtaining diagnostic-quality bilateral decubitus CT myelography in a single session, avoiding the need to schedule separate examinations for the left and right sides on different days.

ABBREVIATIONS: CTM = CT myelography; CVF = CSF-venous fistula; DSM = digital subtraction myelography; SIH = spontaneous intracranial hypotension

Spontaneous intracranial hypotension (SIH) is a debilitating condition that results from leakage of CSF from the spine. In up to one-quarter of patients with SIH, the underlying cause is a CSF-venous fistula (CVF), an abnormal connection between the subarachnoid space of a nerve root sheath and adjacent veins.¹ Targeted treatment of CVFs, by injection of blood and/or fibrin sealant,² endovascular occlusion, or neurosurgery requires accurate localization of the fistula. Performing CT myelography (CTM) or digital subtraction myelography (DSM) with the patient in the lateral decubitus position increases the sensitivity for CVFs by exposing the nerve root sleeves on the dependent side to a higher concentration of contrast.^{1,3,4} Although most CVFs occur in the thoracic spine on the right side,⁵ on which side a CVF will be found cannot be known beforehand. Moreover, CVFs can rarely occur bilaterally.^{6,7} A complete examination, therefore, requires bilateral decubitus myelograms. Currently most centers undertaking lateral decubitus CTM or DSM examine the right and left sides on separate days, primarily because of manufacturer-set dose constraints on the maximum intrathecal iodine dose^{8,9} but also because the contrast is diluted by CSF when turning the patient to the opposite side, which leads to decreased opacification of meningeal diverticula.⁸ This practice is

inconvenient for patients and radiology departments alike, even if studies are scheduled across 2 consecutive days. We report our experience in performing bilateral decubitus CTM in the same session.

MATERIALS AND METHODS

Subjects

Institutional review board approval was not required for this retrospective service evaluation. We evaluated our service by reviewing consecutive patients with SIH who were investigated by same-day bilateral decubitus CTM for a suspected CVF between December 2020 and May 2021, all of whom met the International Classification of Headache Disorders, 3rd edition, criteria for SIH.¹⁰ All patients had undergone brain MR imaging with contrast and spine MR imaging; one of the patients had previously undergone prone CTM, which had negative findings for a cause of the CSF leak.

Procedural Technique

The technique is a modification of that described previously.⁸ Patients were placed in the lateral decubitus position on the CT scanner table with the pelvis raised above their shoulders by a foam wedge and with their arms raised by their faces or above their heads. CT fluoroscopically-guided lumbar puncture was performed at L3–L4 or L2–L3 with a 22-ga spinal needle and the subarachnoid position of the needle tip confirmed by a test injection of 0.5 mL of iohexol containing 300 mg I/mL (Omnipaque, GE Healthcare). The theca was then prepressurized by a slow injection of 10 mL of sterile normal saline in an attempt to encourage leaking and also to dilute the test dose of contrast before 6–8 mL of contrast was injected intrathecally, after which the spine was scanned immediately from the lumbar puncture needle to the

Received December 29, 2021; accepted after revision February 7, 2022.

From the Department of Radiology (L.C.J.), Guy's and St. Thomas Hospitals National Health Service Foundation Trust, St. Thomas' Hospital, London, UK; Department of Neuroradiology (L.C.J.), King's College Hospital National Health Service Foundation Trust, London, UK; and National Institute for Health Research Wellcome Trust King's Clinical Research Facility (P.J.G.), King's College Hospital, London, UK.

Please address correspondence to Lalani Carlton Jones, MA, MBBS, MRCS, FRCR, Department of Radiology, Guy's and St. Thomas Hospitals NHS Foundation Trust, St. Thomas' Hospital, Westminster Bridge Rd, London, SE1 7EH, UK; e-mail: lalani.carltonjones@nhs.net; @NeuroradLal

<http://dx.doi.org/10.3174/ajnr.A7476>



FIG 1. Left T5 CVF with contralateral venous drainage and subsequent treatment. *A*, Axial right lateral decubitus CTM image shows dependent layering of contrast on the right side of the subarachnoid space but no leak. *B*, Axial left lateral decubitus CTM image shows more uniform distribution of contrast within the subarachnoid space following turning of the patient but also abnormal left radicular veins opacified by dense contrast (*dashed arrow*) and a hyperdense right paravertebral vein (*arrow*). *C*, Axial left lateral decubitus CTM MIP image shows transvertebral intraosseous drainage of the CVF to the right side (*arrow*). *D*, Axial posttreatment CT shows contrast-opacified fibrin sealant filling the foramen (*arrow*) and extending into the epidural space of vertebral canal.

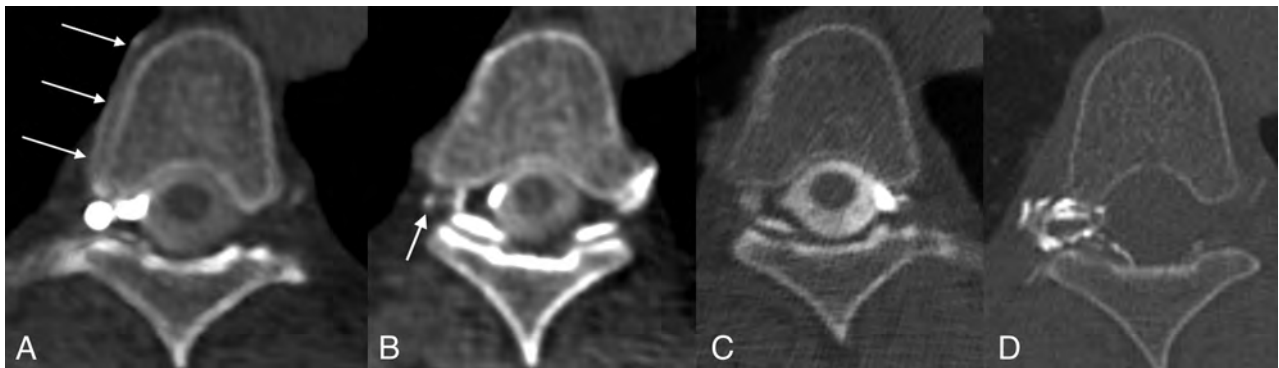


FIG 2. Right T5 CVF and subsequent treatment. *A*, Axial right lateral decubitus CTM image shows a right foraminal meningeal diverticulum and a hyperdense right paraspinal vein (*arrows*). *B*, Axial right lateral decubitus CTM image obtained immediately caudal to (*A*) shows opacification of a small radicular vein (*arrow*). *C*, Axial left lateral decubitus CTM image shows no abnormality. *D*, Axial posttreatment CT shows contrast-opacified fibrin sealant filling the foramen and extending into the epidural space of vertebral canal.

craniocervical junction during breath-holding in maximum inspiration. Acquisition parameters were pitch = 0.984, rotation time = 800 ms, reconstruction thickness = 0.625 mm, automated exposure control, tube current = 300–800 mA, tube voltage = 120 kV(peak). Images were reviewed at the console for signs of a CVF, including a hyperdense paraspinal vein and opacification of radicular veins in the neural foramen adjacent to a meningeal diverticulum. With the needle still in place, the patient was then assisted to turn carefully from the first decubitus position to lie initially prone and then to the opposite lateral decubitus position. The position of the needle was monitored at all times by the neuroradiologist performing the procedure, while additional staff assisted the patient with turning, avoiding bending or twisting of the lumbar spine. A new scan projection radiograph was acquired, and a limited scan was acquired through the needle to check that it had not become displaced from the vertebral canal during patient repositioning. A further 6–8 mL of iodinated contrast was then injected, and scanning of the spine was repeated as on the first side.

RESULTS

Three patients, 54, 64, and 67 years of age, underwent same-day bilateral decubitus CTM during the study period. Two subjects

were women. All subjects had orthostatic headache, and 1 also had cognitive impairment in the form of a frontotemporal dementia-like presentation of SIH. Brain MR imaging showed features of SIH in all cases: All subjects showed diffuse dural enhancement, venous sinus distension, pituitary enlargement, and brain sag; none had subdural fluid collections. The Bern score for brain MR imaging was 8 for all subjects, indicating a high probability of a spinal CSF leak.¹¹ No subjects had spinal epidural fluid collections; thus, a CVF was considered the most likely cause of the SIH, with a distal nerve root sleeve dural tear beyond the epidural compartment being possible but less likely.¹² In 2 cases, the right side was examined first. In all 3 cases, decubitus CTM showed a single CVF, located in the right T11, right T5, and left T5 neural foramina, respectively. In 2 cases, the CVF was on the second side to be examined. The left T5 CVF drained to a right paravertebral vein via an intraosseous vein (Fig 1), the right T11 and right T5 CVFs drained into an ipsilateral paravertebral vein at the same level (Fig 2). The procedures were well-tolerated by the subjects with no adverse events during repositioning aside from minor bending of the spinal needle; in no case was the needle tip displaced from the spinal subarachnoid space, and no cases of subdural or epidural contrast injection occurred. Total

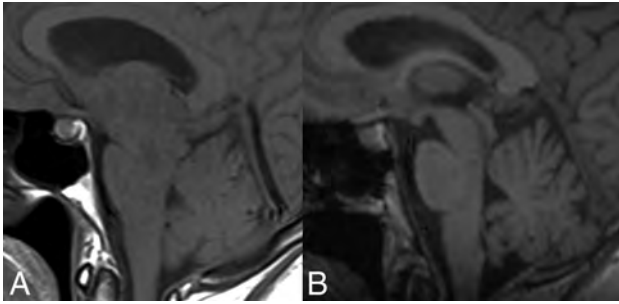


FIG 3. Pre- and posttreatment MRIs of the patient in Fig 2. *A*, Sagittal T1-weighted MR imaging shows brain sag with narrowing of the mamillopontine distance, narrowing of the prepontine cistern, and inferior sloping of the floor of the third ventricle. There is also pituitary enlargement and distension of the straight sinus. *B*, Resolution of these changes following CT-guided injection of fibrin sealant.

contrast volumes injected ranged from 12 to 16 mL, split equally between sides. Each subject subsequently underwent a CT-guided percutaneous injection of fibrin sealant (TISSEEL; Baxter) directed at the CVF, targeting the junction of the diverticulum and the draining vein to place fibrin sealant within and around the diverticulum. This resulted in symptom improvement and improvement of imaging findings of SIH in all cases (Fig 3).

DISCUSSION

This report presents the feasibility of obtaining diagnostic-quality bilateral decubitus CTM during a single session. Hitherto, it has been the usual practice to schedule decubitus CTM or DSM examinations of the right and left sides on separate days to comply with dose constraints for iodinated contrast in view of the possible risks of neurotoxicity, including seizures and arachnoiditis. The manufacturer-set intrathecal dose limits of 3 g of iodine for the nonionic contrast media iohexol and iopamidol were based on earlier toxicity studies of the ionic agent metrizamide, despite evidence that the newer agents were less neurotoxic.¹³ Subsequently, dose-finding studies comparing iomeprol, iopamidol, and iohexol for myelography have found that doses up to 4.5 g of iodine were well-tolerated,¹⁴ and intrathecal doses of up to 6 g of iodine have been used in dynamic fluoroscopic myelography for localizing spinal CSF leaks without adverse effects.¹⁵ We determined, therefore, that the manufacturers' 3 g dose limit should not necessarily be a barrier to performing bilateral decubitus CTM on the same day, and we were able to obtain diagnostic-quality bilateral studies with total doses between 3.6 and 4.8 g. Because this was an off-label use of the contrast medium, patients gave consent regarding this use. Because our prior practice for single-side decubitus CTM had been to use 10 mL of iohexol, 300 mg I/mL, in accordance with a previously reported technique,⁸ we initially used 8 mL of contrast per side for the same-day technique to decrease the risk of achieving suboptimal intrathecal opacification and a nondiagnostic study. When a nondiagnostic study did not occur, we subsequently decreased the dose further to 6 mL per side without any deleterious effect on intrathecal opacification or the ability to identify a CVF. It may be possible to obtain diagnostic-quality bilateral decubitus CTM with as little as 5 mL of contrast per side, thus not exceeding the

recommended dose limit for intrathecal iodine; this dose is the subject of current investigation.

In 2 cases, the CVF was on the second side to be examined. Given the right-sided preponderance of CVFs,⁵ an argument could be made for starting with a right lateral decubitus CTM to maximize the chance of detecting a CVF at the earliest stage, potentially obviating the need to examine the opposite side. However, in view of the reported occurrence, albeit rare, of bilateral CVFs,^{6,7} we recommend always examining both sides even if a CVF is detected on the first side studied.

Benefits of our approach include greater convenience for the patient, including avoidance of a second lumbar puncture for opposite side decubitus CTM on a subsequent day and more efficient use of the CT scanner and neuroradiologist's time. Avoiding a second CT fluoroscopy-guided lumbar puncture also decreases the radiation dose of same-day decubitus CTM compared with 2 procedures on separate days. Potential drawbacks include the risk of needle displacement during repositioning and subsequent injury to neural or vascular structures, as well as the potential for subdural or epidural contrast injection if the needle tip moves, though this did not occur in any of our cases. Although we observed that the spinal needle became bent during repositioning, this result did not have any adverse effect on the subjects or the performance or outcome of the procedure. Although we did not experience any difficulty repositioning patients on the foam wedge, alternative means of elevating the patient's pelvis without requiring movement on the CT table, such as placing an inflatable mattress (HoverMatt; HoverTech International) under the patient's hips and inflating it transiently after the intrathecal injection of contrast, might represent further refinements to the technique.¹⁶

CONCLUSIONS

Same-day bilateral decubitus CT myelography can be performed successfully and can result in a diagnostic-quality examination without adverse effects on the patient. This is more convenient for patients and radiology departments, obviating the need for a second procedure, which may carry potential additional risk.

Disclosure forms provided by the authors are available with the full text and PDF of this article at www.ajnr.org.

REFERENCES

1. Schievink WI, Maya MM, Moser FG, et al. **Lateral decubitus digital subtraction myelography to identify spinal CSF-venous fistulas in spontaneous intracranial hypotension.** *J Neurosurg Spine* 2019 Sep 13 [Epub ahead of print] CrossRef Medline
2. Mamlouk MD, Shen PY, Sedrak MF, et al. **CT-guided fibrin glue occlusion of cerebrospinal fluid-venous fistulas.** *Radiology* 2021; 299:409–18 CrossRef Medline
3. Kranz PG, Gray L, Amrhein TJ. **Decubitus CT myelography for detecting subtle CSF leaks in spontaneous intracranial hypotension.** *AJNR Am J Neuroradiol* 2019;40:754–56 CrossRef Medline
4. Kim DK, Brinjikji W, Morris PP, et al. **Lateral decubitus digital subtraction myelography: tips, tricks, and pitfalls.** *AJNR Am J Neuroradiol* 2020;41:21–28 CrossRef Medline
5. Shlobin NA, Shah VN, Chin CT, et al. **Cerebrospinal fluid-venous fistulas: a systematic review and examination of individual patient data.** *Neurosurgery* 2021;88:931–41 CrossRef Medline

6. Brinjikji W, Savastano LE, Atkinson JLD, et al. **A novel endovascular therapy for CSF hypotension secondary to CSF-venous fistulas.** *AJNR Am J Neuroradiol* 2021;42:882–87 CrossRef Medline
7. Schievink WI, Maya MM, Moser F, et al. **Multiple spinal CSF leaks in spontaneous intracranial hypotension: do they exist?** *Neurol Clin Pract* 2021;11:e691–97 CrossRef Medline
8. Mamlouk MD, Ochi RP, Jun P, et al. **Decubitus CT myelography for CSF-venous fistulas: a procedural approach.** *AJNR Am J Neuroradiol* 2021;42:32–36 CrossRef Medline
9. Pope MC, Carr CM, Brinjikji W, et al. **Safety of consecutive bilateral decubitus digital subtraction myelography in patients with spontaneous intracranial hypotension and occult CSF leak.** *AJNR Am J Neuroradiol* 2020;41:1953–57 CrossRef Medline
10. **Headache Classification Committee of the International Headache Society (IHS) The International Classification of Headache Disorders, 3rd edition.** *Cephalalgia* 2018;38:1–211 CrossRef Medline
11. Dobrocky T, Grunder L, Breiding PS, et al. **Assessing spinal cerebrospinal fluid leaks in spontaneous intracranial hypotension with a scoring system based on brain magnetic resonance imaging findings.** *JAMA Neurol* 2019;76:580–87 CrossRef Medline
12. Farb RI, Nicholson PJ, Peng PW, et al. **Spontaneous intracranial hypotension: A systematic imaging approach for CSF leak localization and management based on MRI and digital subtraction myelography.** *AJNR Am J Neuroradiol* 2019;40:745–53 CrossRef Medline
13. Halpin SFS, Guest PJ, Byrne J. V. **Theory and practice: how much contrast for myelography?** *Neuroradiology* 1991;33:411–13 CrossRef Medline
14. Katayama H, Heneine N, Van Gessel R, et al. **Clinical experience with iomeprol in myelography and myelo-CT: clinical pharmacology and double-blind comparisons with iopamidol, iohexol, and iotrolan.** *Invest Radiol* 2001;36:22–32 CrossRef Medline
15. Piechowiak EI, Pospieszny K, Haeni L, et al. **Role of conventional dynamic myelography for detection of high-flow cerebrospinal fluid leaks: optimizing the technique.** *Clin Neuroradiol* 2021;31:633–41 CrossRef Medline
16. Soderlund KA, Mamlouk MD, Shah VN, et al. **Cerebrospinal fluid-lymphatic fistula causing spontaneous intracranial hypotension in a child with kaposiform lymphangiomatosis.** *Pediatr Radiol* 2021;51:2093–97 CrossRef Medline